Detection of hydrocarbons and their movement in a reservoir using time-lapse Multichannel Transient ElectroMagnetic (MTEM) data

David A. Wright

B.Sc. Geophysics (Edinburgh) 1998

M.Sc. Geophysics (Dunelm) 1999

Thesis submitted for the degree of

Doctor of Philosophy

University of Edinburgh

2004

Abstract

Using two time-lapse surveys over an underground gas storage reservoir in St. Illiers la Ville, in France, I demonstrate the potential for multichannel transient electromagnetic (MTEM) data to detect the presence and movement of hydrocarbons in the earth through a new approach to the acquisition and processing of the data. I introduce a new pre-processing methodology for noise reduction and deconvolution of the system response to recover the impulse response of the earth. The thesis is divided into three parts: overview of electromagnetic methods, modelling, and processing of MTEM data.

I carried out a comprehensive review of all electromagnetic (EM) methods in relation to hydrocarbon exploration. Of all these, the MTEM method provides the best resolution, detectability and spatial coverage of resistive targets. In the MTEM method a transient current is injected into the ground through a grounded dipole source and measurements of induced voltages at many receiver sites form the data for analysis.

1-D modelling indicates that the in-line component of the electric field is most sensitive to a buried resistor. The response of the cross-line component is about two orders of magnitude smaller, while the magnetic field is not sensitive to the resistor at all. Modelling the St. Illiers la Ville data shows that the response of the reservoir occurs between about 3 and 15ms, and at offsets greater than about 750m. I modelled in-line electric field data to test the application of a resistivity analysis using a seismic refraction analogy. The analysis was applied after transforming the data to a wave-like non-diffusive domain in log-time. The results indicate that the approach works only for a two-layer model and breaks down if the resistive layer is thin, typically less than a few hundred metres.

The new MTEM data processing methodology includes improved noise reduction through the application of a dip filter, and deconvolution for the system response each time the source is fired. This enables the impulse response of the earth to be recovered. Processing of two MTEM datasets from St Iliers la Ville reveals both the presence of the gas in the reservoir and the movement of the gas between the two surveys. The reservoir response occurs between about 4 and 13ms on in-line electric field data only. The response is seen only on data collected at an offset greater than 625m. The presence of the gas in the reservoir is also seen on in-line electric field data. The difference between the two data sets reveals an anomaly over one edge of the reservoir and no anomaly outside the reservoir. This indicates that movement of gas within the reservoir between the two surveys can be detected. Even though the changes in the gas content

of the reservoir between the two surveys were small, the repeatability of the data is sufficiently good that these small differences can be detected. The results of data processing, supported by evidence from modelling, demonstrate the ability of the MTEM method for hydrocarbon detection and monitoring.

Acknowledgements

First I would like to thank my supervisors Anton Ziolkowski and Bruce Hobbs. Over the course of this work they have always given freely of their time, provided advice and ideas that have helped me greatly. Their enthusiasm and positive outlook is always refreshing when things look bad. In addition, their detailed comments on numerous drafts of this thesis have greatly improved it. I would also like to thank Anton for funding conference trips to Amsterdam, San Antonio, Florence, Stavanger and Barcelona.

Much of the work in this thesis uses electromagnetic modelling programs. I would like to thank Knútur Árnason, Nigel Edwards and Kurt Strack who have all made their modelling code freely available.

At work I would like to thank Magi for his help with Linux and numerous other computing problems. I would also like to thank all the other PhD students at Edinburgh and the BGS who I have enjoyed/endured the last four years with.

Away from work I would like to thank the many FGM's and FGW's of Hunters Bog Trotters running club in Edinburgh with whom I have spent much of my spare time.

Finally I would also like to thank all of my family and in particular my mum and dad who have provided both moral and financial support as well as proof reading that has finally seen me through to the end. Last but not least, thanks to Megan for putting up with me during possibly the longest thesis writeup in history.

Contents

List of Figures

List of Tables

Conventions, Notation and Definitions

The conventions and notation presented in the thesis are given here and in general follow Hobbs (1992). For specific definitions refer to the main text. SI units are used in general. In cases where an alternative system of units is more commonly employed, the SI equivalent is given.

Scalar and Vector Quantities

Vector quantities are written in a bold typeface, for example $\boldsymbol{E}$, and scalar quantities in normal typeface, for example E.

Space and Time

A right-handed Cartesian reference frame is used throughout this thesis, with the z-axis increasing downwards. Let $\boldsymbol{x} = (x, y, z)$ denote the position vector in the Cartesian reference frame, and $\boldsymbol{e} = (e_x, e_y, e_z)$ denote the unit basis vector so that $\boldsymbol{x} = e_x x + e_y y + e_z z$. Let $r = \sqrt{(e_x x)^2 + (e_y y)^2 + (e_z z)^2}$. Let t denote time.

Special Functions

$$
\begin{array}{lll}
\delta(x) & \int_{-\infty}^{\infty} \delta(x - \eta) f(x) dx = f(\eta) & \text{the Dirac delta function} \\
\delta(\boldsymbol{x}) & \delta(x)\delta(y)\delta(z) & \text{the 3D Dirac delta function} \\
erf(x) & \frac{2}{\sqrt{\pi}} \int_0^x exp(-t^2) dt & \text{the error function} \\
erfc(x) & 1 - erf(x) & \text{complementary error function} \\
\mathcal{H}(t) & \begin{cases} 0 & t < 0 \\ \frac{1}{2} & t = 0 \\ 1 & t > 0 \end{cases} & \text{Heaviside or unit step function}
\end{array}
$$

Integral transforms

The Fourier transform of $\boldsymbol{F}(\boldsymbol{x}, t)$ with respect to t and transform parameter ω is

$$\tilde{\boldsymbol{F}}(\boldsymbol{x}, \omega) = \int_{-\infty}^{\infty} \boldsymbol{F}(\boldsymbol{x}, t) \exp(-i\omega t) dt,$$

where the change of domain is indicated by $\tilde{}$. The inverse transform is

$$\boldsymbol{F}(\boldsymbol{x}, t) = \frac{1}{2\pi} \int_{-\infty}^{\infty} \tilde{\boldsymbol{F}}(\boldsymbol{x}, \omega) \exp(i\omega t) d\omega.$$

The Laplace transform of $\boldsymbol{F}(\boldsymbol{x}, t)$ with respect to t and transform parameter s is

$$\hat{\boldsymbol{F}}(\boldsymbol{x}, s) = \int_0^{\infty} \boldsymbol{F}(\boldsymbol{x}, t) exp(-st) dt,$$

where the change of domain is indicated by $\hat{}$. The inversion formula for the Laplace transform is

$$\boldsymbol{F}(\boldsymbol{x}, t) = \frac{1}{2\pi i} \int_{c-i\infty}^{c+i\infty} \hat{\boldsymbol{F}}(\boldsymbol{x}, s) exp(st) ds.$$

Convolution

Convolution is a mathematical operation which combines two functions in a certain way to produce a third. Under a wide range of circumstances the earth behaves convolutionally. The convolution of $f(t)$ with $g(t)$, denoted by $*$, is

$$f(t) * g(t) = \int_{-\infty}^{\infty} f(\tau) g(t - \tau) d\tau.$$

The Fourier transform of convolution is multiplication: $f(t) * g(t) \leftrightarrow \tilde{f}(\omega)\tilde{g}(\omega)$, where $\leftrightarrow$ denotes a Fourier transform pair. This is the convolution theorem.

SI Base Units

Quantity	Name	Symbol
length	metre	m
mass	kilogram	kg
time	second	s
electric current	ampère	A

SI Derived Units

Quantity	Name	Symbol	SI Equivalent
capacitance	farad	F	C/V
conductance	siemens	S	A/V
electric charge	coulomb	C	$A\,s$
electric potential	volt	V	W/A
energy	joule	J	$kg\,m^2/s^2$
frequency	hertz	Hz	s^{-1}
force	newton	N	$kg\,m/s^2$
inductance	henry	H	Wb/A
magnetic flux	weber	Wb	$V\,s$
power	watt	W	J/s
pressure	pascal	Pa	N/m^2
resistance	ohm	Ω	V/A
stress	pascal	Pa	N/m^2
velocity	metre per second		$m\,s^{-1}$

Symbols

Symbol	Description	Units
$\boldsymbol{B}(\boldsymbol{x},t)$	Magnetic induction	$Wb\ m^{-2}$
c	Equivalent wavefield 'velocity'	$m\ s^{-\frac{1}{2}}$
$\boldsymbol{D}(\boldsymbol{x},t)$	Electric displacement	$C\ m^{-2}$
$\mathfrak{D}$	Electric dipole moment - the product of the source length and input current	$A\ m$
$\boldsymbol{E}(\boldsymbol{x},t)$	The electric field	$V\ m^{-1}$
$\boldsymbol{E}_{xx}, \boldsymbol{E}_{yy}$	Components of the electric field measured parallel to the source dipole	$V\ m^{-1}$
$\boldsymbol{E}_{xy}, \boldsymbol{E}_{yx}$	Components of the electric field measured perpendicular to the source dipole	$V\ m^{-1}$
$\boldsymbol{F}(\boldsymbol{x},t)$	A diffusive field obeying the diffusion equation	
$\boldsymbol{G}(\boldsymbol{x},v)$	The input to deconvolution in log-time in order to recover the equivalent wavefield	
$\boldsymbol{H}(\boldsymbol{x},t)$	Magnetic field	$A\ m^{-1}$
h	The thickness of a layer	m
$\frac{dHz}{dt}$	Rate of change with time of the component of the magnetic field parallel to the z axis	$A\ m^{-1}\ s^{-1}$
i	$\sqrt{-1}$	
$\boldsymbol{J}$	Total electric current density	$A\ m^{-2}$
$\boldsymbol{J}_t$	Charge transport current density	$A\ m^{-2}$
$\boldsymbol{J}_m$	Equivalent current density representing rock magnetization	$A\ m^{-2}$
$\boldsymbol{J}_s$	Imposed source current	$A\ m^{-2}$
m	Cementation factor	
q	$q = exp(v) = 2\sqrt{t}$	$\sqrt{s}$
q_0	The zero offset intercept time in the equivalent wavefield domain	$\sqrt{s}$
$\boldsymbol{R}(\boldsymbol{x},v)$	$\boldsymbol{R}(\boldsymbol{x},v) = \boldsymbol{U}(\boldsymbol{x},exp(v))$, a resampled version of the wavefield $\boldsymbol{U}$	
s,p	Laplace transform parameters	s^{-1}
S_w	Water saturation	

$S(x, t)$	A source term	
T	Resistivity-thickness product	$\Omega\ m^2$
t	Time	s
u	Vector displacement of a point	m
$U(x, q)$	A wavefield	
$U(x)$	Electric potential at point x $E_x = -grad_x U$	V
v	$v = ln(q) = ln(2\sqrt{t}) = \frac{1}{2}ln(4t)$	
α	P-wave velocity	$m\ s^{-1}$
β	S-wave velocity	$m\ s^{-1}$
δ_{TD}, δ_{FD}	Skin depth in the time and frequency domain	m
Δ	Dilatation	
ϵ	Dielectric permitivity	$F\ m^{-1}$
ε_{ij}	The strain tensor	
ω_{ij}	The rotation tensor	
$\lambda,\ \mu$	Lamé parameters	Pa
μ	Magnetic permeability generally taken to be that of free space $\mu_0 = 4\pi \times 10^{-7}$	$H\ m^{-1}$
ρ	Resistivity, the reciprocal of conductivity	$\Omega\ m$
ϱ	Volume density of mass	$kg\ m^{-3}$
$\rho_a^{ET},\ \rho_a^{LT}$	Apparent resistivity at early and late times respectively	$\Omega\ m$
ρ_f	Volume density of free charge	$C\ m^{-3}$
ρ_b	Bulk resistivity	$\Omega\ m$
ρ_w	Formation water resistivity	$\Omega\ m$
σ	Conductivity, the reciprocal of resistivity	$S\ m^{-1}$
σ_{cum}	Cumulative conductance	S
τ_{ij}	The stress tensor	Pa
ϕ	Porosity	
ω	Angular frequency	s^{-1}

Abbreviations

CED Circular Electric Dipole

CGG Compagnie Générale de Géophysique

CS Controlled Source, e.g. an insulated wire loop or a grounded wire

CSM Colorado School of Mines

CSMT Controlled-Source MagnetoTelluric method

DC Direct-Current resistivity methods

DEMS Digital ElectroMagnetic System

DMT DeutschMontanTechnologie

DPM Diffusive to Propagative Mapping

EM ElectroMagnetic, specifically in this thesis all methods based on electromagnetic induction from a controlled source

EMGS ElectroMagnetic Geo Services

EMI ElectroMagnetic Imaging

ET Early-Time, with relation to apparent resistivity curves

FDEM Frequency-Domain EM

GPR Ground Penetrating Radar

HED Horizontal Electric Dipole

HMD Horizontal Magnetic Dipole

IP Induced Polarization

LNPF Local Noise Prediction Filter

LO Long Offset, large separation between source and receiver

LOTEM Long Offset Transient ElectroMagnetic

LT Late-Time, with relation to apparent resistivity curves

MT MagnetoTelluric methods (natural source)

MTEM Multichannel Transient ElectroMagnetic

NS Natural Source

OHM Offshore Hydrocarbon Mapping

PRBS Pseudo-Random Binary Sequence

SBL Sea Bed Logging

SEAMEX SEismic Apparatus for Mineral EXploration

SEG Society of Exploration Geophysicists

TDEM Time-Domain EM

TEM Transient EM

TEAMEX Transient Electromagnetic Apparatus for Mineral EXploration

UTEM University of Toronto EM system

VED Vertical Electric Dipole

VMD Vertical Magnetic Dipole

Chapter 1

Introduction

The techniques currently used around the world in geophysical exploration can generally be divided into three categories; (a) seismic (reflection and refraction), (b) potential field (gravity and magnetics), (c) electromagnetic (EM) and electrical methods. These techniques are used extensively in the search for many natural earth resources including hydrocarbons, minerals, ore deposits, coal, and ground water, to name a few.

In the search for oil and gas the EM method has long been a poor relation to the seismic reflection technique. Reasons for this include the poor resolution, uninterpretability and ambiguity of EM data as well as the complexity of EM wave propagation in the earth. Seismic reflection is excellent at imaging geological structure with high resolution. However, it is very poor at determining the nature of a fluid within a rock (the principal exceptions being the detection of gas from bright spots and the use of amplitude variation with offset (AVO) to find oil and gas). This makes the initial detection of hydrocarbons with seismic methods difficult, this is because the reflection response from an oil-filled rock is very similar to that of one filled with water [1]. This is a huge problem in hydrocarbon exploration where it is crucial to know if a particular structure seen on a seismic section contains water or hydrocarbons. EM methods, on the other hand, are sensitive to changes in the resistivity of a rock and, as oil replaces water in a rock, of all the physical properties of the rock, it is resistivity that is changed most (Wilt & Alumbaugh, 1998), in some cases by several orders of magnitude. Figure 1.1 illustrates the effect that changing hydrocarbon saturation has on the resistivity and P-wave velocity of a rock. This fact makes EM methods capable of detecting hydrocarbons and has been known about since the 1930's (Schlumberger *et al.*, 1934). It

---

[1] When hydrocarbons are replaced by water in the production process in a known reservoir there is a change in acoustic impedance which can be detected. This is what we try to see in time-lapse, 4-D seismic methods.

1

is exploited heavily in resistivity well-logging with electrical measurements accounting for 50% of all borehole measurements. Figure 1.2 shows part of a resistivity well log through an oilfield in the Netherlands with the high resistivity due to the oil-saturated reservoir clearly present at a depth of 880m. This very attractive prospect of being able to discriminate between hydrocarbons and water within a rock is the main reason why EM is still actively pursued in association with hydrocarbon detection to this day, both onshore and offshore, for example Wright *et al.* (2002), Ellingsrud *et al.* (2002).
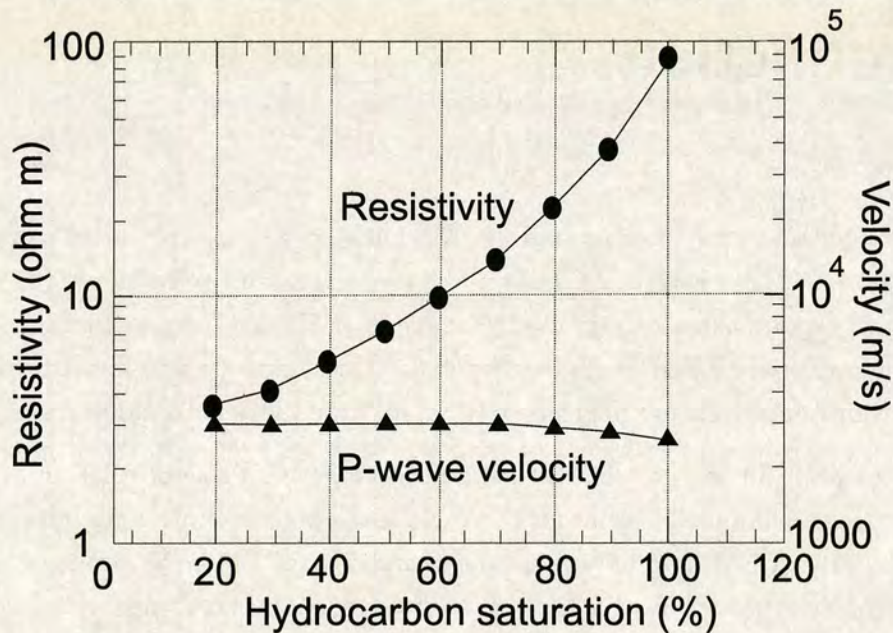
Figure 1.1: The effect of changing hydrocarbon saturation on resistivity and P-wave velocity (After Wilt & Alumbaugh (1998)).

Conventional seismic methods of prospecting for hydrocarbons are indirect and probabilistic. They rely on chains of inference which make it more or less likely to find hydrocarbons at one location than another. An anticline does not invariably contain hydrocarbons and its accurate mapping does not guarantee a success. The limitations of seismic methods are starkly highlighted by the 200 dry holes that are drilled offshore every month worldwide (Hobbs, 2003). It is safe to say that the majority of stratigraphic traps now producing have been discovered by chance, yet according to the United States Geological Survey there are up to 22 billion barrels of undiscovered oil in stratigraphic traps in the USA alone. As noted by Yungul (1996), "the aim of oil finding is to find oil not structure". Direct methods of oil finding fall into two categories. One uses the property that hydrocarbons (or their derivatives) percolate to the surface from the reservoirs underneath where the main accumulations are trapped.

The other recognises their presence from their response to a signal generated on the surface. There is huge benefit to be gained in an EM technique capable of discriminating between hydrocarbons and water over a known structure. For this potential to be realised, the appropriate EM data must be collected and a new processing methodology developed to exploit the data. Advances in technology in the past 10 years have resulted in a new generation of EM recording systems. One such system is the multichannel transient electromagnetic (MTEM) system. This yields unprecedented data volumes and spatial coverage for an EM survey, and increased dynamic range allows data to be recorded at much shorter offsets than was previously possible (Strack 1992, Ch 5, page 140).

With such advancements and all the potential benefits to be gained, there is inevitably a need for new data handling and processing techniques in order to exploit fully the data that are collected. As long ago as 1989 a workshop was held at the SEG annual meeting in Dallas to discuss how best to analyse and present the increasingly large datasets being collected by non-seismic exploration methods (Best & Spies, 1990). The primary advantage in the use of large datasets lies in the additional valid detail that can help constrain the interpretation and reduce ambiguity; knowing how best to go about doing this, however, is not obvious.

Figure 1.2: A resistivity well log through the Schoonebeek oil field in the Netherlands.

A very important concept in handling and interpreting EM data is the dimensionality of the earth. For the sake of simplicity it is often assumed that the earth is flat perhaps not unlike the flat earth of the ancient Hindus carried through the universe on the back of a turtle (Figure 1.3). This is known as the 1-D earth and in some situations is a good approximation to the real earth such as in areas of flat inter-bedded sediments. However, the reality is that real exploration problems involve detecting deviations from one dimensionality. Distortions in EM signals caused by 2-D and 3-D effects are common and the result of a 1-D interpretation in such cases can be quite misleading. Being aware of such distortions is crucial in any interpretation, and high spatial density EM data make identifying such distortions and their subtle variations possible.

3

Figure 1.3: The concept of a 1-D earth widely assumed in EM prospecting (from Zhdanov & Keller (1994)).

Traditionally, EM data are collected at a few sites and then an earth model is constructed based on fitting synthetic responses of simple models to the observations. The models are parameterized in terms of a limited number of resistivities and positional information, and either forward modelling or inversion carried out in 1-3 dimensions. A variety of subsurface images can be constructed, but most ultimately rely on forward calculations based on models with few parameters compared with the amount of raw data acquired. A major disadvantage with the model-fitting approach is that the earth is more complex than the assumed model and an unknown bias is introduced in the inverse problem. When dealing with small single-site datasets this approach is reasonable. However, when dealing with very large multichannel datasets where the coverage is very dense, such an approach clearly does not extract all the possible information from the data. The problem was captured very neatly by Horst Rüter of Deutsch Montan Technologie (DMT) commenting on model-fitting applied to MTEM data. He said

"We spent all this time collecting all these numbers, and in the end we are left with a model with 10 numbers. I want to know what happened to all the other numbers"

Alternative approaches to dealing with EM data have emerged in recent years, centered around similarities between diffusive and non-diffusive wave-like propagation. EM wave propagation is a diffusive phenomenon obeying the diffusion equation, seismic wave propagation is a non-diffusive phenomenon obeying the wave equation. A transformation known as the q transform relates the two equations and inversion of this transformation allows mapping of a diffusive EM wavefield into an equivalent wavefield that obeys the wave equation. Once in this equivalent wavefield numerous processing procedures routinely used in seismic data processing can be applied to the data, and the possibility of extracting resistivity from the data in a way analogous to extracting velocity information in seismic data becomes a possibility, although this has not yet been done successfully. Inversion of the q transform is termed diffusive to propagative mapping (DPM) (Tournerie & Gibert, 1995).

A fundamental difference between this approach and the conventional forward modelling approach is that here the data are processed rather than modelled, with the end result that the data hopefully tell you something about the earth. The approach is also fundamentally different in that most standard EM interpretation is based on the response at late times, whereas DPM uses information contained at very early times. Late time responses are traditionally used because of their simplicity and because it is very difficult to measure accurately at times much before the millisecond range. Oristaglio & Hohmann (1984) noted that "the early-time response deserves much closer attention" but the technology required to measure at early times has only recently become available. This approach is only applicable to densely spaced high quality multichannel EM data, and the understanding and implementation of the DPM method is still in its infancy. It is further complicated by the fact that the transformation of the data to the equivalent wavefield is an inherently ill-posed problem and, as a result, must be calculated with great care. However, the approach does provide a new way of handling EM data, the end result of which may be significantly easier to interpret than was previously the case.

The work in this thesis centres on the analysis of two MTEM datsets collected over a known gas storage reservoir as part of a time-lapse experiment. The aims of the experiment were to detect the gas in the reservoir and the movement of the gas between the two surveys. The data were collected in 1994 and 1996 with no existing standard processing technique for handling such large datasets. As a result, the data were analysed in the conventional model fitting manner and neither of the project aims was achieved (Ziolkowski *et al.*, 1998a). Although some processing techniques are common to all forms of EM data, such as digital notch filtering for removing the effect of electrical pickup, there is no standard processing flow for MTEM data. I have examined the two MTEM datasets in great detail and formulated a processing scheme that is intended for use specifically on MTEM data. Some of the steps are commonly used on other types of EM data and some are specific to multichannel data. Careful consideration has also been given to the order in which the processing steps should be applied.

The initial processing involves recovering the impulse response of the earth ideally, and in the case of the real data, where this was not possible, recovering an approximation to it. I have detected crucial timing errors that have prevented previous workers obtaining favourable results from the same data. Many flaws in the data acquisition parameters have been identified and suggestions for collecting such data in the future are proposed. The results of the initial processing alone appear to indicate the presence of the reservoir and suggest small movements can be detected between the two surveys. These results involve displaying the actual data in a manner similar to seismic data rather than

5

producing a model that appears to fit the data. Analysis of various other components suggests that in-line E_{xx} data produces the largest response when looking for a resistive target.

After recovering the impulse response of the earth, the second phase of the processing is to apply DPM to the data. In the equivalent wavefield domain for the MTEM data I am working on, the theoretical moveout of traces is in the form of straight lines the slope of which is related to resistivity in a manner analogous to seismic refraction (Wilson, 1997). However, Wilson (1997) was not able to recover numerically the correct resistivity values from synthetic MTEM data. I have developed an extension to the work of Wilson (1997) which enables resistivity to be extracted directly from synthetic data in the equivalent wavefield domain in the presence of two layers. However, the refraction analogy was found to break down and give incorrect results when more layers were added.

This thesis deals with developing and applying a novel approach to handling large amounts of EM data in order to detect the presence of a known hydrocarbon accumulation using surface based EM data. The need for a new type of data analysis stems from the amount of extra information contained in datasets with a high spatial density that are not best exploited by standard model-fitting techniques. The idea of displaying the data, or some transformation of it, makes interpretation much easier and to a certain extent de-mystifies the results of EM data analysis, making them more easily understood by non-specialists. The layout of the thesis is as follows.

Chapter 2 summarises the use of EM exploration techniques and in particular transient EM. There is a review of standard EM data analysis and imaging techniques and analysis of how distortions in EM data are handled, as well as a summary of the use of EM in hydrocarbon detection. Chapter 3 develops the theoretical background to similarities in elastic and diffusive wave propagation, and discusses previous work on applying a wave transform to convert EM data to a seismic equivalent wavefield. Chapter 4 describes the data acquisition and the new data processing techniques applied to real MTEM data with examples of the result of each processing step. Chapter 5 presents a modelling study of the sensitivity of different electric and magnetic field components to a buried resistor, the results indicate which components of the real data will be capable of detecting the reservoir and the time at which a response is expected. The results of the new processing applied to two MTEM datasets are presented in Chapter 6. The presence of the reservoir is seen at a time, offset and on a component that agrees with the modelling results presented in Chapter 5. Chapter 7 extends the theory in Chapter 3 to enable the correct resistivity to be extracted from synthetic data for a two layer case. The technique is then demonstrated on noisy synthetic data.

Chapter 2

Electromagnetic Prospecting

2.1 Introduction

The use of EM methods is discussed here with particular reference to time domain EM methods. Electromagnetic methods can be defined as the use of Maxwell's equations in computing earth conductivity, while the calculation of earth resistivity in electrical methods is based on the solution of Laplace's equation. The basic principle of every EM method is to measure or detect the distortion of a source field caused by the presence of a conductive earth in order to determine the earth conductivity structure. If the source field is man-made, the techniques are termed controlled source electromagnetics (CSEM) or active EM; if the source field is natural, the technique is termed natural source (NS) or passive EM. An example of a passive EM technique is the magnetotelluric (MT) method (Cagniard, 1953) which uses naturally occurring currents in the ionosphere as the source field to probe the earth. EM techniques can be further sub-divided into time-domain EM (TDEM) (or transient EM (TEM)) and frequency domain EM (FDEM) techniques depending on how the data are analysed and the source waveform used. The MTEM method is a controlled source time-domain EM method. This chapter gives a review of EM surveying techniques in the time-domain, looking at how such data are traditionally analysed and at problems associated with the data such as distortion of the signal from man-made and geological sources. The role of EM techniques in hydrocarbon detection is also discussed, both on land and at sea. Finally, the many approaches of EM modelling in 1-3 dimensions are discussed.

2.2 Electromagnetic methods

Electromagnetic methods are members of a family of methods commonly known as the geoelectrical methods. These include MT, direct current (DC) resistivity and induced polarization (IP) methods. DC resistivity methods have been in use since the first field experiments by Conrad Schlumberger in 1912 [1]. The DC method is the low frequency limit of the electromagnetic method. Its use in exploration is limited by the fact that the depth of penetration is related to the source-receiver separation, making deep sounding impractical. Also the results are often so ambiguous that the target cannot be detected at all. The magnetotelluric method was developed in an attempt to extend the capabilities of electrical prospecting methods. It makes use of the magnetic coupling that occurs between current filaments flowing in the ground when the current is not DC. This aspect of current behaviour makes it possible for MT and EM methods to provide penetration through a very resistive zone, a case in which DC resistivity can provide little or no penetration (Kaufman & Keller, 1983). The magnetic coupling also means that the depth of penetration of EM and MT is much larger than the source-receiver separation. The MT method has proved effective at determining the resistivity structure of the subsurface at a depth of a few hundred metres to several tens of kilometres. As with DC, MT suffers from some limitations, primary among which is the amount of effort required to record and analyse the field data. The extraction of useful information from what would ordinarily be called electromagnetic noise is a painfully difficult process and, as a result, the MT method often does not provide the precision and accuracy in the time required for exploration purposes. In contrast to MT methods, EM techniques use a known and controlled source of energy rather than having to depend on the use of a random natural EM field. Controlled source MT (CSMT) uses a controlled source at a distance that is much greater than the field penetration depth. It differs from long offset TEM in that the measured response is the ratio of electric and magnetic fields at the receiver and not a single field component (Nekut & Spies, 1989).

The basic principle of all EM methods, namely using a known EM source field to probe the earth and determine something about the earth conductivity structure from the resulting measured response, is fairly simple and well understood. However, the myriad different variants on how this is done often leads to confusion in the understanding of EM methods. In controlled source transient EM alone there are 45 variations of the method resulting from different source and receiver types, field layouts and so on

---

[1] The Schlumberger oil and gas service company was formed on the basis of this work to use electrical measurements to map subsurface rock bodies.

(Vanyan, 1967). Each method requires its own instrumentation and interpretation procedures. This section discusses the various sources, receivers, source functions, field layouts and the corresponding fields generated, as well as an explanation of where each method can be put to best use.

Profiling and Sounding

There are two ways of exploring the resistivity structure of the earth: as a function of depth (known as sounding) or as a function of lateral position for a fixed spacing (known as profiling). In spite of the widespread use of the 1-D earth model in EM sounding, detection of a target using profiling actually precludes the existence of a purely 1-D earth. Sounding assuming a 1-D earth structure is suitable for hydrocarbon and groundwater exploration, while profiling is best for detection of ore bodies which often consist of closed geometric forms for which a 1-D earth model is inappropriate. Interpretation of profiling data traditionally used analytic expressions for spheres or cylinders within a less conducting host to model the data. To date the detection of ore bodies is the application in which EM has had the greatest success. In order to build up an electrical image of the subsurface as a function of depth and lateral position, a combination of sounding and profiling is used. This is becoming more common with the introduction of multi-channel acquisition systems that enable the collection of the large data volumes required. Profiling can also be used to identify lateral changes in the signal that would distort a 1-D interpretation.

Time domain vs Frequency domain systems

Although it is readily shown that time-domain and frequency-domain measurements are uniquely related through the Fourier transform, the operating procedures and interpretation involved in the two approaches is quite different, and in the presence of geological noise a paradox exists between the equivalence of the two methods (Kaufman, 1989).

A transient source signal contains a very wide spectrum of frequencies, whereas a "frequency domain" source signal emits a single frequency. A wealth of information is contained in a transient sounding curve while a similar station for the FDEM method records only the amplitude and phase, just two numbers. In a FDEM system a receiver measures the secondary field of frequency f generated by a source field also of frequency f. The primary field can be thought of as the field measured at the receiver in the absence of the conductive earth. The difference between the primary field and the observed field when the earth is present is called the secondary field. Simple FDEM systems use two or three frequencies transmitted one at a time, while more sophisticated systems use between five and sixteen frequencies to provide better resolution

9

(McCracken *et al.*, 1986). In all FDEM systems the secondary field generated in the earth is always recorded in the presence of the primary field: this limits the detectability of the secondary signal. TDEM systems are usually recorded in the absence of the primary signal which makes the signal more detectable, though some systems record in the presence of the primary field to maximize the input current. Generally FDEM systems are used for shallow engineering, environmental and groundwater studies though they are also used in marine EM work to study earth structure and in the search for hydrocarbons (see pages 27-29).

An important difference between the two types of system is how they probe the subsurface as a function of depth, in general.

High frequencies or early time = Shallow penetration
Low frequencies or later times = Deep penetration

Determining the depth of penetration in EM is not as straightforward as in DC or MT because it is dependent on the source-receiver separation as well as on the frequency. Theoretically the EM fields at any time or frequency are present at all depths, albeit at vanishingly small values. The practical depth of investigation from a geophysical standpoint depends on the accuracy and sensitivity of the instrumentation, the complexity of the geologic section and the ambient or inherent noise levels (Spies, 1989). The skin depth provides a useful rule of thumb, giving the depth at which a plane-wave EM field has fallen to $\frac{1}{e}$, or 37%, of its value at the surface. In the frequency domain this is given by

$$\delta_{FD} = \sqrt{\frac{2}{\sigma\mu\omega}} \qquad (2.1)$$

where ω is the angular frequency of the source signal. In the time domain the maximum transient electric field at any time t is located at a depth of

$$\delta_{TD} = \sqrt{\frac{2t}{\sigma\mu}} \qquad (2.2)$$

where δ_{TD} is the time domain diffusion depth. So the depth of penetration is proportional to $\frac{1}{\sqrt{\omega}}$ in the frequency domain and to $\sqrt{t}$ in the time domain. For TEM the upper limit on the depth of investigation is controlled by the earliest sample time of measurement and the lower limit by the time at which the signal decays into noise. Thus, in an ideal environment, the depth of investigation may be several skin depths while in noisy environments it may be less than one skin depth. In any survey knowledge of the depth of penetration of the transmitted fields is crucial and should be

10

established using modelling before any work is done: this is particularly important in EM since the depth of investigation also depends on the source-receiver separation.

The vast majority of EM surveys carried out nowadays are TEM, and in recent years the TEM method has gone from 'no good' to 'the best' to 'the only one' among the electrical sounding methods (Yungul, 1996). However, in areas of high cultural noise where the TEM signal can be lost, narrow-band filtering of FDEM data can be used to greatly improve the signal-to-noise ratio and provide useable data. TEM measurements require a higher degree of skill on the part of the operator and have considerably more setup and takedown time per station than an FDEM survey. As a result, ground TEM is poor for reconnaissance work but very good for detailed work requiring the highest possible resolution.

Sources and receivers

In EM there are two different possible sources [2] known as a grounded wire and an ungrounded horizontal loop. The ungrounded loop source and all natural sources are known as inductive sources: they create fields which induce horizontal current flow in the subsurface of a 1-D earth and are insensitive to thin resistive layers (Verma & Mallick, 1979).

A grounded-wire is generally preferred for long offsets and deep work because the primary field falls off less rapidly at large offsets from a grounded wire than a loop source. Provided the source-receiver offset is greater than five times the wire length, the source can be treated as an electric dipole (Keller *et al.*, 1984). However, a grounded wire source is more likely to produce a distorted signal than would a loop source if any localized conductor is near the transmitter (Keller *et al.*, 1984). Consequently the transmitter location can have a significant effect on the measured signal for any source-receiver separation.

A loop source may be necessary if the contact resistance of the grounded wire is too high. Loop sources are generally favoured in shallow work and in the detection of highly conductive inhomogeneous regions. The theory and interpretation of measurements carried out with a loop source are also much simpler than those done with a grounded wire because the field from a horizontal loop may be treated as a vertical magnetic dipole if the source-receiver offset is greater than five times the loop side length which is horizontally onmidirectional.

---

[2] A third new source has recently been proposed by Mogilatov & Balashov (1996) called a circular electric dipole (CED). It consists of a number of grounded wires radially symmetric about a central point. It is a purely galvanic or noninductive source. Applications include marine use where the effect of the sea water layer is greatly reduced. However, there are currently very few examples of its use in the literature.

The EM fields for a 1-D conductivity structure may be separated into independent toroidal and poloidal modes about the vertical axis. The toroidal mode is associated with electric currents flowing in loops containing the vertical axis and possesses no vertical magnetic field component. They diffuse downwards and outwards with increasing time building up a system of 'smoke rings' (Nabighian, 1979). Poloidal modes are driven by electric current systems which are always horizontal, and have no vertical electric field component. Because of this distinction, the sensitivity of the two modes to electrical structure is quite different. A grounded wire horizontal electric dipole (HED) includes a combination of toroidal and poloidal modes (galvanic and inductive modes), while an ungrounded loop horizontal magnetic dipole (HMD) produces only poloidal modes [3] and so detects only horizontal current flow, making measurements insensitive to thin resistive layers. Grounded wire sources are therefore favoured in the detection of hydrocarbons which have anomalously high resistivities. The two source types and resulting current flow patterns are illustrated in Figure 2.1(a).

Electromagnetic field receivers come in three possible forms and are similar to those used in MT. A pair of electrodes is used for measuring the electric field and the orientation of the electrodes determines the component of the electric field that is measured, namely Ex or Ey. In the presence of a time-varying magnetic field the electric field, $\boldsymbol{E}$ is defined by,

$$\boldsymbol{E} = \frac{\partial \boldsymbol{A}}{\partial t} - \nabla U \tag{2.3}$$

where $\boldsymbol{A}$ is the magnetic vector potential which is defined as the curl of the magnetic field $\boldsymbol{B}$ and t is time.

In the DC limit, measurement of the E_x component of the electric field which is a mathematically devised quantity is given by,

$$E_x = -grad_x U = -\frac{\partial U}{\partial x} = lim \frac{U(x_2) - U(x_1)}{|x_1 - x_2|}; |x_1 - x2| \to 0 \tag{2.4}$$

where $U(x_1)$ and $U(x_2)$ are the electric potentials at the points x_1 and x_2. Potential is an abstract physical concept, defined as the negative of the work done in moving an electric unit charge from infinity to the point where the potential is being measured. In reality, when talking about the electric field, the measured quantity is the potential

---

[3]Behaviour on the seafloor is fundamentally different where sources and receivers are buried inside a conductive medium rather than lying on a conductive half-space. Now both HED and HMD systems generate and receive both toroidal and poloidal modes and therefore are both sensitive to a resistive seafloor (Chave *et al.*, 1991).

drop between two points in an electric field and is better called voltage.

A horizontal loop is used for measuring the time rate of change of the vertical component of the magnetic field $\frac{dHz}{dt}$. Finally, magnetometers can be used to measure the three components of the magnetic field Hx, Hy and Hz directly, and this measurement can be differentiated to allow comparison with the signal from a horizontal loop. There are several practical and theoretical differences between H and $\frac{dH}{dt}$, for example; H measurements give better results in the detection of good conductors (Mallick & Verma, 1979) and are also superior in calculating apparent resistivities. The various possible receivers are shown in Figure 2.1(b). For a grounded-wire source the number of possible components can be doubled by operating the source in two different orientations perpendicular to one another. The potential amount of different data types that can be collected in a single survey is quite considerable: selection of the appropriate components is very important and often target-dependent.
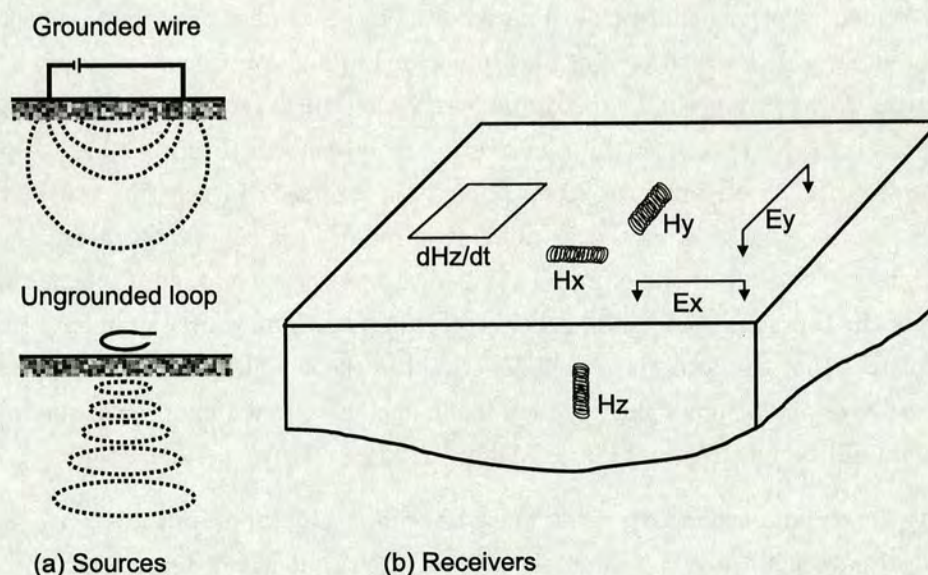
Figure 2.1: The various source and receiver types used in EM surveying (a) Sources showing the patterns of current flow produced by a grounded wire and an ungrounded loop (b) Receivers for measuring 2 orthogonal components of the electric field using grounded wires, 3 orthogonal components of the magnetic field using magnetometers and an ungrounded loop for measuring the time rate of change of the vertical component of the magnetic field.

Source Waveforms

The choice of the source waveform used in EM systems is by no means set. A variety of waveforms exists and the one chosen for a particular application will depend on various factors such as the size of current to be applied, the ability to maintain the shape of the waveform under load and the ease with which a particular shape of waveform can be realized in practice. In seismic exploration the explosive source used can be considered an impulse. In EM an impulsive source is not achievable in practice, since it is not possible to switch a current on and off instantaneously. Instead the source function most commonly used is a step function, often known as switch-on or switch-off, or more confusingly the response is known as the impulse response when $\frac{dHz}{dt}$ is measured. As well as being the easiest to generate, a step function source is rich in high frequencies and EM coupling is often stronger at higher frequencies than low frequencies (Kaufman & Keller, 1983). This waveform is also believed to give a better response in the presence of geological noise for a 3-D body in a conducting host (Eaton & Hohmann, 1987). When collecting more than one record at the same place, the step waveform is repeated several times to produce a bipolar or bipolar continuous waveform. In the bipolar waveform (Figure 2.2b) the signal is recorded during the off-time in the absence of the primary field, and in the bipolar continuous waveform (Figure 2.2a) the primary field is not switched off but instead its polarity is reversed. In practice the continuous waveform is more easily achieved as all that is required is a polarity reversal and not a switching on and off of the equipment. It also has the advantage of using twice the current of the bipolar waveform in order to obtain maximum source moment. However, a drawback is that the secondary field generated in the subsurface must be measured in the presence of the primary field. When using such a source one or all of the following criteria should be met (Nabighian & Macnae, 1991):

1. The primary and secondary fields must be comparable in amplitude;
2. The primary field must be precisely measured so that it can be removed by deconvolution;
3. The primary field is precisely controlled and removed by subtraction.

The wear to the generator when using the bipolar waveform is severe and restricts its use. Bipolar waveforms are used as opposed to a waveform that is always of the same polarity, because averaging of signals of opposite sign is essential in order to minimise effects caused by polarization of the transmitter electrodes. Another form of current waveform is the triangular current waveform. This is used mainly in mineral exploration where the time rate of change of the vertical magnetic field is measured. The derivative of a triangular pulse is a step function which is easier to interpret than any other time response and is better for the detection of good conductors in

14

the presence of poorer ones (West *et al.*, 1984). Another form of source waveform first proposed by Duncan *et al.* (1980) for use in EM is the pseudo-random binary sequence (PRBS) which transmits over a very wide bandwidth (0.03-15KHz) (Figure 2.2d). The measured signal is then cross-correlated in real time with an exact copy of the transmitted waveform. The resulting cross-correlogram is then deconvolved from the system input, the autocorrelogram of the transmitted waveform, to give the impulse response of the earth. This is similar to the approach used in the vibroseis technique of seismic exploration. This source type enables the frequency content of the input sequence to be tuned to the depth of interest: a shallow target would employ a high frequency sequence, while deeper targets would use lower frequencies. "Frequency domain" systems employ a single frequency sinusoidal source. Individual frequencies are transmitted one at a time, a process that is "inefficient and time-consuming" (Duncan *et al.*, 1980). The various source functions are summarised in Figure 2.2.
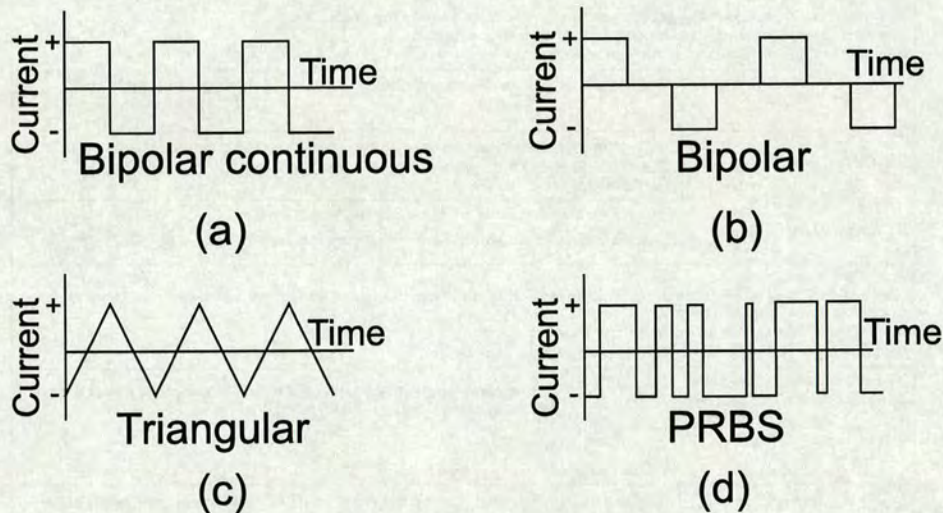
Figure 2.2: The source waveforms most commonly used in EM surveying.

Time Domain Electromagnetic (TDEM) Systems

Although there are a large number of possible configurations in which a TEM system can operate, there are a number of well established systems in use for particular applications. Some of these systems are best known by their commercial names and they are used only for clarity. By far the most widely used systems are those which employ a short grounded wire source and a receiver which detects the time rate of change of the vertical component of the magnetic field or two concentric ungrounded loops. Figure 2.3 summarises all these configurations giving brief examples of their use, advantages and disadvantages. References giving more detailed description of the systems and field examples are also given.
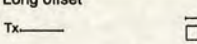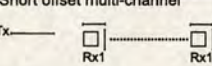
Inductive sources	
Source and receiver coincident **Description:** These three configurations are essentially equivalent. A loop source and either a loop receiver or magnetometer are used. The source is typically a few tens to a few hundred metres long on each side. The side length controls the depth of investigation. **Advantages:** Simple field setup, excellent at detecting horizontal conductive anomalies. **Disadvantages:** Can be strongly affected by near-surface polarization. **Applications:** Mineral exploration, groundwater mapping.	
Single loop	Single loop used both as source and receiver. Simplest TEM configuration. Little used.
Central loop Tx Rx	Loop source with magnetometer or small loop receiver placed in centre of source loop **Examples:** Sirotem MKII system (Buselli & O'Neil, 1977) and EM37 (Geonics Ltd.). Field example in Cooper & Swift (1994).
Co-incident loop Tx Rx	Loop source and receiver of the same size laid next to each other. **Examples:** Sirotem system MK I & II. Field examples given in Taylor et al, (1992).
Separated loops **Description:** The same as above except that the receiver is offset from the source, either by a fixed distance or by varying amounts. Offsets can range from 10m to several km. **Advantages:** Less sensitive to near-surface IP effects. **Disadvantages:** Strongly affected by lateral resistivity gradients.	
(a) Fixed separation (Slingram) (b) Fixed source roving receiver Tx Rx Tx ºRx Loop receiver Dipole receiver	**Examples:** Newmont EMP system (Dickson & Boyd, 1980). Field examples given by Maher (1992). UTEM System (West et al,1984).
Dual-loop Tx Rx	The dual loop configuration is a special case of fixed separation in which the edges of the two loops are in contact. **Examples:** The configuration is discussed by Spies (1975). Field examples are given in Zhang et al,(2000).
Grounded sources	
Long offset Tx Rx	**Description:** Electric dipole source 1-2km long, magnetic and electric field receivers at offsets ranging from 2-30km. Depth of exploration is several kilometres. **Advantages:** Large depth of exploration. Sensitive to resistive targets. **Disadvantages:** Poor spatial coverage, strongly affected by lateral resistivity gradients. **Applications:** Mineral and hydrocarbon exploration, crustal studies. **Examples:** The CSM TEM system (Keller et al, 1984) and the LOTEM system (Strack, 1992). Field examples also given in Strack (1992).
Short offset multi-channel Tx Rx1 Rx16	**Description:** Electric dipole source 250m long, Typically 16 receiver stations measuring both magnetic and electric fields every 125m with a near offset of 250m. Depth of exploration is approximately 1km. **Advantages:** Dense spatial coverage, high resolution data. Sensitive to resistive targets. **Disadvantages:** Limited depth of exploration, time-consuming layout. **Applications:** Hydrocarbon exploration and monitoring. **Examples:** The Teamex system (Strack, 1992), field examples given in Hördt et al, (2000a) and Wright et al,(2002).

Figure 2.3: Summary of the most commonly used TEM configurations.

2.3   Treatment of Electromagnetic Data

The treatment of electromagnetic data is traditionally very different from that of seismic reflection data. Electromagnetic data are generally modelled or inverted in terms of a small number of layers and resistivity values and these initial values may be estimated from apparent resistivities or based on *a priori* knowledge of the area. The model parameters are then varied until the best fit to the real data, in some (often a least-squares) sense, is found. The reason for treating EM data in this way has mainly been due to the poor resolution of EM data and the fact that the spatial density of EM survey data has previously been very sparse, with a single transmitter site and a few receiver sites used. Such sparse data are best studied by modelling or inversion.

Seismic data on the other hand are processed rather than modelled. One of the reasons for this is the prohibitive cost of 3-D computational modelling on large seismic datasets. Also the high resolution of seismic data makes it possible to identify individual reflections from the sub-surface. The result of processing is a seismic image of the sub-surface. As technology in EM equipment has advanced, the amount of data collected in EM surveys has increased rapidly. Numerous receivers and source positions are now occupied and dense data coverage similar to that of a seismic survey is now a possibility. These data bring with them a wealth of new information on the electrical properties of the sub-surface. However, they also present a new challenge in terms of how to handle them. Inversion of such large datasets in terms of a few layer thicknesses and resistivities provides relatively little information compared with the amount of data collected. Also, the computational power required for a full three dimensional inversion of such data is still prohibitive. This section reviews the use of traditional EM data analysis and looks at new imaging methods of EM data analysis.

Apparent Resistivity

Apparent resistivity is defined to be "the resistivity of a half-space which under exactly the same conditions in the field yields the measured voltage" (Sheriff, 1984). The first step in interpreting a sounding curve is usually to transform from the measured field value such as E_x, H_z, etc to an apparent resistivity function $\rho(t)$. Data are generally initially converted to apparent resistivities because the shape of the raw sounding curves do not provide much clue, when inspected visually, as to the true conductivity structure of the earth. Apparent resistivity curves show a similarity to the true resistivity profile which can facilitate initial interpretation. However, the apparent resistivity can be computed only under asymptotic conditions, namely the early time (ET) and late time (LT) conditions. In the early time limit the apparent resistivity approaches the

17

resistivity of the top layer, and in the late time limit it approaches the resistivity of the basement layer. However, outside these two limits the apparent resistivity values can depart widely from those of the true earth section. Even for the simple case of a layered earth, it can be dual-valued or even undefined (Spies & Eggers, 1986). Measuring the magnetic field instead of its time derivative can eliminate some of these problems (Raiche, 1983). Apparent resistivity is simply a form of data normalisation that may simplify comparison with similarly non-normalized data, although data from different source-receiver geometries cannot be compared directly. It has little physical significance except in the case of a homogeneous half-space.

In an attempt to tackle the problem of undefined apparent resistivities at intermediate times, Sheng (1986) developed a single apparent resistivity expression for LOTEM. In some cases, though, the layered earth voltage produced was greater than any voltage that could be produced by a halfspace; in other cases the solution was found not to be meaningful for the whole time range. The use of apparent resistivities is generally best used for determining initial values of layer resistivity for inversion. The early and late-time apparent resistivity expressions for the in-line electric field from a grounded wire source are given in equations (2.5) and (2.6). The field geometry associated with these measurements is shown in Figure 2.4.
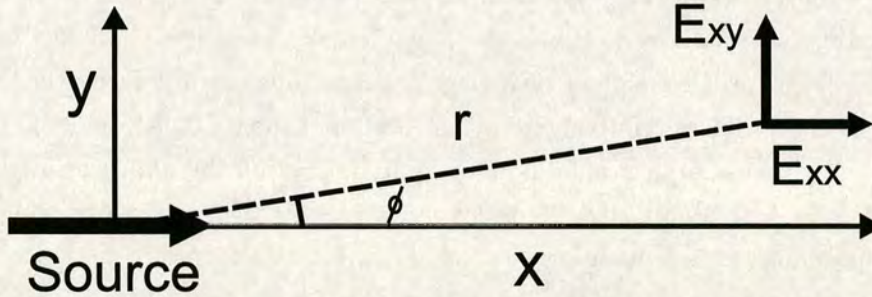
Figure 2.4:   The layout of the in-line and cross-line components in relation to an electric dipole source.

$$\rho_a^{ET}(t) = \frac{4\pi x^3 E_{xx}}{3\mathcal{D}cos^2\phi} \tag{2.5}$$

$$\rho_a^{LT}(t) = \frac{2\pi x^3 E_{xx}}{\mathcal{D}(3cos^2\phi - 1)} \tag{2.6}$$

18

Current use of apparent resistivity includes the ElectroMagnetic Imaging (EMI) method (Tasci & Jordan, 1996; Keller *et al.*, 1996a). It uses early and late-time apparent resistivity formulae to create apparent resistivity cross sections as a function of depth (time) in an attempt to identify the presence of hydrocarbons at depth. The method records the magnetic field or its time derivative. The values presented in such a cross section do not include any interpretation. The interpretation consists of determining if the sections include a recognizable pattern which has been observed over oil and gas fields in a similar setting, An example of results from the method are shown in Figure 2.10.

Forward modelling

Iterative forward modelling is the mainstay of EM data interpretation.

It is a model-based approach to data interpretation which relies upon the iterative refinement of a model through forward modelling until a good fit with experimentally acquired data is achieved. The nature of forward modelling means that the solution is inherently biased by an artificial parameterisation of the earth into a finite number of layers or by the choice of an initial guess model typically required by modelling routines. The problem of inadequate models is particularly common when 1-D models are used to invert data acquired over 2-D and 3-D structures (Goldman *et al.*, 1994). In such cases it is often impossible to fit the data, regardless of the number of layers used. Essentially we are required to know the answer before we start, as the data do not tell us the answer. Results are commonly presented in the form of 2-D pseudo-sections by piecing together the results of many 1-D inversions.

Although a considerable amount of mathematical sophistication has been applied to 2-D and 3-D controlled source inversion over the past few years (Newman & Alumbaugh, 1996), one is often struck by how little information comes out of such a massive computing effort.

"Computational times must be significantly less than geological formation times" (Raiche *et al.*, 2000)

A major reason for this is due to the amount of information contained in EM data, which is a low resolution technique, and the problem is also exacerbated by noise, which can often be larger than the response we are interested in.

Direct Inversion-Imaging

In an attempt to obtain a better picture of the full geoelectric section than is available from apparent resistivity transforms but without the need for a full point-by-point inversion, several fast direct inversion schemes have been developed to produce a conductivity versus depth section that is representative of the true earth. These schemes were originally developed as a processing step, but have been found to be very useful for interpretation in their own right.

The first such scheme, proposed by Macnae & Lamontagne (1987), is termed 'conductivity imaging' and was applied to UTEM (University of Toronto EM) field data. Data amplitudes are first converted for each time sample to an apparent depth of diffusion $'h'$ using the concept of diffusing eddy currents or 'smoke rings' as described in Nabighian (1979). This is designed to estimate the mean depth to which currents have diffused at that time. An approximate representation of the theory of source images (Maxwell, 1892) is then used to produce an apparent depth function that is independent of source-receiver geometry (unlike apparent resistivity). This is an empirically derived method of data presentation. The second step is then to derive a reasonable conductivity function from the depth function. This is done using the slowness (inverse velocity) $\frac{dt}{dh}$, where h is the apparent depth of diffusion and t is time. In the case of a halfspace Macnae & Lamontagne (1987) define the slowness in terms of the apparent depth of diffusion as a function of time to be,

$$\frac{dt}{dh} = \sigma\mu h.$$ (2.7)

Extending equation (2.7)to a continuous conductivity distribution gives,

$$\frac{dt}{dh} = \int_0^h \sigma\mu \ \ dh.$$ (2.8)

The conductivity can then be estimated directly by differentiating equation (2.8) with respect to the reference depth h again to give

$$\sigma_i = \frac{1}{\mu}\frac{d^2 t_i}{dh_i^2}$$ (2.9)

where σ_i is termed the 'imaged conductivity'. An example of an imaged conductivity section obtained using this method from UTEM data in Alberta is shown in Figure 2.5.

The large dark blue zone is a resistive carbonate unit and the dark red zone is due to water saturated porous sediments.
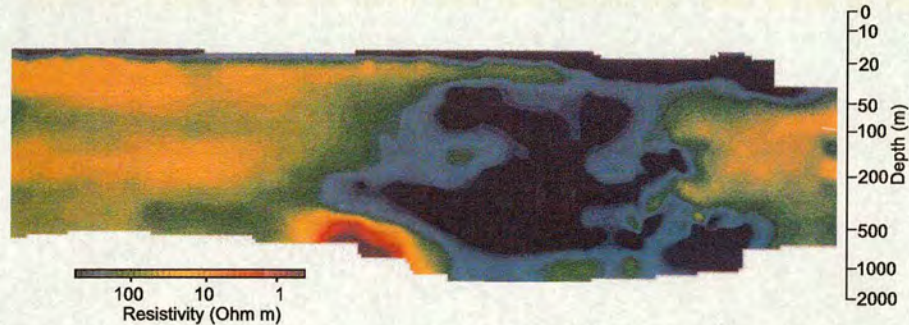
Figure 2.5: Plot of imaged conductivity over a 7.5km profile from southern Alberta. The colour scale is logarithmic, and ranges from 1 Ωm to 1000 Ωm (From Spies & Frischknecht (1991)).

Similar schemes devised by Eaton & Hohmann (1989) and Nekut (1987) also use the variation of the position of the source image with time to determine the resistivity. Their methods differ from that of Macnae & Lamontagne (1987) in that they employ a single image and extract resistivity estimates directly from its velocity $\frac{dh}{dt}$. The method works for a loop or wire source with a vertical magnetic or in-line electric field receiver. Methods like this assume a 1-D conductivity structure and so work best on short offset measurements that are less likely to be influenced by lateral conductivity variations. Their results indicate that conductive to resistive transitions are poorly resolved because TEM measurements with the magnetic field are insensitive to the transition from a less to a more resistive unit. The results were found to be 'essentially the same' as more elaborate 1-D inversion methods. Indeed, in the presence of 3-D structures, Hoekstra *et al.* (1991) found that phantom layers introduced by 1-D inversion did not appear in the 1-D imaging result for the same data.

Smith *et al.* (1994) presented an imaging scheme for coincident loop impulse response TEM data using the depth of the Fréchet kernel maximum to determine the impulse response apparent resistivity. Disappointed with the smoothness of the resultant apparent conductivity/depth curve obtained, they proposed that their result was the combination of the effect of the true conductivity depth section with a smoothing function. Approximating this smoothing function with a boxcar function, its inverse was then used to find an approximation to the true conductivity structure. The resultant 'spiked conductivity' produced a better representation of the true conductivity structure.

Compared with inversion, these methods can be considered to be a one- step forward data transform, whereas inversion is a two-step process that involves finding a best fitting model and evaluating the range of acceptable models which could equally satisfy the data within a given error bound. Since inversion also requires a constraint on the number of layers used, the model may lose detail if too few layers are used.

Electromagnetic Migration

The concept of electromagnetic migration (Zhdanov & Frenkel, 1983; Lee *et al.*, 1987) involves the downward diffusion of observed EM fields whose time flow has been reversed. The total EM field can be split up into a primary field that propagates downwards into the earth and a secondary field that propagates upwards after having been scattered back from internal structure. Given measurements of electric and magnetic fields at the surface it is then possible to separate the primary and scattered fields. The measured surface expression of the secondary field can then be used to reconstruct information about the field inside the earth and hence the geoelectric structure. Before applying the technique the primary field must first be removed from the data, the primary field can be thought of as the background resistivity model which must be known accurately in order to obtain good results. The migration procedure then involves reversing the time flow of the scattered field at each receiver site and diffusing these signals down. The diffused time-reversed fields are known as migrated fields. Their amplitude decays downwards in contrast to the original field whose amplitude increases downwards, this prevents the process being unstable in the presence of noise. The procedure can be carried out in the time or frequency domains. Time domain results are best at determining the position of anomalous structures while frequency domain results are best at imaging the boundary between two layers (Zhdanov *et al.*, 1996). The process is particularly suited to 2-D and 3-D datasets as it is computationally efficient.

Equivalence and Resolution

The resolving power of low-frequency EM methods is intrinsically limited by the spatially smooth nature of the diffusing EM fields. Generally in EM a resolvable feature must have dimensions which are comparable to the distance between the feature and the point at which the field is measured, while in seismic reflection a resolvable feature must have dimensions of the order of the wavelength or more. Resolution and equivalence are closely related concepts in EM. Two geoelectric sections may be considered geophysically equivalent if their EM response within certain error bounds is identical, or if one layer can be replaced by one or more different layers without changing the measured response. Resolution can be defined as the ability to quantify accurately the resistivity and thickness of the layers in the section, and it defines the degree of complexity an EM method is able to resolve. A single complex measurement can resolve no more than a two parameter model e.g. a non-conducting layer of some defined thickness over a uniform halfspace. Several measurements over a limited range may be able to resolve several layers. Many measurements over a wide range may be able to resolve as many as six layers. The limit on resolution is ultimately constrained by

the physics of EM. Even if the dynamic range is infinite, there are still practical limits on what can be resolved. The detail contained in a resistivity well log is far greater than that resolvable by surface EM methods, and it is certainly not necessarily obvious how to convert the well log information into a simpler geoelectric section that may be representative of what will be resolved using surface EM. Calculation of the cumulative conductance, σ_{cum} from the well log enables the identification of the number of layers required and layer boundaries as well as the layer resistivities. Cumulative conductance is defined as

$$\sigma_{cum} = \sum_{i=1}^{n} \frac{h_i}{\rho_i}, \qquad (2.10)$$

where ρi and h_i are the resistivity and thickness of the individual layers in the well log and n is the total number of layers. Straight lines on a plot of cumulative conductance indicate sections of the log that will be seen as a homogeneous layer to surface based EM (Stoyer, 1998). Generating geoelectric well logs is crucial in constraining inversion and in determining the likelihood of detecting a particular target prior to survey. However, all models created from well logs suffer from the problem that well logs seldom reach all the way to the surface. Nevertheless, they are still very important in indicating what level of complexity might be realistic in any inversion or other subsequent processing.

EM methods are generally sensitive to the transverse resistance of a layer, the resistivity-thickness product. Therefore, a thin highly resistive layer is almost indistinguishable from a thicker less resistive layer with the same transverse resistance. This is illustrated in Figure 2.6 where the response for three different models of a resistive layer with the same transverse resistance are plotted alongside the halfspace response of the background resistivity. It can clearly be seen that despite each model being very different the surface response of each is almost identical.
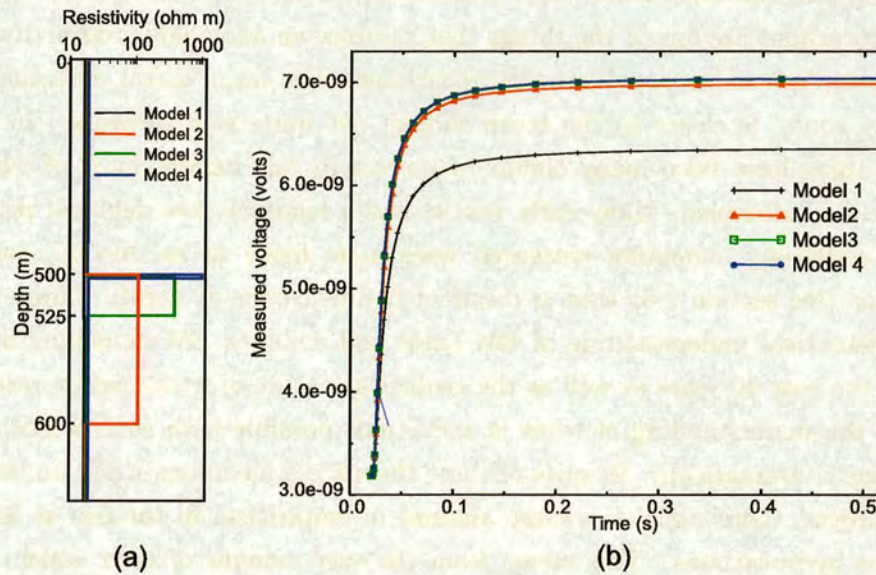
Figure 2.6: Illustration of the equivalent response from targets with the same transverse resistance (a) The models used 1. A 20 Ωm half-space, 2. A 100 Ωm 100m thick layer at 500m depth, 3. A 400 Ωm 25m thick layer at 500m depth, 4. A 1000 Ω m 1m thick layer at 500m depth. (b) The resultant E_{xx} field transient response at 1000m offset for the four models (Results calculated using the 1-D modelling program MODALL (Strack, 1992)).

2.4   EM in Hydrocarbon Detection and Monitoring

Ever since the first electrical resistivity well logs were recorded, it has been known that hydrocarbon reservoirs exhibit anomalously high resistivities (Schlumberger *et al.*, 1934). This knowledge captured the imagination of many geophysicists in the 1930's who believed direct hydrocarbon detection with surface EM methods was possible. The first paper in the very first edition of Geophysics (Blau, 1936) gives an example of one of many baseless methods that existed at the time.

"Another inventor used a short-wave transmitter and a wire, about 100 feet long laid on the ground as an antenna. -There were three dials on the beautifully finished little box; one indicated resistance, the next capacity and the third voltage. The dials were adjusted until a standing wave was set up between the transmitter and the oil sand. The three readings were then multiplied to give the depth of the oil sand in feet."

This section will show that the detection of hydrocarbons using EM is slightly more complicated than this.

The term 'direct hydrocarbon detection' is a particularly grand claim that is not only

25

misleading but also inaccurate. EM methods are sensitive to anomalous resistivities and hydrocarbons are one of the things that produce an anomalous resistivity, but not all resistivity anomalies are due to hydrocarbons. The term 'direct detection of high resistivity zones' is closer to the truth though not quite as impressive. In the past 70 years there have been many claims of success in this regard, most of which have proved to be unfounded. Many early results had a relatively low depth of penetration and the resistivity anomalies measured were more likely to be due to near surface distortions (see section 2.5) than a result of hydrocarbons at depth. Large advances in the theoretical understanding of EM fields and complex EM modelling have been made in the past 30 years as well as the geological nature of hydrocarbon reserves. As a result, the understanding of what is and is not possible with surface EM methods has advanced dramatically. In spite of these theoretical advances in the understanding of the subject, there remains a large amount of empiricism in the use of EM in the search for hydrocarbons. This stems from the vast amount of data which has been collected that are unexplainable in terms of a 1-D layered earth. Effects such as induced polarization and migration of hydrocarbons alter the recorded EM signal. Advances in modelling of multidimensional structures and polarization effects have explained some effects seen in data, but the complexity of the subject dictates that a certain level of empiricism remains.

Almost 70 years on, the anomalously high resistivities associated with hydrocarbon reserves continue to attract interest in EM methods. This section presents a review of this work and looks at the present state of the art in this field.

Detection of resistive layers

The detection of an intermediate resistive layer representing a thin hydrocarbon-bearing reservoir has been studied by several authors (Eadie, 1981; Passalacqua, 1983; Strack *et al.*, 1989b). They all found that employing a grounded electric dipole for both the source and receiver provided superior resolution for the detection of resistive layers. For such a configuration the radial electric field is strongly dependent on the transverse resistance, $T = \rho_i dh$ of a resistive layer where ρ_i is the resistivity of the layer and dh is its thickness while the same layer may be practically invisible to a vertical magnetic receiver. The parameter $\frac{T}{T_1}$ (ratio of the transverse resistance of the thin layer to the transverse resistance of the first layer) provides a useful rule of thumb as to the detectability of a buried resistive layer using the electric dipole-dipole configuration. Passalacqua (1983) found the limit of detectability of a thin resistive layer to be $\frac{T}{T_1} = 0.25$ with the anomaly increasing by a factor of 4 for $\frac{T}{T_1} = 2$. He also found that the parallel or in-line configuration has a much larger response than the perpendicular or cross-line response in the presence of a resistive layer compared to the half-space value.

Analysis of these components can thus help in the identification of buried resistive layers.

Offshore Exploration Techniques

The interest in using electrical techniques in the detection of hydrocarbons is not just limited to land-based techniques. With a large percentage of worldwide oil reserves located offshore it is here that most oil companies are interested in the application of EM methods, not least for the enormous economic saving to be had in reducing the number of dry wells drilled. An offshore well costs on average £5 million (although this figure can be up to £30 million), whereas a land-based well costs around £0.25-0.75 million (Rauzi, 2003), making the risk involved and the potential savings much less. As a result, land based EM for hydrocarbon exploration remains a much under-used method. However, there are fundamental differences between land and marine EM. The main difference arises from the presence of the highly conductive water layer. Typically, the conductivity of sea water is about 4 S/m, while that of water-saturated sediments is about 0.1-1.0 S/m. This has the effect of strongly attenuating the high frequency end of the signal, the result being that only low frequency signals penetrate to the depths required for hydrocarbon exploration. This makes marine EM measurements inherently lower in resolution than land measurements. Marine measurements also suffer from the presence of a large amplitude airwave which travels up through the water column to the surface, then through the air at the speed of light, before travelling back through the water column where it is recorded by a receiver on the seabed. The airwave can often swamp the measured response making identification of the target response difficult; the effect of these two differences is illustrated in Figure 2.7. In Figure 2.7 (right) the early part of the curve is due to propagation in the halfspace, at intermediate times the airwave is present in the marine curve and the land and marine curves are very different. The measured voltage of the marine response is two orders of magnitude smaller than the land transient for the same source moment due to the attenuating effect of the seawater. In land EM the presence or absence of the airwave in the recorded data depends on the source waveform used. For a step function there is a jump instantaneoulsly (actually on a time-scale based on the speed of light) from zero to half the late time value when used at the surface of a uniform earth (Edwards & Chave, 1986). Since the airwave travels at the speed of light its effect has disappeared before measurements begin. For long, continuously changing source waveforms such as PRBS in TDEM or a sine wave in FDEM, the airwave will be recorded . On top of these physical complications, the logistics and technology required for offshore EM, not to mention safety issues, make offshore measurements much more difficult to record and beyond the scope of most academic institutions, where the development of land-based

systems has traditionally taken place (Strack, 1992 Ch1 p6). One major advantage of marine measurements over land is that the ambient noise level on the sea floor is much less than on land, because man-made and cultural noise sources are small or non-existent. This means that low amplitude signals which would be lost in noise on land can be measured on the sea floor.
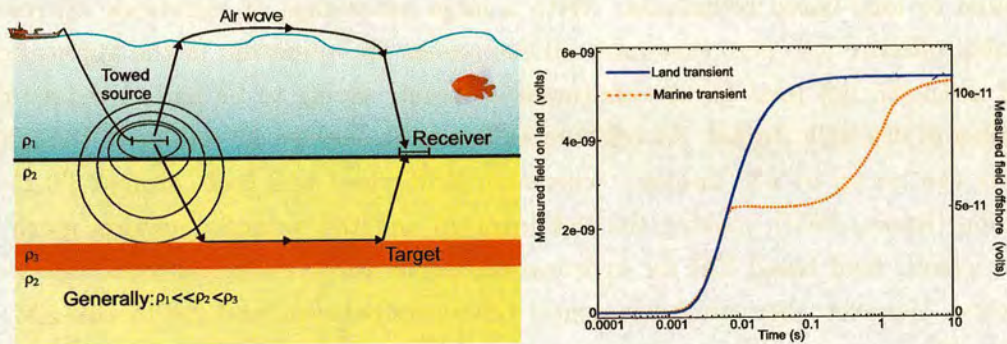
Figure 2.7: TEM on the seafloor. Left: Typical marine EM configuration showing the path of the airwave and the target wave. Right: Transient response over a 20 Ω m halfspace for the land and marine case.

The first theoretical results on the potential of marine EM systems were published by Coggon & Morrison (1970) for a vertical magnetic dipole (VMD) source with both electric and magnetic field receivers. The theory for the horizontal electric dipole (HED) frequency domain method was developed by Chave & Cox (1982). The theory for a variety of transient EM systems was developed by Edwards & Chave (1986), Cheesman *et al.* (1987) and Edwards *et al.* (1986).

The first marine EM systems were developed for investigating solid earth problems. The first such system developed at Scripps Institute of Oceanography was a frequency domain HED-HED system used to investigate the structure of mid ocean ridges (Young & Cox, 1981). Subsequent systems are described by Sinha *et al.* (1990) and Constable & Cox (1996). Transient marine systems have been used for applications such as investigating hydrothermal mounds and the evaluation of marine gas hydrates. The first transient system was developed at the University of Toronto (Cheesman *et al.*, 1990) and used a VMD source, the latest system being a HED-HED system described by Cairns *et al.* (1996).

The use of marine EM for hydrocarbon exploration has not been reported until very recently. A new technique called Sea bed logging (SBL) first described by Eidesmo *et al.* (2002) uses the difference in amplitude of in-line and cross-line electric field amplitudes in the presence of a resistive layer, as first described by Passalacqua (1983) to identify

resistive hydrocarbon filled layers using FDEM measurements. Initial results of data collected using the system described in Sinha *et al.* (1990) are presented in Ellingsrud *et al.* (2002) and they indicate the presence of a small anomaly over a known oil field offshore Angola. However, the anomaly is overshadowed by the response from a more resistive salt structure in the survey area. This technique is currently the only known use of CSEM for offshore hydrocarbon exploration in the world today. Advances in marine magnetotellurics (Constable *et al.*, 1998a,b) due partly to advances in technology, have reduced the period of useful data from 300s to 3s, making it currently the most popular geoelectrical method in hydrocarbon exploration. It is presently more widely used than CSEM, mainly to map sedimentary structure rather than to detect the hydrocarbons themselves.

The geoelectrical properties of hydrocarbon reservoirs

Electrical conduction in the earth is electrolytic for most rocks near the earth's surface, such as sedimentary basins, and propagation of current is by ionic conduction. In most rocks, water is the only constituent with significant conductivity that is present. In clay-bearing rocks , however, the clay itself is conductive and conduction often dominates. The electrical resistivity of porous rocks varies with the volume and arrangement of the pores and even more with the content and amount of contained water. Generally igneous rocks have the highest resistivity, metamorphic, intermediate and sedimentary rocks the lowest. The resistivity of the various rock types found in the earth varies by up to seven orders of magnitude: this is summarised in Figure 2.8.
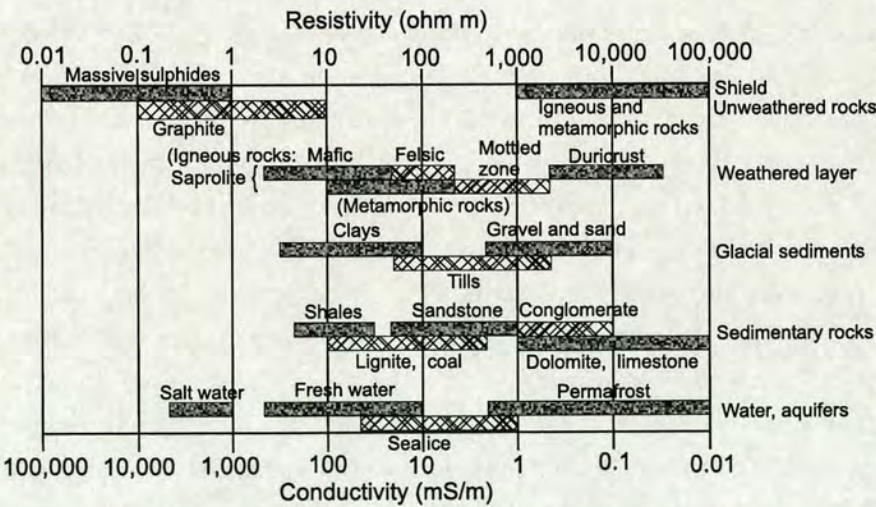
Figure 2.8: The typical range of resistivities found in earth materials (After Palacky (1988)).

29

The resistivity of different rock types is also directly related to lithology because the porosity of the rock and salinity of the contained water are affected. Petroleum bearing rocks are generally porous sandstones and limestones for which it has been observed that resistivity varies approximately as the inverse square of the porosity when the rock is fully saturated with water. This discovery led to an empirical relation between resistivity and porosity known as Archie's Law, equation (2.11) (Archie, 1942)

$$\rho_b = (\frac{\rho_w}{S_w^n \phi^m})$$ (2.11)

where ρ_b is the bulk resistivity of the rock, ρ_w is the resistivity of the formation water, S_w is the water saturation, ϕ is the porosity expressed as a fraction, m is the cementation factor which is determined by the pore geometry, and n is the saturation exponent. Thus the resistivity of a rock increases with increasing oil saturation, increasing water resistivity, decreasing water saturation and decreasing porosity. When the formation becomes shaly this relation no longer applies and further corrections need to be applied. The resistivty of an oil bearing sand can be calculated by setting m and n equal to 2 (Keller, 1971). The effect of increasing oil saturation can be seen by considering a hypothetical reservoir formation with $\rho_w = 1\Omega$m and $\phi = 0.25$. When saturated with water only $S_w = 1$ and the bulk resistivity is 16Ωm. When the same formation is 90 % oil saturated ($S_w = 0.1$), its bulk resistivity is 1600 Ωm, an increase of two orders of magnitude.

The geoelectrical structure of oil and gas traps is determined by four key elements; reservoir, lithology, structure and diagenetic changes (Keller et al., 1996b). The most comprehensive study into the geoelectrical characteristics of these was carried out in the former Soviet Union using electrical log data from over 950 wells (Kirichek et al., 1974). From these data a series of models was created to summarize the geoelectrical responses associated with a range of reservoir types and sizes ranging from large oil fields to non-prospective areas. They show that the resistivity associated with hydrocarbon-bearing reservoirs increases by a factor of 1.5-3 but can be as high as 10 compared with the resistivity associated with water-filled reservoirs. The region directly above the reservoir also exhibits an increase in resistivity by a factor of about 1.5, though again it can be much higher, while in the near surface the resistivity is unchanged or even decreases. It was also found that, in general, gas fields have higher resistivities than oil fields, particularly in small fields. The results also identify the importance of hydrocarbon migration in the response obtained. These results are summarised in Figure 2.9.
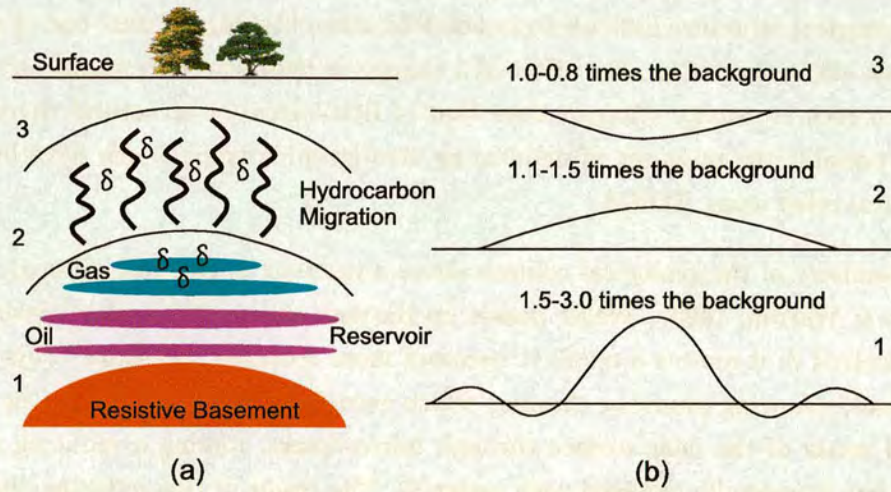
Figure 2.9: A model derived from electrical well logs (a) showing how the presence of hydrocarbons in a reservoir increases the resistivity (b). The model is based on data from 950 drill holes in Russia (After Spies (1983)).

However, comparative studies of well logs over oil and gas fields are inherently difficult due to differences in drilling techniques and log tools, which present problems with log normalization. Keller *et al.* (1996b) found that the results of TDEM sounding were generally more accurate than down-hole methods in determining bulk resistivity values for comparative studies. Their results suggest the TDEM signature of hydrocarbon traps is characterized by anomalously high resistivities similar to those shown in Figure 2.9, except that the response is larger at the edges of the accumulation than in the middle.

Hydrocarbons migrate into a reservoir because of lithologic and structural conditions. Often the presence of a geochemical plume, chimney or halo above the hydrocarbon accumulation will alter the resistivity of a zone of the subsurface formation due to various diagenetic changes in the rock. The response of these secondary alterations is often larger and shallower than the reservoir(s) that formed them (Rice *et al.*, 1981). As a result, they are much more easily detected than the reservoir itself. Consequently, hydrocarbon traps often manifest themselves as much larger targets than the reservoirs alone. The form of these plumes, their presence or otherwise, and geochemical composition depend on several factors. For example, in areas where evaporation exceeds infiltration of precipitation there is an enhanced upward migration of water above the petroleum layer caused by capillary action, while in areas with heavy precipitation the upward migration of fluids is often inhibited (Spies, 1983). The vertical migration of

hydrocarbons results in them crossing structural boundaries, which can make mapping true geological structure difficult to impossible, since lithology is only one of many factors that affect resistivity. The effect of a change in hydrocarbon content on resistivity within a rock is usually stronger than that of lithological or structural changes. This makes possible the prospect of delineating stratigraphic traps which have little or no structural relief using TDEM.

The chemistry of the geological column above a reservoir is generally altered as follows (Duren & Warren, 1995). Water passes up through the reservoir where hydrocarbons are dissolved in it and as a result it becomes more reducing in nature. This results in an isolated reducing plume or chimney which eventually works its way to the oxidizing ground water of the near surface through micro-cracks, forcing a reducing chemistry onto what is normally oxidized rock material. The result of this reducing chemistry is the formation of low resistivity clay at a depth of a few hundred to a few thousand feet. From the surface down to a few hundred feet calcium carbonate and silica are precipitated in the pores of the rock in the near-surface material to form a high resistivity cap. The formation of the low resistivity clay may help to explain why the results of Keller *et al.* (1996a) show the maximum resistivity at the edges of the reservoir and not in the middle. A summary of this is given in Figure 2.10. The presence of such plumes clearly poses a problem for 1-D modelling and inversion.

The induced polarization (IP) prospecting technique is regularly used for detecting geochemical alteration of the shallow subsurface due to the migration of hydrocarbons at depth. Successful results were reported on this by Oehler & Sternberg (1984). A new approach involves detecting the surface accumulation of carbonate and silica as a result of the microseepage of hydrocarbons dissolved in gas using radar waves (Duren & Warren, 1995). A summary of much of the work in detecting and mapping hydrocarbon-related alteration is given in Hughes *et al.* (1985). Despite being easier to detect, such plumes are not necessarily an indication of large accumulations of hydrocarbons at depth; equally the absence of such plumes is not a definite indication of there being no hydrocarbons present. Although not every anomalously high resistivity region is necessarily an oil or gas field, where there is no anomaly present the probability of finding oil or gas is small to zero.

Initial work and 'Electromagnetic reflection'

The early work from the 1930's to 1960's on hydrocarbon detection, although not particularly relevant to modern techniques, is worth mentioning in relation to the effect it had on oil companies' views on EM methods, views which to some extent remain to this day. Three methods based on what was termed 'electromagnetic reflection' are
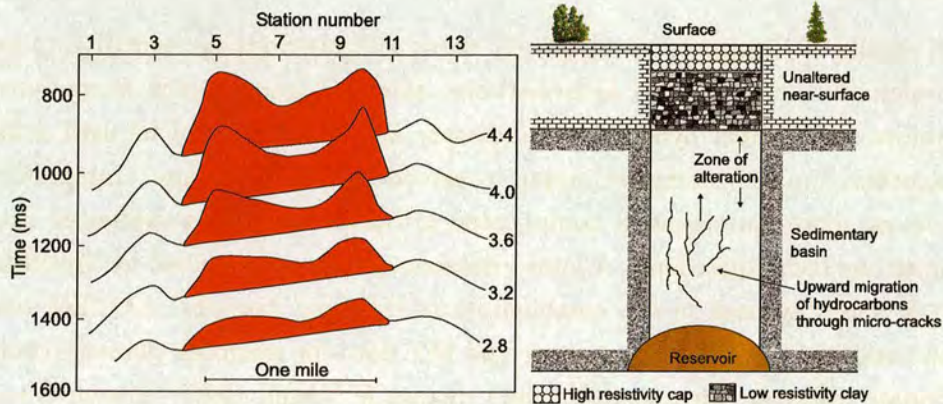
Figure 2.10: Left: Typical response over a hydrocarbon reservoir using the electromagnetic imaging method. A decrease is observed in the middle of the reservoir relative to the edges (Redrawn from Tasci & Jordan (2003)). Right: A model of geochemical alteration above a reservoir that may explain the observed reduction in resistivity in the middle of the reservoir.

the Radoil (Pratt, 1953), Elflex (Evjen, 1948) and Electraflex (Azad, 1973) methods. The Elflex method was by far the most widely used of these methods with hundreds of surveys carried out. Elflex measurements were claimed to be due to EM reflections from oil or gas bearing formations. The Electraflex method employed a dipole-dipole array (collinear grounded-wire source and receiver dipoles). The source signal is an electric surge applied by a condensor. The receiver signal is recorded with the source signal. The method was largely abandoned in the 1950's because it was not known how to interpret the data quantitatively in terms of a layered earth. This configuration is essentially the same as the MTEM data presented in this thesis. Work in the 1950's at the Socony Mobil laboratory showed that for the conductive rocks normally found in sedimentary basins, the transient response to impulse excitation contained such low frequencies that it would be difficult to obtain the resolution needed to identify individual reflected events (Yost, 1952): the results were verified with a series of metallic model experiments (Yost *et al.*, 1952). Based on these results a field evaluation of the EM reflection method was carried out by Orsinger & van Nostrand (1954). These papers showed that EM methods would not be able to resolve such reflections from depths of up to 2000m and as a result, the petroleum industry became disillusioned with TDEM methods and had largely abandoned its use by the 1960's (Yungul, 1996). Theoretical advancements have since shown that low frequency EM data can be mapped to a seismic equivalent domain and individual arrivals can actually be identified. The full background to this is presented in Chapter 3.

33

Integrated work

As the results of Ellingsrud *et al.* (2002) show, EM methods are sensitive to areas of high resistivity which include hydrocarbons, salt and igneous rock formations. EM is therefore not a direct hydrocarbon indicator and ideally should be used in tandem with another complimentary technique to provide a clearer picture. Integrated work is becoming more important as complicated prospects cannot be evaluated using the data from one technique alone. A joint inversion scheme as described by Vozoff & Jupp (1975) is normally used in the combination of different datasets. LOTEM has been used in combination with both seismic and MT data for mapping porosity changes in a carbonate reservoir (Strack *et al.*, 1991) (Strack & Vozoff, 1996). Attempts to image beneath basalt using a combination of four different EM techniques was carried out by Morrison *et al.* (1996) while Withers *et al.* (1994) combined seismic reflection, TEM, MT and gravity data in an attempt to identify hydrocarbon accumulations beneath basalt.

Borehole measurements

The use of EM in boreholes is popular for several reasons. Cross-well measurements (Nekut, 1994; Alumbaugh & Morrison, 1995a,b; Hoversten *et al.*, 2001) provide higher resolution data than surface-based techniques, as the path taken by EM energy from source to receiver is much shorter. Furthermore, offshore borehole measurements do not suffer the same attenuation of high frequency energy due to the seawater, and this also provides better resolution data. Borehole-to-surface studies have been described by Spies & Greaves (1991) and Tseng *et al.* (1998), who found that near-surface conductors can seriously distort the data compared with the crosswell case. Measurements made through steel-cased wells which strongly mask the EM signal and make data difficult to interpret have been studied by Schenkel & Morrison (1994) and Wu & Habashy (1994). Nekut (1995) describes a method which uses gapped well casings to address this problem. In addition, all the metal pipes and infrastructure associated with an oilfield can seriously distort EM signals which can cast serious doubt over the validity of any interpretation. As a result, the vast majority of borehole measurements are used for monitoring, where differences are important and the effects of oilfield infrastructure cancel when differences are taken. The fact that one or two wells already exist in which to make measurements means that the exploration has already been done and so borehole measurements are almost always used to monitor the state of existing fields.

Present Work: Land and Marine EM

Current land-based TEM techniques used for hydrocarbon exploration are mainly LOTEM systems. Two systems have been developed privately by the companies

Stratasearch and Montason and are intended to look for targets within 10,000 feet of the surface either directly or indirectly (Christopherson, 2002). Results obtained by Stratasearch have been published in Keller *et al.* (1996a) and Keller *et al.* (1996b) and have reportedly contributed to the discovery of 6 new oil and gas field discoveries.

Present work offshore is mainly FDEM utilizing the SBL technique of Eidesmo *et al.* (2002) in the detection of hydrocarbons. Two independent companies, EMGS based in Norway and OHM based in England, were set up in 2002 to commercialise this idea. The use of marine TEM in hydrocarbon exploration has so far been limited to numerical studies of the evaluation of gas hydrate deposits (Edwards, 1997).

2.5 Distortion of EM data

The theoretical response of a particular target in a TEM survey is usually determined by modelling the target in one, two and, recently, three dimensions. The concept of the detectability of a conductive or resistive target in a 1-D earth was introduced by Verma & Mallick (1979). This set a qualitative threshold for the difference required between the target response and the background response in order for a target to be considered detectable by surface EM. In practice of course there are many other effects of varying size that can distort, mask or totally obliterate the target response in which we are interested. The response at the receiver can be considered to be made up of the target response as well as geological, man-made and geomagnetic noise. It is essential in any survey to be able to quantify the effect of these noise sources in relation to the target response in order for any meaningful interpretation to be carried out. The interpretational bias introduced by these sources of noise is very much the bane of the EM probing of the earth with virtually no sites in Europe that are EM noise free [4] (Szarka, 1988). This section discusses the effect of these noise sources and how they are dealt with in EM data.

Cultural noise

Man-made or cultural noise can be considered to be due to any construction on or below the surface of the earth and is of either passive or active origin (Ward, 1983). Examples of passive noise sources include pipes, powerlines, rail tracks and fences.

---

[4]Not all EM noise is bad, however, Qian & Pedersen (1991) carried out successful MT studies in China where EM noise from the city of Tangshan was used as an artificial electric dipole source. The background EM signal from the city is equivalent to a dipole moment of 5000-10000 Am in the period range 0.1-10s. This is strong enough to dominate the natural fields in this band up to 50km from the city.

They act as elongated superficial resistivity inhomogeneities. Active sources of EM noise include electric power transmission lines, anti-corrosion systems such as pulsed cathodic protection (PCP) and electric railway lines: these have the effect of producing a parasitic EM field in the earth. Active sources of EM noise are of two main types: harmonics which are stable in time (regular noise), and sudden impulse like disturbances (irregular noise).

Regular active man-made noise is mainly due to power lines consisting of sharp spectral peaks at the mains frequency and its odd harmonics. This noise often has the greatest effect on the raw data, with contamination seen in data from a DC electric railway 30km away. Luckily the effect can be almost totally removed by applying digital true amplitude notch filters (Strack *et al.*, 1989a). The filtering must be applied before stacking as the noise is often not phase-stable over long periods of time and stacking then smears the power line frequency which cannot be removed subsequently by notch filtering. Irregular impulsive disturbances are usually dealt with using a spike detector, although this is difficult to incorporate into TEM data with a short rise time. Another form of spike suppression is the use of selective stacking (section 4.5) in which the statistical distribution of amplitudes are used as a basis for rejection. An impulsive distortion on a single trace can be so large that even after stacking it is bigger than the signal. A visual check of the data before and after stack is a time-consuming but guaranteed way of ensuring such noise is not present in the final stacked data. In some cases the distortion may be so great that certain individual traces have to be edited out.

Passive sources of man-made EM noise act as elongated superficial resistivity inhomogeneities, and their effect on EM data is best understood by modelling (Qian & Boerner, 1995). The effect of long cylindrical conductors has been studied by a number of investigators. Fitterman *et al.* (1989) investigated the effect of buried metal pipes on EM data and found that in general their effect is to reduce the apparent resistivity over the entire time range observed with a corresponding decrease in interpreted resistivity. The effect of pipes just 5-15cm in diameter buried between 25 and 100m below a profile can be to reduce the interpreted resistivity by up to a factor of 50 whilst still fitting 1-D models, usually of a deep buried conductor. This can be particularly misleading as soundings made near pipes on the surface often exhibit completely incompatible behaviour with such an interpretation and such data are rejected while more subtle distortions are not recognised and result in a false interpretation. Nekut & Eaton (1990) found that soundings can be distorted up to several kilometres away from a pipeline with inversion results being incorrect for depths greater than the lateral distance to the pipeline. When the source-receiver offset is less than the offset to the

pipe, the pipeline anomaly is very small for depths of investigation less than the offset to the pipe for a grounded-wire source. Pipeline effects observed in the field have been found to be smaller than those observed by modelling. Pipeline responses are smaller if the pipe is buried in a thin resistive surface layer or has a high resistivity coating. Results obtained with the central loop configuration are more strongly affected than grounded dipole sources.

Attempts have been made to remove the effects of pipes in EM data by stripping the response of cultural conductors from measured data (Polzer et al., 1990). The method relies on the estimation of the secondary current flowing within a conductor by direct measurement and subtracting it from the measured data. The technique has been successfully applied to UTEM data, but ultimately doubt remains as to whether features in the data are real or artefacts of removing the response of the pipe. In carrying out any survey it is wise first to carry out a general mapping of passive man-made conductors using a conductivity meter.

Geological noise

The effect of geological noise is quite different from that of man-made noise in EM data in that its removal by processing or modelling is virtually impossible. The term applies to any effect in the data resulting from the sub-surface geology that is not produced by the survey target. Another possible term for such effects is 'unwanted signal'. In many ways the effect is more problematic than cultural noise, as subtle distortions can seriously bias estimates of earth resistivity while still fitting 1-D earth models, resulting in an inaccurate interpretation.

Static shift and band limited responses

Two effects of geological noise caused by near-surface conductors are regularly observed in TEM data with a grounded wire source; they are known as static shift and band limited responses. Near-surface conductors are ubiquitous in the earth, due to localised weathered zones or conductive patches of clay. Understanding the response of these conductors is essential if the deeper geoelectric section is to be interpreted with any confidence.

The static shift in TEM data occurs in much the same way as a near-surface weathered zone produces a static shift in seismic data. In adopting a field layout similar to that of seismic reflection, the movement of the source introduces a new problem regarding shallow effects. If these effects were constant over the length of the profile, interpretation of results in terms of deeper horizons would be unaffected. However, if the changes in shallow effects are greater than the deep effect for which we are looking, then the

problem becomes far more serious. The effect is caused by inhomogeneous current flow around lateral discontinuities. Newman (1989) reproduced static shift effects numerically by 3-D modelling of the magnetic field response of near surface conductors that could represent a localised weathered zone or a conductive patch of clay. Such shifts also arise when the source is placed on an area of low resistivity in order to inject more current into the ground. Static effects are also seen in the magnetic and electric field response to a grounded wire source and electric fields are strongly affected by the ground in the immediate vicinity of the electrodes, whereas the magnetic field is a weighted integral of all subsurface currents. When compared with 1-D curves on a log-log plot, a parallel shift is seen in the 3-D decay curve but not a change in its shape; differentiating the field data therefore removes the effect of the static shift (Hördt *et al.*, 2000). This effect is similar to the static shift seen in MT (Jones, 1988) but in MT it is only the electric field that gives rise to the static shift, not the magnetic field. If a static response arises, the response is distorted at later times by as much as an order of magnitude. In such a case large errors will be present if a layered earth interpretation model is used unless the static shifts are removed from the data. The calibration factor (Strack, 1992, Ch3 p62) is used extensively with grounded source soundings to correct for static shifts. The finding that TEM soundings with a grounded source produce static shifts contrasts sharply with that of a loop source. When a loop source is used over a near surface conductor the conductor's response is observed over a short time range not detectable at late times (Spies, 1980; Sternberg *et al.*, 1988).

Band limited responses take the form of an increase, decrease or reversal in the measured voltage response. The response is band limited in time and occurs only at early times, typically less than 5ms. At later times the response is not affected by the conductor. The nature of the distortion depends on the relative location of the profile to the conductor. An elegant explanation of how these responses occur is given by Gunderson *et al.* (1986). For a wire source and magnetic field receiver, the distortion only occurs at or near the receiver. With electric field receivers, by virtue of reciprocity for an electric dipole source, the distortion is the same whether the conductor is near the source or the receiver (Qian, 1994). In multicomponent surveys this fact can be used to help identify the effect of such conductors. For this reason it is essentially impossible to fit a layered earth model to the first 5ms of such data and this portion of the data is rarely modelled.

Induced Polarization

Induced polarization effects are caused by a frequency-dependent barrier to current flow. These commonly form at the interface between ionic-conducting groundwater and semi-conducting ore minerals or mineralized rocks. Frequency-dependent conductivity may

also be present in sedimentary rocks and clay bearing sands. It is generally assumed in EM that the conductivity is frequency-independent and IP effects are ignored. However, there are cases in which the EM response of the ground is frequency-dependent and IP effects are significant. Morrison *et al.* (1969) were the first to show that it was possible for a transient decay curve to change sign with time because the conductivity of the ground was a complex function of frequency (polarizable). This is especially true for loop-loop configurations, in particular the coincident and central loop configuration where negative transients are commonly seen. Negative transients are theoretically impossible for these configurations in a frequency-independent linear medium (Weidelt, 1982; Guptasarma, 1984). Further understanding was only made possible with the advent of 3-D modelling schemes. These showed that localised early time sign changes observed in field data that could not be produced by a polarizable layer were due to localised surficial polarizable patches (Hohmann & Newman, 1990) or polarizable 3-D bodies at depth (Flis *et al.*, 1989) in the case of later sign changes. Surficial effects are seen only in coincident loop data; in separated loop data at 150m the effect is not detectable (Hohmann & Newman, 1990). For the effect of a body at depth to be measured, it must be strongly polarizable.

The IP method makes use of the polarization properties of rocks to detect targets. It operates in the frequency range 0.01-10Hz while the frequency range of EM measurements is 10hz-10khz (Smith & West, 1989). The polarization properties of rocks in the IP frequency range are well documented; however, much less is known about their properties in the EM frequency range. It is possible to have a pronounced IP effect in EM data that does not appear in IP data over the same area. This can make identification of IP effects in EM data difficult. An IP effect for electric field data from a grounded source is shown in Figure 2.11 at around 100ms.
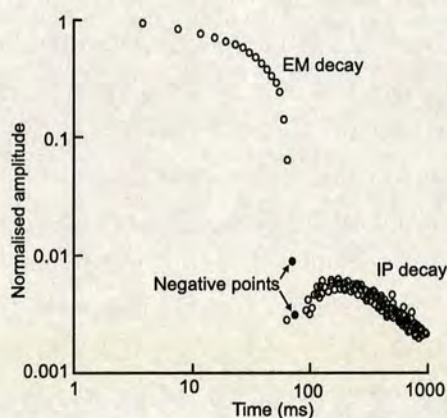
Figure 2.11: An IP effect seen in electric field data from a 1500m long grounded source at 2km offset in Canada (After Eadie (1981)).

Three dimensional effects

The other main source of geological noise is associated with the effect of vertical geological contacts and three dimensional structural effects. Any EM data collected in the presence of such structures clearly cannot be interpreted with any confidence in terms of a 1-D layered earth model. Understanding these effects is extremely important as EM methods used in support of hydrocarbon exploration are commonly employed in complex geological settings and many mineral targets are located near contact zones. The effects of these structures are generally studied in one of two ways. Either the effects are calculated directly through forward modelling (Gunderson *et al.*, 1986; Newman *et al.*, 1987) or by applying 1-D inversion to multidimensional data (Newman *et al.*, 1986). Most attempts at interpretation are based on trial and error though such interpretation is made more difficult by the increased range of equivalence that 2-D and 3-D parameters introduce.

Analysis of real and modelled central loop and LOTEM configuration data in the presence of a fault (Hoekstra *et al.*, 1991) and structural highs and lows (Goldman *et al.*, 1994) indicates that data for the LOTEM configuration are severely distorted by the presence of structure, with 1-D interpretation bearing poor resemblance to the known geological structure. Central loop data are far less affected, except near vertical boundaries, where ficticious layers are introduced by 1-D inversion. The response from a vertical contact due to an electric dipole source is particularly large, with the contact anomaly as much as 30 times that of a deeper target anomaly and significant contact effects seen up to 1km from the boundary (Wilt & Becker, 1986). An attempt to interpret 3-D effects quantitatively in magnetic field LOTEM data was carried out by

Hördt *et al.* (1992). The effect of 3-D structure on electric field measurements has not to my knowledge been studied.

An alternative approach to interpreting 3-D effects that is based purely on examination of the spatial and temporal behaviour of the data was proposed by Garg & Keller (1986). When data are recorded at multiple receiver locations, the spatial structure of the EM field reveals the effect of 3-D structure in the earth more clearly than the temporal structure. This can then be used to provide a rough model of the subsurface for subsequent inversion, or may even allow an adequate interpretation to be made based purely on manipulation of the spatial and temporal spectra of the EM field. Another 3-D effect, and perhaps the most obvious example of where the earth is not 1-D, is where severe topography is associated with the survey area. Topographic effects for LOTEM data were studied by Hördt & Müller (2000) who found that data collected in areas of extreme topography are distorted. The effects seen are similar to that of current channelling through a near-surface conductive body i.e., a mountain.

The use of more than one component can be very helpful in the identification of distortions caused by 3-D effects. If a good fit to the data is made to one component of the data, these parameters can be used to calculate forward curves for the other measured components. If there is a good fit, it can be assumed that a 1-D interpretation is valid; if there is a significant misfit, it is likely that multi-dimensional effects are present and an alternative approach to interpretation is needed.

Other sources of noise

Other sources of noise include instrumental, geomagnetic fluctuations and motion-induced noise. Instrumental noise can occur due to clock drift, inability of amplifiers to handle the large dynamic range encountered in the field, and electrical interference between receiver boxes (Helwig *et al.*, 1995). Fluctuations in geomagnetic fields which form the signal in MT can also affect EM data. Generally their period is more than 1 second, with higher frequencies attenuated in the conductive ionosphere. Their effect is relatively unimportant except in very low frequency EM. Above 1Hz the main source of geomagnetic noise occurs from atmospheric lightning discharges around the earth, referred to as 'spherics'. These often appear as spikes in EM data. Motion-induced noise occurs in magnetic field sensors by movement of the sensor within the Earth's magnetic field. Since the Earth's field is 10^6 times larger than the typical fields measured in EM, vibrations of the sensor induced by the wind can result in appreciable noise voltages.

41

2.6 Modelling EM Data

The subject of EM modelling is almost as old as the EM technique itself. Any interpretation of EM data has always relied on being able to model the data computationally to some extent. The foundation of EM modelling was presented in a series of classic papers by James Wait and Bimal Bhattacharya and took the form of analytic solutions for various source types in the presence of geometrical objects such as spheres, cylinders and two plane layers of differing conductivity. Much of the pioneering work in this field was carried out in the 1970's and 1980's by the late Gerald Hohmann and colleagues at the university of Utah, publishing in excess of 50 papers on this topic in the pages of *Geophysics* alone. EM modelling is much more complicated than the modelling of seismic wave propagation because EM modelling requires a complete solution to a formal boundary value problem which is a very time-consuming process, since the solution is obtained from the vector diffusion equation (Lee *et al.*, 1989).

'Despite the elegance of the mathematical treatment and the apparent simplicity of the final results, the numerical evaluation of EM field components turns out to be exceedingly difficult'

Nabighian (1979)

A variety of 3-D modelling approaches now exist. They are based on integral equation (IE) (Newman *et al.*, 1986), finite element (Pridmore *et al.*, 1981) and finite difference (Mehanee & Zhdanov, 2003) techniques. These solutions were obtained in the frequency domain at discrete frequencies with the time-domain response being obtained by taking the inverse Fourier transform. Direct calculation in the time domain may also be done, using an explicit time-stepping technique. This approach is more time-consuming than the frequency domain approach but the result provides more insight into the TEM process within the whole spectrum, from very early to very late times. Time-stepping solutions have been obtained in 3-D for the integral equation formulation by San Filipo *et al.* (1985), and for the finite difference approach by Wang & Hohmann (1993). A 2-D time stepping solution for the finite element approach was presented by Kuo & Cho (1980). For the sea-floor 2.5-D finite element results have been derived in the time domain by Everett (1990) and in the frequency domain by Unsworth *et al.* (1993). It should be noted that all these methods discretize the EM field to some extent with the accuracy and stability of the result often strongly dependent on the scheme used. As a result different approaches can give quite different results. This is because the dynamics of discretization are described by coupled partial differential equations with fewer degrees of freedom than field components (Árnason, 1995). A novel approach to

modelling EM data was carried out by Lee *et al.* (1989). They used similarities between the diffusion and wave equations to transform data computed in an equivalent wavefield to data obeying the diffusion equation, the results were found to compare favourably with the 2-D fintite difference results of Oristaglio & Hohmann (1984).

Comprehensive reviews of the subject can be found in Hohmann (1988), Tabarovsky *et al.* (1996) and Zhdanov *et al.* (1997).

Chapter 3

Elastic and diffusive wave propagation

3.1 Introduction

At low frequencies, electromagnetic propagation in a conductor obeys the diffusion equation while seismic wave propagation obeys the wave equation. The diffusion and wave equations are partial differential equations with the same spatial but different time derivatives. They can be related via an integral equation known as the q transform. This chapter begins by deriving the diffusion equation using Maxwell's equations as the starting point. Hooke's law and Newton's equation of motion are used as the starting point for deriving the wave equation, which is given in Appendix A. The q transform which transforms the wave equation into the diffusion equation is then introduced. Inversion of this transform (i.e. converting from the diffusion to the wave equation), which requires the solution of an integral equation, is then reviewed. The more specific case of inverting the q transform for MTEM data from a grounded wire source to extract resistivity information is then presented.

3.2 Electromagnetic Wave Propagation in the Earth

Maxwell's Equations

The propagation of electromagnetic waves in the earth is described by Maxwell's equations in the time domain (3.1-3.4). They are the starting point for obtaining an understanding of how EM fields can be used to study the structure of the earth and determine its electric and magnetic properties. The equations are based on the experimental work of Ampère, Faraday and Coulomb among others. They are therefore empirical but nevertheless do describe most macroscopic EM phenomena.

$$\nabla \times \boldsymbol{H}(\boldsymbol{x}, t) = \frac{\partial \boldsymbol{D}(\boldsymbol{x}, t)}{\partial t} + \boldsymbol{J}_c(\boldsymbol{x}, t) + \boldsymbol{J}_s(\boldsymbol{x}, t), \quad (Ampère's \ law) \tag{3.1}$$

$$\nabla \times \boldsymbol{E}(\boldsymbol{x}, t) = -\frac{\partial \boldsymbol{B}(\boldsymbol{x}, t)}{\partial t} - \boldsymbol{K}_s(\boldsymbol{x}, t), \qquad (Faraday's \ law) \tag{3.2}$$

$$\nabla \cdot \boldsymbol{D}(\boldsymbol{x}, t) = \rho_f, \qquad\qquad (Coulomb's \ law) \tag{3.3}$$

$$\nabla \cdot \boldsymbol{B}(\boldsymbol{x}, t) = 0, \qquad\qquad (Continuous \ flux \ law) \tag{3.4}$$

where $\boldsymbol{H}(\boldsymbol{x}, t)$ is the magnetic field intensity, $\boldsymbol{D}(\boldsymbol{x}, t)$ is the electric displacement, $\boldsymbol{J}_c(\boldsymbol{x}, t)$ is the conduction current, $\boldsymbol{J}_s(\boldsymbol{x}, t)$ is the source volume density of electric current, $\boldsymbol{E}(\boldsymbol{x}, t)$ is the electric field intensity, $\boldsymbol{B}(\boldsymbol{x}, t)$ is the magnetic induction, $\boldsymbol{K}_s(\boldsymbol{x}, t)$ is the source volume density of magnetic current and ρ_f is the volume density of free charge (Wilson, 1997). The terms $\boldsymbol{K}_s(\boldsymbol{x}, t)$ and $\boldsymbol{J}_s(\boldsymbol{x}, t)$ relate to sources and so describe prescribed features on the upper boundary only. The total electric current density $\boldsymbol{J}(\boldsymbol{x}, t)$ is made up of two components and can be written as

$$\boldsymbol{J}(\boldsymbol{x}, t) = \boldsymbol{J}_c(\boldsymbol{x}, t) + \boldsymbol{J}_s(\boldsymbol{x}, t), \tag{3.5}$$

The electric current density and the volume charge density are related through the continuity equation (3.6):

$$\nabla \cdot \boldsymbol{J}(\boldsymbol{x}, t) + \frac{\partial \rho_f}{\partial t} = 0. \tag{3.6}$$

Equations (3.1-3.4) are uncoupled differential equations of the five vector functions $\boldsymbol{E}(\boldsymbol{x}, t)$, $\boldsymbol{B}(\boldsymbol{x}, t)$, $\boldsymbol{H}(\boldsymbol{x}, t)$, $\boldsymbol{D}(\boldsymbol{x}, t)$ and $\boldsymbol{J}(\boldsymbol{x}, t)$ and from them there appears no obvious

relationship between the behaviour of the EM field and the subsurface structure of the earth or its properties. However, they are coupled through three relationships known as the the constitutive equations (3.7-3.9) which illustrate where such dependancies arise and reduces the number of basic vector field equations from 5 to 2.

$$\boldsymbol{J}_c(\boldsymbol{x},t) \;=\; \sigma\boldsymbol{E}(\boldsymbol{x},t), \qquad (Ohm's\ \ law) \qquad\qquad (3.7)$$

$$\boldsymbol{D}(\boldsymbol{x},t) \;=\; \epsilon\boldsymbol{E}(\boldsymbol{x},t), \qquad\qquad\qquad\qquad (3.8)$$

$$\boldsymbol{B}(\boldsymbol{x},t) \;=\; \mu\boldsymbol{H}(\boldsymbol{x},t), \qquad\qquad\qquad\qquad (3.9)$$

where σ is the electrical conductivity of the medium, ϵ is the dielectric permittivity and μ is the magnetic permeability.

In each of the equations (3.7-3.9) the properties σ, ϵ and μ are tensors since the other terms in each equation are vectors. For most EM earth problems the following assumptions are made in order to simplify the analysis and make these properties real scalar functions of position only.

1. All media are linear, isotropic and homogeneous, and possess electrical properties which are independent of time, temperature, frequency and pressure.

2. Magnetic permeability μ is assumed to be that of free space, i.e.,

$$\mu = \mu_0 = 4\pi \times 10^{-7} H/m$$

with the magnetization of subsurface rocks assumed to be zero.

Under such assumptions these tensors become scalars. These assumptions are widely made in CSEM techniques as they are generally a good approximation to the earth we encounter. However, it is important to be aware of situations where these assumptions are invalid. The following exceptions apply,

1. In the presence of high concentrations of iron-rich minerals containing magnetite or pyrrhotite, a large relative permeability $\frac{\mu}{\mu_0} > 1$ can occur.

2. Superparamagnetism or magnetic viscosity due to time dependent susceptibility in lateritic soil cover and over basalt have been found to distort TEM data (Buselli, 1982; Lee, 1984).

3. Where fine layering is not resolved but instead results in an anisotropic bulk response. There are separate CSEM methods that are designed to measure conductivity anisotropy, for example to determine bedding orientation (Moran & Gianzero, 1979).

4. Where the conductivity is frequency dependent and induced polarization (IP) effects are present. There are also techniques designed to specifically detect IP effects such as electrolytic polarization at the surface of metallic mineral grains (Sumner, 1985) which is used in mineral exploration.

5. Time dependent electric conductivity can occur due to varying moisture content in surface soils which can have a significant effect in shallow investigations.

Over the frequency range used in CSEM (typically 0.1hz-10khz) the electrical conductivity of most rocks is, to a good approximation, real and frequency-independent, implying that the EM fields are governed by a diffusion process rather than a wave propagation process [1] the displacement current $D(x, t)$ can usually be ignored as $|J(x, t)| >> \left| \frac{\partial D(x,t)}{\partial t} \right|$.

In EM methods the quasi-stationary version of Maxwell's equations holds as displacement currents are negligible and (3.1) and (3.3) can be written as

$$\nabla \times H(x, t) = J(x, t), \qquad (3.10)$$
$$\nabla \cdot D(x, t) = 0. \qquad (3.11)$$

For homogeneous earth materials of conductivity 10^{-4} S/m or greater, the free charge ρ_f dissipates in less than 10^{-6} s (Stratton, 1941). So for geophysical prospecting in which frequencies less than 10^5 Hz are used, $\frac{\partial \rho_f}{\partial t} \approx 0$ and the continuity equation (3.6) becomes

$$\nabla \cdot J(x, t) = 0 \qquad (3.12)$$

---

[1] At high frequencies (>1Mhz), the imaginary component of the conductivity can become sufficiently large that the fields propagate as waves. The ground penetrating radar (GPR) CSEM method uses propagating EM waves and operates in the range 10 to 100MHz, the so-called 'dielectric' regime. The high attenuation rate of these fields limits the usefulness of radar techniques to investigation of shallow subsurface layers

which is the divergence of (3.10). At the boundary between two layers of different conductivity surface charges accumulate and equation (3.12) is not equal to zero.

The Diffusion Equation

It can be shown that the quasi-static approximation is valid and that the fields in CSEM obey the diffusion equation, by manipulating Maxwell's equations as follows. Taking the curl of (3.1) and (3.2) gives

$$\nabla \times (\nabla \times \boldsymbol{H}(\boldsymbol{x}, t)) - \nabla \times \left(\frac{\partial \boldsymbol{D}(\boldsymbol{x}, t)}{\partial t} \right) = \nabla \times \boldsymbol{J}_c(\boldsymbol{x}, t) + \nabla \times \boldsymbol{J}_s(\boldsymbol{x}, t), \qquad (3.13)$$

$$\nabla \times (\nabla \times \boldsymbol{E}(\boldsymbol{x}, t)) + \nabla \times \left(\frac{\partial \boldsymbol{B}(\boldsymbol{x}, t)}{\partial t} \right) + \nabla \times \boldsymbol{K}_s(\boldsymbol{x}, t) = 0. \qquad (3.14)$$

Substituting the constitutive equations (3.7-3.9) into (3.13) and (3.14) gives

$$\nabla \times \nabla \times \boldsymbol{H}(\boldsymbol{x}, t) - \epsilon \nabla \times \frac{\partial \boldsymbol{E}(\boldsymbol{x}, t)}{\partial t} = \sigma \nabla \times \boldsymbol{E}(\boldsymbol{x}, t) + \nabla \times \boldsymbol{J}_s(\boldsymbol{x}, t), \qquad (3.15)$$

$$\nabla \times \nabla \times \boldsymbol{E}(\boldsymbol{x}, t) + \mu \nabla \times \frac{\partial \boldsymbol{H}(\boldsymbol{x}, t)}{\partial t} + \nabla \times \boldsymbol{K}_s(\boldsymbol{x}, t) = 0. \qquad (3.16)$$

Provided that the vector functions $\boldsymbol{E}(\boldsymbol{x}, t)$ and $\boldsymbol{H}(\boldsymbol{x}, t)$ are piecewise continuous and possess continuous first and second derivatives, the operators $\nabla \times$ and $\frac{\partial}{\partial t}$ may be interchanged (Ward & Hohmann, 1988). Equations (3.15) and (3.16) can then be re-written as

$$\nabla \times \nabla \times \boldsymbol{H}(\boldsymbol{x}, t) - \epsilon \frac{\partial}{\partial t}(\nabla \times \boldsymbol{E}(\boldsymbol{x}, t)) = \sigma \nabla \times \boldsymbol{E}(\boldsymbol{x}, t) + \nabla \times \boldsymbol{J}_s(\boldsymbol{x}, t), \qquad (3.17)$$

$$\nabla \times \nabla \times \boldsymbol{E}(\boldsymbol{x}, t) + \mu \frac{\partial}{\partial t}(\nabla \times \boldsymbol{H}(\boldsymbol{x}, t)) + \nabla \times \boldsymbol{K}_s(\boldsymbol{x}, t) = 0. \qquad (3.18)$$

Substituting the expressions for the quantities $\nabla \times \boldsymbol{H}(\boldsymbol{x}, t)$ and $\nabla \times \boldsymbol{E}(\boldsymbol{x}, t)$ given in equations (3.1) and (3.3) then gives,

$$\nabla \times \nabla \times \boldsymbol{E}(\boldsymbol{x}, t) + \mu \epsilon \frac{\partial^2 \boldsymbol{E}(\boldsymbol{x}, t)}{\partial t^2} + \mu \sigma \frac{\partial \boldsymbol{E}(\boldsymbol{x}, t)}{\partial t} \tag{3.19}$$

$$= -\mu \frac{\partial \boldsymbol{J}_s(\boldsymbol{x}, t)}{\partial t} - \nabla \times \boldsymbol{K}_s(\boldsymbol{x}, t),$$

$$\nabla \times \nabla \times \boldsymbol{H}(\boldsymbol{x}, t) + \mu \epsilon \frac{\partial^2 \boldsymbol{H}(\boldsymbol{x}, t)}{\partial t^2} + \mu \sigma \frac{\partial \boldsymbol{H}(\boldsymbol{x}, t)}{\partial t} \tag{3.20}$$

$$= -\epsilon \frac{\partial \boldsymbol{K}_s(\boldsymbol{x}, t)}{\partial t} - \sigma \boldsymbol{K}_s(\boldsymbol{x}, t) + \nabla \times \boldsymbol{J}_s(\boldsymbol{x}, t).$$

In order to see why the quasi-static approximation holds and displacement currents are negligible it is instructive to take the Fourier transform of the left hand side of equations (3.19) and (3.20) to give,

$$\nabla \times \nabla \times \tilde{\boldsymbol{E}}(\boldsymbol{x}, \omega) - k^2 \tilde{\boldsymbol{E}}(\boldsymbol{x}, \omega) \tag{3.21}$$

$$\nabla \times \nabla \times \tilde{\boldsymbol{H}}(\boldsymbol{x}, \omega) - k^2 \tilde{\boldsymbol{H}}(\boldsymbol{x}, \omega) \tag{3.22}$$

where

$$k^2 = \mu \epsilon \omega^2 - i \mu \sigma \omega \tag{3.23}$$

Substituting in values for μ, ϵ and σ for earth materials at a frequency of 10^5Hz the ratio $\frac{\mu \epsilon \omega^2}{\mu \sigma \omega} \approx 10^{-5}$ with this value getting smaller for lower frequencies. The term $\mu \epsilon \omega^2$ describes displacement currents while $\mu \sigma \omega$ is due to conduction currents, it is therefore reasonable to assume that in CSEM the displacement current term is negligible and can be dropped. Similarly the source term $-\epsilon \frac{\partial \boldsymbol{K}_s(\boldsymbol{x}, t)}{\partial t} - \sigma \boldsymbol{K}_s(\boldsymbol{x}, t)$ from equation 3.20 has a Fourier transform

$$i \omega \epsilon \tilde{\boldsymbol{K}}_s(\boldsymbol{x}, \omega) - \sigma \tilde{\boldsymbol{K}}_s(\boldsymbol{x}, \omega) \tag{3.24}$$

and for the frequencies of interest the term $i \omega \epsilon \tilde{\boldsymbol{K}}_s(\boldsymbol{x}, \omega)$ can be dropped.

Dropping these terms and substituting the constitutive equations 3.7 and 3.9 into equations 3.1 and 3.2 respectively gives

$$\nabla \times \boldsymbol{H}(\boldsymbol{x},t) = \sigma \boldsymbol{E}(\boldsymbol{x},t) + \boldsymbol{J}_s(\boldsymbol{x},t), \tag{3.25}$$

$$\nabla \times \boldsymbol{E}(\boldsymbol{x},t) = -\mu \frac{\partial \boldsymbol{H}(\boldsymbol{x},t)}{\partial t} - \boldsymbol{K}_s(\boldsymbol{x},t). \tag{3.26}$$

Similarly, dropping displacement terms from equations 3.19 and 3.20 gives

$$\nabla \times \nabla \times \boldsymbol{E}(\boldsymbol{x},t) + \mu \sigma \frac{\partial \boldsymbol{E}(\boldsymbol{x},t)}{\partial t} = -\mu \frac{\partial \boldsymbol{J}_s(\boldsymbol{x},t)}{\partial t} - \nabla \times \boldsymbol{K}_s(\boldsymbol{x},t), \tag{3.27}$$

$$\nabla \times \nabla \times \boldsymbol{H}(\boldsymbol{x},t) + \mu \sigma \frac{\partial \boldsymbol{H}(\boldsymbol{x},t)}{\partial t} = -\sigma \boldsymbol{K}_s(\boldsymbol{x},t) + \nabla \times \boldsymbol{J}_s(\boldsymbol{x},t). \tag{3.28}$$

Using the vector identity,

$$\nabla \times \nabla \times \boldsymbol{A} \equiv \nabla \nabla \cdot \boldsymbol{A} - \nabla^2 \boldsymbol{A} \tag{3.29}$$

equations 3.27 and 3.28 can be writtten

$$\nabla^2 \boldsymbol{E}(\boldsymbol{x},t) - \mu \sigma \frac{\partial \boldsymbol{E}(\boldsymbol{x},t)}{\partial t} \tag{3.30}$$

$$= \mu \frac{\partial \boldsymbol{J}_s(\boldsymbol{x},t)}{\partial t} + \nabla \times \boldsymbol{K}_s(\boldsymbol{x},t) + \nabla \nabla \cdot \boldsymbol{E}(\boldsymbol{x},t),$$

$$\nabla^2 \boldsymbol{H}(\boldsymbol{x},t) - \mu \sigma \frac{\partial \boldsymbol{H}(\boldsymbol{x},t)}{\partial t} \tag{3.31}$$

$$= \sigma \boldsymbol{K}_s(\boldsymbol{x},t) - \nabla \times \boldsymbol{J}_s(\boldsymbol{x},t) + \nabla \nabla \cdot \boldsymbol{H}(\boldsymbol{x},t).$$

Expressions for $\nabla \nabla \cdot \boldsymbol{E}(\boldsymbol{x},t)$ and $\nabla \nabla \cdot \boldsymbol{H}(\boldsymbol{x},t)$ in terms of electric and magnetic source terms can be derived from equations 3.25 and 3.26. Taking the divergence of 3.25 gives

$$\nabla \cdot \nabla \times \boldsymbol{E}(\boldsymbol{x},t) = -\mu \frac{\partial \nabla \cdot \boldsymbol{H}(\boldsymbol{x},t)}{\partial t} - \nabla \cdot \boldsymbol{K}_s(\boldsymbol{x},t). \tag{3.32}$$

51

Using the result that, for all twice differentiable functions $\boldsymbol{E}$, $\nabla \cdot \nabla \times \boldsymbol{E} = 0$ gives

$$\mu \frac{\partial \nabla \cdot \boldsymbol{H}(\boldsymbol{x}, t)}{\partial t} = -\nabla \cdot \boldsymbol{K}_s(\boldsymbol{x}, t), \tag{3.33}$$

$$\nabla \cdot \boldsymbol{H}(\boldsymbol{x}, t) = -\frac{1}{\mu} \int_{\tau=0}^{t} \nabla \cdot \boldsymbol{K}_s(\boldsymbol{x}, \tau) d\tau. \tag{3.34}$$

Taking the divergence of (3.26) gives

$$\nabla \cdot \nabla \times \boldsymbol{H}(\boldsymbol{x}, t) = \sigma \nabla \cdot \boldsymbol{E}(\boldsymbol{x}, t) + \nabla \cdot \boldsymbol{J}_s(\boldsymbol{x}, t). \tag{3.35}$$

Again using the result that, for all twice differentiable functions $\boldsymbol{H}$, $\nabla \cdot \nabla \times \boldsymbol{H} = 0$ gives

$$\sigma \nabla \cdot \boldsymbol{E}(\boldsymbol{x}, t) = -\nabla \cdot \boldsymbol{J}_s(\boldsymbol{x}, t) \tag{3.36}$$

$$\nabla \cdot \boldsymbol{E}(\boldsymbol{x}, t) = -\frac{1}{\sigma} \nabla \cdot \boldsymbol{J}_s(\boldsymbol{x}, t). \tag{3.37}$$

Substituting (3.37) into (3.30) and (3.34) into (3.31) yields

$$\nabla^2 \boldsymbol{E}(\boldsymbol{x}, t) - \mu\sigma \frac{\partial \boldsymbol{E}(\boldsymbol{x}, t)}{\partial t} =$$
$$\mu \frac{\partial \boldsymbol{J}_s(\boldsymbol{x}, t)}{\partial t} + \nabla \times \boldsymbol{K}_s(\boldsymbol{x}, t) - \frac{1}{\sigma} \nabla\nabla \cdot \boldsymbol{J}_s(\boldsymbol{x}, t) \tag{3.38}$$

$$\nabla^2 \boldsymbol{H}(\boldsymbol{x}, t) - \mu\sigma \frac{\partial \boldsymbol{H}(\boldsymbol{x}, t)}{\partial t} =$$
$$\sigma \boldsymbol{K}_s(\boldsymbol{x}, t) - \nabla \times \boldsymbol{J}_s(\boldsymbol{x}, t) - \frac{1}{\mu} \int_{\tau=0}^{t} \nabla\nabla \cdot \boldsymbol{K}_s(\boldsymbol{x}, \tau) d\tau. \tag{3.39}$$

Equations 3.38 and 3.39 can then be written as

$$\boxed{\nabla^2 \boldsymbol{F}(\boldsymbol{x}, t) - \mu\sigma \frac{\partial \boldsymbol{F}(\boldsymbol{x}, t)}{\partial t} = \boldsymbol{S}(\boldsymbol{x}, t)} \tag{3.40}$$

which is the vector diffusion equation in $\boldsymbol{F}$ with source term $\boldsymbol{S}(\boldsymbol{x}, t)$. When $\boldsymbol{F}$ represents the electric filed the source term is given by

$$\boldsymbol{S}(\boldsymbol{x}, t) = \mu \frac{\partial \boldsymbol{J}_s(\boldsymbol{x}, t)}{\partial t} + \nabla \times \boldsymbol{K}_s(\boldsymbol{x}, t) - \frac{1}{\sigma} \nabla \nabla \cdot \boldsymbol{J}_s(\boldsymbol{x}, t) \tag{3.41}$$

and when $\boldsymbol{F}$ represents the magnetic field

$$\boldsymbol{S}(\boldsymbol{x}, t) = \sigma \boldsymbol{K}_s(\boldsymbol{x}, t) - \nabla \times \boldsymbol{J}_s(\boldsymbol{x}, t) - \frac{1}{\mu} \int_{\tau=0}^{t} \nabla \nabla \cdot \boldsymbol{K}_s(\boldsymbol{x}, \tau) d\tau. \tag{3.42}$$

The wave equation for an elastic wavefield $\boldsymbol{U}(\boldsymbol{x}, t)$ subjected to an external source $\boldsymbol{S}(\boldsymbol{x}, t)$ is,

$$\boxed{\nabla^2 \boldsymbol{U}(\boldsymbol{x}, t) - \frac{1}{c^2} \frac{\partial^2 \boldsymbol{U}(\boldsymbol{x}, t)}{\partial t^2} = \boldsymbol{S}(\boldsymbol{x}, t)} \tag{3.43}$$

The wave equation is derived in full in Appendix A.

Inductive and Galvanic responses

In any EM survey it is important to develop a strong current around the exploration target. When a body of anomalous resistivity embedded in a host medium is excited by an EM field, two modes of excitation can occur, known as inductive (or eddy or vortex) currents and galvanic (channelling or gathering) currents. A horizontal electric dipole source excites both galvanic and inductively coupled modes (Walker & West, 1992). The response of a given target depends on the interplay between galvanic and inductive effects, which tend to work in opposition. The relative strength of inductive and galvanic currents is also geometry-dependent. The current flow associated with each of these two modes is illustrated in Figure 3.1.

The inductive response results from the direct interaction of the target with the incident field. It is characterized by electric currents circulating in closed loops within the target. For a buried resistive layer if the current at the base of the overburden is mainly horizontal inductive effects dominate. In this case the electric field is transverse to the target.

The galvanic response appears when the normal component of the electric field hits the boundaries of a target. At the boundary electric charges appear so as to fulfil the continuity of the current at the discontinuity of σ (Nabighian & Macnae, 1991). This distribution of charges creates a secondary electric field that, in turn, causes the external currents to be channelled into the target when it is conductive and or diverted away from it when it is resistive. The strength of the channelling effect increases with increasing conductivity contrast and with increasing target length along the incident current direction. The galvanic response is characterized by currents flowing along open paths between two extremities of a body (Bourgeois et al., 2000). In the presence of a buried resistive layer if significant vertical components of electric current flow are generated the galvanic response is strongly affected by a thin resistive layer. The magnetic field is now polarized transverse to the target.

Any electromagnetic field, in a homogeneous, source-free region may be decomposed into a part for which the electric field is transverse to a resistivity interface (TE mode) and a part for which the magnetic field is transverse to the same resistivity interface (TM mode). The TE mode describes inductive current flow and the TM mode describes galvanic current flow. Maxwell's equations can be solved for a layered earth using scalar potentials in terms of the TE and TM modes (Strack, 1992). If we consider the case of a buried hydrocarbon layer, in the TM mode the electric field enters the hydrocarbon layer under a critical angle and propogates along the layer. In the TE mode the electric field will only be reflected from the layer.
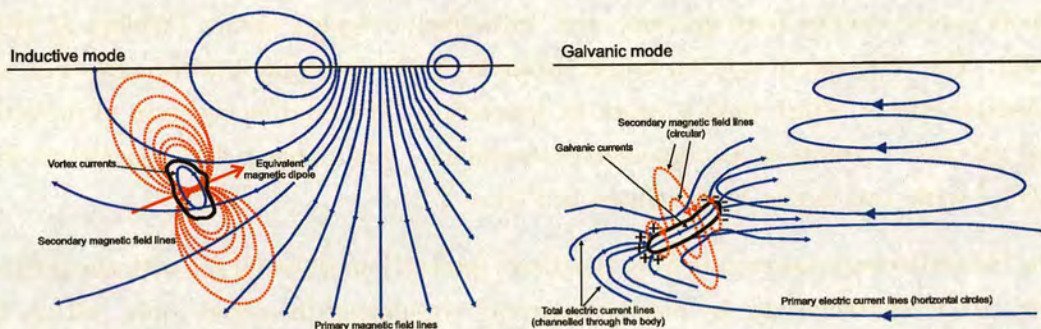
Figure 3.1: The two modes of current excitation that take place within a body of anomalous resistivity. Left: The inductive mode. Right: The galvanic mode (After Bourgeois et al. (2000)).

3.3 Similarities Between Elastic and Diffusive Wave Propagation

In the last 20 years much work has been done in exploiting the mathematical similarities between the diffusion equation and the wave equation. The main reason why seismic methods have long been preferred to EM is because of the ease of interpreting seismic reflections. Electromagnetic sounding data are notoriously difficult to interpret and the identification of individual reflections is not possible. Ground penetrating radar has generally been seen as the EM equivalent of seismic reflection because at the frequencies involved displacement currents are important and it obeys a wave-like equation rather than a diffusion equation. Another method in which EM and seismic methods are closely related is the electroseismic method (Martner & Sparks, 1959) which uses a seismic source but records the resultant EM fields due to a piezoelectric effect. This section concentrates on work done in low frequency EM in finding and using similarities with wave propagation to enable EM data to be interpreted more easily.

The earliest studies to demonstrate a link between the diffusion and wave equations were carried out by Kunetz (1972), Weidelt (1972) and Levy *et al.* (1988) but were limited to MT problems in a layered earth. The first attempt at a mathematical transform between fields satisfying the diffusion and wave equations was proposed by Lavrent'ev *et al.* (1980) using equations for scalar fields. This result was tested by Filatov (1984) using CSEM data with only limited success. The transform known as the q transform was then generalized by Lee *et al.* (1989) to include vector EM fields and arbitrary sources. In general, any component of the EM field that satisfies a diffusion equation in the t domain can be uniquely transformed to a wavefield that satisfies the corresponding wave equation in a fictitious pseudo-time q domain. This transform was initially used as a way of modelling EM data by transforming data created using standard seismic modelling software which obey the wave equation into diffusive data. This approach is very desirable as effective models can be generated using simple seismic ray-tracing algorithms whereas the EM response for the same model requires a complete solution to a formal boundary value problem which is a very time-consuming process. Results obtained using this process were found to agree well with the solution obtained using the direct time-domain finite difference solution of Oristaglio & Hohmann (1984).

Perhaps more interesting, however, is the calculation of the inverse q transform which relates a diffusive EM response to one in an equivalent wavefield known as the q domain (Lee *et al.*, 1989) which obeys the wave equation. This has the potential to produce electromagnetic reflectivity images similar to non-migrated seismic sections. The velocity of the inverse transformed wavefield is $c = \sqrt{\frac{\rho}{\mu}}$ which is proportional to the square

55

root of electrical resistivity ρ. This opens up the possibility of extracting resistivity information directly from the data. It may eliminate the need for model fitting or inversion to fit a few parameters to large volumes of data. The first implementation of inversion of the q transform to map conductivity directly was carried out by Lee & Xie (1993). They successfully imaged a dipping conductor between two boreholes using synthetic EM data; their result is shown in Figure 3.2. However, their result uses an impulse source and acknowledges that this is not achievable in practice. The effect of a realistic source in calculating the equivalent wavefield is studied in section 3.5. The inverse transform was also used to image a massive graphite conductor using real EM data (Gershenson, 1997). de Hoop (1996) derived a correspondence principle, which related 2-D transient diffusive electromagnetic fields with electric field in the vertical plane and 2-D seismic waves with particle velocity in the vertical plane. The process of transforming a diffusive EM field into an equivalent wavefield which obeys the wave equation by inverting the q transform was termed diffusive-to-propagative mapping (DPM) by Tournerie & Gibert (1995) who inverted the q transform for MT data in the frequency domain. The analytic solution for an electric field line source in the q domain was derived by Wilson (1997). This result is discussed in detail in section 3.5. Most recently an experimental validation of inverting the q transform was carried out successfully in a laboratory scale-model experiment by Das *et al.* (2002).
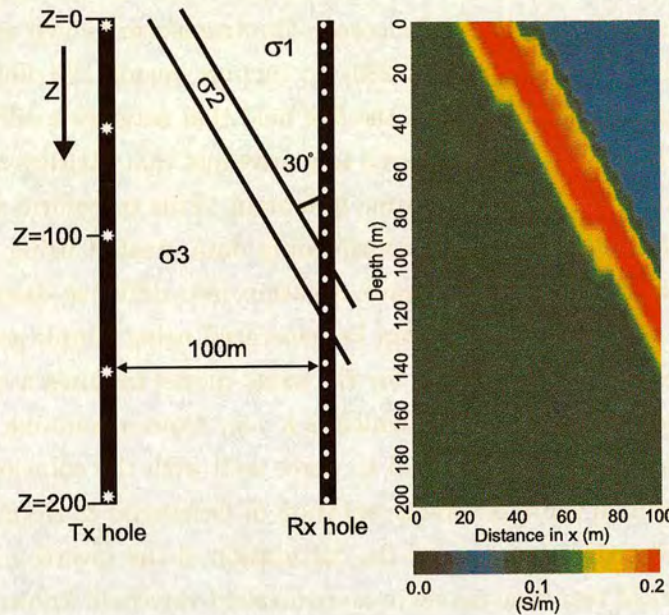
Figure 3.2: The first demonstration of the successful application of q transform inversion in order to extract conductivity values, $\sigma_1 = 0.05$ S/m, $\sigma_2 = 0.2$ S/m and $\sigma_3 = 0.1$ S/m (After Lee, 1993).

3.4   The equivalent wavefield concept and the q transform

Propagation of a diffusive EM wavefield $\boldsymbol{F}(\boldsymbol{x}, t)$ is governed by the diffusion equation while propagation of a non-diffusive elastic wavefield $\boldsymbol{U}(\boldsymbol{x}, t)$ is governed by the wave equation. The source-free versions of these equations are given in (3.44) and (3.45).

$$\nabla^2 \boldsymbol{F}(\boldsymbol{x}, t) = \mu\sigma\frac{\partial \boldsymbol{F}(\boldsymbol{x}, t)}{\partial t} \tag{3.44}$$

$$\nabla^2 \boldsymbol{U}(\boldsymbol{x}, t) = \frac{1}{c^2}\frac{\partial^2 \boldsymbol{U}(\boldsymbol{x}, t)}{\partial t^2} \tag{3.45}$$

The equivalent wavefield concept relates diffusive EM propagation to non-diffusive propagation provided equivalent source and boundary conditions are satisfied (Wilson, 1997). The concept is a special case of a more general theorem relating the solutions of two partial differential equations that have the same spatial, but different temporal derivatives (Bragg & Dettman, 1969). The q transform (3.46) (Lee *et al.*, 1989) provides a means of calculating a diffusive response $\boldsymbol{F}(\boldsymbol{x}, t)$ from its equivalent wavefield $\boldsymbol{U}(\boldsymbol{x}, q)$ where q is a time-like variable with dimensions of square-root of time ($\sqrt{s}$). It should be remembered that the equivalent wavefield is a concept and not a physically occurring phenomenon. The q transform is as follows:

$$\boldsymbol{F}(\boldsymbol{x}, t) = \frac{1}{2\sqrt{\pi t^3}} \int_0^\infty q\, exp(-\frac{q^2}{4t})\boldsymbol{U}(\boldsymbol{x}, q)dq \tag{3.46}$$

Derivation of the q transform

The q transform is derived here starting from the wave and diffusion equations and follows the approach of Lee *et al.* (1989) and Wilson (1997).

Set up the initial value problem as follows

$$
\begin{aligned}
\nabla^2 \boldsymbol{F}(\boldsymbol{x}, t) - \mu\sigma\frac{\partial \boldsymbol{F}(\boldsymbol{x}, t)}{\partial t} &= \boldsymbol{S}(\boldsymbol{x}, t), & \boldsymbol{x} \in \mathcal{V},\ t > 0 \\
\boldsymbol{F}(\boldsymbol{x}, 0) &= \boldsymbol{\alpha}(\boldsymbol{x}), & \boldsymbol{x} \in \mathcal{V} \\
\boldsymbol{F}(\boldsymbol{x}, t) &= \boldsymbol{f}(\boldsymbol{x}, t), & \boldsymbol{x} \in \partial\mathcal{V},\ t > 0
\end{aligned}
\tag{3.47}
$$

and

$$
\begin{aligned}
\nabla^2 U(x, q) - \frac{1}{c^2} \frac{\partial^2 U(x, q)}{\partial q^2} &= T(x, q), & x \in \mathcal{V},\ q > 0 \\
U(x, 0) &= 0 & x \in \mathcal{V} \\
\frac{\partial U(x, 0)}{\partial q} &= \alpha(x), & x \in \mathcal{V} \\
U(x, q) &= u(x, q), & x \in \partial\mathcal{V},\ q > 0
\end{aligned}
\tag{3.48}
$$

In the above equations $F(x, t)$ is a diffusive field with source term $S(x, t)$ and $U(x, q)$ is a wavefield with source term $T(x, q)$. The equations hold in a homogeneous, isotropic region $\mathcal{V}$ with boundary $\partial\mathcal{V}$. Taking the Laplace transform of (3.47) and (3.48) with respect to t and q with transform parameters s and p respectively we obtain

$$
\nabla^2 \hat{F}(x, s) - s\mu\sigma \hat{F}(x, s) = \hat{S}(x, s) - \alpha(x), \quad x \in \mathcal{V}
$$

$$
\hat{F}(x, s) = \hat{f}(x, s), \qquad x \in \partial\mathcal{V}
\tag{3.49}
$$

$$
\nabla^2 \hat{U}(x, p) - \frac{p^2}{c^2} \hat{U}(x, p) = \hat{T}(x, p) - \alpha(x), \quad x \in \mathcal{V}
$$

$$
\hat{U}(x, p) = \hat{u}(x, p), \qquad x \in \partial\mathcal{V}
\tag{3.50}
$$

We now require that $c^{-2} = \sigma\mu$, where c is the velocity term in equation (3.45), and make the substitution $p = \sqrt{s}$ in (3.49) and the definition

$$
\hat{R}(x, s) \equiv \hat{F}(x, s) - \hat{U}(x, \sqrt{s})
\tag{3.51}
$$

then by subtracting (3.49) from (3.50) we see that $\hat{R}(x, s)$ obeys

$$\nabla^2 \hat{\boldsymbol{R}}(\boldsymbol{x}, s) - \frac{s}{c^2} \hat{\boldsymbol{R}}(\boldsymbol{x}, s) = \hat{\boldsymbol{S}}(\boldsymbol{x}, s) - \hat{\boldsymbol{T}}(\boldsymbol{x}, \sqrt{s}), \quad \boldsymbol{x} \in \mathcal{V}$$

$$\hat{\boldsymbol{R}}(\boldsymbol{x}, s) = \hat{\boldsymbol{f}}(\boldsymbol{x}, s) - \hat{\boldsymbol{u}}(\boldsymbol{x}, \sqrt{s}), \quad \boldsymbol{x} \in \partial\mathcal{V}$$

(3.52)

Let us require that the boundary, and source terms in (3.52) match, i.e.

$$\hat{\boldsymbol{f}}(\boldsymbol{x}, s) - \hat{\boldsymbol{u}}(\boldsymbol{x}, \sqrt{s}) = 0 \qquad (3.53)$$

and

$$\hat{\boldsymbol{S}}(\boldsymbol{x}, s) - \hat{\boldsymbol{T}}(\boldsymbol{x}, \sqrt{s}) = 0 \qquad (3.54)$$

so that all the terms on the right hand side of (3.52) are identically zero. Then we may cite a uniqueness theorem and declare that $\hat{\boldsymbol{R}}(\boldsymbol{x}, s) \equiv 0$ must be the only solution and in this case

$$\hat{\boldsymbol{F}}(\boldsymbol{x}, s) = \hat{\boldsymbol{U}}(\boldsymbol{x}, \sqrt{s}). \qquad (3.55)$$

From the definition of the Laplace transform this can then be written

$$\hat{\boldsymbol{F}}(\boldsymbol{x}, s) = \int_0^\infty \boldsymbol{U}(\boldsymbol{x}, q) exp(-\sqrt{s}q) dq. \qquad (3.56)$$

Using the result that for real $q > 0$

$$\mathcal{L}\left[\frac{q}{2\sqrt{\pi t^3}} exp(-\frac{q^2}{4t})\right] = exp(-\sqrt{s}q) \qquad (3.57)$$

(Erdélyi 1954, equation1, page 245) we take the inverse Laplace transform of equation (3.56) and obtain the q transform

$$F(x,t) = \frac{1}{2\sqrt{\pi t^3}} \int_0^\infty q\,exp(-\frac{q^2}{4t})U(x,q)dq \qquad (3.58)$$

Evaluating the q transform

It is possible to evaluate the q transform without actually having to calculate the integral in (3.46). Consider again the source-free diffusion equation (3.44) and the wave equation (3.45). In the Laplace transform domain these equations are, respectively,

$$(\nabla^2 - s\mu\sigma)\hat{F}(x,s) = 0, \qquad (3.59)$$

$$(\nabla^2 - \frac{p^2}{c^2})\hat{U}(x,p) = 0, \qquad (3.60)$$

where s and p are the Laplace transform parameters for the diffusive and wave domains respectively.

To convert the diffusion equation into the wave equation we simply write $s = p^2$, $\hat{F}(x,s) = \hat{U}(x,p)$ and $\mu\sigma = c^{-2}$. This gives the q transform in the Laplace transform domain:

$$\hat{F}(x,p^2) = \hat{U}(x,p) \qquad (3.61)$$

The time-domain form of the q transform (3.46) is recovered by taking the inverse Laplace transform of (3.61). The procedure for evaluating the diffusive response $F(t)$ of an equivalent wavefield $U(q)$ via the q transform and the equivalent wavefield of a diffusive response via the inverse q transform is summarised below,

Given an equivalent wavefield $U(q)$	Given a diffusive wavefield $F(t)$
1. Calculate its Laplace transform $\hat{U}(p)$	1. Calculate its Laplace transform $\hat{F}(s)$
2. Set $\hat{F}(s) = \hat{U}(\sqrt{s})$	2. Set $\hat{U}(p) = \hat{F}(p^2)$
3. Inverse Laplace transform yields $F(t)$	3. Inverse Laplace transform yields $U(q)$

Analytic calculation of the equivalent wavefield for a switch-off electric field current dipole

One particular example of a diffusive wavefield is that generated by a switch-off electric current dipole on the surface of the earth. This step function form of the source function is the most common type employed in TDEM. Starting with the analytic solution for such a source wavefield the equivalent wavefield is derived analytically with a view to recovering the same form for the equivalent wavefield numerically.

The electric field response of an electric dipole source parallel to the x-axis recorded by a receiver electrode also aligned parallel to the x axis is termed $\boldsymbol{E}_{xx}$, this is known as the in-line component of the electric field. If the receiver electrode is aligned perpendicular to the source the measured response is termed $\boldsymbol{E}_{xy}$, this is known as the cross-line component of the electric field. The layout of these components is illustrated in Figure 3.3.
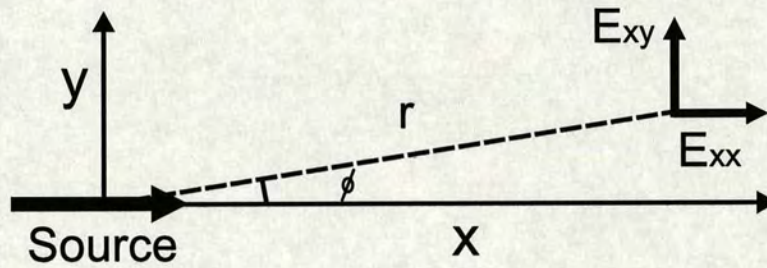
Figure 3.3: The layout of the in-line and cross-line components in relation to an electric dipole source.

Mathematically the analytic form of such a transmitter waveform is defined by Weir (1980) to be

$$\boldsymbol{E}_{xx}(r, t > 0) \quad = \quad \frac{\mathcal{D}}{2\pi\sigma r^3}(erf(\frac{r}{c2\sqrt{t}}) - \frac{2}{\sqrt{\pi}}\frac{r}{c2\sqrt{t}}\exp(-\frac{r^2}{c^2 4t})) \tag{3.62}$$

$$= \quad \frac{\mathcal{D}}{2\pi\sigma r^3}(F1(t) - F2(t)), \tag{3.63}$$

$$\boldsymbol{E}_{xx}(r, t < 0) \quad = \quad -\frac{\mathcal{D}}{2\pi\sigma r^3}(1 - 3\cos^2\phi), \tag{3.64}$$

$$\boldsymbol{E}_{xy}(t > 0) \quad = \quad 0, \tag{3.65}$$

where

$$F1(t) \quad = \quad erf(\frac{r}{c2\sqrt{t}}), \tag{3.66}$$

$$F2(t) \quad = \quad \frac{2}{\sqrt{\pi}}\frac{r}{c2\sqrt{t}}\exp(-\frac{r^2}{c^2 4t}), \tag{3.67}$$

$$\mathcal{D} \quad \text{is the moment of the dipole,}$$

$$c^2 \quad = \quad (\mu\sigma)^{-1}, \tag{3.68}$$

and

$$erf \quad \text{is the error function.}$$

Following the procedure for inverting the q transform via the Laplace transform domain given on page 61 the first step in obtaining the equivalent wavefield is to take the Laplace transform of (3.62). This is done individually for the two functions $F1(t)$ and $F2(t)$ defined by comparing equations (3.62) and (3.63). Starting with $F1(t)$ the Laplace transform of (3.66) is given in (3.69) and making the substitution $s = p^2$ yields (3.70). Calculation of the inverse Laplace transform is laid out in equations (3.71-3.76).

$$\hat{F}(s) \quad = \quad \frac{1}{s}(1 - \exp(-\frac{r}{c}\sqrt{s})) \tag{3.69}$$

(Erdélyi, 1954, Equation (6), page 176)

$$\hat{U}(p) = \hat{F}(p^2) \quad = \quad \frac{1}{p^2}(1 - \exp(-\frac{r}{c}p)) \tag{3.70}$$

From (Erdélyi, 1954, Equation (2), page 241) for $a > 0$.

$$\mathcal{L}_{p \to q}^{-1} \left[\frac{1}{p}(1 - \exp(-ap)) \right] = \begin{cases} 1 & 0 < q < a \\ 0 & q > a \end{cases} \tag{3.71}$$

$$= \mathcal{H}(a - q). \tag{3.72}$$

From (Erdélyi, 1954, Equation (10), page 130)

$$\mathcal{L}_{p \to q}^{-1}[\frac{1}{p}\hat{u}(p)] = \int_0^q u(v)dv. \tag{3.73}$$

Hence

$$U1(q) = \mathcal{L}_{p \to q}^{-1} \left[\frac{1}{p^2}(1 - \exp(-\frac{r}{c}p)) \right] = \int_0^q \mathcal{H}(\frac{r}{c} - v)dv \tag{3.74}$$

$$= \begin{cases} q & 0 < q < r/c \\ r/c & q \geq r/c \end{cases} \tag{3.75}$$

$$= q\mathcal{H}(\frac{r}{c} - q) + \frac{r}{c}\mathcal{H}(q - \frac{r}{c}), \tag{3.76}$$

where it is understood throughout the above that $q > 0$.

Taking the second term $F2(t)$, (3.77), its Laplace transform is given by (3.78). Making the substitution $s = p^2$ yields (3.79) and the equivalent wavefield is recovered by taking the inverse Laplace transform (3.80-3.82).

$$F(t) = F2(t) = \frac{2}{\sqrt{\pi}} \frac{r}{c2\sqrt{t}} \exp(-\frac{r^2}{c^24t}) \tag{3.77}$$

$$\hat{F}(s) = \frac{r}{c\sqrt{s}} \exp(-\frac{r}{c}\sqrt{s}) \tag{3.78}$$

(Erdélyi, 1954, Equation (27), page 146)

$$\hat{U}(p) = \hat{F}(p^2) = \frac{r}{cp} \exp(-\frac{r}{c}p) \tag{3.79}$$

$$U2(q) = \mathcal{L}_{p \to q}^{-1}[\hat{U}(p)] \tag{3.80}$$

$$= \mathcal{L}_{p \to q}^{-1}[\frac{r}{cp} \exp(-\frac{r}{c}p)] \tag{3.81}$$

$$= \frac{r}{c}\mathcal{H}(q - r/c) \tag{3.82}$$

(Erdélyi, 1954, Equation (1), page 241)

63

Combining these two results $U1(q)$ and $U2(q)$) yields

$$
\begin{aligned}
\boldsymbol{U}_{xx}(r,q) &= \frac{\mathcal{D}}{2\pi\sigma r^3}(U1(q) - U2(q)) & (3.83) \\
&= \frac{\mathcal{D}}{2\pi\sigma r^3}\left(q\mathcal{H}(\frac{r}{c} - q) + \frac{r}{c}\mathcal{H}(q - r/c) - \frac{r}{c}\mathcal{H}(q - r/c)\right) & (3.84) \\
&= \frac{\mathcal{D}}{2\pi\sigma r^3}q\mathcal{H}(\frac{r}{c} - q) & (3.85)
\end{aligned}
$$

for $q > 0$.

Equation (3.85) is the equivalent wavefield of the diffusive response generated by an in-line switch-off electric current dipole. It can be seen that this equation has its maximum value when $q = \frac{r}{c}$. When the function is plotted as a function of the time-like variable q and offset r it can be seen that the location of the maxima lie on a straight line.

Figure 3.4 shows the diffusive switch-off response (3.62) as a function of time t and c (related to resistivity) (left) and the corresponding equivalent wavefield (3.85) as a function of the time-like variable q and c (right) for a source-receiver offset of 1000m.
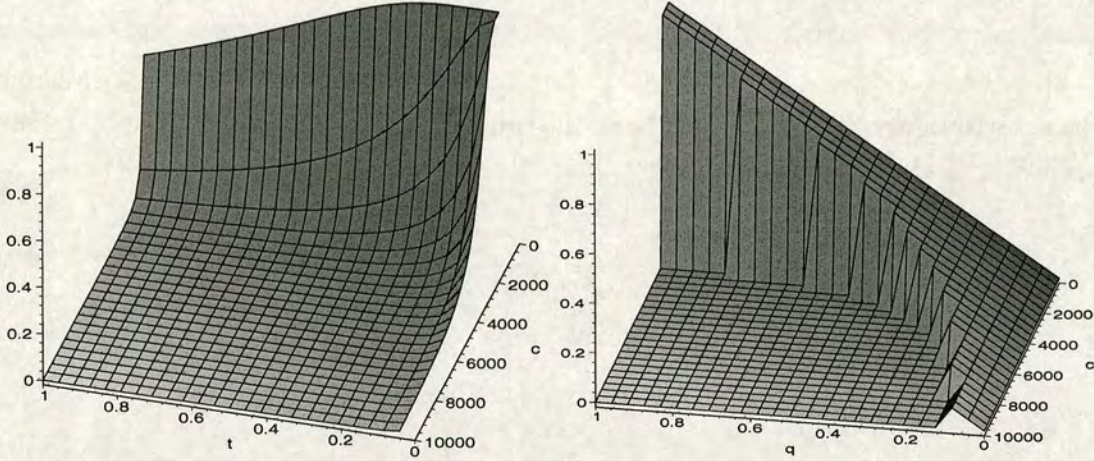
Figure 3.4: Recovering the equivalent wavefield. Left: The analytic switch off transient response as a function of time and c (resistivity) at 1000m. Right: The equivalent wavefield of (a) as a function of the time-like variable q and c (resistivity).

3.5 Diffusive to propagative mapping by deconvolution in log-time

Unfortunately the numerical calculation of an inverse Laplace transform is a fundamentally ill-posed problem (Oliver, 1994). It can clearly be seen from the two plots in Figure 3.4 that transforming from the smooth diffusive function on the left to the equivalent wavefield function on the right which is sharp with an abrupt vertical slope at $q = \frac{r}{c}$ will be difficult to achieve numerically. In order for DPM to be used successfully it is therefore required that a way be found of reformulating the transformation to the equivalent wavefield that does not require working in the Laplace transform domain. It was noted by Lee (1988) and Gershenson (1993) that by moving to logarithmic sampling in both time and the time-like variable q the q transform could be re-formulated as a convolution. This section describes the work of Wilson (1997) in reformulating the inverse q transform as a deconvolution in logarithmic time for in-line electric field transient electromagnetics.

To re-formulate the q transform as a convolution first rearrange the q transform (3.46) as follows

$$2\sqrt{\pi t}\boldsymbol{F}(\boldsymbol{x}, t) = \frac{1}{t} \int_0^{+\infty} q exp(-\frac{q^2}{4t})\boldsymbol{U}(\boldsymbol{x}, q) \, dq. \tag{3.86}$$

By applying the substitutions $q = exp(u)$ and $t = \frac{1}{4}exp(2v)$ the q transform is converted to the logarithmic time domain v:

$$\sqrt{\pi} \exp(v)\boldsymbol{F}(\boldsymbol{x}, \frac{1}{4}\exp(2v))$$
$$= \int_{-\infty}^{+\infty} 4\exp(2(u-v))\exp(-\exp(2(u-v)))\boldsymbol{U}(\boldsymbol{x}, \exp(u)) \, du, \tag{3.87}$$
or
$$\boldsymbol{G}(v) = \int_{-\infty}^{+\infty} W(v-u)\boldsymbol{R}(u)du \tag{3.88}$$
$$= W(v) * \boldsymbol{R}(v), \tag{3.89}$$

65

where $*$ represents the convolution operation, and

$$G(\boldsymbol{x}, v) = \sqrt{\pi} \exp(v) \boldsymbol{F}(\boldsymbol{x}, \frac{1}{4}\exp(2v)) \tag{3.90}$$

$$\boldsymbol{R}(\boldsymbol{x}, v) = \boldsymbol{U}(\boldsymbol{x}, \exp(v)) \tag{3.91}$$

$$W(v) = 4\exp(-2v)\exp(-\exp(-2v)). \tag{3.92}$$

The time and time-like variables t, v and q are related as follows, $t = \frac{1}{4}exp(2v)$, $v = \frac{1}{2}ln(4t)$, $q = exp(v)$ and $q = 2\sqrt{t}$.

Equation (3.89) is a convolution equation, so the the q transform has been re-formulated as a convolution. Inversion of the q transform can now be carried out by deconvolving for $\boldsymbol{R}(v)$ and then converting from logarithmic sampling v to the q domain. Given a diffusive wavefield $\boldsymbol{F}(\boldsymbol{x}, t)$ the procedure for calculating its equivalent wavefield $\boldsymbol{U}(\boldsymbol{x}, q)$ is outlined in Figure 3.5.
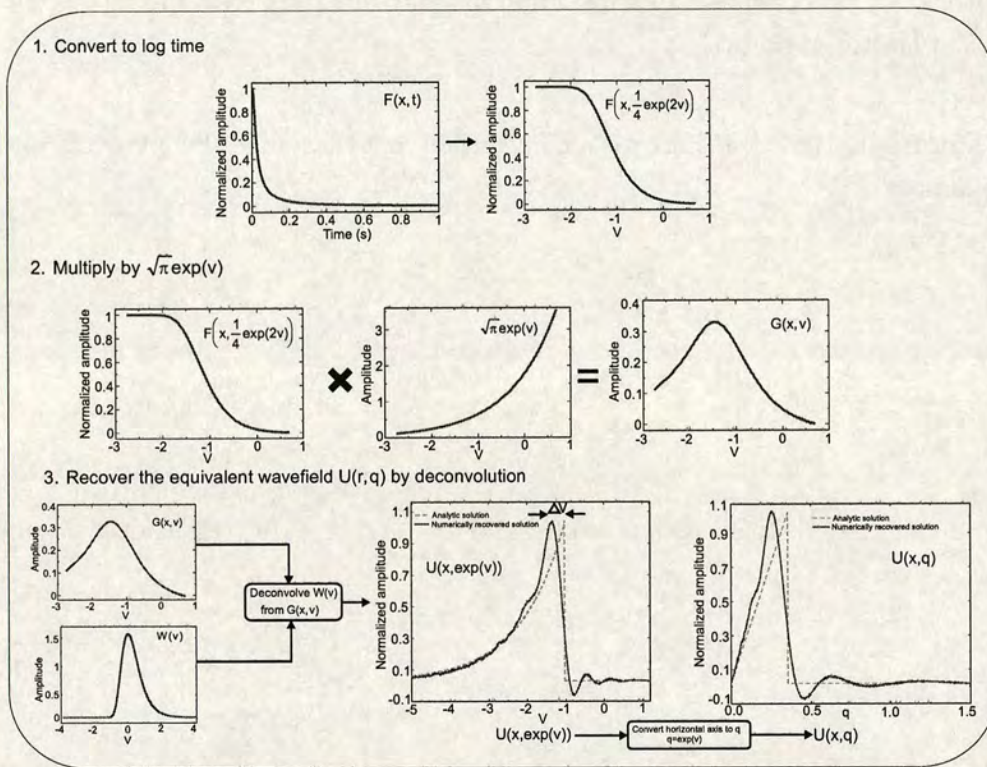
Figure 3.5: The procedure for numerically calculating the equivalent wavefield of the in-line switch off electric field response by deconvolution in log-time.

This procedure was applied by Wilson (1997) to various halfspace and 1-D earth models in an attempt to produce the same result as was produced analytically in equation

66

(3.85). However, the result obtained for the resistivity was always incorrect by the same factor regardless of whether a halfspace or 1-D layered earth model was considered. The difference between the analytic and the numerically recovered waveform is shown in Figure 3.5. In order to facilitate a meaningful interpretation from this result Wilson *et al.* (1998) suggested applying a calibration correction to give the right result for the resistivity. The problems associated with such a correction when the input resistivity values are not known, however, are quite considerable. This is discussed in more detail in chapter 7. The fact that the resistivity values obtained for a multi-layered earth are wrong by the same factor as the results for a halfspace is a very important result as this means that in spite of the fact that the exact value of the resistivity is not known the relative difference in resistivity between two layers can be determined. Also if a way can be found of determining the correct resistivity for the first layer it should also give the correct answer for deeper layers.

Chapter 4

MTEM Data Acquisition and Pre-processing

4.1 Introduction

The data presented in this thesis were collected during a six year project to try and determine the effectiveness of TEM in detecting and monitoring hydrocarbons. This chapter gives a review of the project and discusses the data acquisition procedure for the data that were collected. A data processing scheme specific to the data collected is proposed that makes allowances for limitations in the data. As a result of careful analysis of the data, a new idealised processing scheme is proposed, to be applied to new data that meet certain criteria, enabling the earth response function to be recovered. The new method is the subject of a patent application (Appendix D).

4.2 Project History

The data presented in this thesis were collected during a project that was a collaboration between the University of Edinburgh, The University of Cologne, Deutsch Montan Technologie (DMT) and Compagnie Générale de Géophysique (CGG). The project began in 1992 after being awarded a European Commission THERMIE contract entitled 'Delineation and Monitoring of Oil Reservoirs using Seismic and Electromagnetic Methods' (Contract number OG/0305/92/NL-UK) and funding of 1,000,000 Ffr from Elf (now TotalFinaElf). The primary goal of the project was to develop a method to detect hydrocarbons directly using multichannel transient electromagnetic (MTEM)

soundings: a secondary goal was to develop a method to monitor the movement of hydrocarbons in a known reservoir.

Finding a Site

Finding a site suitable for achieving the first goal is in theory simple: find an onshore oil or gas field with a clean oil-water contact that is relatively shallow and has a good resistivity contrast between the reservoir and the overlying strata. A major problem, however, is that every onshore oil and gas field is serviced by a large network of steel pipes which are used for monitoring and production. When such pipes are in close proximity to an electromagnetic survey they will generate an induced EM field in response to the source field which will be measured by the receivers. As discussed in section 2.5 there is no way of eliminating or removing the spurious field caused by such pipes. The effect of such pipes can be identified by the presence of strong spatial variations in the recorded data. Conclusively demonstrating the first goal in the presence of such effects then becomes almost impossible as often the pipe network is present over the same region as the reservoir that is the target of the study. Proving that the response seen over the survey area is a result of hydrocarbons at depth and not from near-surface conductors such as pipes then becomes impossible.

A total of 11 sites in 6 countries were considered for the project with numerical modelling of the predicted reservoir response carried out for 7 of them (Ziolkowski *et al.*, 1998a). In most cases the modelling indicated that the response would be too insensitive to changes in reservoir parameters, or, where there was a good sharp response, the pipe network prevented detection of the response. Another problem that relates to the secondary goal of the project is that in order to detect movement of hydrocarbons within the reservoir there must be no change in the infrastructure of the site between the two surveys. For example, any changes in the pipe network between the two surveys would cast serious doubt over the validity of any conclusions drawn. If the only change between the two surveys is the position of the hydrocarbon/water contact, then the effect of the pipes will cancel when the data are differenced. A summary of all the sites considered is given in table 4.1.

Fully two years after the project started a suitable site which satisfied all the criteria mentioned above was found and chosen for the project.

Reservoir name & location	Reservoir type	Depth & thickness (m)	Resistivity contrast (Ωm)	Reason for rejecting site
Fontaine au Bron, Paris Basin France	Oil field	1800 na	na	Reservoir too deep and predicted response too small
Ceré la Ronde, Paris France	Gas storage	1000 & 15	20:300	Alterations to the pipe network between the two surveys
Bierwang, Bavaria Germany	Gas storage	1600 & 40	4:50	Expected reservoir response too small. Also volume changes do not cause detectable changes at bottom conditions as it is a closed type reservoir
Wytch Farm, Dorset England	Oil field	900 & 55	1:10	Pipeline effects were too strong for direct detection. Also environmental restrictions prevented acquisition of a meaningful dataset
Schoonebeek, Netherlands	Oil field	880 &40	1:2000	Very dense network of over 560 wells over the reservoir
Bergen, Rügen Island Germany	Oil field	2300 & 70m	1:10	Reservoir is too deep. There were also severe environmental restrictions
Stenlille, Copenhagen Denmark	Gas storage	1700 &35	2:5	Resistivity contrast too small
Coulommes--Vaucourtois, France	Oil field	1850 & na	na	Reservoir too deep
Golzow, Berlin Germany	Gas storage	na & na	na	Reservoir was still in the development stage at the time of the surveys
St. Illiers la Ville, Paris Basin France	Gas storage	500 & 25	20:400	This site was selected for the project as it met all the required criteria

Table 4.1: The reservoirs considered when choosing a site for the project.

71

The St. Illiers la Ville Reservoir

The site eventually selected for the project is an underground gas storage reservoir located 30km West of Paris near the town of Saint Illiers la Ville in the Paris basin. It is a sandstone anticline 25m thick with 30% porosity at a depth of about 500m. Its areal extent is approximately 2000×3000m. The gas bearing reservoir has a resistivity of approximately 400 Ωm while the resistivity of the overlying rock is around 20 Ωm. This provides a readily detectable target at a shallow depth which is ideal for the project. The network of pipes across the reservoir is also relatively small and concentrated mostly in a small section to the west of the profile. Figure 4.1 shows the location of the MTEM profile relative to the reservoir edge and the monitoring wells which are denoted by white circles. The blue contour lines show the depth in metres to the top of the anticline which within the reservoir edge contains the gas. It can be seen that at some points over the profile the reservoir is as little as 380m below the surface. The fact that the pipes are not near the survey profile means this site is suitable for trying to achieve the first goal. A schematic cross section of the reservoir along with a resistivity well log from the reservoir are shown in Figure 4.2.

The reservoir structure was discovered in the 1970's following the shooting of two seismic lines by Shell. On the basis of these data Shell decided to drill a well into the top of the anticline. The well was dry (i.e. the reservoir was full of brine) and the site was subsequently acquired by Gaz de France, who have used it as a gas storage facility since about 1975. France has very little natural gas reserves of its own and therefore has to import gas and store it in underground reservoirs such as this in order to supply the extra demand for gas during the winter. Gas is pumped into the reservoir at a constant rate throughout the year. In summer the supply of gas to the reservoir exceeds demand and the amount of gas in the reservoir increases. The reservoir is fullest in October when the gas-water contact is at its lowest point. In winter, as the demand for gas increases the amount of gas in the reservoir decreases, the gas-water contact moves up as a result, reaching its highest level in April when the reservoir is emptiest. As resistive gas is replaced by more conductive salt water, the resistivity of several million cubic metres of reservoir rock changes. In addition to the movement of the gas-water contact the pressure within the reservoir also changes, with pressure increasing as gas the amount of gas in the reservoir increases. The pressure in the reservoir dropped by 10% between the two surveys.

The location of gas within the reservoir is known precisely from constant monitoring at over 40 wells. These facts make the site suitable for trying to achieve the second goal.
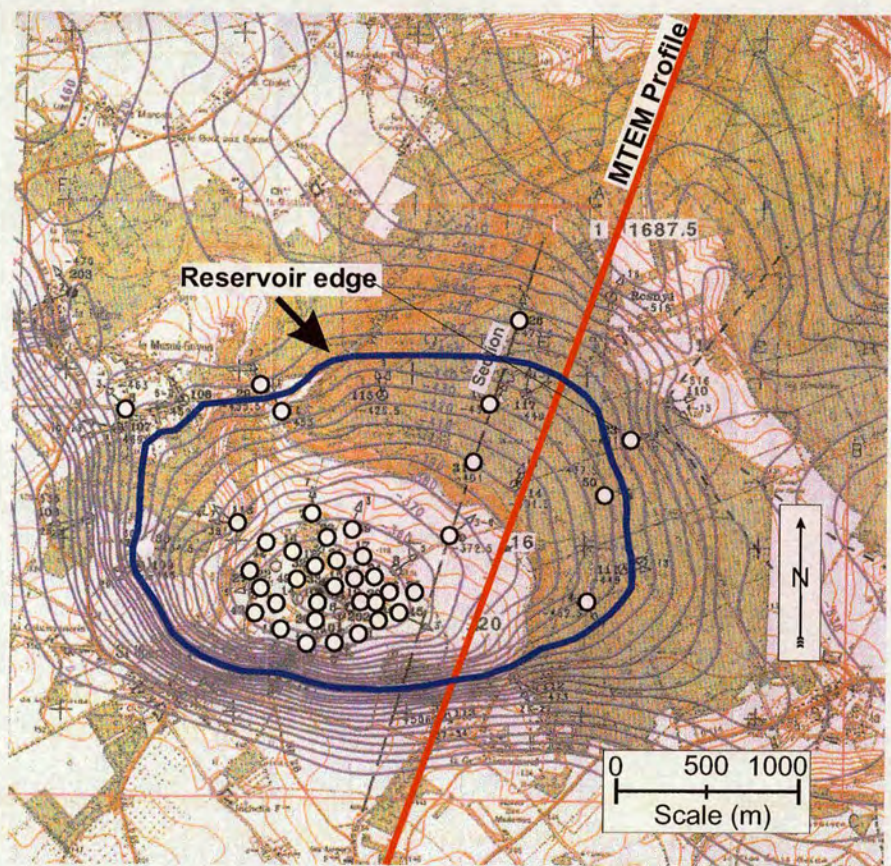
Figure 4.1: The location of the MTEM profile relative to the edge of the reservoir and monitoring wells (denoted by white circles). The contours denote the depth to the top of the anticline in metres. The contour interval is 10m and the dark blue line showing the reservoir edge represents a depth of 450m.

The Surveys

Two MTEM surveys were carried out over the St. Illiers la Ville reservoir in 1994 and 1996. The first survey took place over ten days in October 1994 when the level of gas in the reservoir was close to maximum. The second survey was planned for April 1996 when the level of gas in the reservoir was at a minimum. Due to operational difficulties at the site, the second survey did not start until August 1996.

Modelling of the reservoir by Hördt *et al.* (1995) prior to the second survey indicated that the change in the EM response between maximum and minimum gas levels would be about 5% and would be accompanied by a lateral movement of the gas-water contact of about 100m. As a result of the delay, the estimated decrease in the gas volume between the 2 surveys was only 1.8% (because of the increase in gas content between

73
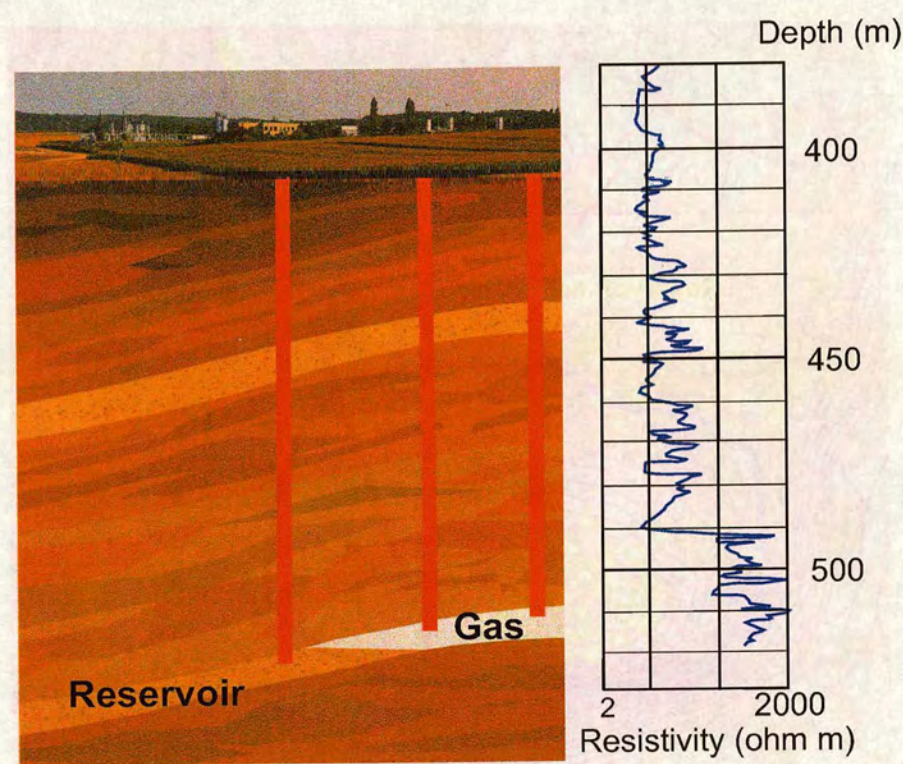
Figure 4.2: The reservoir at St. Illiers la Ville. Left: Schematic cross section through the reservoir showing the monitoring wells and the gas-water contact. Right: Part of a resistivity well log through the reservoir which starts at 490m.

April and August). This caused an estimated change in the EM response of 0.5% and a lateral movement of the gas-water contact of just 8m (Ziolkowski *et al.*, 1998a). Even with a data repeatability of 1%, the actual differences in the reservoir are below the limit of what was originally thought possible to resolve. The project ended in 1998 without either of the objectives of the project being achieved and with much of the data unprocessed. Subsequent results of processing some of the data were published by Hördt *et al.* (2000) and are shown in Figure 4.3. It can be seen that the differences are more or less random with no systematic signal apparent. Work on this PhD started in October 1999 after the initial project had ended.
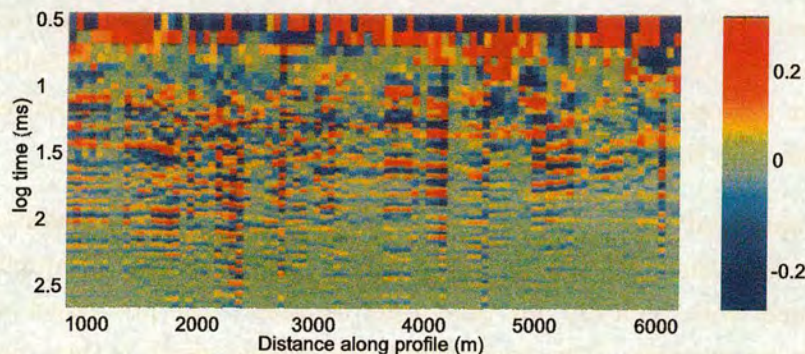
Figure 4.3: The result of Hördt *et al.* (2000). Differences of the derivative of the Saint Illiers la Ville data in the log-time domain. The differences have been CMP-sorted, spatially stacked and colour-coded along the profile as a function of time.

4.3 MTEM Data Acquisition

The MTEM System

As mentioned in section 2.2, the MTEM field system (shown in Figure 4.5) is a modification of the LOTEM system (Figure 4.4) in terms of the source used and the fields that are measured. However, the field layout is more akin to that of seismic reflection profiling. Indeed, the acquisition system used called TEAMEX (Transient Electromagnetic Apparatus for Mineral Exploration) was developed by DMT and is a direct outgrowth of SEAMEX, the DMT seismic acquisition system. The system in the configuration we had consisted of 16 boxes with 2 recording channels in each box. The electric field signals were recorded with commercial copper-copper sulphate non-polarising electrodes placed 125m apart and connected by a wire placed in the soil. The vertical rate of change of the magnetic field was recorded with a square multi-turn wire loop with 50m sides placed on the ground. The system had an increased dynamic range that allowed data to be collected at much nearer offsets than before. The MTEM method also yielded data volumes and spatial coverage that were unprecedented for an EM survey at the time. The source was a Zonge transmitter that produced a bipolar continuous current waveform switching between plus and minus 30 ampères. Current was injected into the ground via two vertical pipes 250m apart and connected to the transmitter by a wire. A much smaller source is required than in LOTEM as the target is relatively shallow and a smaller dimension of 250m is more compatible with the dipole approximation, thus leading to a higher spatial resolution.

The field layout

The field layout for the data acquisition is shown in Figure 4.5. For a particular source position the source is 'fired' and the resultant transients are recorded simultaneously on 2 channels at 16 positions. The near offset is just 375m, the spacing between receiver boxes is 125m, and the source interval is 250m.

The source was 'fired' 50-100 times for both in-line and cross-line orientations at each location. For each 'shot' a record was made of 2048 samples at 1 ms sampling interval at each channel with typically 384 pre-trigger samples. The pre-trigger samples are used to make an estimate of the background telluric field which is then removed from the measured transient to reduce the dc level at the
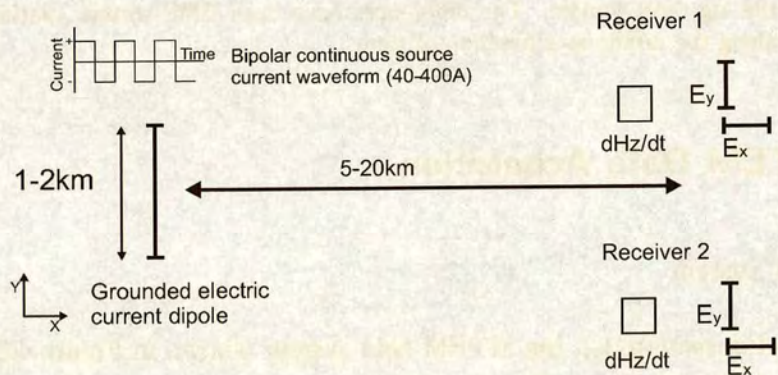
Figure 4.4: The field layout for a LOTEM survey.
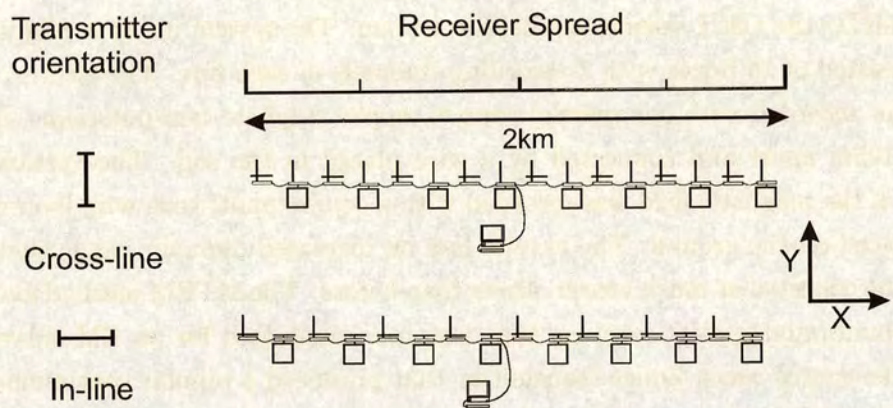
Figure 4.5: Field layout for an MTEM survey showing transmitter and receiver orientation for the cross-line and in-line source orientations. The receiver line has 16 boxes, each with two channels. The 32 recorded transient responses from the 16 boxes were downloaded onto the hard disk of a computer before the source current was reversed.

beginning of the transient to zero: this is done in the receiver box. This is necessary because the telluric field is many orders of magnitude larger than the field we are trying to measure and so this step is necessary to give maximum available dynamic range. This works only because the telluric field varies so slowly.

The electric field parallel to the transmitter was recorded at every receiver station. For the in-line configuration this component is called E_{xx} and for the cross-line component E_{yy}. The electric field perpendicular to the transmitter was recorded at odd numbered boxes and the time derivative of the vertical component of the magnetic field was recorded at even numbered boxes. For the in-line configurations these are called E_{xy} and $\frac{dH_{xz}}{dt}$ respectively and for the cross-line configuration E_{yx} and $\frac{dH_{yz}}{dt}$. In the naming of the components the first subscript refers to the source orientation and the second to the orientation of the receiver. Figure 4.6 summarises the layout of all the components.
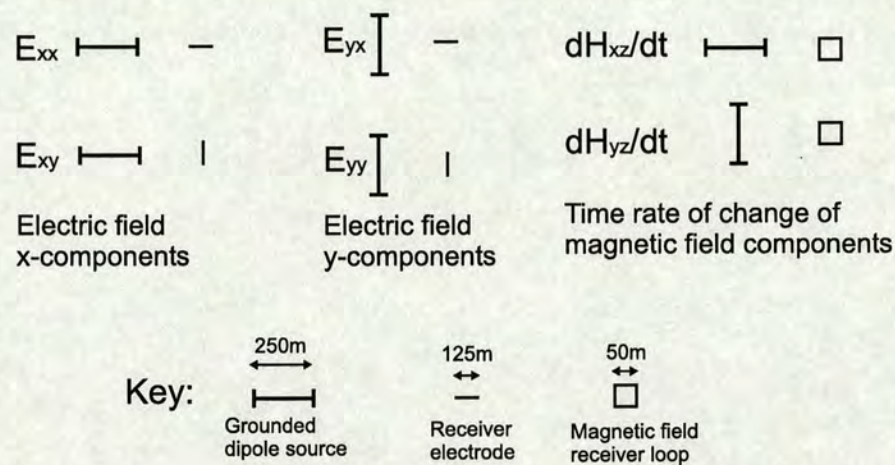
Figure 4.6: The orientation of source and receiver for each of the 6 components that were measured.

The profile across the reservoir had a source profile 7km in length with a total of 29 source locations and 32 receiver box locations. The layout of source and receiver locations relative to the reservoir edge is shown in Figure 4.7. The length of the receiver profile was only 2km, a limit that was imposed by the range of transmission within the recording system. Each survey was carried out using 2 receiver spreads, making a total receiver spread length of 4km. First receiver box numbers 10-40 shown in Figure 4.7 were occupied in a northern spread and the source was moved along the profile occupying the 29 source locations in both the in-line and cross-line positions. The receiver spread was then moved down the profile and box numbers 42-72 were occupied in a southern spread. The source was then moved along the profile in the same way as was done for the northern spread. This approach to the data acquisition is much faster

than moving the entire source and receiver profile every time a new source position is occupied and considerably reduced the time spent in the field. For the electric field data, because an electric current dipole source is being used, reciprocity allows the location of the source and receiver to be alternated and still obtain equivalent results. This is important in moving the source relative to the receivers as some of the data will have the source north of the receiver and some will have it to the south. However, it should be noted that reciprocity does not hold for the magnetic field data.

In each of the two surveys 29 source locations with in-line and cross-line configurations used at each location were fired and recorded at 16 boxes with 2 channels per box for both the northern and southern spread. This works out at $29 \times 2 = 58$ source positions recorded by $16 \times 2 \times 2 = 64$ receivers. This produces roughly 3700 source-receiver pairs for each survey and typically 50-100 transients were recorded for each source-receiver pair. This means that the two surveys yielded approximately 500,000 individual transients. The task of extracting meaningful information from all this data is discussed in the next section.
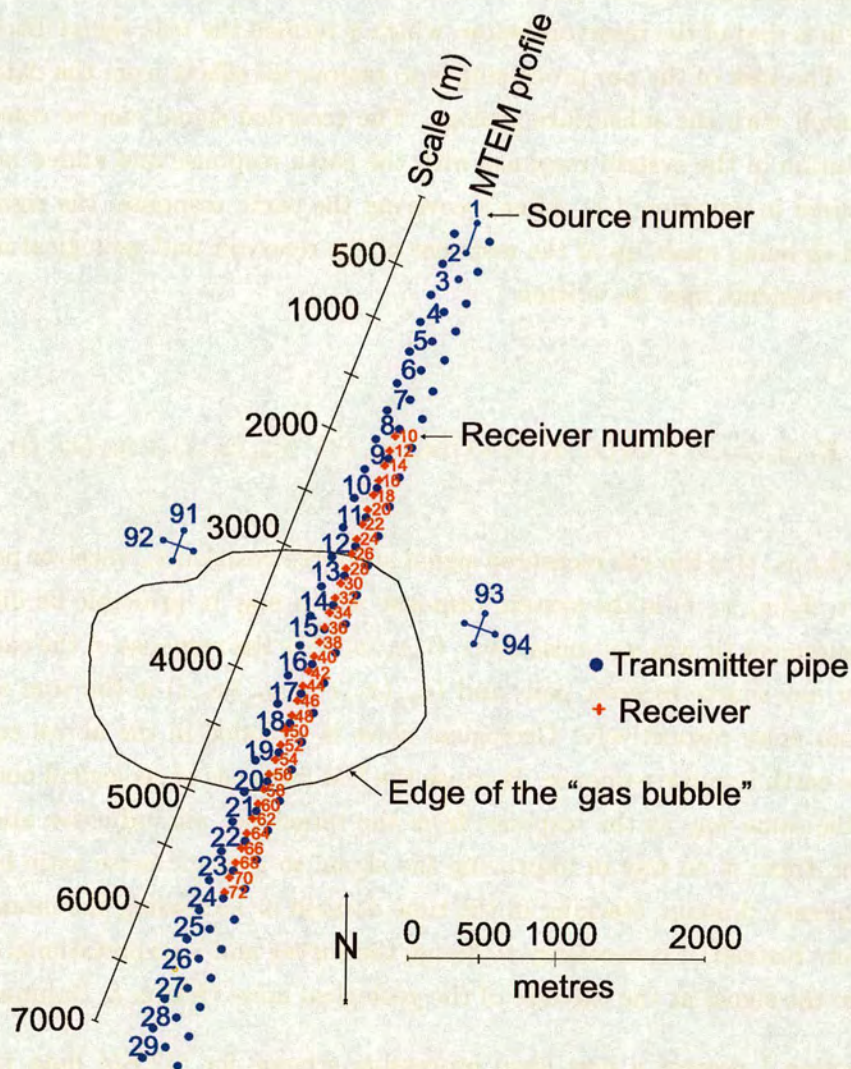
Figure 4.7: Layout of the entire survey, showing source locations (blue) and receiver locations (red) in relation to the edge of the gas bubble.

79

4.4 MTEM Data Processing (Ideal Approach)

Components of the measured signal

The signal recorded at the receivers of the MTEM system is the result of many different effects which influence the EM *pulse* between the source and receiver. The effect we are interested in is that of the reservoir below, which is termed the *true signal* (Strack, 1992, Ch3 p49). The task of the pre-processing is to remove all effects from the data that are not associated with the subsurface geology. The recorded signal can be considered as the convolution of the system response with the earth response and added noise. This is summarised in equation 4.1. After recovering the earth response, the signal can be considered as being made up of the response of the reservoir and geological noise. The measured transients may be written

$$E_k(x_s, x_r, t) = S_k(x_s, x_r, t) * G(x_s, x_r, t) + (n_{p_k}(x_r, t) + n_{r_k}(x_r, t)) \qquad (4.1)$$

where $E_k(x_s, x_r, t)$ is the kth measured signal at source position x_s, receiver position x_r, and time t, $S_k(x_s, x_r, t)$ is the system response which may in principle be different for each measurement (it was not measured), $G(x_s, x_r, t)$ is the response of the earth, which is fixed for any source-receiver pair, and $(n_{p_k}(x_r, t) + n_{r_k}(x_r, t)$ is the sum of periodic and random noise respectively. Geological noise is included in the above equation as part of the earth impulse response. Because the EM response of geological noise sources arises in the same way as the response from the target i.e. via inductive and galvanic interaction, there is no way of improving the signal to geologic noise ratio by filtering in the frequency domain, stacking in the time domain or increasing the moment of the transmitter. Instead, it is necessary to design the survey and interpretational procedure to enhance the signal at the expense of the geological noise (Eaton & Hohmann, 1987).

In this section I present a new ideal processing scheme for MTEM data in order to recover the earth response which can then be used as the input for diffusive to propagative mapping (Chapter 7), provided that the noise level is generally below 3% and distortion free. In the process of carrying out this work many problems were found with the way the St. Illiers la Ville data were collected. As a result, improved acquisition procedures are suggested as well as a pragmatic approach to processing of the data, the results of which are shown in Chapter 6.

Periodic Noise

As discussed in section 2.5, noise is ubiquitous in electromagnetic data. This poses a problem in interpretation in all cases but particularly where DPM is to be applied, due to the ill-posedness of the transform. For this reason successful noise suppression is particularly important. There are various noise removal techniques which can be applied to remove certain types of noise, depending on whether the noise is periodic or random in nature. The noise that usually has the largest effect on the raw data is due to pickup from mains electricity supplies at 50Hz and odd harmonics of 150, 250, 350 and 450Hz[1]: this can often be 100 to 1000 times larger in amplitude than the geophysical signal being measured. This is removed by digital notch filtering. [2]

This must be applied pre-stack on a trace by trace basis as the noise is not phase stable over long periods of time. The filter I applied has the ability to search a frequency window either side of the harmonic value as the peak value of the noise can vary due to surges in the power supply. An example of a single raw transient and its frequency spectrum before and after notch filtering are shown in Figure 4.8.

---

[1]The reason only odd harmonics are present is because of the power system generating the noise. Harmonics arise because of unbalanced or non-linear loads. In three-phase power systems odd-order harmonics are additive while the even order harmonics cancel out (Carlson & Pearlman, 1993).

[2]A novel alternative method to removing noise caused by electrical pickup was proposed by Qian & Qian (1985) and Spies (1988b) for use on magnetometers that measure the magnetic field directly. The method involves a cancelling antenna wrapped around the EM receiver equipment, the cancelling antenna is provided with an AC EM field that is 180 degrees out of phase and of the same amplitude as the ambient powerline noise, the AC field is provided by a noise antenna, a phase-locked loop and an amplifier. The noise antenna receives the ambient powerline noise, the phase-locked loop locks onto and tracks the frequency of the noise, and the amplifier provides the required amplification. This method has the advantage that the noise is suppressed before it is recorded and so the effective dynamic range of the recording system is increased, which also results in a greater depth of penetration of the measured signal.
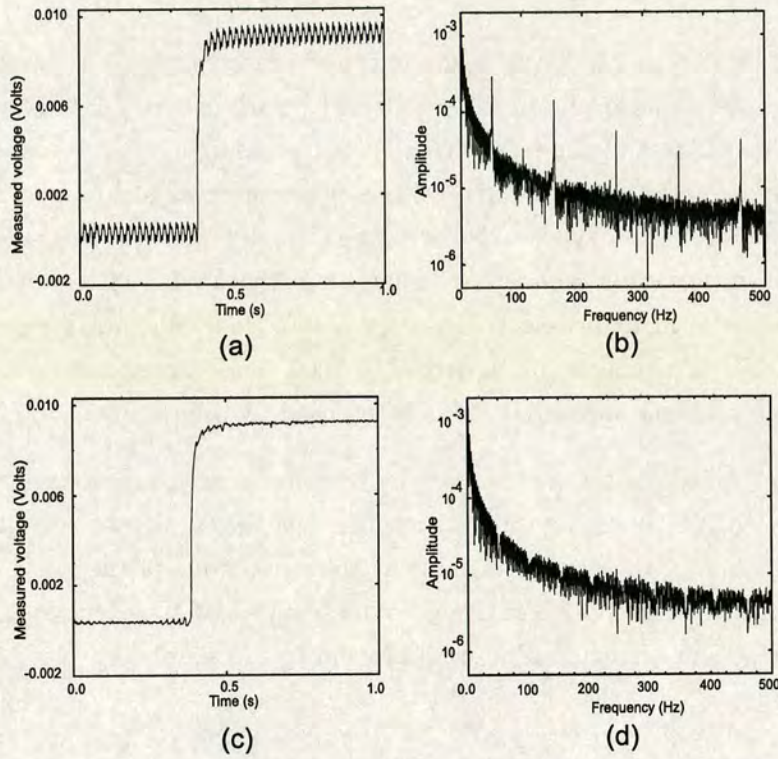
Figure 4.8: Notch filtering: (a) A raw transient. (b) Amplitude spectrum of the trace shown in (a). (c) The same transient as that shown in (a) after notch filtering. (d) The amplitude spectrum of the trace shown in (c).

Random noise removal

Random noise is generally not nearly as big a problem as periodic noise in EM data. However, notch filtering can usually do a very good job of removing periodic noise leaving random noise as the main source of noise. The vast majority of TEM data is associated with the magnetic field, and multicomponent measurements of this field are used to remove random noise in the central-loop configuration by using the fact that in a 1-D earth the signal from the earth is purely vertical H_z which means that the horizontal components H_x and H_y record the noise. An example of this is the local noise prediction filter (LNPF) method described by Spies (1988a). This approach breaks down in the presence of 2-D or 3-D structures when there is signal in the horizontal component, as this introduces a bias in the result. Apart from this technique the main technique used to reduce random noise in EM data is selective stacking (Strack *et al.*, 1989a; Stephan & Strack, 1991) (see pages 92-99). Many of the acquisition and processing systems used for EM systems have been developed at academic institutions on modest budgets (Strack, 1992). In 1988 a new system called DEMS IV (Digital ElectroMagnetic

System) was launched by the University of Cologne and it was revolutionary in that it was the first system which stored all the raw transients to enable prestack processing. Previous systems had stacked the traces in the box. For the Saint Illiers la Ville data generally between 50 and 100 traces were recorded for each source-receiver pair, each transient had to be transmitted to the controlling PC before recording the next one as the boxes could store only one transient per channel. I have applied two signal enhancement techniques to the data before stack to reduce the level of random noise which is usually only tackled by stacking. These techniques exploit the constancy of the signal for a suite of traces collected for the same source-receiver pair, while the random noise varies from trace to trace. The techniques are called F-X deconvolution and dynamic S/N filtering (Canales, 1984; Gulunay, 1986). The theory of the two techniques is very similar: a Fourier transform is applied to the data to convert from the time domain (x, t) to the frequency domain (x, ω) so that a time slice becomes a frequency slice. Each sample in the transformed data then has both real and imaginary components. Events with similar dips appear as a sinusoidally complex signal along a given frequency slice and can be written as $cos(\omega t) + isin(\omega t)$. For traces in the same source-receiver pair (provided there are no synchronisation errors) the signal is the same and occurs at the same place for each trace. The dip of the signal is therefore the same for each trace and the signal is predictable (Canales, 1984), whereas the noise, which does not have a constant dip from trace to trace, is not predictable.

F-X deconvolution is a method of random noise attenuation by FX prediction. The first step is to perform a Fourier transform over a time gate for every trace. The spatial variation of each Fourier amplitude is then examined. For traces in the same source-receiver pair the signal is linear across traces, giving rise to Fourier amplitudes that are the sum of complex sinusoids, one for each event. The signal energy in a trace amplitude is therefore predictable as a linear combination of adjacent trace amplitudes. In contraast the the component of the noise energy which fluctuates randomly from trace to trace is unpredictable. A prediction error filter is estimated using a least mean square error criterion. The output of the prediction error filter is an estimate of the unpredictable part of the trace amplitudes. Subtracting the prediction errors from the original trace amplitudes, and performing an inverse Fourier transform , gives the F-X deconvolution predicted output.

Dynamic S/N filtering enhances lateral coherency by weighting each frequency by a function derived from the local signal-to-noise ratio. The filter used is an amplitude-only, frequency domain, convolutional weighted filter given by equation 4.2

$$Weight(f) = \frac{S(f)^2}{S(f)^2 + N(f)^2}.$$ (4.2)

So for high S/N ratios the weight factor tends to 1 while for small S/N ratios the weight factor tends to zero. To calculate the weighting function, a window over which the dip is fairly linear is chosen and the traces are then converted to the (ω, x) domain. Moving from one trace to the next at a constant frequency the signal contribution to each complex frequency sample should change only by a constant phase shift. The noise contribution to each sample is assumed to be random. So each complex frequency sample is is equal to the sum of a random noise component and a signal component which changes only in phase from trace to trace.

Considering each frequency slice seperately, the signal power plus noise power can be estimated by summing the products of each ensemble sample and its complex conjugate. Each product contains a signal squared plus a noise squared amplitude, plus cross-products of noise and signal. These complex cross-products cancel out if the signal does not correlate with the noise. Therefore, the result of the sum will be the number of traces in the ensemble multiplied by the the average signal and noise power at that particular frequency.

An estimate of the signal power is found by summing the products of each trace sample and the complex conjugate of the adjacent trace sample. Each product yields a signal power multiplied by an unknown, but constant, phase term, plus random cross-product terms of noise, and noise with signal terms. The magnitude of the sum of all adjacent trace products will be the number of traces in the ensemble minus one multiplied by the average signal power. Again it is assumed that the random cross terms do not correlate, and will cancel on summation.

Techniques such as these reduce white noise and effectively predict signals in regions with a poor signal-to-noise ratio (Alsdorf, 1997). They were developed primarily to tackle noise in seismic data, particularly organised noise produced by other seismic vessels in the vicinity of a survey. In applying them to EM data the primary concern is that they do not alter the signal. Figure 4.9 shows the result in the time (left) and frequency domain (right) of applying F-X deconvolution and dynamic S/N filtering to some particularly noisy data after notch filtering. The improvement in the signal-to-noise ratio compared to the trace where only notch filtering was applied is immediately apparent. However, despite this improvement, it is not possible to know whether the signal has been affected. Figure 4.10 shows the same result, only this time applied

84

to some noise-free data. It can be seen that in this case the effect of applying both techniques is almost undetectable, suggesting that only noise is affected by these techniques. A final test of whether only random noise is being removed is to study the difference between the filtered and unfiltered data i.e. what the filter has removed from the transient. Figure 4.11 shows the difference between the filtered and unfiltered data shown in Figures 4.9-4.10. It can be seen that for the noise-free data the difference is effectively zero and any differences present appear to be random in nature: the result for the noisy data is approximately 10% of the amplitude of the transient itself and appears random in nature. Reassuringly there are no coherent events present at around 384ms where the rise of the transient occurs. The application of these techniques offers the possibility of reducing the random noise content of particularly noisy data that would not otherwise be usable. This is particularly true where only a few traces are present and the improvement in signal-to-noise ratio obtained by stacking is small.
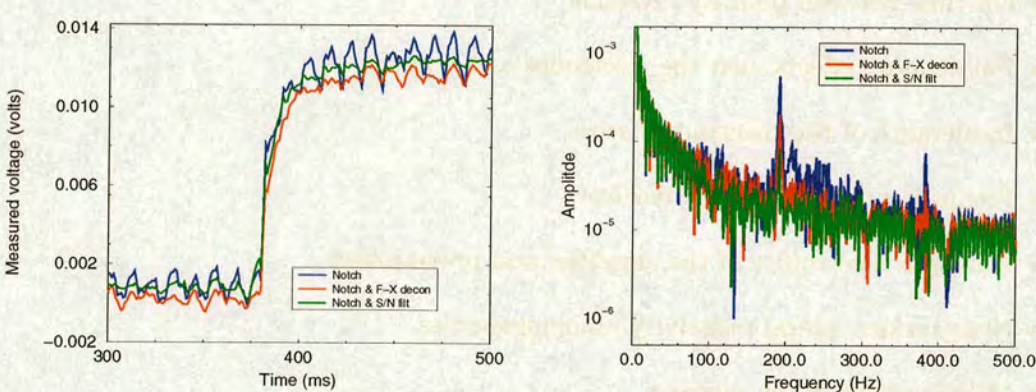
Figure 4.9: The result of applying F-X deconvolution and dynamic S/N filtering to particularly noisy data after notch filtering and the result of notch filtering only. Left: Time domain. Right: Frequency domain.

Deconvolution of the system response

The simplest way to remove the system response from the measured data is to measure it and deconvolve it from the data.

Excluding external sources of noise, the theoretical response of a polarity reversing transmitter at the receiver is influenced by the following effects (Strack, 1992, page 49):

- Deviation of the current waveform from a step function

85
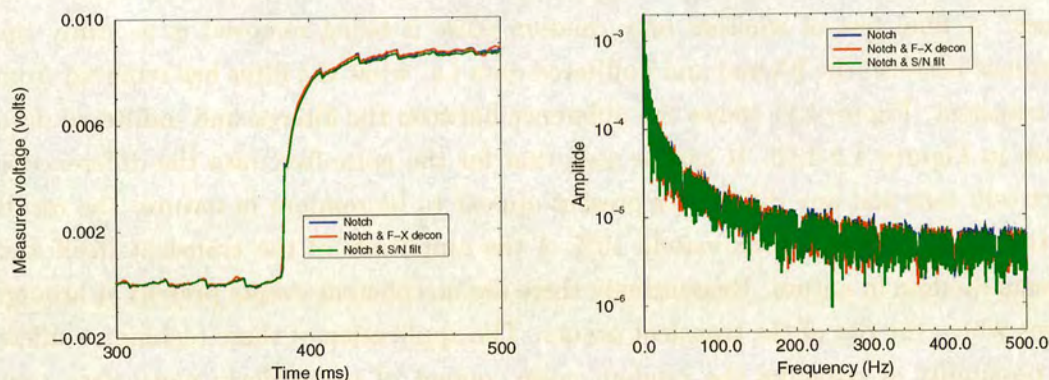
Figure 4.10: The result of applying F-X deconvolution and dynamic S/N filtering to quiet data after notch filtering and the result of notch filtering only. Left: Time domain. Right: Frequency domain.

- Off-time between polarity reversals

- Polarization effects near the electrodes and sensors

- Inductance of the transmitter wire

- Frequency response of the receiver

- Analogue electronics of the amplifier and preamplifier

- Near-surface lateral resistivity inhomogeneities

- Misalignment of the receiver

- A/D converter temperature drift

All of these effects when convolved with each other yield the *true* system response. They must be eliminated from the measured signal in order to obtain the *true* signal. The last three items on the list are not included in system response measurements but the effect of temperature drift on modern A/D converters is negligible, and misalignment errors can be prevented by careful field procedures. Near-surface variations can cause a static shift but this should be eliminated when the response is differentiated (Hördt *et al.*, 2000). An alternative to deconvolving for the system response when using a forward modelling approach is to convolve the system response with the synthetic data to enable comparison. As a rule of thumb, this approach must be used if the length of the system response is more than one third of the length of the transient (Strack, 1992, page 52).

86
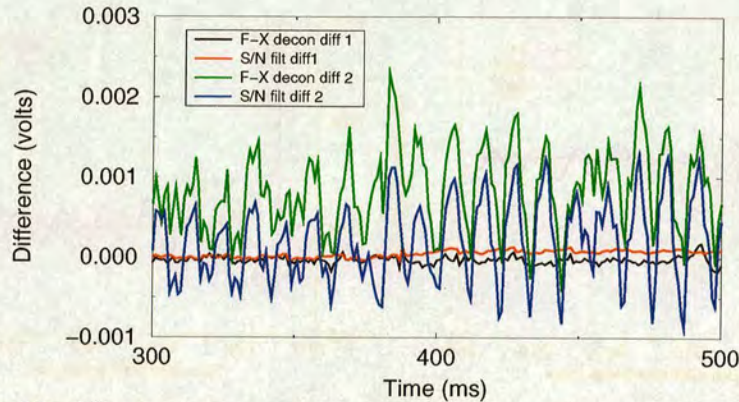
Figure 4.11: The difference between applying notch filtering only and applying notch filters followed by F-X deconvolution or dynamic S/N filtering. Red and black lines are the differences for the quiet data shown in Figure 4.10. Green and blue lines are for the noisy data shown in Figure 4.9.

The most noticeable difference between raw data and data that has been deconvolved for the system response is a separation of the two curves at very early times with the amplitude of the deconvolved data being larger than the raw data (Keller *et al.*, 1984).

Many previous studies have measured the system response in the laboratory using a switchbox to generate the square wave which is recorded and used in the deconvolution which is applied poststack. Many measurements are recorded and the stacked average used. More recently attempts have been made to measure the system response in the field under load. The system response of the Saint Illiers la Ville data was measured in the field during the 1996 survey. The response for E_{xx}, E_{yy} and $\frac{dH_{xz}}{dt}$ was measured about 50 times for three input source currents of 8, 16 and 32A. The stacked and normalised response of the measured E_{xx} and $\frac{dH_{xz}}{dt}$ system response for these three source currents is shown in Figure 4.12.

It can be seen from Figure 4.12 that the response is not linear with an increase in current. It was initially believed that linearity held and that a suitable system response could be obtained for all the source currents that were used to acquire the data simply by interpolating between the three measured responses. The reason the system response had not been measured more often at Saint Illiers la Ville was that measurements of the system response made in May 1993 in Specking, Germany, had indicated that it was a perfect step function and so did not need to be measured during the survey. In spite of this I initially deconvolved the data using the 16A system response because this was the source current most commonly used during the two surveys. However, after processing a large amount of the data I discovered that some of the results of the

87
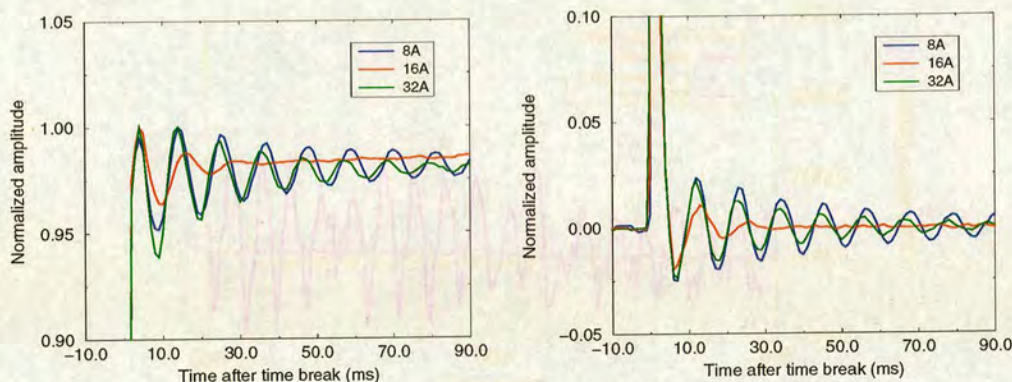
Figure 4.12: The normalized and stacked system response measured in the field for 3 different source currents. Left: E_{xx} system response. Right: $\frac{dH_{xx}}{dt}$ system response.

deconvolution led to unphysical results. Figure 4.13 shows the stacked earth impulse response for a source-receiver pair from the 1996 E_{xx} data. The earth impulse response is obtained by differentiating the step response and the system response and then deconvolving for the system response. The source current used to acquire this data was 44A and it can be seen that the response goes negative at about 3.5ms; this is physically impossible for the E_{xx} component, as it implies that the current flow has reversed. It is physically possible, however, to obtain such a reversal in the E_{yy} component. The impulse response should always remain positive. The red curve in Figure 4.13 is the result of simply differentiating the data and not deconvolving for the system response and it can be seen that the response now stays positive. This would suggest that the system response for 44A which was not measured is quite different from the one for 16A which was used in the deconvolution. The fact that the correct system responses were not measured in the field and that the system response varies in an unpredictable manner under load has serious implications. Using the wrong system response leads to physically unrealistic results, therefore it is not possible to apply deconvolution to the Saint Illiers la Ville data and still be confident of any conclusions drawn from results that are in many cases impossible to explain. It was also discovered that the system response data that were measured were aliased, which meant the true impulse response function of the earth could not be recovered. The TEAMEX recording system had a low-pass filter that was sufficiently steep to prevent aliasing of the measured transient response at offsets hundreds of metres from the source, but was insufficient to prevent aliasing of the system response measurement. Thus, even if the system response measurements had been made with TEAMEX, they would have been useless for deconvolution.
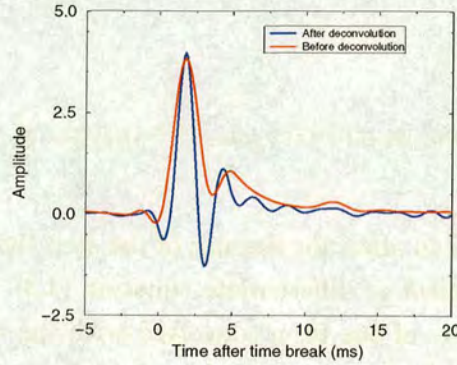
Figure 4.13: The stacked result of deconvolution using the wrong source current (blue) and the result of simply differentiating the data (red).

The discovery that the system response is not stable under load and varies unpredictably with the source current means that in order for the system response to be deconvolved correctly it should be recorded every time the source is fired. Only then can we be sure that we are deconvolving for the system response function that has been convolved with the recorded data. It can be seen from equation 4.1 that in order to solve for the response of the earth $G(x_s, x_r, t)$, the system response $S_k(x_s, x_r, t)$ must be known for every k. The system response for the electric field should be measured with two electrodes placed very close (of the order of a few cm) to the source, with the known distance between them very close (of the order of a few cm) to avoid generating voltages that are too large. Also, a much smaller sampling interval should be used to provide better definition of the very short period over which changes occur Ziolkowski *et al.* (1998a).

4.5 Data Processing (Pragmatic Approach)

Having discussed the various reasons why deconvolution of the system response cannot be applied to the data I now outline a pragmatic approach to data processing. This approach is not being advocated as a routine way to handle such data, but is proposed to enable interpretable results to be obtained from data that are far from ideal.

It can be seen from Figure 4.12 (left) that the deviation from a perfect step function is a ripple of the order of a few percent. If we ignore this ripple, we may approximate the measured response $E_k(x_s, x_r, t)$ as the convolution of the response of the earth with

a step function, or Heaviside function $\mathcal{H}(x_s, x_r, t)$. An approximation to equation 4.1 can then be written as:

$$E_k(x_s, x_r, t) \approx s_k(\mathcal{H}(x_s, x_r, t) * G(x_s, x_r, t) + (n_{p_k}(x_r, t) + n_{r_k}(x_r, t))), \qquad (4.3)$$

where s_k is a scaling factor to allow for the size of the step that is input, since $|\mathcal{H}| = 1$ for $t > 0$. It is now convenient to differentiate equation (4.3). The differentiation of a convolution is the derivative of one term convolved with the remaining part. Because the derivative of a Heaviside function is a delta-function, and the convolution of a delta-function with any function is the function itself, we have

$$E'_k(x_s, x_r, t) \approx G(x_s, x_r, t) + (n'_{p_k}(x_r, t) + n'_{r_k}(x_r, t)), \qquad (4.4)$$

where $E'_k(x_s, x_r, t)$ is the time derivative of the measured transient response and $(n'_{p_k}(x_r, t) + n'_{r_k}(x_r, t))$ is the derivative of the noise, and is still noise. Thus, for these data, differentiation of the measured responses is an approximation to the impulse response of the earth $G(x_s, x_r, t)$ plus noise. The signal-to-noise ratio can be increased by stacking.

Differentiation

Differentiation is usually applied to EM data when deconvolution is to be carried out, as a delta-function input cannot be realized for an EM system; instead a square wave is input and a step response is measured which is subsequently differentiated. Deconvolution is much more stable after both the transient and system response have been differentiated. Another reason for differentiating the data is that the time derivative is independent of static shift factors (Hördt *et al.*, 2000). Differentiation also eliminates the need for complicated scaling procedures when comparing time-lapse data. After differentiation the response, for these data, is reduced in time to approximately 25-40ms making much of the measured two-second-long transient redundant. The red curve in Figure 4.13 shows a differentiated transient with a response of only about 15ms. The only drawback of differentiation is that it adds high frequency noise to the data although this does not appear to be a significant problem.

Interpolation

Interpolation of the data from 1 to 0.1ms is carried out using cubic-spline interpolation. This is applied in order to increase the number of data samples and provide better definition of the short time period over which changes occur. The interpolation can be carried out at any point before stack but the best result was obtained by applying it after the differentiation.

Timing Errors

After I had begun to differentiate the data I found a very important error in the timing. It had been known that there were timing errors of the order of a few milliseconds between traces in different source-receiver pairs and between the two surveys (Ziolkowski *et al.*, 1998a). However, it was assumed that the timing of the current switch for a given suite of traces for the same source in the same location was always the same (Ziolkowski *et al.*, 1998a). After differentiating all traces in the same source-receiver pair I found that this was not the case and that a timing correction was necessary to ensure a reasonable response after stack. Figure 4.14 (left) shows differentiated traces from the same source-receiver pair and the need to apply a timing correction before stacking. Figure 4.14 (right) shows the same data after applying the timing correction. If this timing error is not corrected for, it is unlikely any meaningful results will be obtained by stacking as the response is then smeared over a broad time range as a result of stacking traces that are not aligned in time. The timing correction is made by scanning a time window around the onset time of the transient and noting the time of the peak of each differentiated trace within this time window: static corrections are then assigned to each trace based on correcting all traces to a particular time. The statics can then be applied to the differentiated traces or applied to the same traces before differentiation, so that F-X deconvolution or dynamic S/N filtering can be applied. Had the system response been measured every time the source was fired these timing errors would have been corrected for by deconvolving for the system response. This is described in Appendix D.

Stacking

Stacking is considered by many to be the most important step in seismic data processing (Naess & Burland, 1985) and is of similar importance in the processing of electromagnetic data. It is the processing step which most improves the signal-to-noise ratio. The success of stacking in increasing the signal-to-noise ratio is to some extent dependent on the characteristics of the noise in the data and the type of stacking applied. For example, only if we have uncorrelated noise in the data is there generally no need to
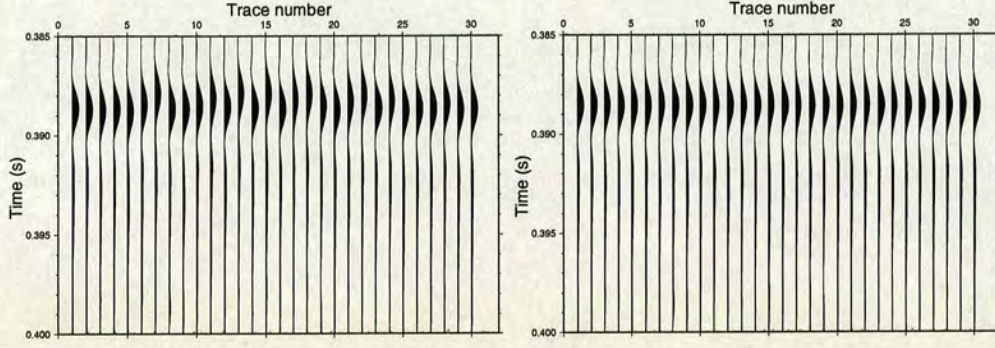
Figure 4.14: Traces in the same source-receiver pair. Left: Before timing correction. Right: After timing correction.

use an alternative to the standard mean stack: in the presence of correlated noise alternative stacking procedures are available. We also need to consider the information bearing signal too; for example, we want to preserve the amplitude and shape of the signal during stacking. In the following section the term stacking refers to stacking repeat signals with the same source-receiver geometry. A trace is defined to be a single time series.

The most commonly used type of stacking in data processing is the mean stack. Given the n measured transients for the same source-receiver pair $E_k(x_s, x_r, t)$ a better estimate of $E(x_s, x_r, t)$ may be made by stacking. When applying a mean stack the improved estimate is,

$$\bar{E}(x_s, x_r, t) = \frac{1}{n} \sum_{k=1}^{n} E_k(x_s, x_r, t), \qquad (4.5)$$

where n is the fold of the stack. If each trace can be considered as the same signal plus Gaussian noise, the signal-to-noise improvement in the stacking process should be $(n)^{\frac{1}{2}}$. This is the maximum improvement obtainable and the conditions to achieve this are that the amplitude of each trace over the same time zone should be equal, and that no dc should exist on any traces (dc is removed by the differentiation step). The mean stack only attenuates spurious noise events by an amount proportional to their relative rate of occurrence in the stack. When the noise event is much stronger than the background noise level, conventional stacking by averaging is not a sufficiently powerful tool (Haldorsen & Farmer, 1989) and the average is corrupted by the outlying sporadic

92

noise amplitudes. This problem is exacerbated when only a small number of traces are to be stacked. Most of the alternatives to straight stacking are rather empirical in nature; that is, they are not designed as a mathematical consequence of established assumptions and design criteria.

The median stack is an alternative stacking procedure which is insensitive to abnormal strong noise amplitudes occurring on a small number of input traces or coherent noise events which occur at the same time as the primary signal on less than half of the traces. It is a simple procedure where the stacked trace is given the median value of amplitudes across the gather at each time sample, the median being found by sorting the amplitudes for each time from smallest to biggest and selecting the one in the middle.

A problem with the median stack is that a coherent noise event is not suppressed when it is present on more than half the traces in the same source-receiver pair. Also, abrupt changes in amplitude between consecutive samples on the output trace may occur and this will in effect mean the introduction of high frequency noise into the data. The introduction of this high frequency noise can to a large extent be avoided by using a summation of several amplitudes situated around the middle position after reorganizing the input values in increasing order. This can be achieved using the alpha-trimmed mean (Watt & Bednar, 1983); also known as the symmetric selective stack, it is defined as,

$$\bar{E}_{\alpha mean}(x_s, x_r, t,) = \frac{1}{n-r} \sum_{k=\frac{r}{2}+1}^{n-\frac{r}{2}} E_k(x_s, x_r, t), \qquad (4.6)$$

where n is the total number of samples, r is the total number of samples rejected, $\frac{r}{2}$ on either side of the distribution. After reorganising the data into increasing order as was done for the median stack, a number of amplitudes at each end are trimmed and excluded from the stack. The fraction of samples that are excluded depends on the trimming parameter α, where α is defined as $\alpha = \frac{r}{2n}$ with $0 < \alpha < 0.5$. By varying α we get a result that will partly have the properties of the mean stack and partly those of the median stack. The alpha-trimmed mean method is a rather general method that may give good results when α is chosen appropriately. A natural extension of the method is to make α a function of the data itself such as the standard deviation.

A fourth possible stacking procedure is the area-defined rejection stack (Strack *et al.*,

1989a), also known as the diversity stack (Sheriff & Geldart, 1995). Amplitude frequency distributions are first calculated by sliding overlapping windows over the sorted amplitude curves for each time sample of all transients, a percentage of the area under each distribution curve symmetric about the maximum is calculated, and all data within that are kept.

Weighted stacking (equation 4.7) involves applying predetermined weights w_k to individual traces

$$\bar{E}_{weighted}(x_s, x_r, t) = \left(\sum_{k=1}^{n} w_k\right)^{-1} \sum_{k=1}^{n} w_k \cdot E_k(x_s, x_r, t). \tag{4.7}$$

It is mainly used in seismic data processing in the CMP domain where near-offset traces are weighted higher than those at greater offsets because they are less contaminated by multiple energy (Hatton *et al.*, 1986). In EM data the traces being stacked are all from the same source-receiver offset and so have equal weighting, but, an extreme form of weighted stacking is commonplace in EM data. Whenever a noisy trace is present it is best simply to eliminate the entire trace altogether: this is equivalent to giving noisy traces a weighting of 0 and all other traces a weighting of 1. This is defined as the trace kill weighted mean stack.

"It is almost always better to throw away noisy data than to include it. A very powerful processing technique, which is not used as much as it should be, is simply to look at the data and delete portions that appear to be mainly noise"

(Sheriff & Geldart, 1995)

Figure 4.15 shows the ratio of high energy noise to ambient noise after stack for data contaminated by high energy noise bursts at a level of ten times the ambient noise level, using the mean, median and three different levels of alpha trimmed mean stacks. The ability of the selective stacking methods to reduce high energy noise bursts is clear. However, a problem of selective stacking procedures is that, while they suppress high energy noise bursts, they bias the estimate of the mean for coherent data (Macnae *et al.*, 1984). In the presence of ambient noise only, a median stack will increase the noise level by 15% (or 1dB) compared to a conventional mean stack independent of the fold (Haldorsen & Farmer, 1989). For a rejection rate of 50% the noise is increased by 5% (0.4 dB) and for 25% rejection the noise increase is 2%. This is equivalent to reducing the stacking fold from 60 to 54 and 58 respectively. The resulting increase in

background noise levels must be weighed against the potential gain in having a process that is minimally affected by transient noise.
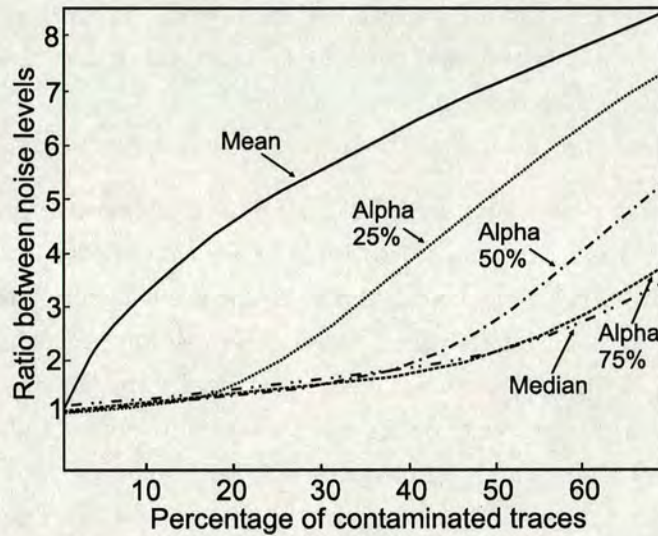

Figure 4.15: Estimates of the residual noise level for data contaminated by high-energy noise bursts at a level of ten times the ambient noise. The noise level is taken relative to the residual noise in a conventional stack with only ambient noise present. Results are shown for a conventional mean stack, alpha trimmed mean stacks with rejection rates of 25, 50, 75% and a median stack. (Redrawn from Haldorsen & Farmer (1989)).

In order to determine which stacking procedure to apply to the Saint Illiers la Ville data I applied all the procedures described above to both noisy and quiet data for both large and small folds of coverage. Figure 4.16 (a) shows part of the first 7 traces in the same source-receiver pair for noisy data at an offset of 1750m with a large amplitude high energy noise spike present on the third trace. The portion of the transient between 500 and 600ms is shown, since the transient at this point has reached the DC level, and so the amplitude of the transient should be constant. This allows the various stacking procedures to be compared. Figure 4.16 (b) shows the result of stacking the seven traces shown in (a) using seven different stacking techniques. The effect of the high energy noise burst present on the third trace is clearly seen in the straight mean stack and also has an effect on the area defined rejection stack. The noise burst on the third trace has no effect on the trace kill mean stack as it has been killed before stacking. The trace kill mean result, the three alpha trimmed mean stacks and the median stack all look quite similar. The main difference is the introduction of high frequency noise in the median and alpha trimmed mean stacks. For noisy low fold data the best result is obtained by killing noisy traces that will contaminate the stack followed by a conventional mean stack. This method also contains no unknown artefacts which can occcur as a result of

selectively excluding individual points within a trace. Figure 4.16 (c) shows the result of stacking 100 traces from the same source-receiver pair as the traces shown in Figure 4.16(a). The mean stack is still affected by the large amplitude noise burst present on the third trace. The area defined rejection stack appears to work much better when applied to a large number of traces. The alpha trimmed mean now appears to be better than the trace kill mean at reducing random noise but this must be offset against the addition of high frequency noise and the possibility of artefacts being introduced.

Figure 4.17 is the same as Figure 4.16, but for relatively noise-free data from an offset of 725m. The gain applied to the traces is six times that shown in Figure 4.16. The first seven traces from the same source-receiver pair are shown in Figure 4.17 (a) and appear to consist of uncorrelated noise only. The result of stacking these traces is shown in Figure 4.17 (b). The results of all seven stacks appear very similar with the median and alpha trimmed mean stacks again contaminated by high frequency noise. These stacks also contain a high amplitude event at around 590ms which increases in amplitude for larger values of α. Analysis of the traces shown in Figure 4.17(a) shows that there is not a coherent event present in the seven traces at 590ms. This is an example of an artefact that selective stacking can introduce to the result. The area defined rejection stack appears to be almost identical to the mean stack, suggesting no improvement. The result of stacking all 100 traces from the same source-receiver pair is shown in Figure 4.17 (c). The seven stacked traces in this plot are all essentially the same except for the high frequency noise that has been introduced to the median and alpha trimmed mean stacks. Interestingly, the event at 590ms that appeared for some of the selective stacks in Figure 4.17 (b) is no longer present.

On the basis of these results, the stack that gives good results which are reliable for a range of noise levels and folds of stack is a weighted trace kill mean stack. While selective stacks can give better results on low-fold data, they introduce both high frequency noise and artefacts into the result such as that present on the alpha trimmed mean stacks at 590ms in Figure 4.17 (b). Applying a weighted trace kill mean stack involves visually studying all the individual traces and removing any particularly noisy ones before stack. This is a time consuming task, but visually checking the traces prior to stack is worthwhile, as problems such as the timing error would not be detected otherwise.

In the Saint Illiers la Ville data the response is only about 25-40ms long after differentiation so only this portion of the trace needs to be examined. This means that only noise bursts present in this portion of the data need to be removed. If all traces with a noise burst on them were to be killed, the stack would include very few traces, but by killing only traces that have large amplitude noise occurring at the same time as

96

the 25-40ms response, the number of traces that are stacked is still quite large. If the whole trace is used in the processing, the weighted trace kill mean stack may not be suitable, as too many traces would have at least one high energy noise event.

Figure 4.16: The result of various stacking procedures applied to noisy data at an offset of 1750m. (a) The first 7 traces of data in the source-receiver pair to be stacked. (b) The result of applying various stacking techniques to the traces shown in (a). (c) The result of applying various stacking techniques to 100 traces in the same source-receiver pair as the traces shown in (a).

98
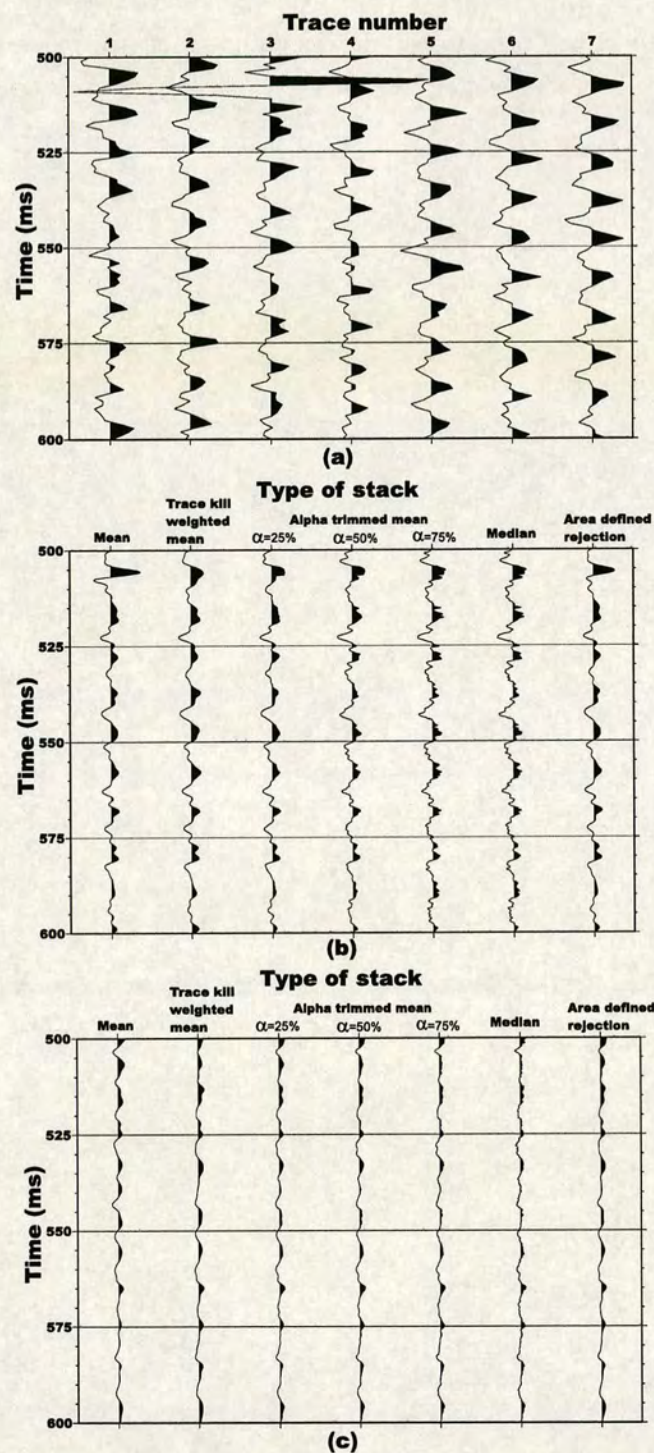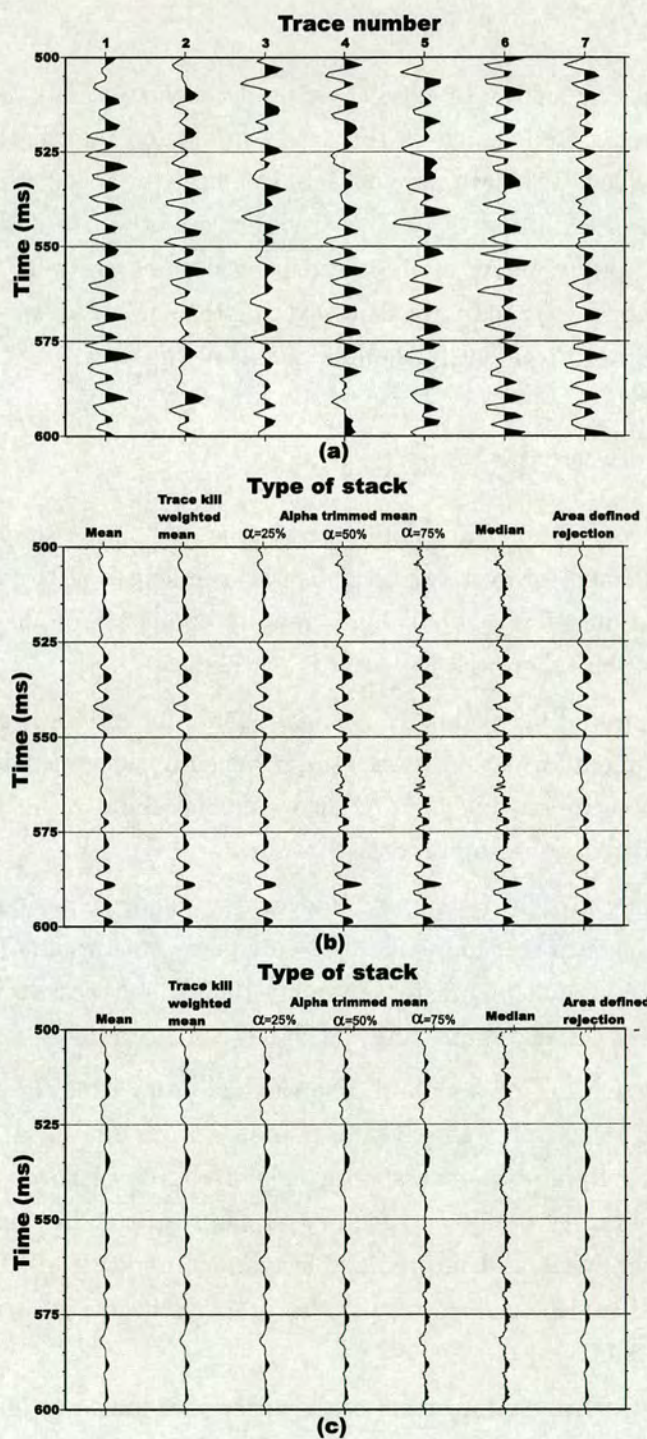
Figure 4.17: The result of various stacking procedures applied to data at an offset of 750m. (a) The first 7 traces of data in the source-receiver pair to be stacked. (b) The result of applying various stacking techniques to the traces shown in (a). (c) The result of applying various stacking techniques to 100 traces in the same source-receiver pair as the traces shown in (a).

99

4.6 Summary

At the time of the first survey in 1994 the size of the survey and the amount of data acquired represented a step change in the data volume and information for a transient electromagnetic survey. The data were collected to meet the specifications of traditional inversion methods of data analysis as no alternative method of data analysis existed at the time. As a result, many of the acquisition parameters were far from ideal for applying data processing geared towards recovering the equivalent wavefield. One result of this chapter has been to identify the limitations of the data:

- Limitations of the data

  1. In order to obtain information about the late-time response each transient was collected for over two seconds, yet the length of the response after differentiation is only about 20ms, ie only about 1% of the data contain any information before the DC level is reached.

  2. The sampling interval of 1ms is inadequate for a data processing approach. Early time information is essential if the equivalent wavefield which requires converting to log-time is to be recovered successfully. A sampling interval of 0.05-0.01ms would be better.

  3. Recording at a finer sampling interval for a shorter period, say 100ms. Provided the data transmission rate is adequate, this would allow the data to be collected many times faster, enabling 1000-2000 traces to be stacked instead of 50-100, greatly improving the signal-to-noise ratio.

  4. The system response should be measured every time the source is fired and used to deconvolve the system response from the data that is measured. Measuring the system response only a couple of times in the field or in the laboratory is not satisfactory as the response has been shown to vary in a non-linear and unpredictable manner under load. In some cases this resulted in deconvolved results that imply a negative current flow, which is not possible.

  5. The data have timing errors of the order of $\pm$ 2ms, not just between surveys as was known, but between traces within the same source-receiver pair. This was detected only after the data had been differentiated. Failure to correct for these timing errors will result in the response being smeared when stacked. Had the system response been measured for every shot these timing errors would have been eliminated in the deconvolution.

Additional processing techniques that tackle random noise have been tested and found to work well. They are:

- New processing techniques

    1. Random noise can be effectively suppressed by using a frequency domain filtering technique such as F-X deconvolution or dynamic S/N filtering to predict the signal which is constant within traces in the same source-receiver pair. Random noise varies between traces and so is unpredictable, subtracting the unpredictable part from the measured signal removes noise leaving only the signal. It has been shown that these techniques preserve the amplitude and shape of the signal whilst significantly reducing random noise.

    2. Selective stacking techniques have been shown to introduce artefacts on low fold data that can be avoided by visually inspecting and killing noisy traces before applying a conventional mean stack. This also prevents the introduction of high frequency noise associated with selective stacking procedures.

A pragmatic processing scheme for recovering an estimate of the earth impulse response is given in Figure 4.18. The timing correction must be applied before applying F-X deconvolution or dynamic S/N filtering, otherwise the signal will not occur at the same time across all traces. A flow chart for an idealised processing flow is given in Figure 4.19. The differentiation step is classified as optional and it may not be necessary if deconvolution can be carried out successfully on the step function. Although this is more unstable than deconvolution of two spike functions, it avoids having to convert back to the step function after deconvolution: this would be required in order to apply equivalent wavefield processing, which is discussed in Chapter 7.
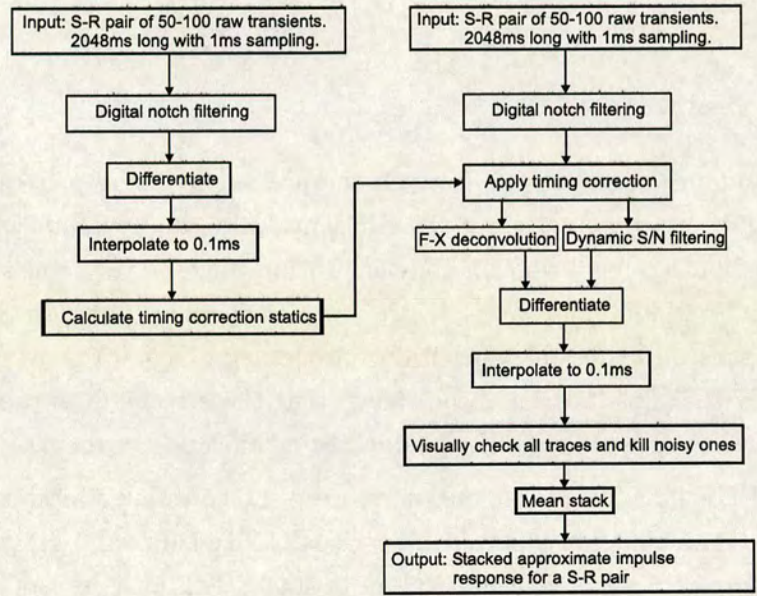
Figure 4.18: Flow chart for the pragmatic approach to data processing applied to the Saint Illiers la Ville data.
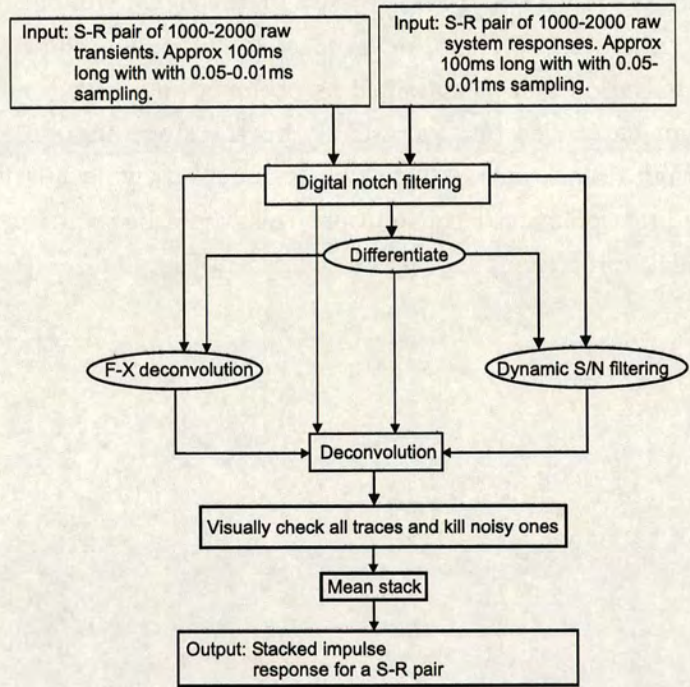
Figure 4.19: Flow chart for the ideal approach to MTEM data processing.

Chapter 5

Sensitivity of different components to a buried resistor

5.1 Introduction

This short chapter provides a modelling analysis of all the electric and magnetic field components measured in the field and their sensitivity to a thin buried resistor. Modelling results show the field strength of the total electric field set up at the surface of the earth around a source dipole as well as individual components of the electric field. Individual transients at various points along a profile are then plotted with and without a resistor present. In addition to assessing whether such a resistor can be detected it is also important to know the size of the field that each component will measure. Analysis of the voltages obtained in this modelling study can indicate if such a response can be seen in real data. The models are kept as simple as possible in order to show the best case scenario for detection of a buried resistor. Responses deemed undetectable in this study will definitely not be detected in real data.

5.2 Expected responses of different components

The Saint Illiers la Ville data is unprecedented in two ways: first the volume of data collected, second the number of different components of the electromagnetic field that were collected. To a certain extent the reason for collecting four different electric field components was simply because it was possible and there is little point in having spare channels in the field and not recording something on them. Although this thesis is not

concerned with a model-fitting approach it is instructive to know which components are likely to contain the largest signal from the sub-surface and which are sensitive to buried resistors.

To get an idea of the largest possible signal that can be recorded for the simple case of a thin buried reservoir, I carried out 1-D modelling of all the components that were measured in the field. The modelling code MODALL (Strack, 1992) was used, the results of testing the code against two other 1-D modelling codes and the analytic solution over a halfspace are given in Appendix B. The results of the tests indicate that all the modelling codes are in agreement with each other and the analytic solution at times greater than 0.05ms. At earlier times the results become unstable and are not in agreement and such early times are therefore not used. The model used comprises a top layer 500m thick with a resistivity of 20 Ωm, underlain by a thin resistor of resistivity 400 Ωm and thickness 25m which represents the reservoir, this is in turn underlain by a halfspace of resistivity 20 Ωm. A second model comprising a uniform halfspace of resistivity 20 Ωm was also computed for comparison with the other model so that it could be seen which components are most sensitive to a thin buried resistor and also at what time and for what offsets a response is expected.

These two models represent the simplest possible case and are calculated in order to get an idea of which components produce the maximum response from a thin buried resistor. The real data will, of course, be influenced by many other layers of slightly varying resistivity above the reservoir as well as two- and three-dimensional structure, not to mention noise. These models represent the absolute best case scenario for detectability of the reservoir. Components that do not produce a large response in this case will certainly not detect the reservoir in real data.

However, components of the electric or magnetic field that are insensitive to the reservoir are not necessarily useless. Features seen in these components can be compared with other field components measured at the same place where a large response from the reservoir is expected. If the features appear on both components they cannot be the result of the reservoir. Also, mapping the distribution of distorted transients using a number of different components is useful in identifying areas of multidimensional earth structure. The results of this modelling are also useful in building confidence into any conclusions that are drawn. Events that appear in the data at the correct time and on components known to be sensitive to the reservoir that are not observed over the reservoir on components known to be insensitive to the reservoir are more likely to be a result of the reservoir than events that appear to contradict the modelling results.

The electric field

The electric field set up around an x-directed grounded wire dipole source is shown in Figure 5.1 in the DC limit for a homogeneous earth. In all the Figures in this chapter the x-axis is the horizontal axis and the y-axis the vertical axis. The dipole nature is clearly mapped out by the arrows denoting the direction of the field at points around the source and the colour indicating the field strength at any point. In a field survey it is of course only a component of the field, not the total field, that is measured. Figure 5.2 shows the pattern of the component of the electric field that would be measured by a 1m receiver electrode aligned with the source in the x-direction, in response to a 1A 1m long source. Figure 5.3 shows the pattern of the component of the electric field that would be measured by a receiver electrode aligned in the y-direction with an x-directed source.

From Figure 5.2 it can clearly be seen that the largest signal is recorded by the E_{xx} and E_{yy} components. These correspond to an x-directed receiver at an angle ϕ of 0 or 90 degrees to the source respectively. The minimum amplitude occurs at an angle of 54.7 degrees to the source. In the presence of a uniform halfspace the response of the E_{xx} and E_{yy} components is identical as shown in Figures 5.4-5.8 (left). In contrast, the response measured by receivers that are perpendicular to the source shown in Figure 5.3 is maximum at an angle of 35.3 degrees to the source and a minimum at an angle of 0 or 90 degrees. Indeed, in the presence of a uniform halfspace or any 1-D layered structure, the response from the E_{xy} and E_{yx} components recorded at 0 or 90 degrees to the source is zero as shown in Figures 5.4-5.8 (left) . All decay voltages that are measured perpendicular to the transmitter wire are due to two- or three-dimensional structure.

It can be seen by comparing the maximum field strength in Figures 5.2 and 5.3 that the in-line field maximum is about 5 times greater than the cross-line field maximum. Electric field components were recorded at Saint Illiers la Ville for the maximum in-line configurations and the minimum cross-line configurations.

As can be seen from Figures 5.4-5.8 for an azimuthal angle ϕ=0 or 90 degrees between the source and receiver, only the configuration of source and receiver aligned in the same direction is sensitive to a buried resistive layer. When the source and receiver are perpendicular to one another at an azimuthal angle ϕ=0 or 90 degrees the 1-D response is zero.

It can be seen from Figure 5.4 that that at 500m offset the E_{xx} component in the presence of the reservoir is the same as the halfspace response while the E_{yy} response is slightly different and the E_{xy} and E_{yx} components are zero at all offsets. At an offset

of 1000m, shown in Figure 5.5, in response to a buried resistor, the E_{xx} component is increased relative to the halfspace response, while the E_{yy} response is decreased relative to the halfspace response. In addition, at an offset of 1500m or more, the E_{yy} response in the presence of a buried resistor actually decreases below the initial value before increasing; this effect can be seen in Figures 5.6-5.8 (left). The relative difference in amplitude between the halfspace response and the buried resistor response increases with increasing offset. However, the absolute size of the difference decreases with offset and so may actually be undetectable at large offsets as noise masks the response and more stacking is needed.

In all the results shown in this chapter a source dipole moment of 1 Am is used measured by a receiver 1m long. The voltage calculated for a realistic situation can be estimated by multiplying the modelled values by the source length, receiver length and source current.
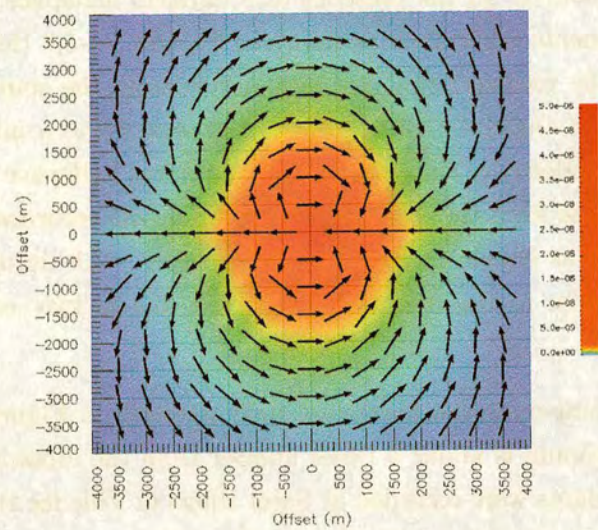
Figure 5.1: The total vector electric field pattern produced by an x-directed dipole source. The arrows denote the direction of the field at any point around the source and the colour scale the field strength.
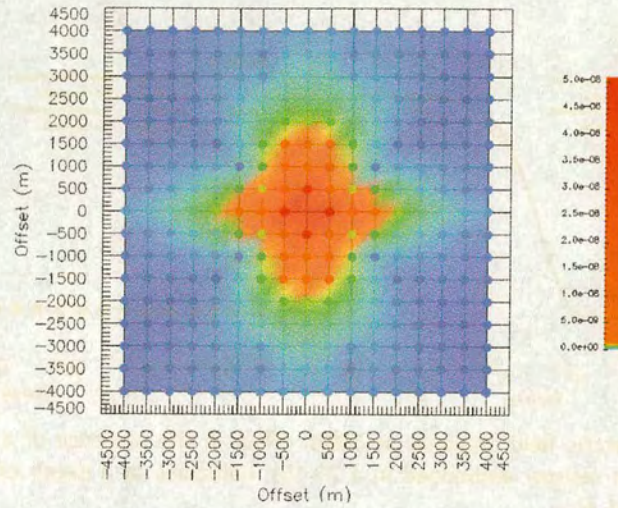
Figure 5.2: The electric field pattern produced by an x-directed dipole source recorded with x-directed receivers. The circular points denote the data values from which the plot was produced.
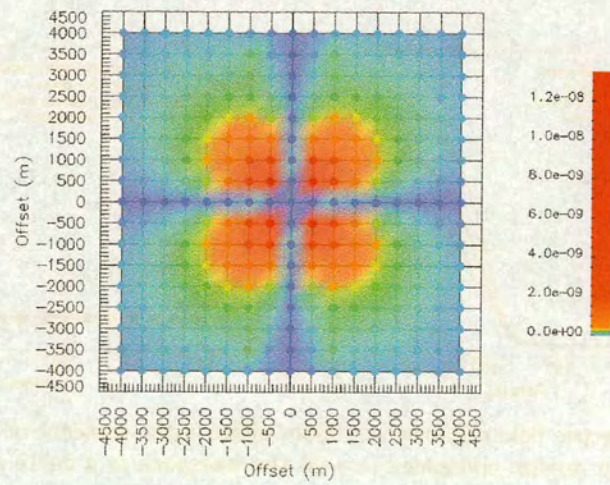
Figure 5.3: The electric field pattern produced by an x-directed dipole source recorded with y-directed receivers. The circular points denote the data values from which the plot was produced.

107
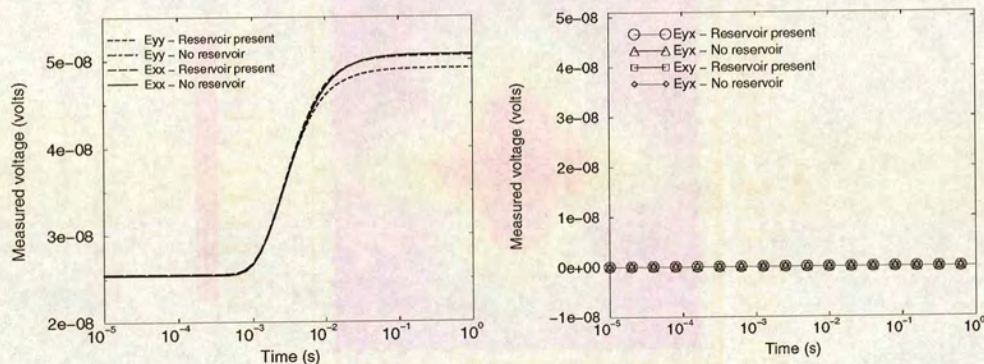
Figure 5.4: The electric field response at 500m offset in the presence of a 20 Ωm halfspace, and a 25m thick 400 Ωm resistor embedded in a 20 Ωm halfspace at a depth of 500m. Left: E_{xx} and E_{yy}. Right: E_{xy} and E_{yx}.
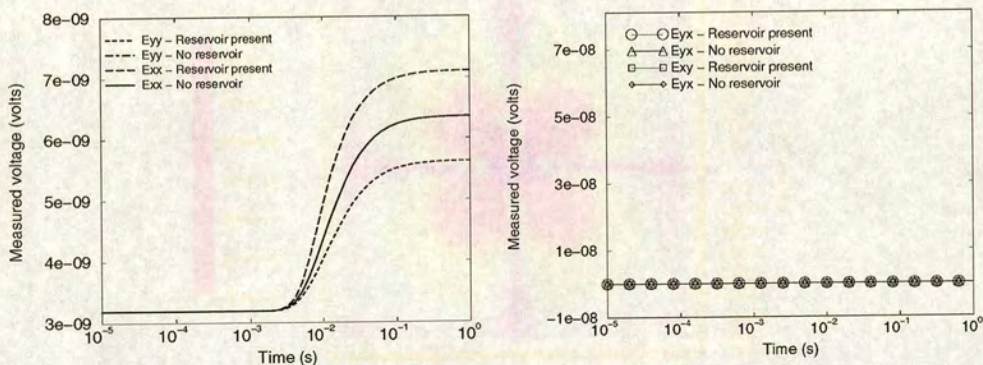
Figure 5.5: The electric field response at 1000m offset in the presence of a 20 Ωm halfspace, and a 25m thick 400 Ωm resistor embedded in a 20 Ωm halfspace at a depth of 500m. Left: E_{xx} and E_{yy}. Right: E_{xy} and E_{yx}.
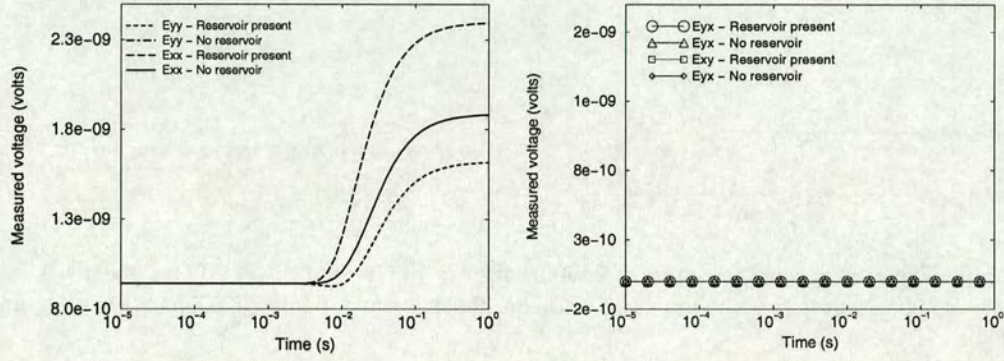
Figure 5.6: The electric field response at 1500m offset in the presence of a 20 Ωm halfspace, and a 25m thick 400 Ωm resistor embedded in a 20 Ωm halfspace at a depth of 500m. Left: E_{xx} and E_{yy}. Right: E_{xy} and E_{yx}.

Figure 5.7: The electric field response at 2000m offset in the presence of a 20 Ωm halfspace, and a 25m thick 400 Ωm resistor embedded in a 20 Ωm halfspace at a depth of 500m. Left: E_{xx} and E_{yy}. Right: E_{xy} and E_{yx}.

109

Figure 5.8: The electric field response at 2500m offset in the presence of a 20 Ωm halfspace, and a 25m thick 400 Ωm resistor embedded in a 20 Ωm halfspace at a depth of 500m. Left: E_{xx} and E_{yy}. Right: E_{xy} and E_{yx}.
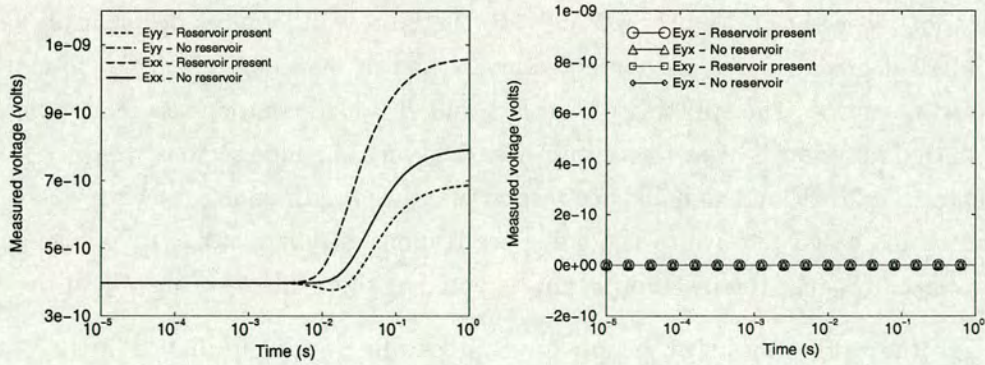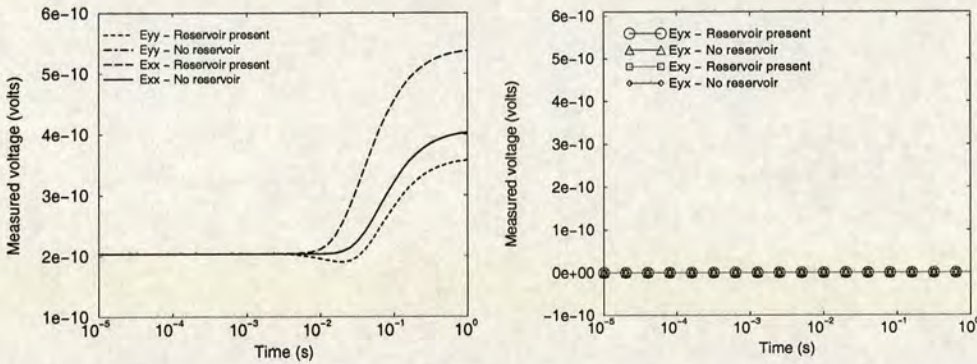
Differences

The results shown for the in-line and cross-line components at an angle of 0 or 90 degrees to the source shown in Figures 5.4-5.8 show the responses for the electric field components that were measured at Saint Illiers la Ville. In addition, it is worth studying the response of a buried resistor at every position around the source to see if there is another source-receiver geometry that is optimum for detecting thin buried resistors. The difference between the halfspace response and the buried resistor response for an x-directed source and an x-directed receiver is shown in Figure 5.9, while the difference for an x-directed source and a y-directed receiver is shown in Figure 5.10. As with the total responses shown in Figures 5.2 and 5.3, the largest differences occur at an angle of 0 and 90 degrees for the x-directed receivers and at 35.3 degrees to the source for y-directed receivers. The splitting of the E_{xx} and E_{yy} field components in response to a thin buried reservoir is clear to see in Figure 5.9, with the blue regions showing where the response is less than the halfspace response and the red regions showing where the response is increased relative to the halfspace response. This positive difference splits into two lobes because the reservoir is not detected at short offsets in the E_{xx} direction.

Therefore the optimum survey setup for sources and receivers aligned in the same direction is to have the receivers at an angle of 0 and 90 degrees (this is the angle ϕ in Figure 3.3), the greatest difference being between the E_{xx} and E_{yy} components, which respond to the resistor in different ways. To record these components on a single line the source and receiver must be rotated 90 degrees to record the other component. For the case of an x-directed source and y-directed receivers the optimum layout for detecting resistors is to have the receivers at an angle, ϕ, of 35.3 degrees to the source;

110

the E_{xy} and E_{yx} responses are identical for a 1-D earth.

The splitting of the E_{xx} and E_{yy} components is also seen in the presence of a conductor, Figure 5.11 shows the difference in the response between a 20 Ωm halfspace and a 25m thick 1 Ωm conductor buried at a depth of 500m in a 20 Ωm halfspace. Now the E_{xx} response is reduced relative to the halfspace response while the E_{yy} response is increased, the opposite to what is seen in the presence of a resistor. The difference in behaviour of the E_{xx} and E_{yy} components may be understood by considering two different modes of current flow generated by the dipole source. The E_{xx} and E_{yy} components each contain poloidal and toroidal mode contributions and whether a particular 1-D structure increases or decreases the amplitude of the measured electric field depends on the balance between the 2 modes. The splitting of these two components is quite obvious in a model as simple as this, but in more complicated realistic resistivity profiles the splitting is far more complicated. This behaviour has been known about for many years in 'frequency domain' marine EM and is discussed in detail by MacGregor (1997).

In order to see where the response of the reservoir will be detected for the processing scheme applied to the real data, the transients in Figures 5.4-5.8(left) were differentiated and the difference taken between the reservoir model and the halfspace model and also between the E_{xx} and E_{yy} components in the presence of the buried reservoir. The results of this are shown in Figure 5.12. It can be seen from these results that, when taking the difference of the derivative, the in-line E_{xx} response is bigger than the E_{yy} response, although the biggest difference is seen when the difference between the E_{xx} and E_{yy} component is taken. Any differences seen in the real data that are due to changes in the reservoir will be very small because differences are being taken between two transients in which the reservoir is present, the difference being due to a change in the amount of gas in the reservoir and not to there being a reservoir or not. However, Figure 5.12 does show where any response from the reservoir will be seen for particular offsets after data processing, for example, for the E_{xx} component at 1000m offset the maximum response from the reservoir is seen at 4ms, the effect of the reservoir is first seen at about 2ms and is not present after about 15ms. These values can be used as a rough guide as to where the effect of the reservoir should be expected.

Figure 5.9: Difference plot of the buried resistor response minus the halfspace response for an x-directed source and x-directed receivers. The circular points denote the data values from which the plot was produced.
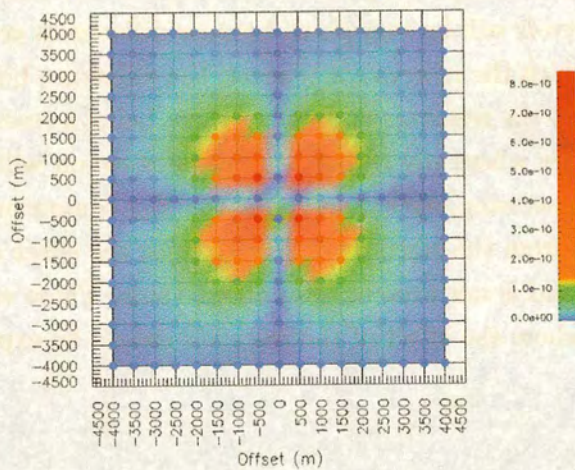
Figure 5.10: Difference plot of the resistor response minus the halfspace response for an x-directed source and y-directed receivers. The circular points denote the data values from which the plot was produced.

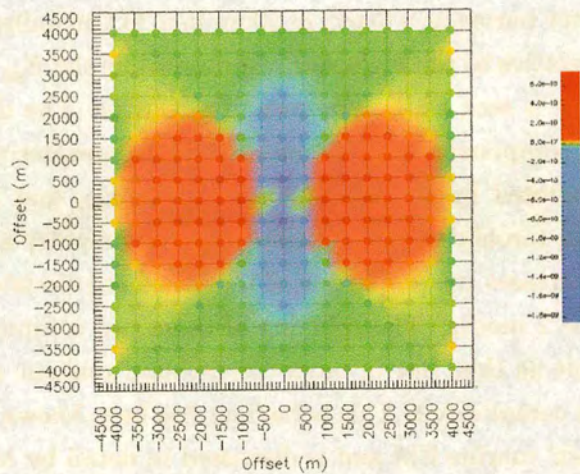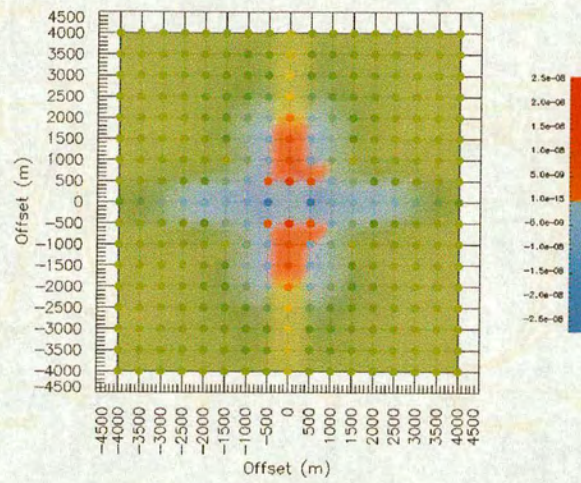Figure 5.11: Difference plot of the buried conductor response minus the halfspace response for an x-directed source and x-directed receivers. The circular points denote the data values from which the plot was produced.
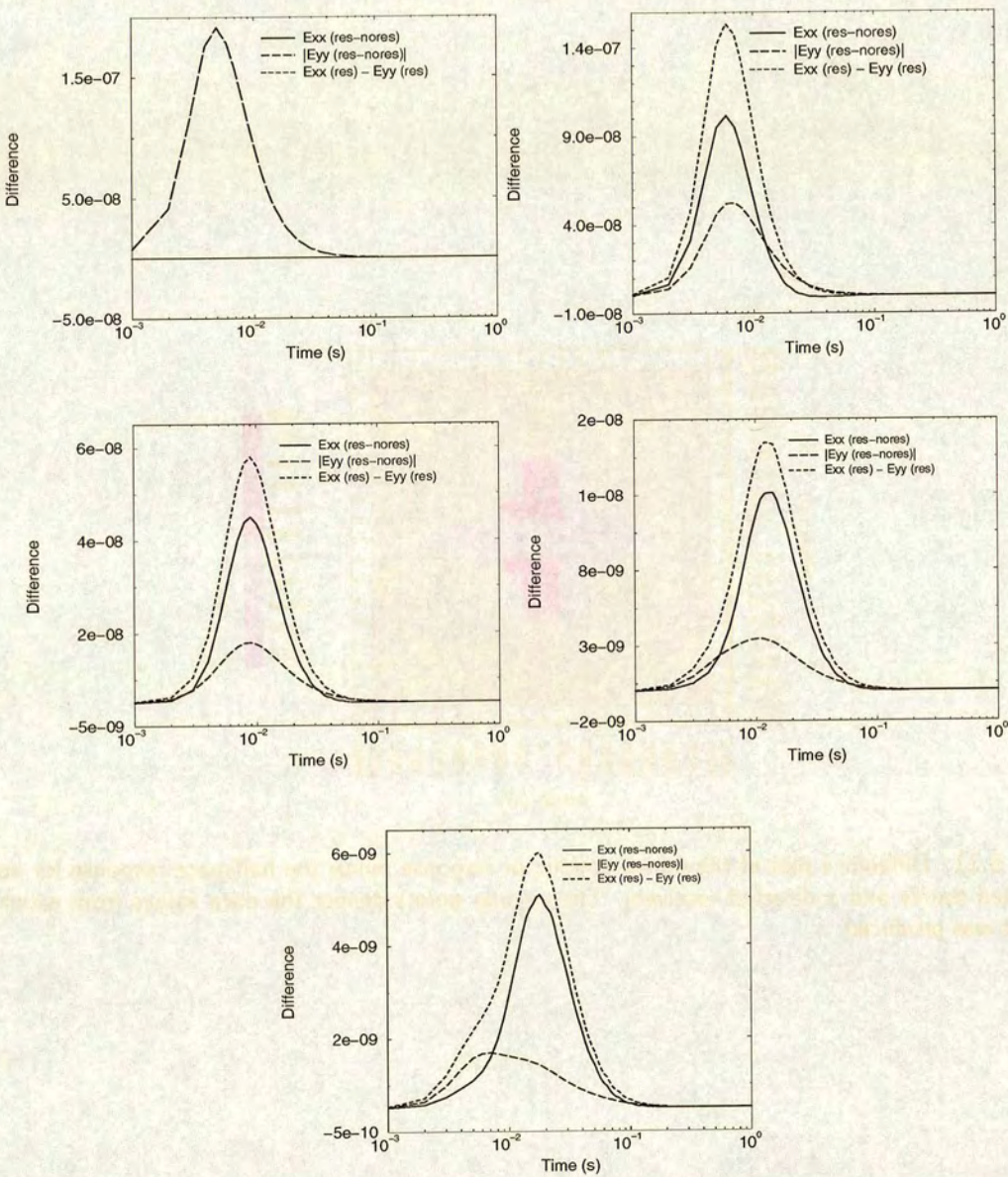
Figure 5.12: Differences in the electric field due to a buried resistor. **Top:** Left-500m offset. Right-1000m offset. **Middle:** Left-1500m offset. Right-2000m offset. **Bottom:** 2500m offset.

The magnetic field

The pattern of the vertical component of the magnetic field set up around an x-directed grounded wire dipole source is shown in Figure 5.13. Receivers aligned with the y and x-axis record the H_{yz} and H_{xz} component of the magnetic field respectively. Transients recorded along these axes are shown in Figure 5.14 left and right respectively. As with the electric field components E_{xy} and E_{yx} the H_{xz} component of the magnetic field is zero in the presence of a uniform halfspace. There is a response on the H_{yz} component but as can be seen from Figure 5.14 (left) the vertical component of the magnetic field is insensitive to a thin resistive layer at all offsets. The magnetic field is therefore of no use in detecting resistive hydrocarbons. However, it can be used to identify distortions in the data by spatially correlating effects seen on the E_{xx} or E_{yy} data with those seen on magnetic field data at the same location. Such effects cannot be due to a buried resistor.
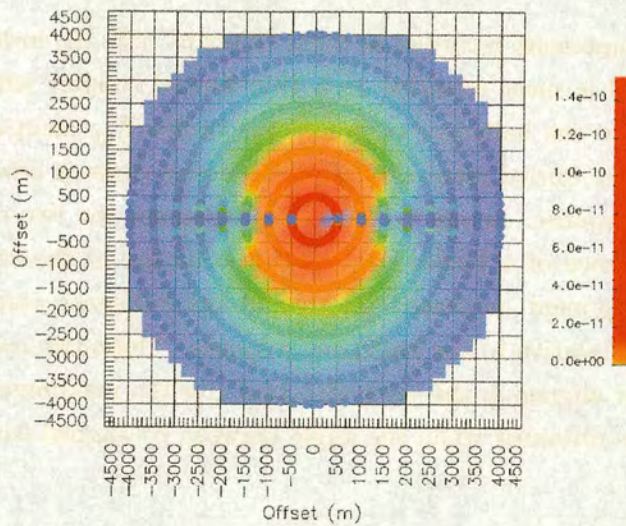
Figure 5.13: The vertical magnetic field pattern produced by an x-directed dipole source. The circular points denote the data values from which the plot was produced.

115
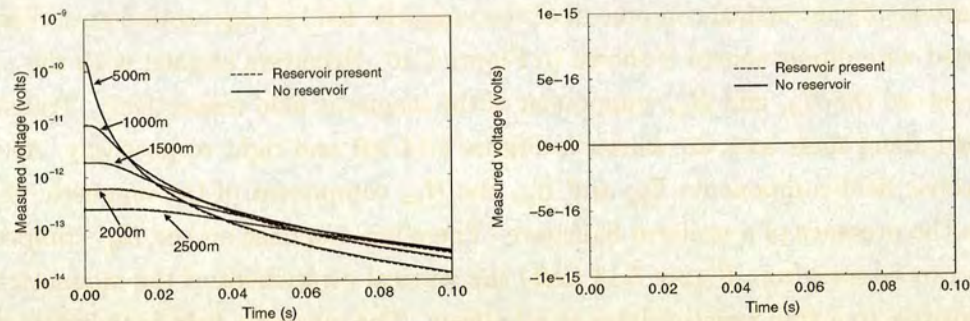
Figure 5.14: Response of the vertical magnetic field with and without a high resistivity reservoir present for various offsets. Left: H_{yz}. Right: H_{xz}. The recording position of each trace is given by the black squares in Figure 5.13.

5.3 Summary

Of all the field components recorded at Saint Illiers la Ville the in-line E_{xx} component of the electric field is most sensitive to a thin buried resistor with the decay curve increased relative to the halfspace response, the in-line E_{yy} component is the second most sensitive to the buried resistor but the the decay curve is now decreased relative to the halfspace response. In the presence of a halfspace the two components are the same. In the presence of a buried conductor the nature of the splitting is different, with the E_{xx} component decreased relative to the halfspace response and the E_{yy} response increased relative to the halfspace response. These two configurations for the source and receiver aligned in the same direction give the maximum response, with the minimum response obtained when the angle between co-aligned source and receiver is 54.7 degrees.

The cross-line components E_{xy} and E_{yx} are not sensitive to a buried resistor when the azimuthal angle ϕ between the source and receiver is 0 or 90 degrees (this is what was measured in St.Illiers la Ville), indeed the 1-D response is zero. The maximum response occurs when the angle, ϕ, between the source and receiver is 35.3 degrees although this is only a fifth the size of the in-line maximum. In a 1-D earth these two components are identical, so differences in these components can indicate the presence of non 1-D structure

The vertical component of the magnetic field is insensitive to a thin buried resistor, as with the cross-line electric field the H_{xz} response is zero for a halfspace, in the

116

presence of a buried resistor this component is still zero. The H_{yz} component is similarly unresponsive to the resistor, although this component does record a response in the presence of a halfsapce, the response is the same when the resistor is present.

Chapter 6

Results of Data Processing

6.1   Introduction

As discussed in Chapter 4 the data collected at Saint Illiers la Ville were far from
ideal and many improvements can be made in any future system. However, in spite of
this, the pragmatic approach to data processing has been applied here in an attempt
to extract some useful information from the data. The results from the modelling in
Chapter 5 indicate that the in-line E_{xx} component of the electric field will be most
responsive to the reservoir. For this reason this component is studied in this chapter in
detail. Results are presented in the form of common-offset sections of the derivative of
the approximate impulse response and differences in the approximate impulse response
between the two datasets. Distortions in the data are studied and their distribution
mapped. Results from other components are discussed briefly and the results seen
in the E_{xx} data explained by convolving synthetic data with a more realistic source
function.

6.2   Analysis of the data

The in-line E_{xx} data can be split into three basic categories, namely good relatively
noise free data that rises smoothly from zero to a constant dc level, relatively noise free
data that does not rise smoothly from zero but is somehow distorted with the transient
crossing the zero-level, and finally very noisy data that is rendered useless by the very
low signal-to-noise ratio. This section studies the distribution of these various types of
transients as a function of position and offset.

119

Distribution of good and noisy data

The distribution of good and noisy data as a function of position along the profile and S-R offset is shown in Figure 6.1. It can be seen that for the data collected in both 1994 and 1996 there are almost no good data present beyond an offset of 2000m. In order to get reasonable data at offsets greater than 2000m more transients have to be stacked than was possible for these data. Although it was originally intended to measure the same data in the 1996 survey as the 1994 survey not all of the same source and receiver locations were occupied during the second survey. The amount of the 1994 and 1996 data collected at each offset is shown in Figure 6.2; it can be seen that there was almost no data recorded at offsets of less than 750m in 1996. This was because the time and money available for this survey was less and so data were only recorded at offsets believed to be sensitive to the reservoir. Offsets between 750m and 1500m have the greatest coverage of data recorded in both surveys, the result of processing these data will be studied in more detail here.
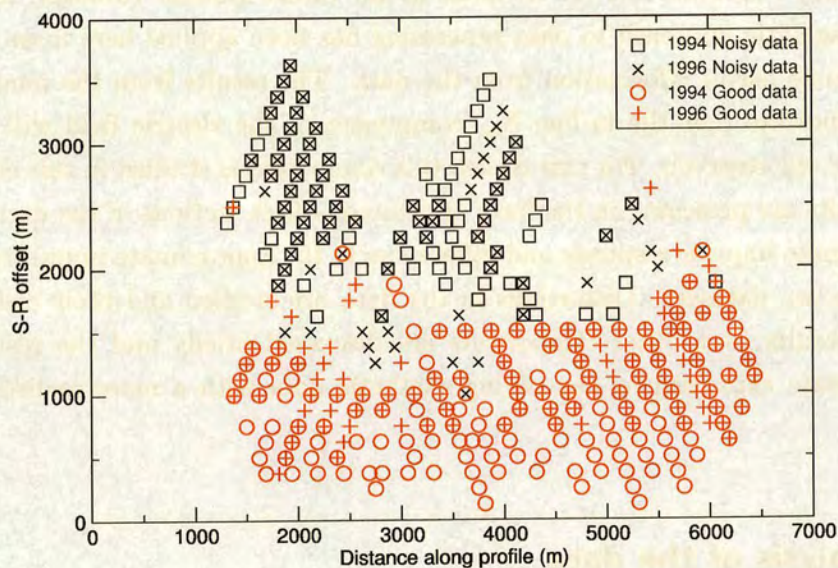
Figure 6.1: The distribution of good and noisy in-line E_{xx} data.
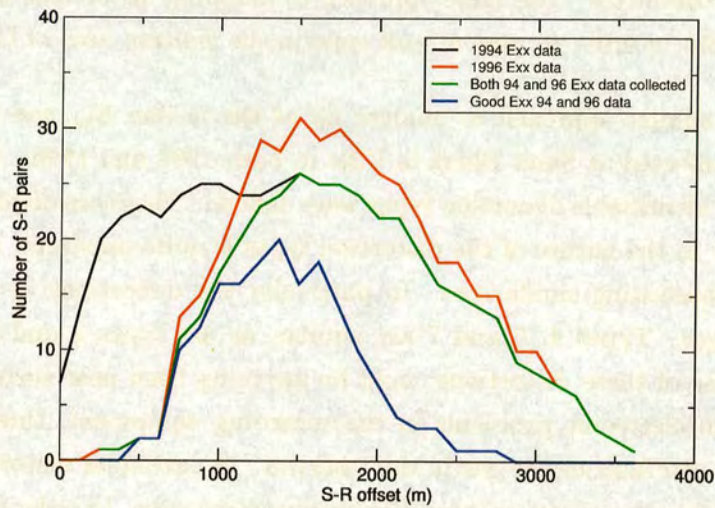
Figure 6.2: The availability of E_{xx} data from 1994, 1996 and both years

Distorted data

Transients recorded in the field that do not conform with the type of signal expected from theory are known as distorted transients (Strack, 1992, p102). Many transients collected in the field do not display the simple form as shown in Figure 2.6 that is predicted by 1-D theory. A characteristic of many distorted transients is that the signal crosses the dc level; these signals are called *reversals* and are theoretically impossible in layered earth structures; they are indicative of 3-D structure or contamination by cultural noise such as pipes.

'*Where reversals occur one should carefully eliminate all impossible options and pinpoint the conductivity anomaly by getting as much field data as possible*'

(Strack, 1992)

Very little was known about what caused these distortions until advances in computing power in the past 20 years made three dimensional modelling of the electromagnetic field in the earth possible. Using these new modelling codes the effect of various two and three dimensional structures and polarizable bodies were able to be studied and many of the distortions seen in real data were recreated numerically. The spatial mapping of distorted transients was used by Stoyer & Damron (1986) to map a fault zone in Milford

121

Valley, Utah, and the distorted responses reproduced using physical scale modelling and 3-D modelling. They also reproduced other distortions by modelling a buried pipe as a long cylindrical conductor. The same approach to mapping distortions was carried out by Stephan (1989) in order to map a fault zone in the Haltern area of Germany.

I have taken a similar approach to analyse all of the in-line E_{xx} and cross-line E_{xy} and E_{yx} data collected at Saint Illiers la Ville in both 1994 and 1996. A total of nine different clearly identifiable distortion types were defined. These are displayed in Figure 6.3. The variety in the nature of the distortion types is quite apparent, however, there are also some interesting similarities. In particular the distortions in types 3 and 5 are mirror images. Types 4, 5 and 7 are similar, as are types 2 and 6 and types 1 and 9. The cause of these distortions could be anything from near surface conductors such as pipes to electronic problems in the recording equipment, three dimensional structures such as a fault or the gas in the reservoir. In particular distortions are often associated with the edge of two or three dimensional structures. In order to gain a better understanding of what might be the cause of the distortions, their spatial distribution was plotted as a function of position and offset in order to see if any patterns are present. Figure 6.4 shows the distribution as a function of source-receiver offset and distance along the profile. It can clearly be seen that the distribution of the distortions as a function of position along the profile has a definite pattern. The distortions form two distinct clouds centered around 2900m and 5000m; these also happen to be the known edges of the gas reservoir. It is also interesting to note that some distortion types are found exclusively on one side of the reservoir while others can be seen on both sides. Interpreting distorted transients as being due to a particular structure is very risky, as noted by many authors. Figure 6.5 shows a plot similar to Figure 6.4 but for the E_{xy} and E_{yx} data. The distribution of distortions in these components is quite different from that seen in the E_{xx} data, as might be expected. As was shown in section 5.2, the response measured by these components is zero in a 1-D earth. Only offsets up to 1250m could be studied, as beyond this the signal in these components was lost in the noise. It is likely that the distortions seen in these data are due to near-surface effects as there appears to be no clustering or obvious pattern.

Distortions caused by cross-talk between channels in the electronics of the recording system and interference from the timing trigger were studied by Helwig *et al.* (1995) with some of the reversals seen on field data being reproduced in the laboratory. Identification of these distortions can be done by comparing the same data from 1994 and 1996; distortions generated by the electronics will not be present in both sets of data. An analysis of whether the problem of cross-talk was limited to certain receiver boxes could not be studied, as the survey log sheets do not specify which box was used to
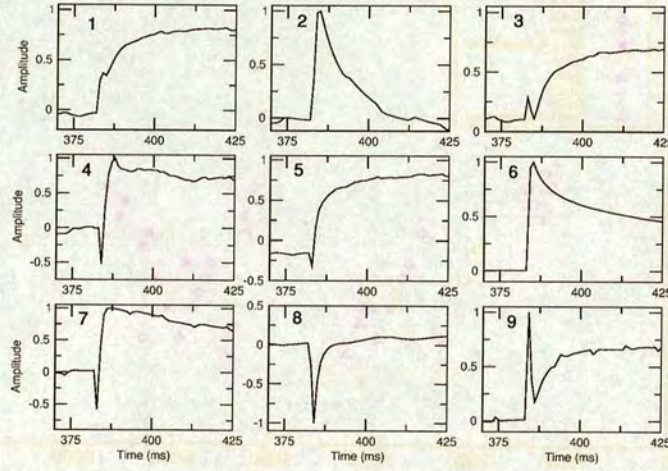
Figure 6.3: The 9 different types of distortion identified in the in-line and cross-line data.

record the data. A clear example of distortions generated by electronics and not geology are the two cases of distortions that alternate polarity across every transient in a source-receiver pair, also the small clustering of five type 2a distortions are likely to be due to a problem in a single receiver box (type 2a distortions are the same as type 2 but larger in amplitude and narrower in time); these are plotted in Figure 6.4. The type 2 and type 8 distortions may also be due to the equipment as they are so unlike the theoretical step response. The identification of distorted transients is a very laborious task that is difficult to automate due to the wide variety of different types of distortion present. While very large peaks are easily identified in an automated process, more subtle distortions such as type 6 are more difficult to identify without looking at the data. The clustering of the distorted E_{xx} transients around the reservoir edges suggests the resistivity discontinuity at the edge of the reservoir may distort the data. The clustering is not very tight around the edges but this may be due to the fact that the reservoir is at a depth of around 500m. It is also very likely that some distortions in the data are caused by effects generated in the near-surface, such as pipes. The identification and removal of distorted data is a crucial part in any processing flow as they will seriously affect any interpretation if included.
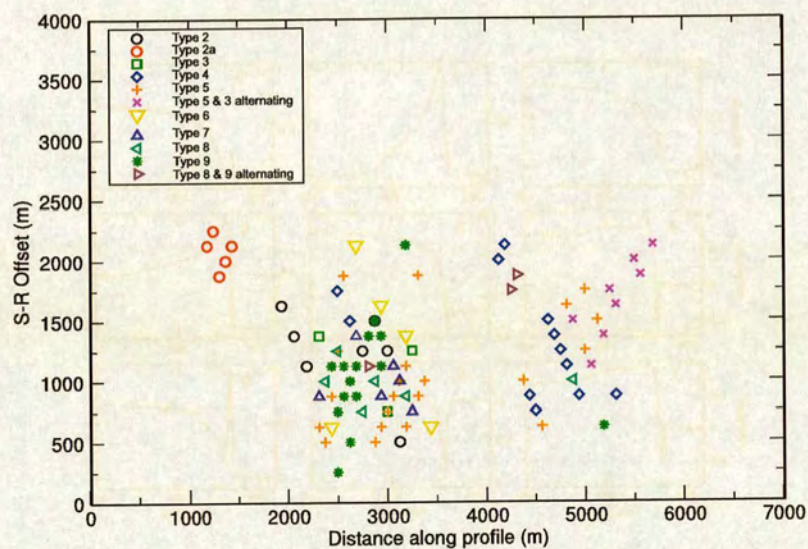
Figure 6.4: Distribution of the 9 distortions as a function of offset and distance along profile in the E_{xx} data (Type 2a distortions are the same as type 2 but larger in amplitude and narrower in time).
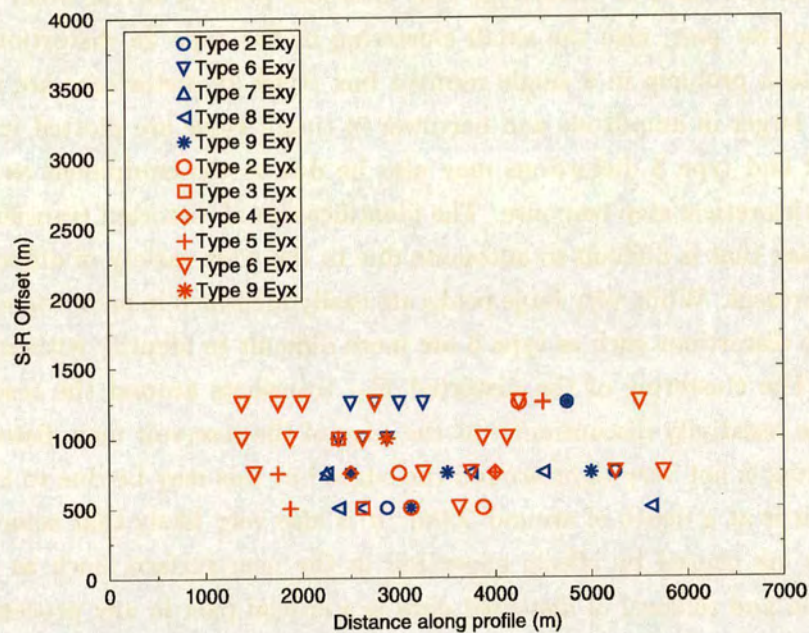
Figure 6.5: Distribution of the 9 distortions as a function of offset and distance along profile for the E_{xy} and E_{yx} data.

Repeatability

Repeatability is here defined to be the ability to measure the same result in the same place at two different times. If two results are identical the repeatability is 100%. One of the goals of the project was to detect the movement of gas within the reservoir between the two surveys and a repeatability of 99% was set as the minimum required to see such differences if data were collected when the gas in the reservoir was maximum and minimum (Ziolkowski *et al.*, 1998a). As mentioned in Chapter 4 this was not the case and the change in response between the two surveys was calculated to be about 0.5%. I studied the repeatability of different components of the data by taking the difference between the stacked approximate impulse response for data, where both the source and receiver are outside the reservoir. Any differences seen in these data will give an idea of the repeatability possible in measurements over the reservoir and will indicate whether the repeatability is good enough to detect differences in the reservoir. Figure 6.6 shows the difference for E_{xx} data at offsets of 750, 1000 and 1500m offset and E_{yy} data at an offset of 1000m. It can be seen that the repeatability of the E_{xx} data at 750 and 1000m is about 99.5 %, possibly even higher for the 750m data. The repeatability of all these components is greater than 99%. These results are very encouraging, as they suggest that the detection of changes in the reservoir may still be possible. Figure 6.7 shows a similar plot for the magnetic field and the cross-line electric field components at 1000m offset. These components are known from the results presented in Chapter 5 to have a very small response, and it can be seen that the repeatability is very poor, particularly for the cross-line components. These components will certainly not detect any changes in the reservoir and the large differences present between data that are supposed to be the same suggests that even the signal is not much bigger than the noise.
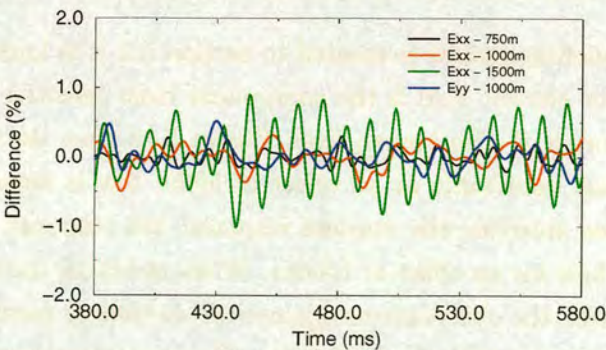
Figure 6.6: Differences in the in-line electric field data taken outside the reservoir.

125
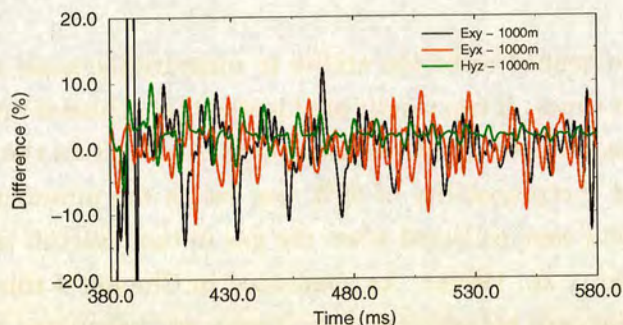
Figure 6.7: Differences in the cross-line electric field and magnetic field taken outside the reservoir.

6.3   In-line E_{xx} data

The processing flow shown in Figure 4.19 has been applied to all the E_{xx} data for both 1994 and 1996 up to an offset of 2250m. The equivalent wavefield of the data cannot be used to recover resistivity because of timing errors which prevent the time origin being known. The coverage available in the CMP domain is also very poor, which means there is not enough cover. As a result, the recovered stacked approximate earth impulse responses have been sorted into common-offset sections. Common-offset sections are a good way of displaying the results, as different offsets penetrate to different depths in the subsurface. Also for a given section a 1-D earth would give the same response across the whole profile. Analysis of the spatial and temporal variation of the response when studied as a function of offset can therefore be used to detect changes in the subsurface with the offset at which the effects appear controlled by the depth of burial of the anomalous body. A similar approach has been applied in the past by Garg & Keller (1986). The electromagnetic imaging method of Tasci & Jordan (1996) looks at spatial and temporal changes within a cross-section to identify if a recognizable pattern is present which has been observed over hydrocarbon accumulations in a similar setting.

From the simple modelling results presented in section 5.2 it is known that the in-line E_{xx} component of the electric field is the component most sensitive to the presence of a thin buried resistor; it is also known from Figure 5.12 that the effect of a resistor buried at 500m is not detectable at an offset of 500m but is detectable at an offset of 1000m. Also, when studying the impulse response, the response of the resistor is a maximum at about 5ms for an offset of 1000m. When studying the results that follow, it is important to check the observations against the modelling results to see if what is seen is in general agreement with the modelling. The modelling is very simplified but it is still useful in determining where and when a change in response is likely to be seen.

Figure 6.8 shows three common-offset sections of the derivative of the approximate impulse response from the 1994 data [1]for offsets of 375m (top), 500m (middle) and 625m (bottom). The derivative of the approximate impulse response is plotted because the impulse response is always positive; for display purposes differences show up best when plotting positive and negative values. A cross-section of the reservoir in relation to the distance along the profile is displayed beneath the bottom section so that correlation of events seen in the data and the location of the reservoir can be made at a glance. The results appear to be fairly uniform across the profile for the 375m and 500m sections. This is a reassuring sign, as the responses in these sections have travelled only in the first few hundred metres of the subsurface and their uniformity suggests that the shallow subsurface across the whole profile is quite uniform, which will make identification of any deeper responses from the reservoir easier to identify, knowing that near-surface effects are minimal. The 625m section is interesting as it is the shortest offset at which the reservoir is likely to be detected and a slight disturbance can be seen at a time of about 3.5ms at a distance of between 3500m and 4500m along the profile. This region coincides with the shallowest part of the reservoir, as can be seen from the cross-section at the foot of the figure. Because this reservoir is not a natural hydrocarbon reservoir there is no possibility that over geological time the sub-surface resistivity structure above the reservoir has been altered by chemical alteration due to the upward migration of hydrocarbons (it has been used to store gas for less than three decades) as was discussed in section 2.4.

Figure 6.9 shows common-offset sections of the derivative of the approximate impulse response at an offset of 750m for the 1994 data (top) and 1996 data (middle). The bottom plot is the difference $Diff_{xx}^{E(94-96)}$ between the approximate earth impulse response for the same source-receiver pairs for 1994 $\bar{G}_{xx}^{E(94)}(x_s, x_r, t)$ and 1996 $\bar{G}_{xx}^{E(96)}(x_s, x_r, t)$, where $\bar{G}_{xx}$ denotes the stacked approximate earth response as defined in equation 4.5.

$$Diff_{xx}^{E(94-96)} = \bar{G}_{xx}^{E(94)}(x_s, x_r, t) - \bar{G}_{xx}^{E(96)}(x_s, x_r, t). \qquad (6.1)$$

It can immediately be seen from this figure that there is clearly an event present over the middle of the reservoir and it is very similar in both the 1994 and 1996 data. The location of this event is the same as the smaller disturbance that was seen on the 625m common-offset section shown in Figure 6.8 but is larger in amplitude. Outside the reservoir the data appear to be uniform. Three of the traces that make up the

---

[1]No data was collected at any of these offsets in the 1996 survey.

section of 1996 data shown in Figure 6.9 are shown in Figure 6.10. One trace is from a distance along the profile of 2000m for which both the source and receiver are outside the reservoir, one is from a distance of 3400m along the profile at the northern edge of the reservoir and one trace is from a distance of 4000m along the profile with both the source and receiver over the reservoir.

The left hand plot in Figure 6.10 is of the approximate impulse response and the plot on the right is the derivative of the approximate earth impulse response. It can be seen that the nature of the response changes quite clearly on the reservoir, over the edge of the reservoir and off the reservoir, with the response near the edge being a transition between the two other cases.

The plot of the difference section shown in the bottom of Figure 6.9 is interesting, as a small change is seen between the two surveys and the positive change is consistent with there being more gas in the reservoir in 1994 than in 1996. It is quite surprising that any change should be seen between the two datasets given the small change in gas content between the two surveys. Lack of any other differences between the two datasets outside the reservoir is very encouraging, again illustrating how repeatable the data are. The greater the repeatability of the data in places where no changes in rock resistivities are taking place, the more likelihood there is of detecting changes where they are taking place, for instance in the reservoir.

Figure 6.11 has the same layout as Figure 6.9, but the data are for an offset of 875m. It can again be seen that there is an event present at about 4ms in both the 1994 and 1996 data. The event is larger in amplitude then that seen in the data at 750m offset and also extends further across the length of the profile. The plot of the difference shown at the bottom of Figure 6.11 is not as encouraging as the one for an offset of 750m, with differences of both polarity present and no real correlation with the reservoir. In looking at the difference section it is important to remember that it is not a straight difference of the two sections displayed above it but a difference of these two sections before they were differentiated. As a result, some differences seen in the difference section may not appear to correlate exactly with differences seen in the two common-offset sections displayed above it.

Figure 6.12 again has the same layout as the previous figures but the data are now for an offset of 1000m. It can be seen that a red event is again present at about 4ms in both the 1994 and 1996 data and that it occurs over the reservoir. Interestingly, the shape of this event appears to be quite different for the 1994 and 1996 data but the shape of the blue event around it is almost identical for both years. A response for the same source-receiver pair from 1994 and 1996 outside the reservoir at a distance along
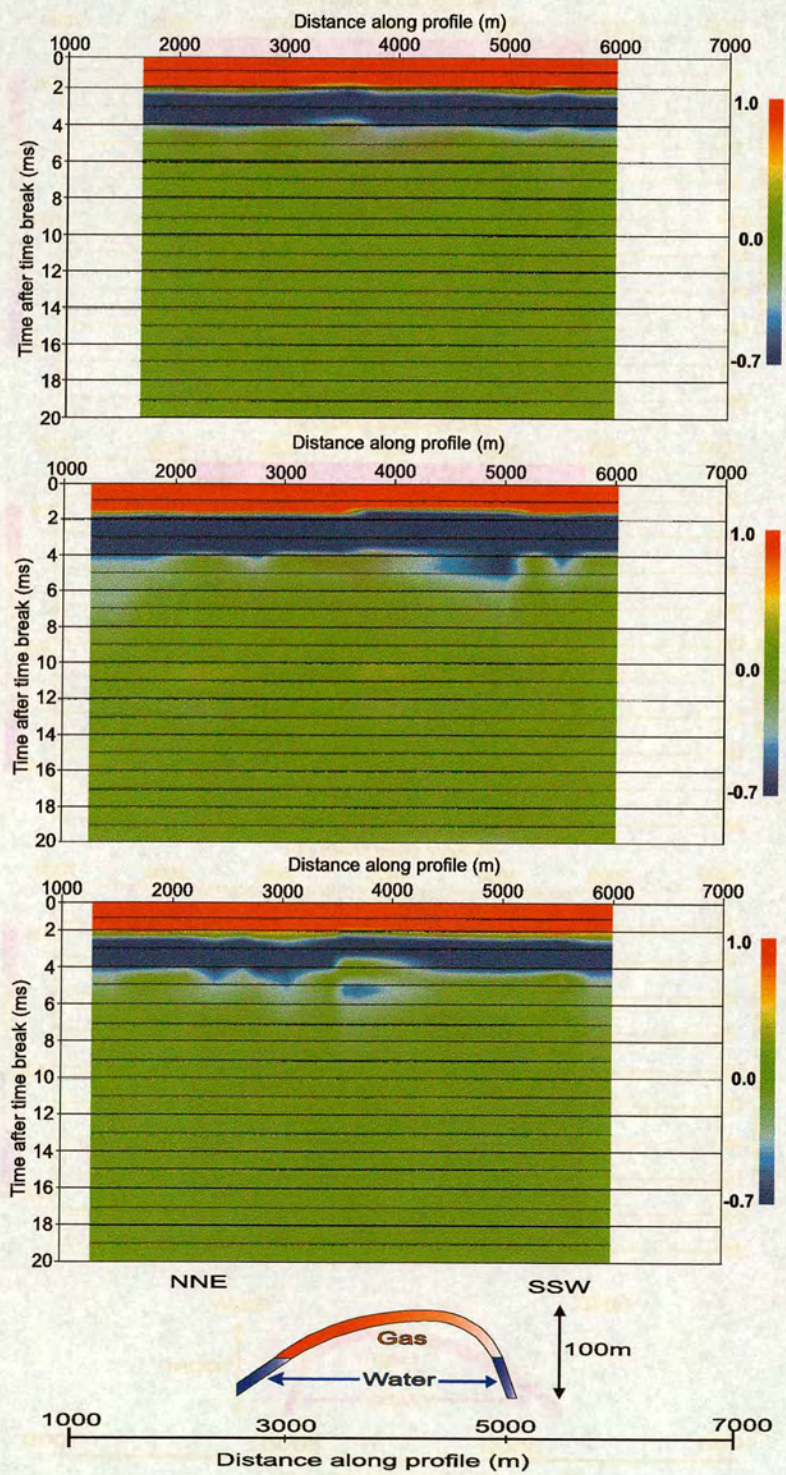
Figure 6.8: E_{xx} common-offset sections of the derivative of the approximate impulse response for offsets of 375m (top) , 500m (middle) and 625m (bottom) from the 1994 data.
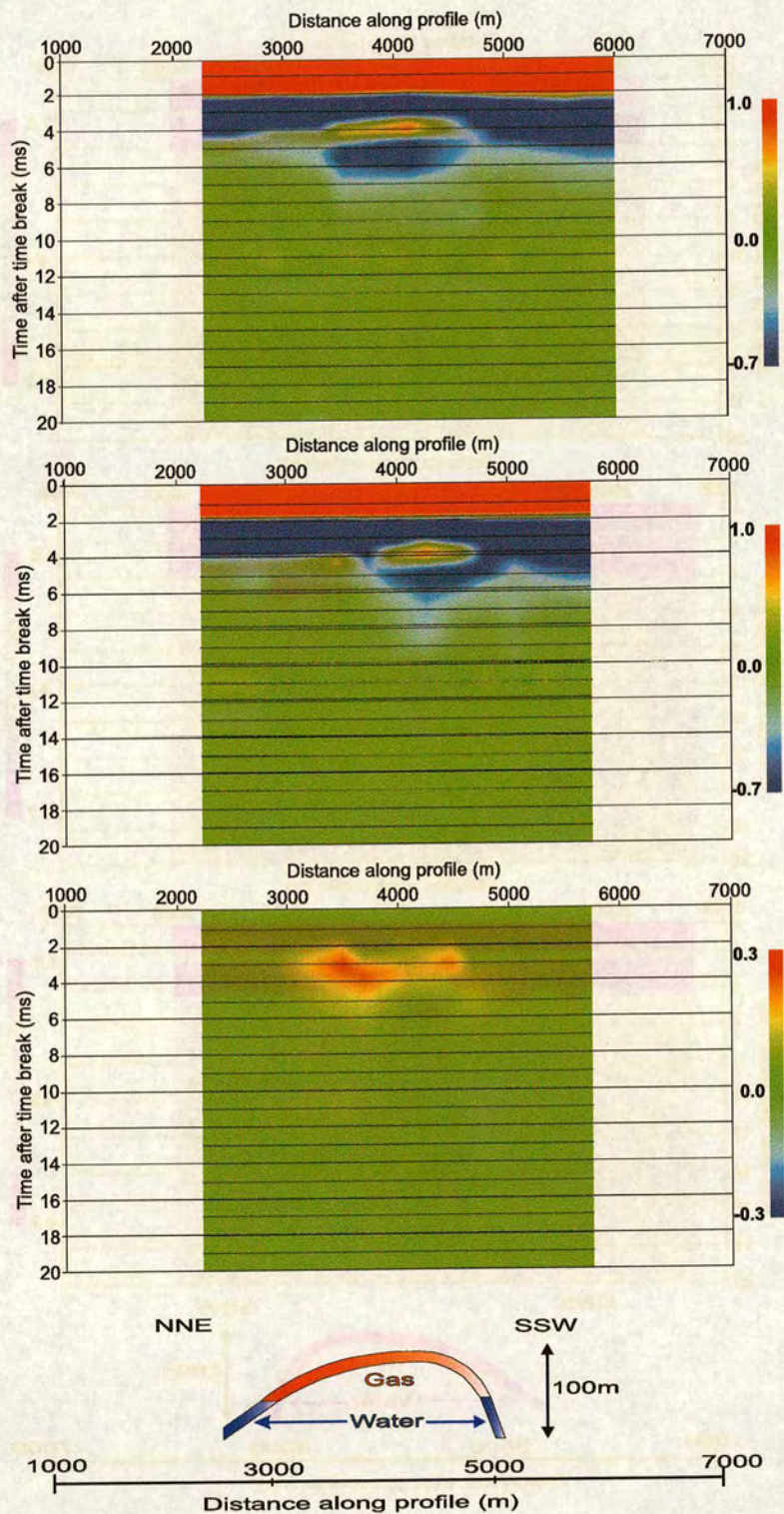
Figure 6.9: E_{xx} 750m common-offset sections of the derivative of the approximate impulse response. Top: 1994 data. Middle:1996. Bottom: The difference between the 1994 and 1996 approximate impulse responses.
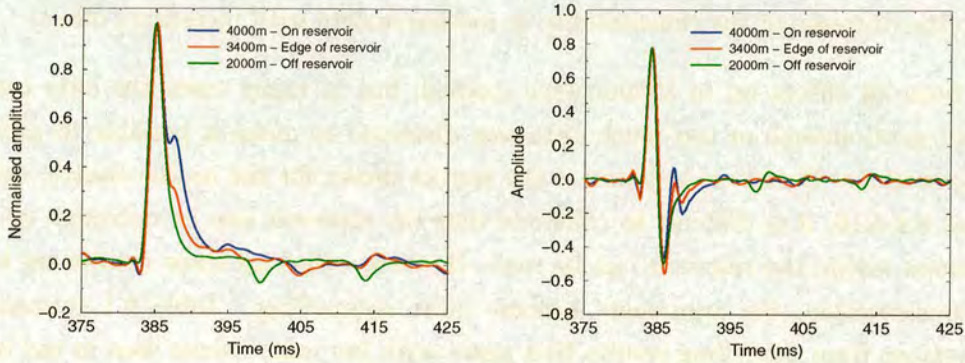
Figure 6.10: Plot of three traces from the 1996 common-offset section shown in figure 6.9 inside, outside and near the edge of the reservoir. Left: The approximate impulse response. Right: The derivative of the approximate impulse response.

the profile of 1875m is shown in Figure 6.13. The left hand plot is of the approximate impulse response and the one on the right of its derivative, which is what is plotted in the colour section in Figure 6.12. Similar plots are shown in Figure 6.14 for data recorded over the reservoir at a distance of 4000m along the profile and in Figure 6.15 for data recorded over the edge of the reservoir a distance of 2900m along the profile. These plots are quite similar to the traces shown in Figure 6.10 for data at an offset of 750m. Again there is a transition near the edge, but now the response seen over the reservoir is more distinct. The difference section for these data shown in Figure 6.12(bottom) is quite similar to the one for the 750m common-offset section shown in Figure 6.9 with a positive difference again seen over the reservoir that is largest at the southern edge of the reservoir. Other small negative differences are also seen but again we only seeing differences occurring where we would expect to see them.

Figure 6.16 again has the same layout as the previous similar figures but the data are now for an offset of 1500m. Due to distortion and the poor quality of much of the data for this offset over the north end of the profile these sections only show data from a distance of 3200m to 6500m along the profile and so do not cross the northern edge of the reservoir. The results are again very similar to those from offsets of 875m and 1000m with the red event now seen at a time of just over 4ms. Again its horizontal edge coincides with the edge of the reservoir. At the southern end of the profile, outside the reservoir between 5300m and 6300m, the response is noticeably different than for shorter offsets; however, it is almost identical in 1994 and 1996. The plot of the difference shown in the bottom plot of Figure 6.16 has a positive anomaly, which coincides with the southern edge of the reservoir. In addition to this event, which may

be due to the reservoir, there are several other differences seen both inside and outside the reservoir at times of up to 18ms. Most of these differences are likely to be noise due to the decrease of the repeatability of measurements with increasing offset.

Data from all offsets up to 2250m were studied, but in many cases the data quality was not good enough or too much data was distorted to make it possible to produce similar sections. Based on only one of the results shown for the in-line electric field in Figures 6.8-6.16, it is difficult to conclude that the reservoir can be detected, or that differences within the reservoir can be seen. However, when all these results are taken into consideration, the arguments become quite compelling. Table 6.1 summarises observations from modelling results that agree with the main events seen in the data.

Observation from modelling	Observation from real data
In-line E_{xx} data cannot detect a thin resistor buried at 500m depth at offsets of 500m or less.	Common-offset sections for 375m and 500m are uniform across the length of the profile. No response is seen over the reservoir.
A thin resistor buried at 500m is first detected at an offset of between 500m and 1000m.	Common-offset section for 625m shows a small disturbance over the middle of the reservoir where it is shallowest. At 750m the disturbance is seen in the same place and is bigger.
The relative response from the reservoir gets larger as the source-receiver offset increases.	The response is seen to increase gradually from 625m, where it is barely detectable, to 1500m.
The effect of the reservoir is present from about 3ms.	The response believed to be from the reservoir occurs at between 3 and 5ms.
There was more gas in the reservoir in 1994 than 1996 so the difference $94 - 96$ should give a positive anomaly.	Difference sections from 750m and 1000m show a positive anomaly across the reservoir with almost no differences seen outside the reservoir.
Differences may be seen at the edge of the reservoir due to lateral movement of the gas-water contact, or over the length of the reservoir due to a 10% drop in pressure within the reservoir between the two surveys.	The 1500m difference section has a positive anomaly present at the southern edge of the reservoir. The 1000m difference section has a positive anomaly across the reservoir that is maximum at the southern edge.

Table 6.1: Summary of observations from modelling and real data that support hydrocarbon detection.

Figure 6.11: E_{xx} 875m common-offset sections of the derivative of the approximate impulse response. Top: 1994 data. Middle:1996. Bottom: The difference between the 1994 and 1996 approximate impulse responses.

133
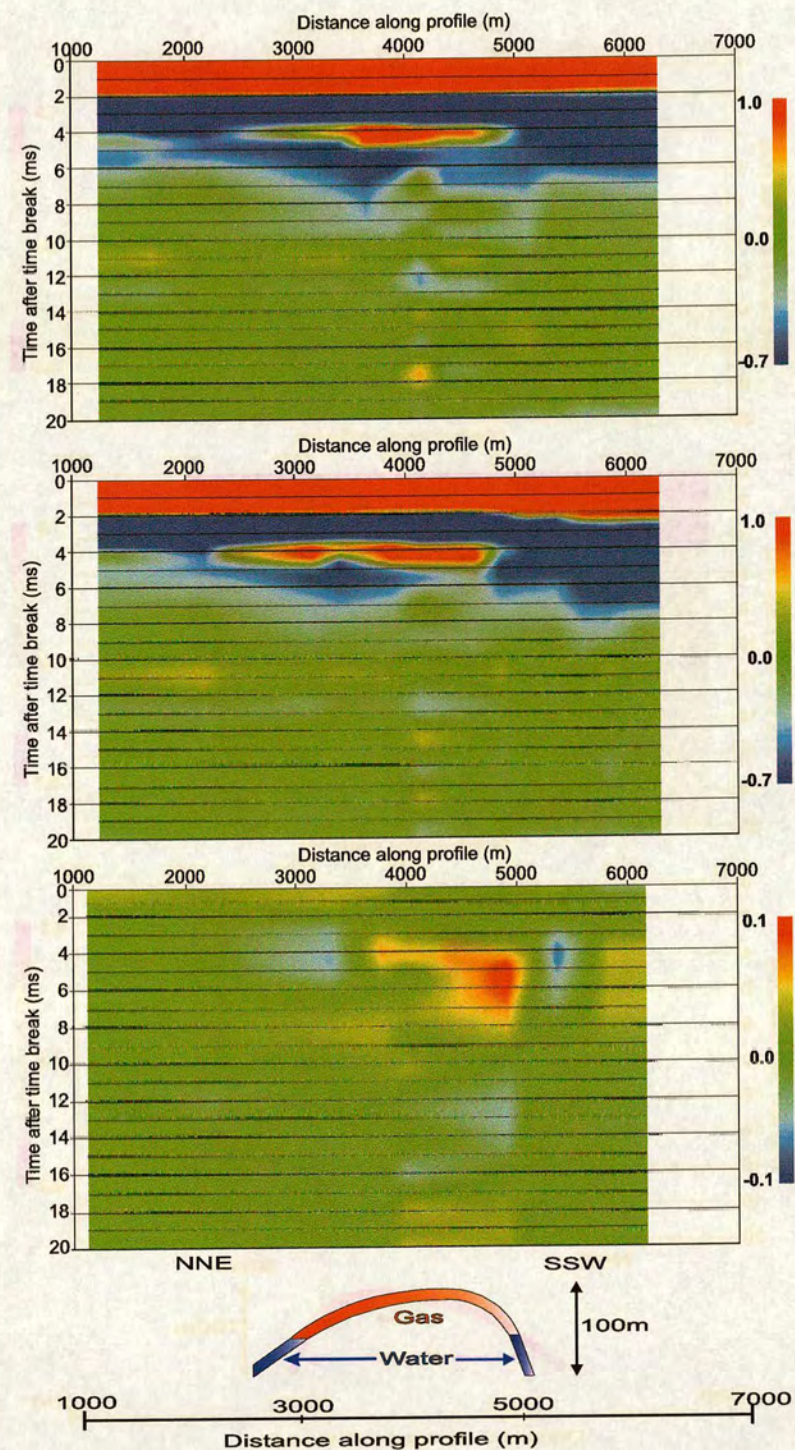
Figure 6.12: E_{xx} 1000m common-offset sections of the derivative of the approximate impulse response. Top: 1994 data. Middle:1996. Bottom: The difference between the 1994 and 1996 approximate impulse responses.
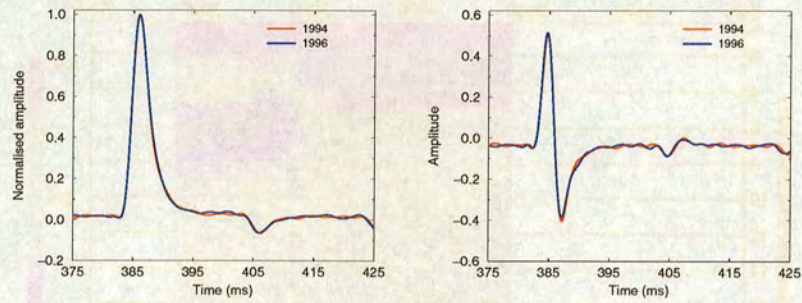
Figure 6.13: Responses recorded at 1000m offset outside the reservoir at a distance of 1875m along the profile for the 1994 and 1996 data. Left: The approximate impulse response. Right: The derivative of the approximate impulse response.
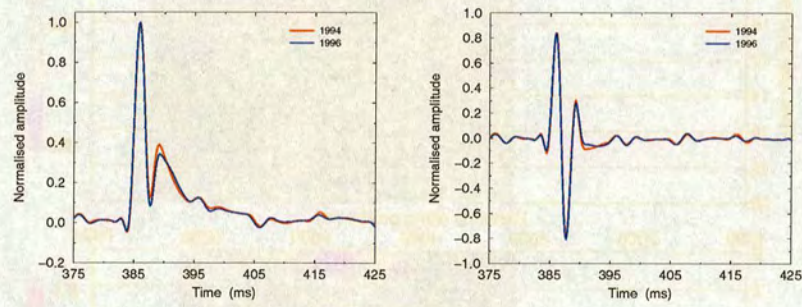
Figure 6.14: As in Figure 6.13 but recorded above the reservoir at a distance of 4000m along the profile.
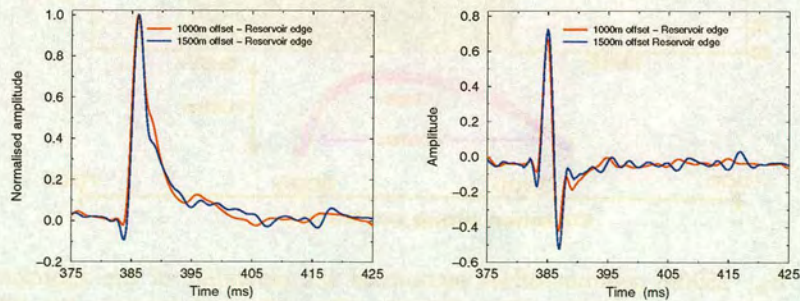
Figure 6.15: As in Figure 6.13 but recorded over the edge of the reservoir at a distance of 2900m along the profile.
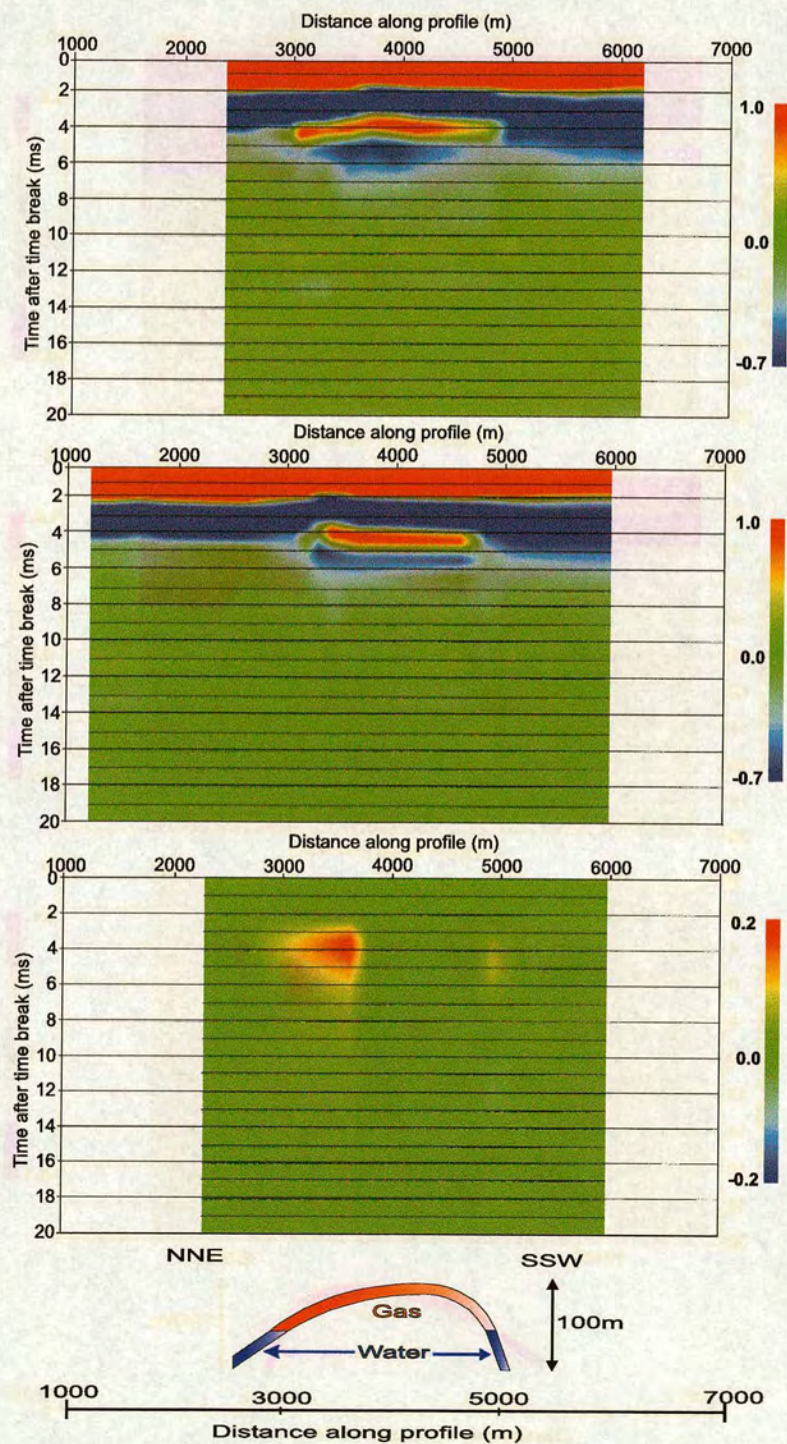
135
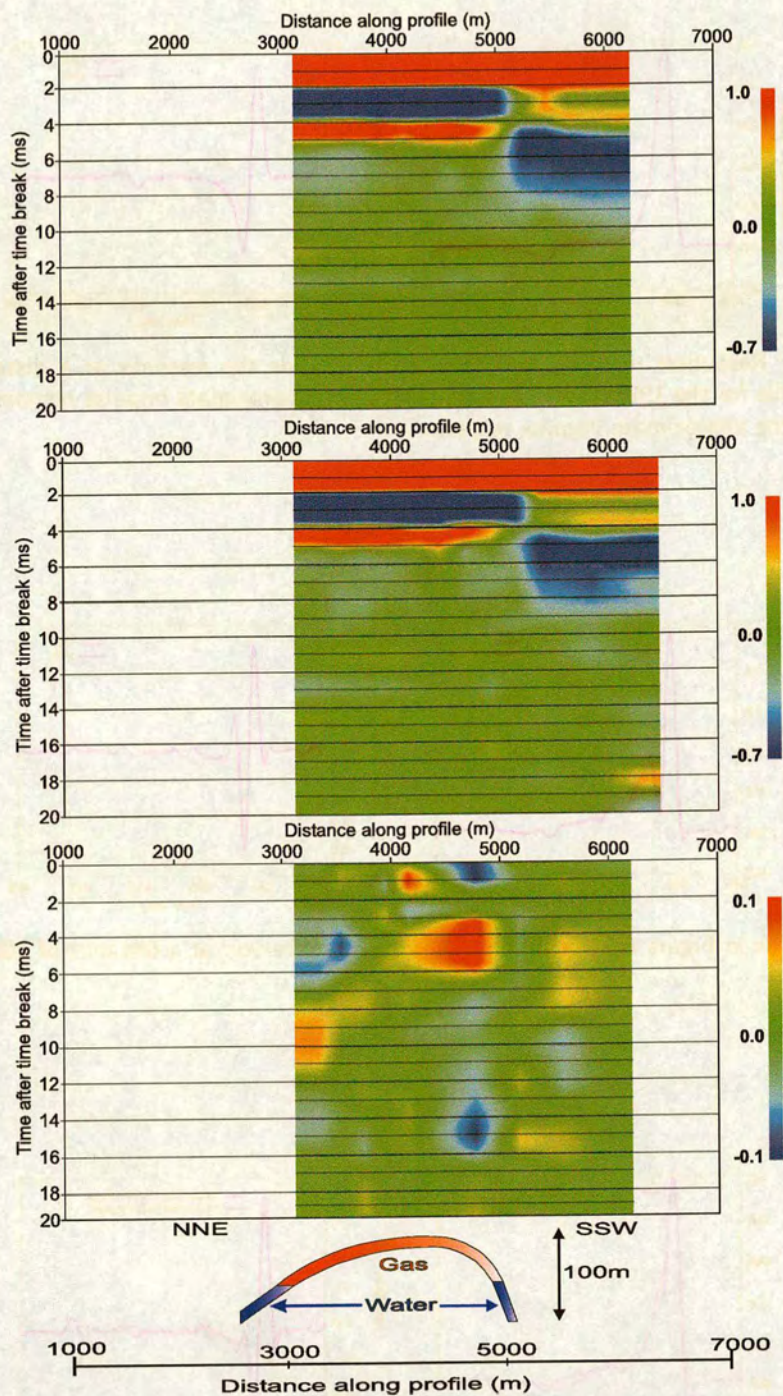
Figure 6.16: E_{xx} 1500m common-offset sections of the derivative of the approximate impulse response. Top: 1994 data. Middle:1996. Bottom: The difference between the 1994 and 1996 approximate impulse responses.

Modelling the reservoir response [2]

The results shown for the in-line E_{xx} electric field data appear to show the presence of the reservoir, but being able to model this response using a buried resistor would add further confidence to the result. Modelling carried out in this section uses the 1-D modelling code written by Nigel Edwards of the University of Toronto (Edwards, 1997), the code is tested against other 1-D codes in Appendix B. Standard 1-D modelling results produce a transient response from a specified start time such as 1ms up to any chosen end time. Two such transients are shown in Figure 6.17(left) for an offset of 1000m, the black curve is the response to a 20 Ωm halfspace and the blue curve the response to the same halfspace but with a 25m thick 500 Ωm resistor embedded in it at a depth of 500m. The derivative of these two transients is shown in Figure 6.17(right). It can clearly be seen that only one peak is present in this plot whereas the traces shown in Figure 6.14 have two distinct peaks present on them. This presents a problem in that even in this simple case the data and the modelling are not in agreement. However, it must be remembered that the real data is not recorded only after $t = 0$, data are being recorded before the shot is fired as well. At the instant the source is fired the recorded voltage jumps on the speed of light time scale to half its final value (Weir, 1980) as can be seen from the transients in Figure 6.18(left). This rise to half the peak value is recorded in the real data and so must also be considered in the modelling. The same transients as shown in Figure 6.17 are shown in Figure 6.18 only now some samples are included before the source is fired in order to capture this instantaneous rise. It can be seen from Figure 6.18(right) that there are now two peaks present in the modelled data, the result can be explained as follows. Let the electric field transient E be the response to a step function $\mathcal{H}$ (Heaviside step function). Then we can write

$$E = \mathcal{H} * G \tag{6.2}$$

where G is the impulse response of the earth. Thus

$$E' = \delta * G = G \tag{6.3}$$

where $'$ represents the derivative with respect to time. In reality though, we do not

---

[2] The results shown in this section are the result of work carried out by Bruce Hobbs of the University of Edinburgh.

achieve a δ-function at time $t = 0$ in G because (i) the source that is put into the ground is not a perfect step and (ii) the derivative E' is calculated from measurements of E recorded at discrete time intervals. Let us suppose that instead of a δ-function we recover the function A where

$$A = \alpha^2 t e^{-\alpha t} \tag{6.4}$$

the integral of this function, say R is

$$R = (1 - (1 + \alpha t))e^{-\alpha t} \tag{6.5}$$

which replaces $\mathcal{H}$. The functions A and R for a value of $\alpha = 1250$ are shown in Figure 6.19. If we now let F be the response to the rise R then

$$
\begin{align}
F &= R * G \tag{6.6} \\
&= R * E' \tag{6.7} \\
&= R' * E \tag{6.8} \\
&= A * E. \tag{6.9}
\end{align}
$$

The function A was calculated using a value for α of 1250, this was then convolved with the transients E shown in Figure 6.18(left) to yield F, and its derivative F' which is plotted in Figure 6.20(left). To allow comparison the result from Figure 6.14 is plotted alongside it. It can be seen that now the modelled result has two distinct peaks with the size of the second peak being greater in the presence of a resistor.
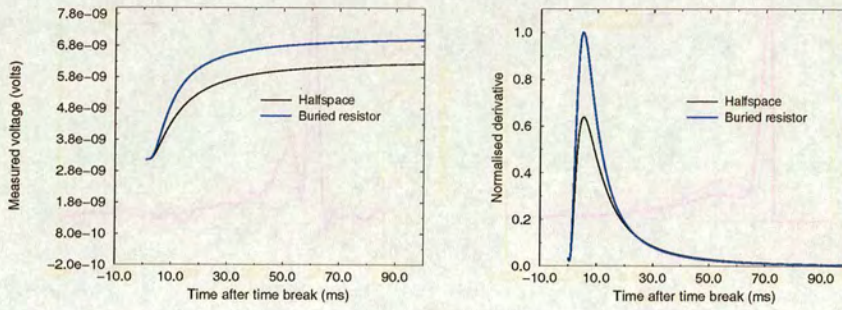
Figure 6.17: Left: The 1-D transient response at 1000m offset to a halfspace and a resistor buried in a halfspace recorded after the timebreak. Right: The derivative of the traces on the left.
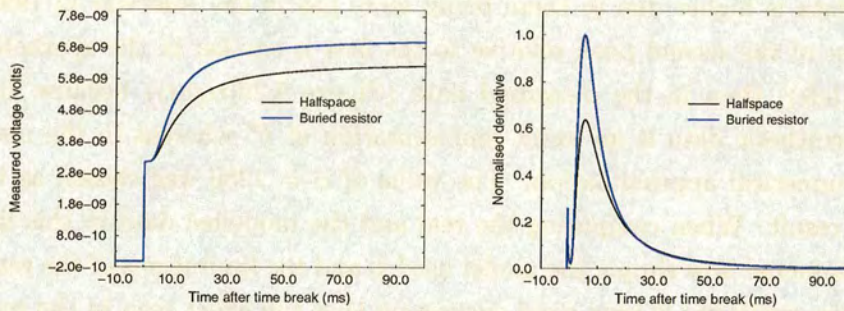
Figure 6.18: The 1-D transient response at 1000m offset to a halfspace and a resistor buried in a halfspace recorded before, during and after the timebreak. Right: The derivative of the traces on the left.
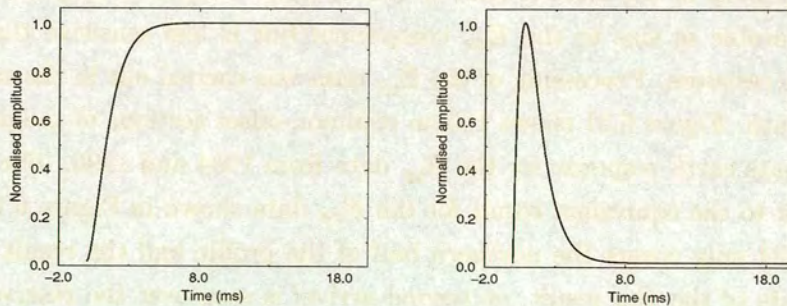
Figure 6.19: Left: The function R (equation 6.5) for $\alpha = 1250$. Right: The function A (equation 6.4) for $\alpha = 1250$.
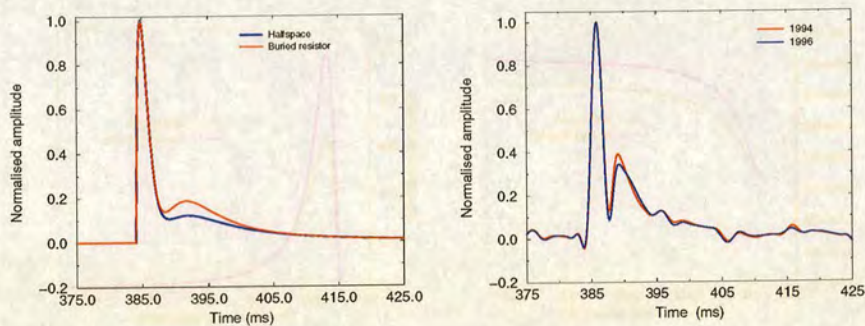
Figure 6.20: The derivative of the impulse response at 1000m offset. Left: Recovered numerically using the functions shown in figure 6.18 and 6.19. Right: The response seen over the middle of the St. Illiers la Ville reservoir

The result is very similar to the result seen in the real data where the second peak of the 1994 data is higher due to there being more gas in the reservoir in 1994 than 1996. The rise of the second peak relative to the first is smaller in the synthetic data (Figure 6.20(left)) than in the measured data (Figure 6.20(right)) because the first peak in the synthetic data is an exact representation of F' whereas in the measured data it is a numerical approximation. The value of $\alpha = 1250$ was chosen as it gives a reasonable result. When comparing the real and the modelled data in this figure it must be remembered how simple the model used is and the limitations of the real data, despite this the similarity is very good suggesting that the effect seen in the real data is due to the presence of the reservoir.

6.4 Cross-line Electric Field E_{yy}

The E_{yy} component of the electric field is known from Chapter 5 to produce a signal that is comparable in size to the E_{xx} component but is less sensitive than the E_{xx} component to resistors. Processing of the E_{yy} data was carried out in the same way as for the E_{xx} data. Figure 6.21 shows 1000m common-offset sections of the derivative of the approximate earth response for the E_{yy} data from 1994 and 1996. The results are quite different to the equivalent result for the E_{xx} data shown in Figure 6.12. Useable data from 1994 only covers the northern half of the profile and the result appears to be the opposite of the E_{xx} result, no second arrival is seen over the reservoir but one is present outside the reservoir. The result for 1996 covers the whole profile and is very similar to the 1994 result. However, the response seen south of the reservoir on the 1996 data is quite different from the response seen to the north of the reservoir.
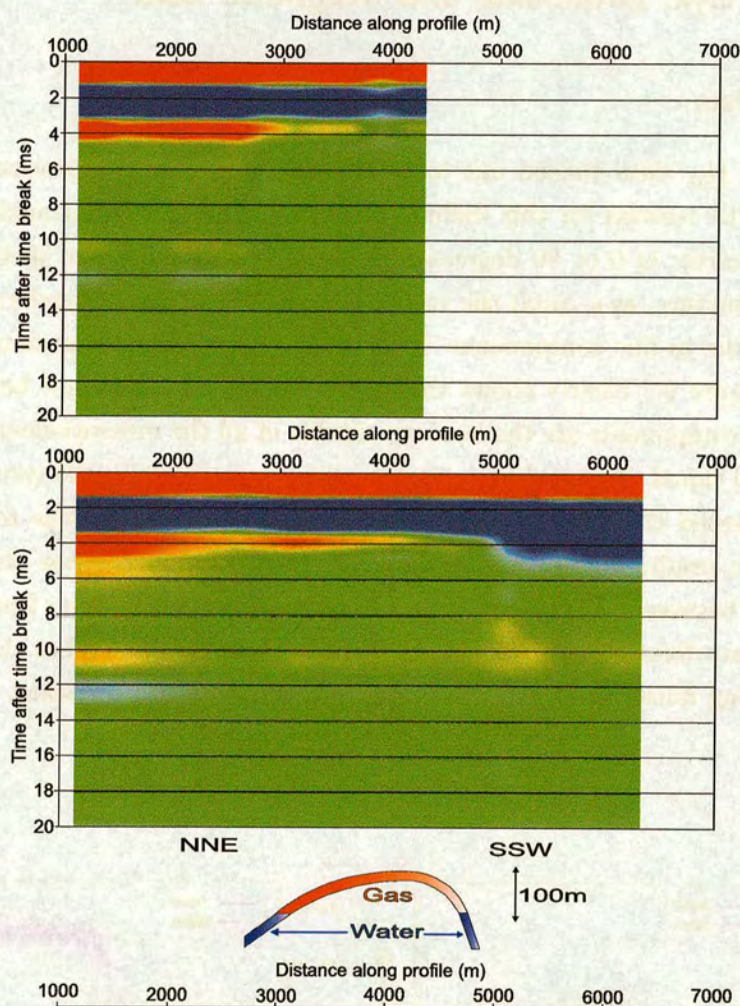
Figure 6.21: E_{yy} 1000m common-offset sections of the derivative of the approximate impulse response. Top: 1994 data. Bottom: 1996 data

Much of the E_{yy} data was of a poor quality and results from other offsets were similarly inconclusive. The E_{yy} component responds to resistive targets in the opposite sense to the E_{xx} component and this may make detection of the reservoir on this component more difficult using this processing scheme as the response will be reduced relative to the background response not increased as it is for the E_{xx} component. However, this would not explain the different nature of the response seen on either side of the reservoir in the 1996 data.

141

6.5   Exy, Eyx, Broadside and Magnetic field

Exy and Eyx data

The E_{xy} and E_{yx} data turned out to be of little use after the processing had been completed. The reasons for this include the fact for an azimuthal angle between the source and receiver of 0 or 90 degrees a response is only measured in the presence of 2-D or 3-D structure, as a result the voltages recorded are about 2 orders of magnitude less than for the in-line components. In many cases the signal was completely lost in the noise. Figure 6.7 clearly shows that when taking the difference between the two surveys these components are the least repeatable of all the measurements taken due to the very small signal. These observations are in agreement with the results of Chapter 5 which suggested that the signal present in these components was too small to be detected. The results obtained from data for these components was also found to be very variable between adjacent source-receiver pairs, as can be seen from Figure 6.22. Analysis of data from these components turned out to be little more than an exercise in manipulating noise, as a result no more of the results of processing these data are shown.
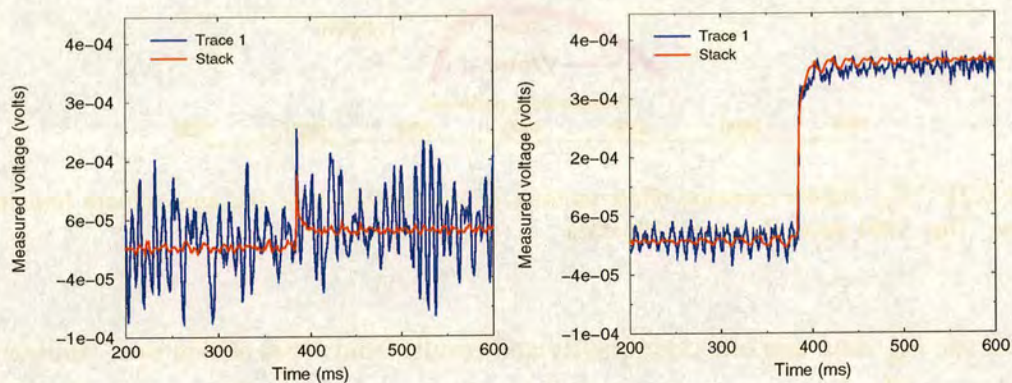
Figure 6.22: Plots of E_{xy} data showing extreme data variability at an offset of 750m for adjacent sources. Results shown are for a single trace and after stacking all the traces in the same source-receiver pair.

These components may be useful in detecting areas of non 1-D structure as in a 1-D earth the response of the two components, E_{xy} and E_{yx} should be the same, for example a plot of the difference $E_{xy} - E_{yx}$ across a survey should identify areas where the assumption of a 1-D earth is not valid. Also these components may be useful in identifying the source of distortions seen on other components. However, in order

to obtain the signal-to-noise ratio required to extract useful information from these components many more traces must be stacked.

Broadside Data

In addition to all the components mentioned so far and studied in Chapter 5 there was additional electric field data collected known as broadside data. The sources used for these data are shown in Figure 4.7 numbered 91-94 and were recorded by receivers along the profile. These data include some parts where receivers are over the reservoir and some where they are not, however, as shown in Figures 5.2-5.3 the amplitude of the recorded response varies by several orders of magnitude as the angle between source and receiver dipole changes from 0 to 45 degrees. In addition the offset between the source and receiver for broadside data varies between about 1000m and 4000m. These two factors mean that in addition to any response from the reservoir there are varying amplitude effects due to varying offsets and the constantly changing angle between the source and receiver. This makes it essentially impossible to interpret the data based on its spatial and temporal features. A study by Keller (1984a) found that even in areas of lateral homogeneity transient EM data recorded at different angles to the source were significantly different even after correcting for the difference in angle. In areas of non 1-D structure the data behave very differently at different angles to the source. In spite of this there is one receiver location for which the source and receiver are in-line and this data can be compared with the E_{xx} and E_{yy} data collected along the profile. Sources 91 and 92 are on the edge of the reservoir and data recorded at receivers 31 and 32 are on the reservoir. The 1994 and 1996 E_{xx} and E_{yy} data for these source and receiver positions are shown in Figure 6.23. These data are very similar to the data obtained over the reservoir for the E_{xx} and E_{yy} data. The data from sources 93 and 94 which are outside the reservoir are distorted with a type 3 distortion shown in Figure 6.3. Data from these sources cross the reservoir edge boundary where there is clearly non 1-D structure present. This may explain why these data are distorted. Broadside data is of little practical use because data collected at different angles between the source and receiver and different source-receiver offsets cannot be compared with any confidence due to the large variation of amplitude with angle which is difficult to correct for accurately.

Magnetic field data

As shown by the modelling results in Figure 5.14 the vertical component of the magnetic field is not sensitive to a thin buried resistor. As a result this data component will not be able to detect the presence of the reservoir. Processed results for these data did not show any correlation with the reservoir and are not shown here. Unlike the E_{xy} and

143
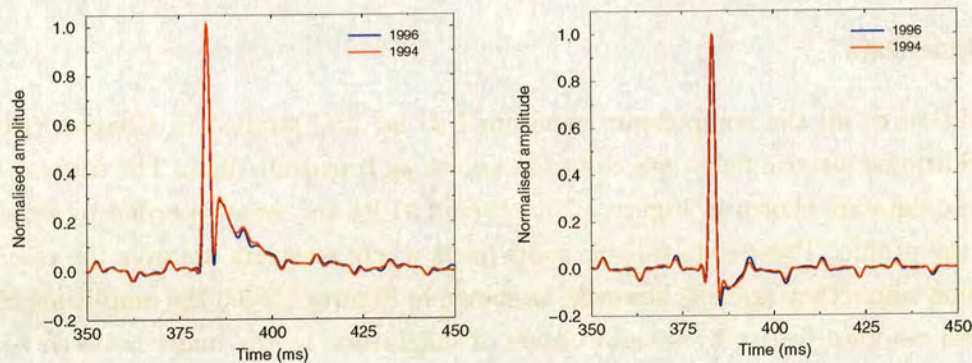
Figure 6.23: The derivative of the approximate impulse response for broadside sources recorded in-line over the reservoir. Left: E_{xx}. Right: E_{yy}.

E_{yx} components there is little to be gained from increasing the fold of the magnetic field data since this component cannot detect thin hydrocarbon filled resistors. Data from the magnetic field can, however, be useful in providing information on the presence of conductive anomalies in a survey area.

6.6   Summary

The results from the processing of the Saint Illiers la Ville datasets indicates that hydrocarbons can be detected using the in-line E_{xx} component of the electric field, there is also good reason to believe that the movement of hydrocarbons may also be detected using this component. The repeatability of the E_{xx} data is excellent and at offsets of 1000m or less it is well above the level of 99% that was hoped for before the project.

The E_{yy} data proved to be of little use in detecting the reservoir. Different responses were seen north of the reservoir, over the reservoir and south of the reservoir making the results inconclusive, despite modelling suggesting a detectable response may be present.

The usefulness of other components in detecting a thin hydrocarbon bearing layer is small to zero, this finding agrees with modelling results that suggest these components are either totally insensitive to a buried resistor (magnetic field) or zero in a 1-D earth (E_{xy} and E_{yx}). Broadside data are also of little use as it is almost impossible to compare results from different angles between the source and receiver and different offsets due

to the large amplitude variations between them.

If the results seen in Figures 6.8-6.16 are not due to the presence of gas in the reservoir then the only other possible explanation for the event seen at between 3ms and 5ms that coincides with the lateral extent of the reservoir is the presence of monitoring wells or near-surface conductors such as pipes in the vicinity of the survey. I believe these effects can be ruled out for two reasons to do with the geometry. First, it can be seen from Figure 4.1 that most monitoring wells in the reservoir are very close together and to the west of the MTEM profile. Such a distribution of pipes could not produce the very abrupt change in signature at the gas bubble edges. If the monitoring wells had any effect, it would be more concentrated in the south of the profile and its effect would fall off gradually with distance from the pipes. This is not what is seen which suggests strongly that what we observe is the effect of the gas in the reservoir below. Second, processed data from short offsets of 375m and 500m shown in Figure 6.8 do not show the second peak at about 4ms. This agrees with modelling results, which indicate that the reservoir is not detectable at such short offsets. If the effect seen over the reservoir was in fact due to near surface conductors, the short offset data would be similarly affected. Also the effects of such conductors tend to manifest themselves as strong spatial variations between adjacent source-receiver pairs (Hördt et al., 2000), these effects, although they are observed in some parts of the data have not been included in the final results presented here. These lines of reasoning suggest that what we are seeing is the effect of the reservoir. In addition the modelling approach presented on pages 137-140 shows how the response seen over the reservoir can be reproduced using synthetic data.

Chapter 7

Direct Resistivity Determination

7.1 Introduction

Extracting resistivity information directly from electromagnetic data without the need for inversion and model fitting has never before been successfully applied to real data and remains an area of active research. This chapter presents a modification to the calculation of the equivalent wavefield by deconvolution in log-time in order to determine the correct resistivities from the slope of the moveout curve in the equivalent wavefield domain $U(x,q)$. The motivation for attempting to extract resistivity information directly from the data comes from an analogy to seismic refraction of arrivals in the equivalent wavefield domain that was made by Wilson (1997). The technique is applied to synthetic data models that increase in complexity from halfspace models to 2 layer and 3 layer models and models with realistic amounts of various types of noise. The effect of the source geometry is also studied and finally the problems associated with applying the technique to the Saint Illiers la Ville data are discussed.

Establishing an analogy with seismic refraction

It is known from the analytic solution of the equivalent wavefield over a uniform halfspace (equation 3.85) that the maxima of traces occur at $q = \frac{x}{c}$ and since $c = \sqrt{\frac{\rho}{\mu}}$ it should be possible to extract the resistivity information of the input diffusive synthetic transients from the moveout slope in the equivalent wavefield domain. However, this equation only holds on the surface of a uniform halfspace and so only describes the moveout of the direct wave, or incident field. It says nothing about the scattered field, which contains information about resistors in the earth. However, Wilson (1997) found that when the equivalent wavefield was calculated over a multi-layered earth model the

slope of the first arrival changed, and beyond a certain offset the slope was related to the resistivity of the deeper layer. This is analogous to seismic refraction in which the slope of the first arrival is related to the velocity of the layer through which the wave has travelled. Initially the first arrival travels through the top layer only, but beyond a certain offset the first arrival comes from a deeper layer and the slope of the movout is related to the velocity of the deeper layer. The analogy was found to hold for two layer models and a three layer model with a thick (700m) middle layer by Wilson (1997) although the resistivity value obtained is always wrong by the same factor as can be seen from Figure 3.5. No attempt was made to test the analogy using more complex models or to extend the analogy in order to see if depth information could be obtained using theory from seismic refraction. The possibility of extracting resistivity information from EM data using this technique was the basis of the paper by Ziolkowski & Hobbs (1998) but no further work has been done on exploring the possibilities of the analogy to date. This chapter addresses the problem of obtaining the correct resistivity values in the presence of two layers and tests the refraction analogy using more complicated earth models.

7.2 Problems associated with recovering the equivalent wavefield

The reason the resistivity result obtained by Wilson (1997) is always wrong by the same factor is because there is a fundamental problem associated with numerically recovering the equivalent wavefield waveform. As was first noticed by Slob *et al.* (1995), the true equivalent wavefield cannot be perfectly recovered: instead the result that is obtained is a smoothed version of the analytic waveform with its peak closer to the centre of the waveform.

"In theory, there is no difference between theory and practice. But, in practice, there is!"
Jan L.A. van de Snepsheut (1953-1994)

The position of the peak of the waveform is entirely what the determination of resistivity values is based on; recovery of the exact shape of the waveform is not as important. This is similar to seismic refraction in which all the information is contained in the arrival time of the first arrival.

Recall from section 3.5 the form of the numerically recovered waveform by deconvolution in log-time. The result of applying deconvolution in log-time to synthetic data is to

recover a wavefield whose peak values occur at $v = ln(\frac{x}{c}) - \Delta v$ in the $(\boldsymbol{x}, v)$ domain and at $q = exp(-\Delta v)\frac{x}{c}$ in the $(\boldsymbol{x}, q)$ domain: this is illustrated for a 10 Ω m halfspace in Figure 7.1.
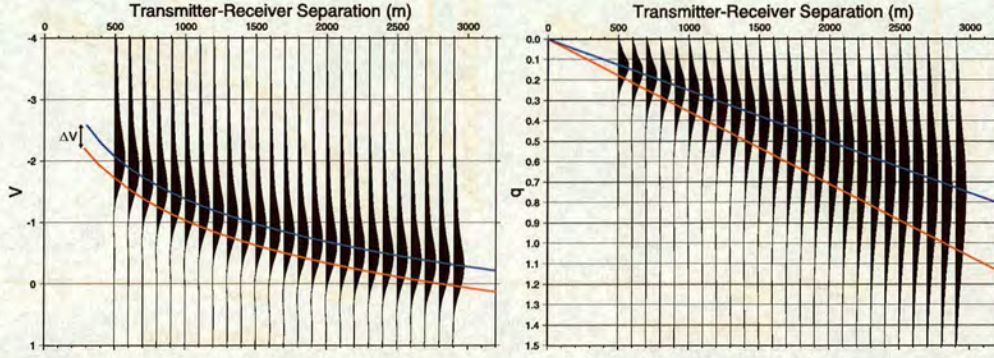
Figure 7.1: The result of applying DPM by deconvolution in log-time over a 10 Ωm half space with the theoretical (red) and numerically recovered (blue) moveout curves overlain. Left: Result in the $\boldsymbol{R}(\boldsymbol{x}, v)$ domain. Right: Result in the $\boldsymbol{U}(\boldsymbol{x}, q)$ domain.

This means that the peak values of the numerically recovered equivalent wavefield in the $\boldsymbol{R}(\boldsymbol{x}, v)$ domain are all shifted by a constant factor Δv for all offsets (Figure 7.1 (left)). Therefore, in the $\boldsymbol{U}(\boldsymbol{x}, q)$ domain the maximum values of traces in the recovered equivalent wavefield all lie on a straight line but the slope is not equal to $\frac{x}{c}$ (Figure 7.1 (right)). As a result, the resistivity obtained from the slope is always wrong by the same factor.

Based on observations from synthetic models involving a layered earth structure, the numerically recovered moveout curve in the equivalent wavefield domain has the form $q = exp(-\Delta v)\frac{x}{c}$ up to the crossover distance x_{cross} for which the value of the q domain 'velocity' c is governed by the resistivity ρ of the top layer. Beyond x_{cross} the moveout is of the form $q = (q_0 + \frac{x}{c})exp(-\Delta v)$ where the value of c is now controlled by the resistivity of the second layer (Wilson, 1997). If the correct position of the peak of the waveform could be recovered, the moveout would be a straight line of the form $q = q_0 + \frac{x}{c}$ (Ziolkowski & Hobbs, 1998). The value of q_0 is given by the zero offset 'intercept time', it is the minimum 'time' taken to travel down to a 'refracting' layer and back up at zero offset. This relation between the slope of the moveout curve and earth resistivity is completely analogous to the relationship between the seismic velocity of a layer and the slope of the moveout curve in seismic refraction. In seismic refraction the moveout curves are straight lines of slope $\frac{1}{V_n}$ where V_n denotes the seismic velocity of the nth layer. The moveout in seismic refraction is given by $t = t_0 + \frac{x}{v}$ where x is the source-receiver offset, t_0 is the zero offset intercept time and v is the velocity of the

149

layer in question. The analogy between the two is summarised in Figure 7.2.
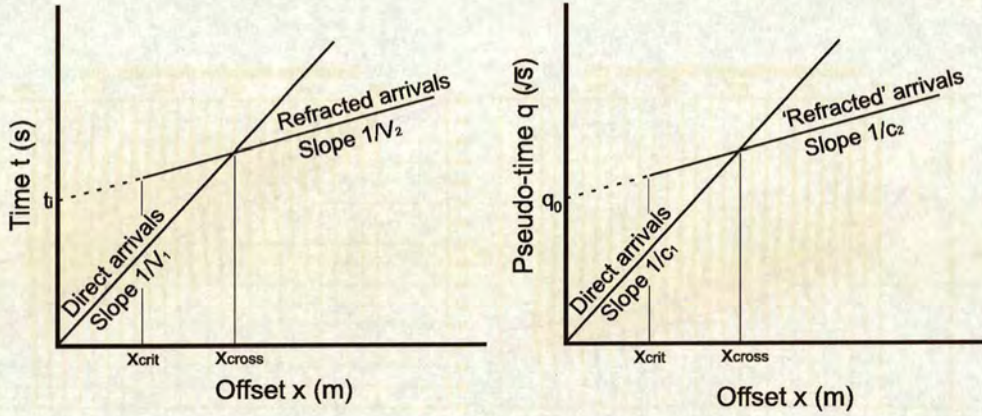
Figure 7.2: Illustration of the similarity between the behaviour of arrivals in seismic refraction (left) and those observed for transient electric field data in the equivalent wavefield domain $U(x, q)$ (right).

The problem of recovering a smoothed version of the equivalent wavefield with the peak in the wrong place is not restricted to recovering the waveform by deconvolution in log-time, but is a result of the shape of the waveform we are trying to recover. Another method of inverting the q transform is by singular value decomposition. This involves discretising the integral in the q transform and has been applied by Oliver (1994), Lee & Xie (1993) and Das et $al.$ (2002) to invert the q transform. It was also applied by Wilson (1997) to synthetic MTEM data and was found to give a similar result to that obtained by deconvolution in log-time.

Applying a correction to compensate for the position of the peak in the recovered equivalent wavefield being moved towards the centre of the waveform was proposed by Wilson et $al.$ (1998). This procedure can give good results on simple two-layer noise-free synthetic data where the input values are known but does not appear justified in more complicated situations for a number of reasons.

First, when carrying out deconvolution by least squares Wiener filtering, it is necessary to add a small percentage of white noise in order to down-weight the output amplitude spectrum at frequencies where the input amplitude is very low. This is done by increasing the zero-lag coefficient of the autocorrelation function $\phi_{SS}(0)$ in the normal equations (7.1)

$$
\begin{pmatrix}
(1+e)\phi_{SS}(0) & \phi_{SS}(-1) & .... & \phi_{SS}(-m) \\
\phi_{SS}(1) & (1+e)\phi_{SS}(0) & .... & \phi_{SS}(1-m) \\
.... & .... & .... & .... \\
\phi_{SS}(m) & \phi_{SS}(m-1) & .... & (1+e)\phi_{SS}(0)
\end{pmatrix}
\begin{pmatrix}
f_0 \\
f_1 \\
.... \\
f_m
\end{pmatrix}
=
\begin{pmatrix}
\phi_{SE}(0) \\
\phi_{SE}(1) \\
.... \\
\phi_{SE}(m)
\end{pmatrix} . \tag{7.1}
$$

I have found that the amount of white noise e that is added also has an effect on the resistivity value that is obtained. The resistivity values obtained for a 10 Ωm half space with various levels of white noise added in the deconvolution step are shown in Figure 7.3. It can be seen from this figure that as less white noise is added the value of the resistivity obtained becomes closer to the correct answer. Figure 7.4 shows the recovered equivalent wavefield waveform for various amounts of white noise and it can clearly be seen how important the addition of the white noise is in obtaining a stable solution to the deconvolution. The more white noise that is added, the more stable the result, and the more it resembles the analytic solution. However, adding more white noise also has the effect of moving the peak of the recovered wavefield further towards the centre of the waveform, making it appear earlier, and as a result making the calculated resistivity higher than the actual resistivity. The result is also affected by the amount of noise present in the data, since noisy data will require more white noise to obtain a stable result than less noisy data. As a result, applying a calibration to real data in order to determine the correct resistivity value appears to be difficult, if not impossible, to implement. Adding white noise in order to produce a stable result is similar to the effect of a regularisation parameter, α, used in singular value decomposition. In the presence of noisy data this parameter must be made larger in order to give a stable result (Lee & Xie, 1993).

It is clear that in order to extract the correct resistivity values from data in the equivalent wavefield domain, a different approach is required.
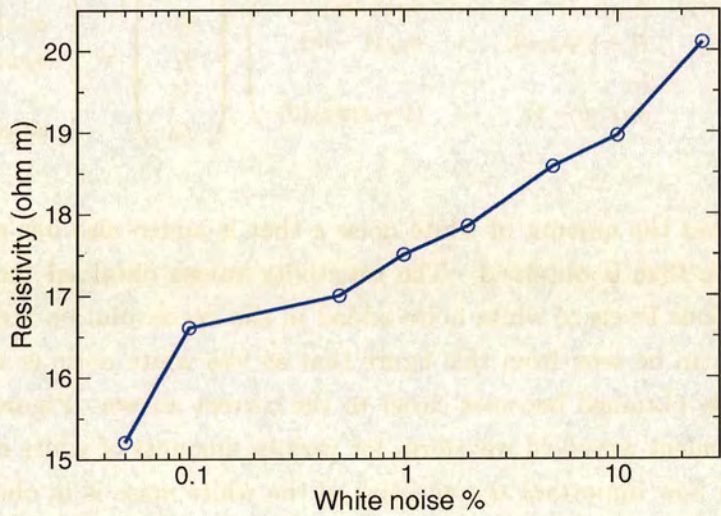
151

Figure 7.3: The resistivity obtained over a 10 Ωm halfspace as a function of the percentage of white noise added in the deconvolution.
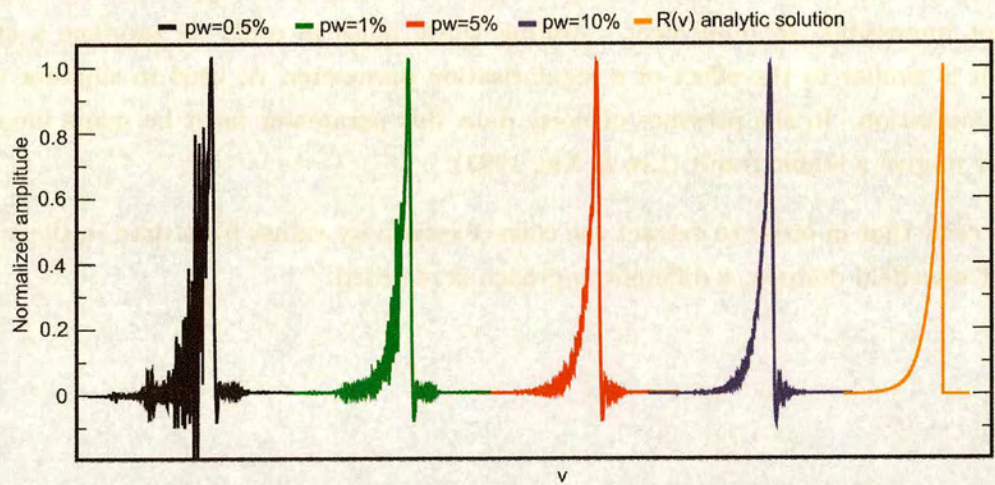
Figure 7.4: The effect of adding white noise during deconvolution in recovering the equivalent wavefield waveform over a 10 Ωm halfspace.

152

Deconvolution in log-time for an impulse source term

The main problem in recovering resistivity values from the equivalent wavefield is due to the shape of the waveform we are trying to recover. The wavefield we are trying to recover is for a switch-off electric field dipole source. The results of Lee & Xie (1993), shown in Figure 3.2 demonstrate that the correct values for conductivity can be obtained. The source used to create their data, however, is an impulse magnetic dipole source.

In order to prove that the equivalent wavefield concept works, and that the right resistivity can be obtained, given a more easily recoverable equivalent wavefield waveform, the following approach was taken. Choose the waveform to be recovered by deconvolution in log-time to be symmetric as opposed to the asymmetric waveform that is recovered for the switch-off electric dipole source. Then the peak of the numerically recovered waveform should be in the correct place giving the correct resistivity value. Consider an impulse point source term in the equivalent wavefield domain: for such a source the source term $S(x,t)$ in the wave equation 3.43 is a delta function in pseudo-time (q) and space (x),

$$S(x,q) = \mathcal{D}\delta(x)\delta(q). \tag{7.2}$$

The analytic solution to the wave equation for such a source in the q domain is,

$$U(x,q) = \frac{-\mathcal{D}}{4\pi x c^2}\delta(q - \frac{|x|}{c}). \tag{7.3}$$

This function is a delta function at $q = \frac{x}{c}$ in the q domain which is symmetric. Note that there is no q multiplying the delta function in equation 7.3, whereas in equation (3.85) there is a q multiplying the heaviside function in the switch-off response solution to the equivalent wavefield. Assuming a delta function in the q domain is therefore quite different to assuming one in the time domain. By considering the shape of the waveform we want to recover first and then working backwards we can get an understanding of the input wavefied needed to numerically recover the correct answer Taking the q transform of equation 7.3 gives the diffusive response,

153

$$F(x,t) = \frac{-\mathcal{D}}{8\pi^{\frac{3}{2}}} \frac{1}{t^{\frac{3}{2}}c^3} exp(-\frac{x^2}{4c^2 t}). \tag{7.4}$$

Starting from this diffusive response, equation (7.4), deconvolution in log-time is applied to recover the equivalent wavefield and extract the resistivity from the data. The result for a 10 Ωm half space, along with all the steps involved, is shown in Figure 7.5 with the theoretical result shown by the dotted orange line. Comparing Figures 7.5 and 3.5 the effect that the shape of the waveform to be recovered has on the result can clearly be seen. Figure 7.5 illustrates that when trying to recover a symmetric waveform, inversion of the q transform by deconvolution in log-time gives the correct answer. In recovering the equivalent wavefield it is important to remember that for a meaningful interpretation, that is, to get the correct resistivity, it only requires the peak of each trace to be in the right place. Recovery of the exact shape of the waveform is not as important.
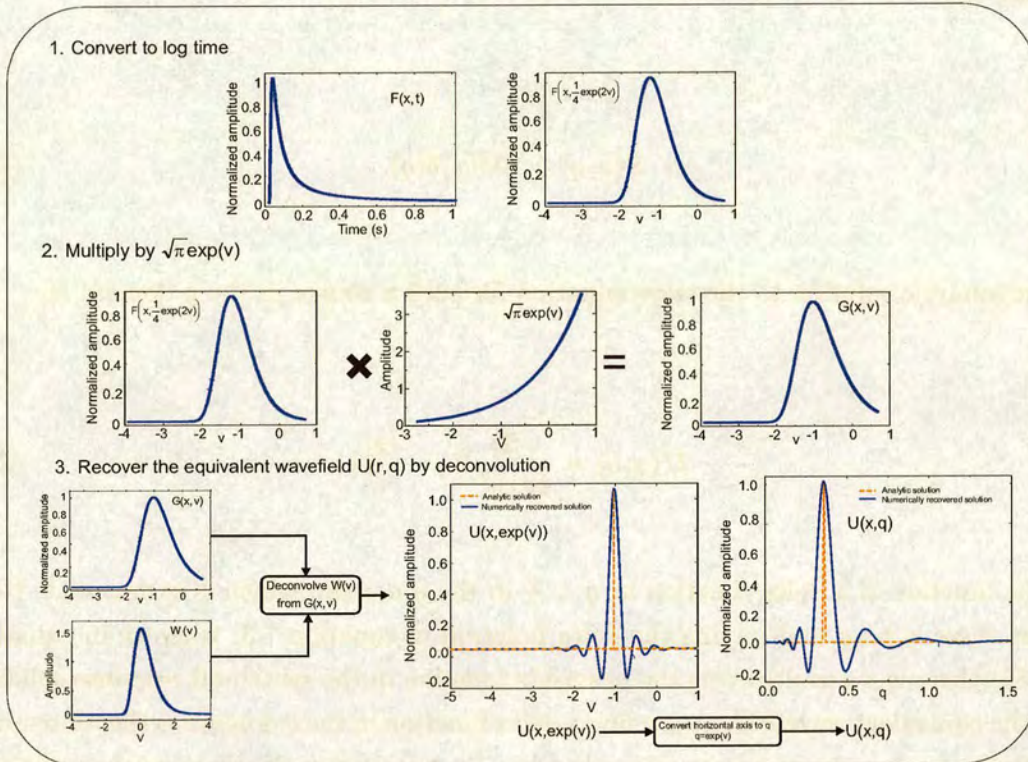

Figure 7.5: The procedure for numerically applying DPM by deconvolution in log-time to a waveform which in the equivalent wavefield domain is a delta function at $q = \frac{x}{c}$.

154

7.3 The impulse and step responses

As discussed in section 3.5, the application of DPM to a switch-off electric dipole field at the surface of the earth does not produce the correct result, and hence the correct resistivity cannot be extracted from the data. This is due to the shape of the waveform that we are trying to recover. Because it is not symmetric, the peak of the recovered waveform is moved towards the centre of the waveform and the equivalent wavefield cannot be perfectly recovered (Slob et al., 1995). The position of this peak determines the value of resistivity that is obtained. However, when DPM is applied to a diffusive field produced by an impulse source for which the equivalent wavefield is a delta function at $q = \frac{x}{c}$, the correct result for the resistivity is obtained exactly. The shape of the waveform that is recovered from the deconvolution in this case is symmetric.

Thus, if a way can be found of transforming the switch-off electric field response to that of the impulse response before applying DPM, it should be possible to obtain the correct result and extract the correct resistivity from data generated by a switch off in-line electric field transmitter current.

Given that the derivative of a Heaviside step function is a delta function, it would appear that all that needs to be done to convert the switch-off response to an impulse response is to differentiate it. However, this is not the case. Taking the derivative of the switch-off response given in equation 3.62 gives

$$-\frac{\partial}{\partial t}\boldsymbol{E}_{xx}(x, t > 0) = \frac{\mathcal{D}}{2\pi\sigma x^3}exp(-\frac{x^2}{c^2 4t})\frac{2}{\sqrt{\pi}}\frac{x^3}{8c^3}t^{-5/2}. \tag{7.5}$$

Which can be written as

$$-\frac{\partial}{\partial t}\boldsymbol{E}_{xx}(x, t > 0) = \frac{\mathcal{D}}{8\pi^{\frac{3}{2}}}\frac{1}{c^3}\frac{1}{\mu t^{\frac{5}{2}}}exp(-\frac{x^2}{c^2 4t}) = \frac{1}{\mu t}\boldsymbol{F}(x, t). \tag{7.6}$$

This is the same as equation 7.4 except for a the multiplicative factor $\frac{1}{\mu t}$. It was shown by Wilson (1997) that the equivalent wavefield of this function is given by

$$\boldsymbol{U}(x, q) = \frac{\mathcal{D}}{2\pi\sigma x^3}\left[\frac{x}{c}\delta'(q - x/c) + \delta(q - x/c)\right] \qquad x/c > 0. \tag{7.7}$$

Equation 7.7 contains the derivative of a delta function which is not differentiable in the strict sense. The delta function is not actually a function but a distribution, that is, a mathematical expression that is well defined only when integrated. It can clearly be seen that this function is not the same as the equivalent wavefield for an impulse source given in equation 7.3. This is illustrated in Figure 7.6.
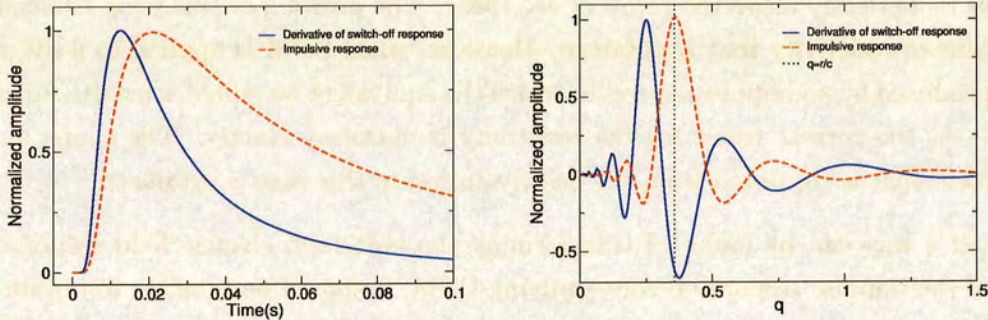
Figure 7.6: The derivative of the switch-off electric field response (blue) and the 'impulse' response (red). Left: In the time domain. Right: The numerically recovered equivalent wavefield.

The response given in equation 7.5 is plotted in Figure 7.6 (left) along with the impulse response from equation 7.4 that is known to give the correct answer after DPM. It can be seen immediately that the position of the peak in these two curves occurs in different places. The result of applying DPM to these two curves is shown in Figure 7.6 (right). It can be seen that the position of the peak recovered from the derivative of the switch-off response does not occur at $q = \frac{x}{c}$ and that the output waveform from the deconvolution is not symmetric. To obtain the correct resistivity we therefore have to transform the switch-off response into the impulse response before applying DPM. Simply differentiating the switch-off response does not achieve this.

7.4 Converting the switch-off response into the impulse response

In this section I describe a method that enables the impulse response to be recovered from the analytic switch-off response. There are three key steps and the order is important. The three steps are: (1) conversion to log-time, (2) differentiation and (3) multiplication by $\sqrt{\pi}exp(v)$. The transformation is perhaps better re-phrased as a conversion of the switch-off response to the function $G(x,v)$ (equation 3.90) for an impulse source, as it is this function which is the input for the deconvolution that is recovered by this transformation.

Before it can be shown that $G(x,v)$ for an impulse source has been recovered, it is necessary to know mathematically the form of this function. Starting from the analytic expression for an impulse response (7.8), the function $G(x,v)$ is recovered by following the procedure outlined in Figure 7.5; this involves converting to log-time (7.9) and multiplying by $\sqrt{\pi}exp(v)$ (7.10) which simplifies to give (7.11).

$$F(x,t) = \frac{-\mathcal{D}}{4\pi x}\frac{1}{2\sqrt{\pi t^3}}\frac{x}{c}exp\left(-\frac{x^2}{4c^2t}\right) \tag{7.8}$$

$$F(x,\frac{1}{4}exp(2v)) = \frac{-\mathcal{D}}{\pi c}\frac{exp\left(-\frac{x^2}{c^2exp(2v)}\right)}{\sqrt{\pi exp(6v)}} \tag{7.9}$$

$$\sqrt{\pi}exp(v)F(x,\frac{1}{4}exp(2v)) = \frac{-\mathcal{D}}{\pi c}\sqrt{\pi}exp(v)\frac{exp\left(-\frac{x^2}{c^2exp(2v)}\right)}{\sqrt{\pi exp(6v)}} \tag{7.10}$$

$$= \frac{\mathcal{D}}{\pi c}\frac{exp\left(-\frac{x^2}{c^2exp(2v)}\right)}{exp(2v)} \tag{7.11}$$

$$= G(x,v) \tag{7.12}$$

Having established the form of the function $G(x,v)$ for an impulse source that we are trying to reproduce, now consider the analytic solution for the in-line switch-off electric field response again (7.13). The series of steps required to convert the switch-off response to the function $G(x,v)$ for an impulse source are conversion to log-time, differentiation and multiplication by $\sqrt{\pi}exp(v)$. These steps are applied analytically to equation (7.13). Converting to log-time by making the substitution $v = \frac{1}{2}ln(4t)$ gives (7.14). This function is then differentiated to give (7.14) which simplifies to (7.16). The final step is then to multiply by $\sqrt{\pi}exp(v)$ to give (7.17) which simplifies to (7.18).

$$\boldsymbol{E}(x,t) = \frac{\mathcal{D}}{2\pi\sigma x^3}\left[erf(\frac{x}{c2\sqrt{t}}) - \frac{2}{\sqrt{\pi}}\frac{x}{c2\sqrt{t}}exp(-\frac{x^2}{c^24t})\right] \quad (7.13)$$

$$\boldsymbol{E}(x,\frac{1}{4}exp(2v)) = \frac{\mathcal{D}}{2\pi\sigma x^3}(erf(\frac{x}{c\sqrt{exp(2v)}})$$
$$-(\frac{2x}{c\sqrt{\pi}}\frac{exp(-\frac{x^2exp(-2v)}{c^2})}{\sqrt{exp(2v)}}) \quad (7.14)$$

$$\frac{\partial}{\partial v}\boldsymbol{E}(x,\frac{1}{4}exp(2v)) = \frac{\mathcal{D}}{2\pi\sigma x^3}(-\frac{2x}{c\sqrt{\pi}}\frac{exp(-\frac{x^2exp(-2v)}{c^2})}{\sqrt{exp(2v)}}$$
$$+\frac{2x}{c\sqrt{\pi}}\frac{exp(-\frac{x^2exp(-2v)}{c^2})}{\sqrt{exp(2v)}}$$
$$-\frac{4x^3exp(-2v)}{\sqrt{\pi}c^3}\frac{exp(-\frac{x^2exp(-2v)}{c^2})}{\sqrt{exp(2v)}}) \quad (7.15)$$

Which simplifies to

$$= \frac{\mathcal{D}}{\sigma}(-\frac{2exp(-2v)exp(-\frac{x^2exp(-2v)}{c^2})}{\pi^{\frac{3}{2}}c^3\sqrt{exp(2v)}}) \quad (7.16)$$

$$\sqrt{\pi}exp(v)\frac{\partial}{\partial v}\boldsymbol{E}(x,\frac{1}{4}exp(2v)) = \frac{\mathcal{D}}{\sigma}(-\frac{2exp(-v)exp(-\frac{x^2e^{(-2v)}}{c^2})}{\pi c^3\sqrt{exp(2v)}}) \quad (7.17)$$

$$= -\frac{2\mathcal{D}}{\sigma\pi c^3}(\frac{exp(-\frac{x^2}{c^2exp(2v)})}{exp(2v)}) \quad (7.18)$$

It can be seen by comparing the function $\boldsymbol{G}(x,v)$ for an impulse source (7.11) and the function that was derived from the in-line switch-off electric field source (7.18) that these two functions are identical apart from a slightly different amplitude scaling factor. This is shown in Figure 7.7 where equation 7.11 is plotted along with the function $\boldsymbol{G}(x,v)$, calculated numerically from equation 7.4 and $\boldsymbol{G}(x,v)$ calculated numerically from the analytic switch-off response following the steps described above. It can be seen that after normalisation these functions are identical.

The effects of adding different amounts of white noise in the deconvolution to recover the equivalent wavefield for an impulse source are shown in Figure 7.8. Figure 7.8 (left) is the result at an offset of 100m over a halfspace, while Figure 7.8 (right) is for an offset of 3500m in the presence of two layers. It can be seen that in both cases the addition of white noise does not have an effect on the position of the peak of

the recovered waveform. This was not the case when trying to recover the equivalent wavefield waveform given in equation 3.85.
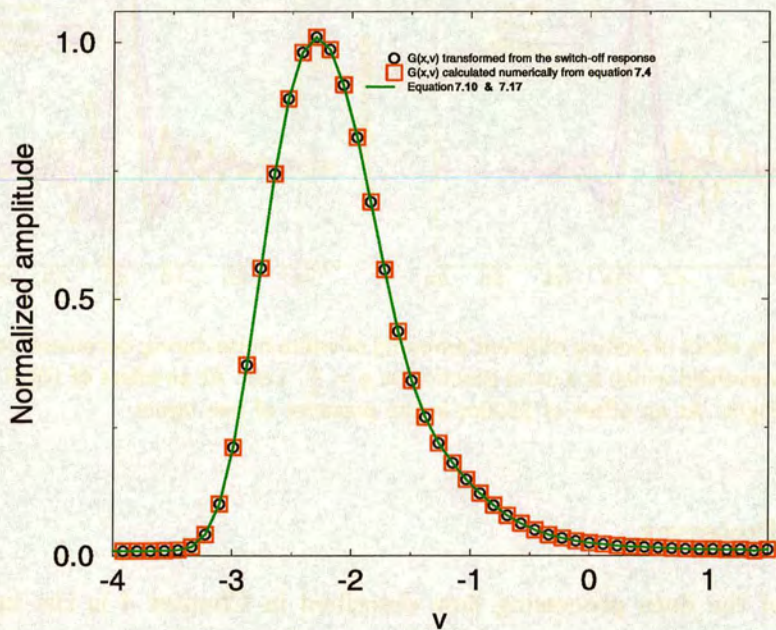

Figure 7.7: The function $G(x, v)$ after normalisation: after numerically transforming the switch-off response using the steps outlined on page 157 (circle), for an impulse source (equation 7.4) calculated numerically (square), and plots of the analytic expressions (equation 7.18 and 7.11 respectively) for these two cases (line).

159
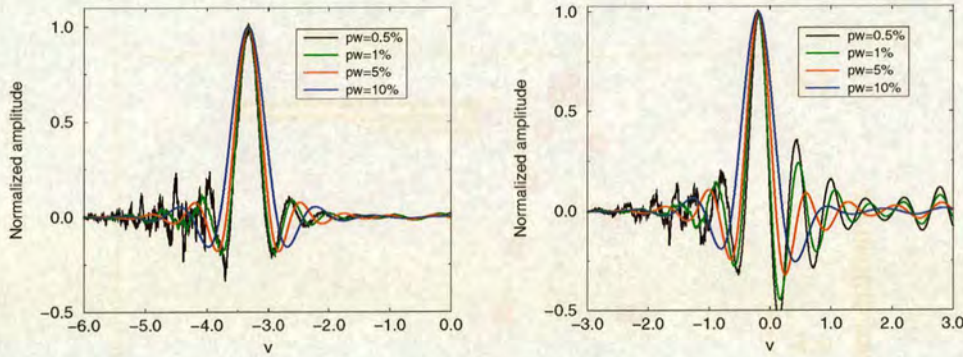
Figure 7.8: The effect of adding different amounts of white noise during deconvolution in recovering an equivalent wavefield which is a delta function at $q = \frac{x}{c}$. Left: At an offset of 100m in the presence of one layer. Right: At an offset of 3500m in the presence of two layers.

DPM Data Processing

The result of the data processing flow described in Chapter 4 is the input to DPM processing. So the input is the earth response function with the noise removed. The data may or may not have been differentiated in order to perform the deconvolution. However, in order to apply DPM processing, the input must be the deconvolved step function and not its derivative. If the data has been differentiated it must be integrated in order to recover the step response. Data are then converted to the log-time domain v where the data can be differentiated and the final step is to multiply by $\sqrt{\pi} exp(v)$. This recovers the function $\boldsymbol{G}(x, v)$ which is the input to the deconvolution step. In order to perform the deconvolution correctly, the entire function $\boldsymbol{G}(x, v)$ should be recorded, rising smoothly from zero and then falling smoothly to zero again, otherwise artefacts due to the discontinuity in the function will appear in the deconvolved function. The amount of this function that is recorded depends on the sampling interval of the data and the length of time the transient is recorded for. Figure 7.9 shows the amount of the function $\boldsymbol{G}(x, v)$ that is recorded for three different sampling rates and transient lengths. Figure 7.9 (left) was recorded at an offset of 500m and Figure 7.9 (right) was recorded at an offset of 3000m. In each plot the red line is the range used for the synthetic data, the green line is for a sampling interval of 1ms and a transient length of 2048ms which is the same as the Saint Illiers la Ville data, and the blue line is for a sampling interval of 0.05ms and a transient length of 100ms. It can be seen that a short sampling interval is important for capturing the rise of the function at early times but a long transient length is needed to capture the fall of the function to zero. However, it is not necessary to record for these long times once the dc value has been reached; the

transient length can be extrapolated to later times so that the function $G(x,v)$ decays smoothly to zero.

Depending on the noise content present in the data, a low pass filter can be applied at this point, as conversion to log-time will introduce high frequency noise at later times. Deconvolution of the function $W(v)$ (equation 3.92) is then applied to recover the function $R(x,v)$ and the equivalent wavefield domain can be recovered by converting from the v to the q domain using $q = exp(v)$. The processing flow is summarised in the flow chart in Figure 7.10.
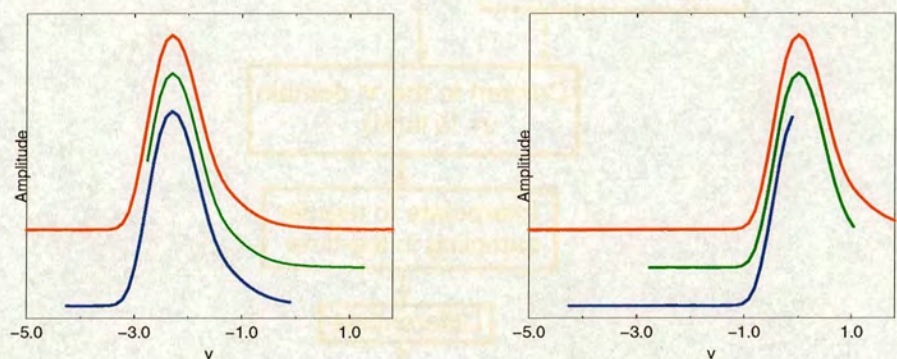
Figure 7.9: The length of the function $G(x,v)$ recorded using different sample rates and transient lengths. Left: At an offset of 500m. Right: At an offset of 3000m. The red line shows the range of values measured for the synthetic data used in this chapter, the green line is for a sampling interval of 1ms and a transient length of 2048ms, and the blue line is for a sampling interval of 0.05ms and a transient length of 100ms.

Input: Stacked impulse or step response for a S-R pair

Has data been differentiated?

Yes

No

Integrate to recover step response

Convert to the 'v' domain
$v = \frac{1}{2} \ln(4t)$

Interpolate to regular sampling in log-time

Differentiate

Multiply by $\sqrt{\pi} \exp(v)$

Low-pass filter

Taper so that **G**(x,v) rises and falls smoothly from zero

Deconvolve for W(v)

Convert to the 'q' domain
$q = \exp(v)$

Output: **R**(x,v)
The input for resistivity analysis

Output: **U**(x,q)
The equivalent wavefield

Figure 7.10: Flowchart for DPM processing.

7.5 Demonstration of direct resistivity determination using synthetic data

Having shown theoretically how to transform the switch-off transient response into the response to a directed point source, where the correct resistivity can be extracted from the data, I next demonstrate the technique with synthetic data. The simplest case of a source on the surface of a homogeneous halfspace is considered first for resistivities ranging from 10 to 500 Ωm. I then study the effect of source geometry on resistivity determination. The model is then extended to two layer cases with a resistive and conductive basement and a 3 layer (sandwich) case representing a buried reservoir. I then simulate real data by adding both periodic and random noise to the synthetic data: this gives an idea of the acquisition parameters required in the field if resistivity is to be determined accurately.

Resistivity determination over a halfspace

I produced synthetic data, generated over a 10, 100 and 500 Ωm halfspace. A total of 25 traces were produced, in each case with a near offset of 500m and a receiver interval of 100m, giving traces at an offset range from 500-2900m. I then transformed the initial data $\boldsymbol{E}(x,t)$ to the form $\sqrt{\pi}exp(v)\frac{\partial}{\partial v}\boldsymbol{E}(x,\frac{1}{4}exp(2v))$ using the technique described in section 7.4. The 1-D modelling code MODALL (Strack, 1992) was used to produce the synthetics, the result of testing the code is given in Appendix B.

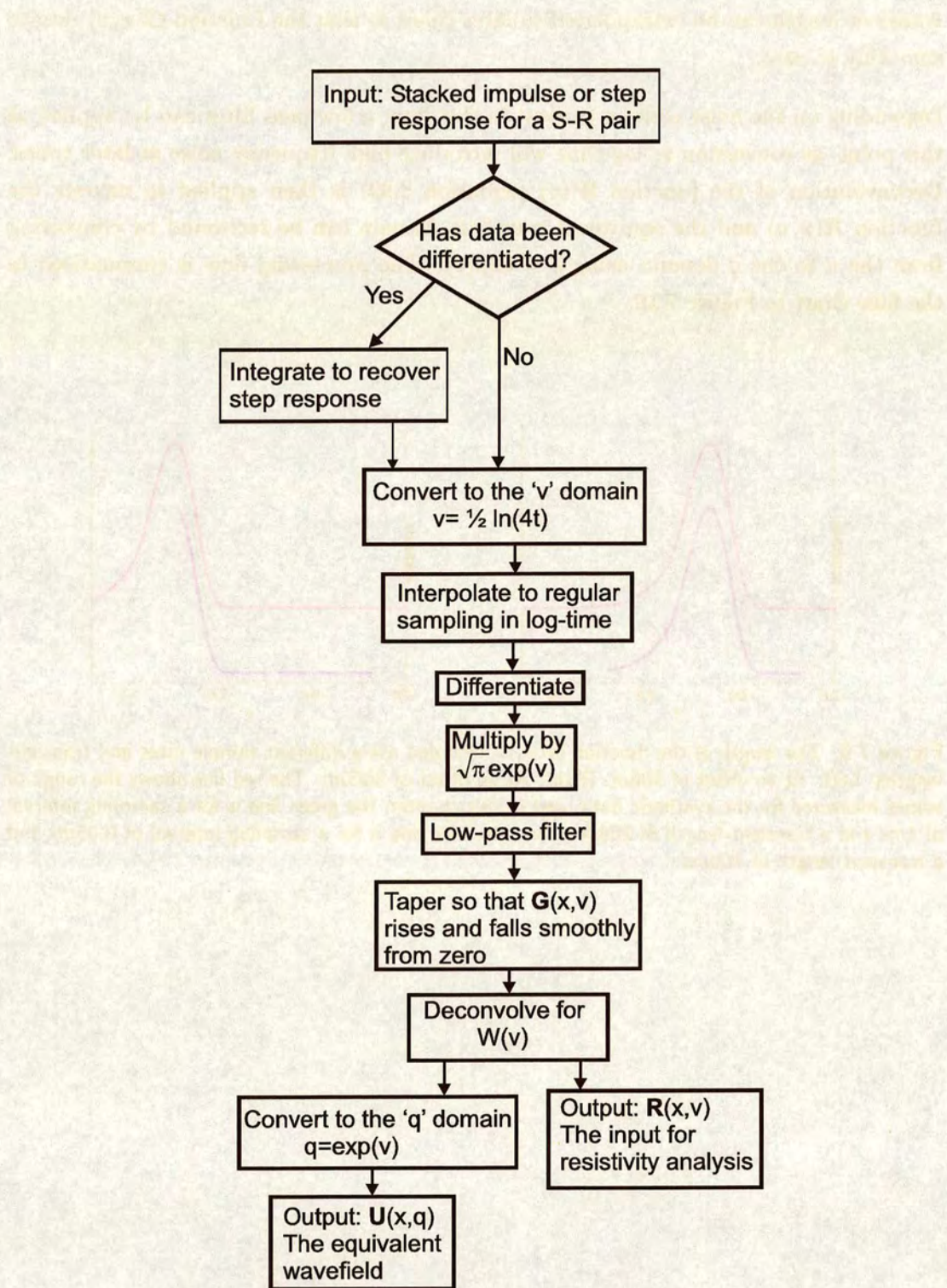The transformed data $\sqrt{\pi}exp(v)\frac{\partial}{\partial v}\boldsymbol{E}(x,\frac{1}{4}exp(2v))$ were converted to the $\boldsymbol{R}(x,v)$ domain by deconvolution of the function $W(v)$ (equation (3.92)). According to Ziolkowski & Hobbs (1998), the moveout of data in the equivalent wavefield domain is of the form $q = q_0 + \frac{x}{c}$. For a halfspace $q_0 = 0$ so in the v domain where $v = ln(q)$ the moveout is of the form $v = ln(\frac{x}{c})$. The result of the deconvolution is shown in Figure 7.11 (left) with the theoretical moveout curve shown in red. The data were then converted to the equivalent wavefield domain $\boldsymbol{U}(x,q)$ where the moveout is in the from of a straight line. This result is shown in Figure 7.11 (right): the theoretical moveout curve is overlain in green. It can clearly be seen from this figure that the peak of the waveform is now in the correct place and the correct resistivity can be obtained.

163
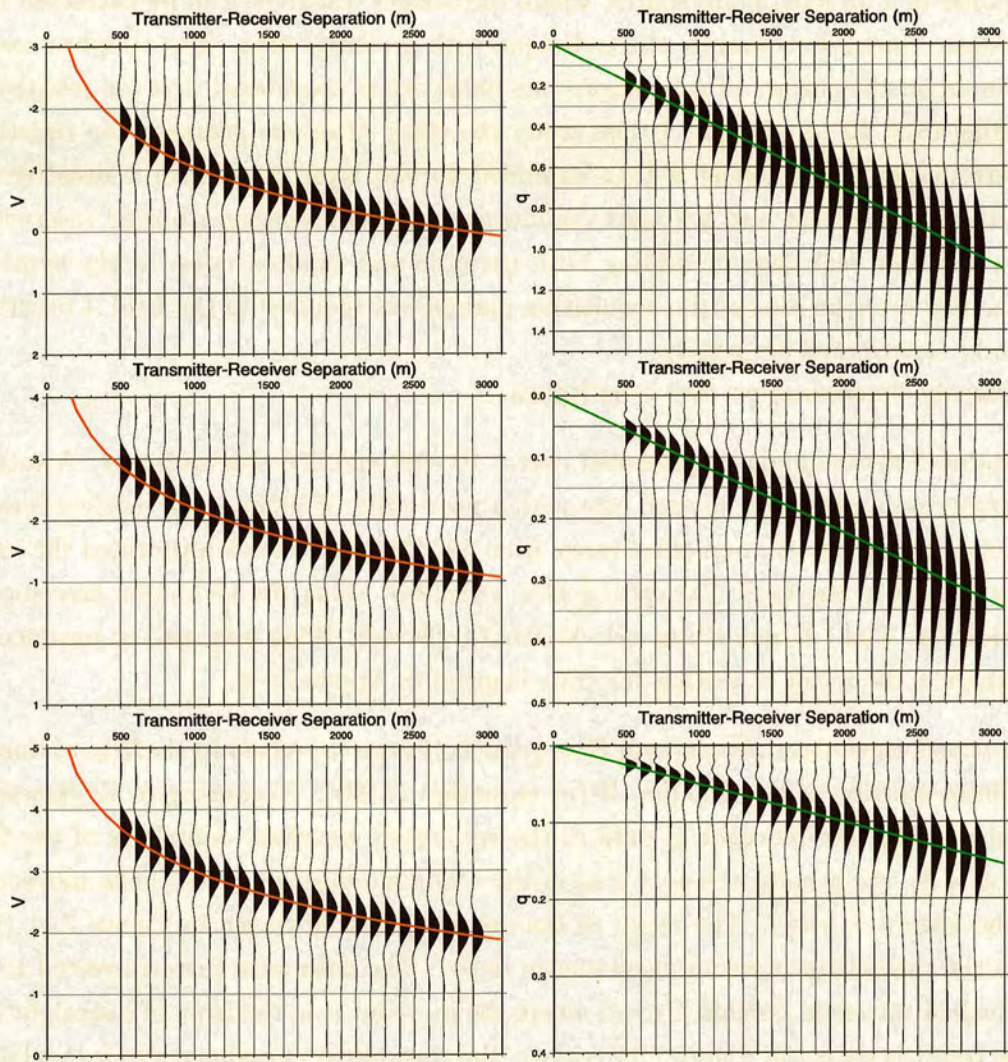
Figure 7.11: Resistivity determination over a halfspace. Left: Result of deconvolution $\boldsymbol{R}(x,v)$ after transforming the data to the form $\sqrt{\pi} exp(v) \frac{\partial}{\partial v} \boldsymbol{E}(x, \frac{1}{4} exp(2v))$. Top 10 Ωm, middle 100 Ωm and bottom 500 Ωm. The theoretical moveout curve is overlain in red. Right: The equivalent wavefield $\boldsymbol{U}(x,q)$ of the traces on the left. The theoretical moveout curve is overlain in green.

In seismic data processing, velocity information is extracted from the data in the common mid-point (CMP) domain by performing velocity analysis and selecting the stacking velocity based on the results of a semblance plot. In order to obtain the resistivity from EM data a 'resistivity analysis' can be applied in much the same way. I applied the analysis in the $R(x, v)$ domain where the 'EM wavelet' is the same on all traces, as can be seen from Figure 7.11. This involves varying the resistivity, ρ, and the intercept time $v_0 = ln(q_0)$ for the moveout curve over a wide range of values. The values of v_0 and ρ which maximise the stack provide information on sub-surface resistivity. For the top layer $v_0 = -\infty$ since the zero offset arrival time must be $t_0 = 0$ and $v_0 = \frac{1}{2}ln(4t_0)$. In the presence of more than one layer the value of v_0 for the second arrival provides information on the depth to the top of that layer.

The result of performing the analysis on the data in Figure 7.11 is shown in Figure 7.12. Plots a-c are for a 10 Ωm halfspace using traces at an offset of 100-1000m (a), 1100-2000m (b) and 2100-3000m (c). Plots d-f and g-i are equivalent results for a 100 and 500 Ωm halfspace respectively. In each case the maximum value occurs at the correct resistivity value, however, this is only obvious for the data recorded at short offsets shown in Figure 7.12. For data recorded at longer offsets the semblance value for larger resistivities increases. For resistivity values that are less than the correct value though the semblance value is the same for all offsets. The correct resistivity of the top layer is therefore identified as the value for which there is no variation in the semblance value with increasingly large negative values of v. Below this value the semblance values decreases quickly while above this value the semblance value remains close to the maximum. This effect is greater for data recorded at longer offsets. The result of the analysis for different offsets illustrates the diffusive nature of the data even in a non-diffusive wave-like domain, with the correct resistivity value more obvious in short offset data.

165

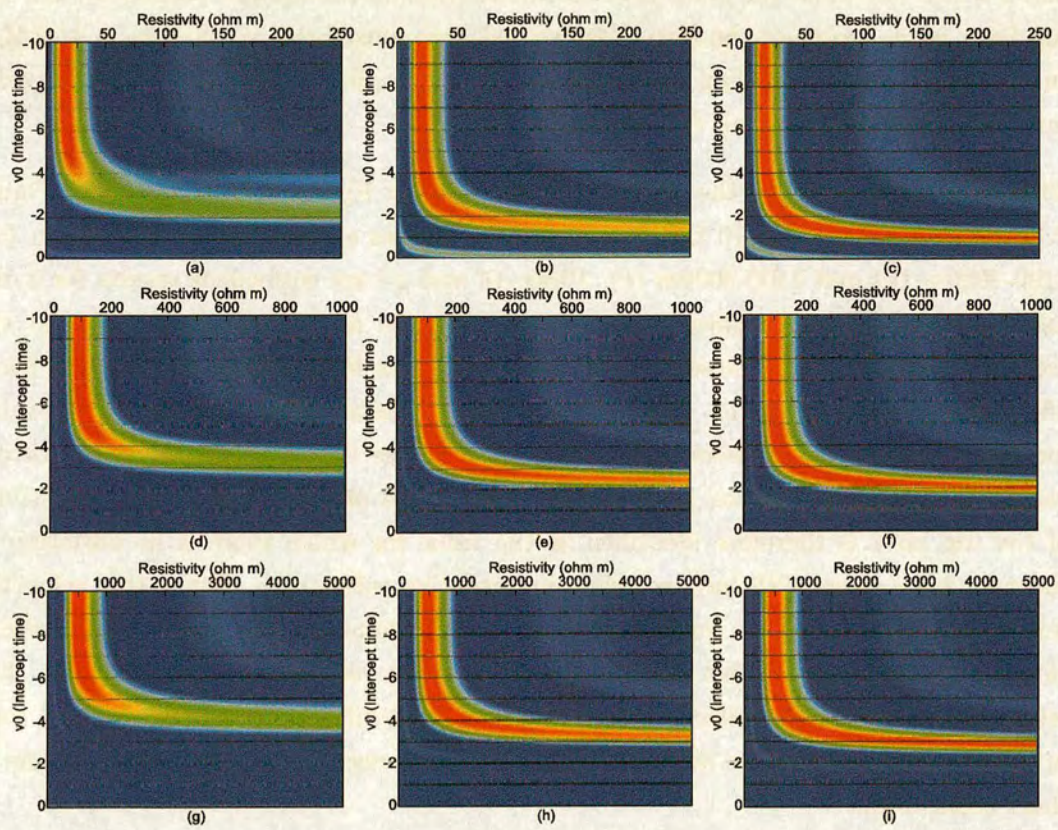Figure 7.12: The result of resistivity analysis over a halfspace. **Top**: Results for a 10 Ωm halfspace (a) 100-1000m (b)1100-2000m (c)2100-3000m. **Middle**: Results for a 100 Ωm halfspace (d) 100-1000m (e)1100-2000m (f)2100-3000m. **Bottom**: Results for a 500 Ωm halfspace (g) 100-1000m (h)1100-2000m (i)2100-3000m. The scaling in each plot is the same to enable comparison.

166

The effect of source geometry on resistivity determination

In all the results presented so far the source used in the modelling has been a point dipole source whose magnitude is defined by the dipole moment $\mathcal{D}$, which is simply the product of the dipole length and the input current. In reality, of course, the source has a physical geometry and, as mentioned in section 2.2, the grounded wire source acts like a dipole at offsets approximately five times greater than the dipole length. For long offset studies this approximation holds, but in short offset studies such as MTEM the effect of the source geometry must be considered. In determining resistivity values the source geometry will affect the values obtained at short offsets and give an incorrect value for the resistivity of the top layer.

To address this problem I have produced synthetic data using the 1-D code TEMD written by Knútur Árnason of the Icelandic Energy Authority. The code takes account of the source geometry by integrating over the length of the source dipole (The result of testing the code is given in Appendix B). Three different source lengths of 125, 250 and 500m centered on the origin were used. For each source length synthetic data from 100-1500m[1] offset were calculated with a receiver separation of 100m. The data I produced were generated over 1, 10 and 100 Ω m halfspaces. From these data the equivalent wavefield was calculated in the same way as the data in section 7.5 page 163. The results shown in Figure 7.13 are the resistivity values calculated from the peak values of individual traces using $c = \frac{x}{q}$ and $\rho = c^2\mu$. They show that the resistivity value at near offsets is increased due to the shortened distance from the end of the transmitter to the receiver. Because these results are based on single traces, they give a clear picture of where the dipole approximation is valid, since the results are not influenced by the moveout of other traces. As the receiver approaches the edge of the transmitter, the resistivity tends to ∞ as the effective offset tends to 0. It can be seen that the rule of thumb that the dipole approximation holds for offsets five times the source length is valid. For example, at offsets of 625m and 1250m, the resistivity values obtained for the 125m and 250m long sources respectively are essentially those of the halfspace. It can be seen that the effect of the source is independent of the resistivity of the first layer.

The results in Figure 7.13 show how source geometry affects the resistivity values obtained at single points. However, in determining the resistivity of a layer, and where the response from one layer stops and that of a deeper layer begins requires analysis of the moveout of a number of traces. This cannot be done based on a single trace.

---

[1] The nearest offset possible is half the source length, otherwise the receiver is within the source. Therefore, for the 250m and 500m source lengths the near offset is 200m and 300m respectively.

Applying 'resistivity analysis' to a number of traces, as would be done to real data, gives a different value for the resistivity. Figure 7.14 shows the resistivity value obtained as a result of applying resistivity analysis to between two and fourteen traces for sources of length 125, 250 and 500m over 1, 10 and 100 Ωm halfspaces. The resistivity values are now less than that of the halfspace because the moveout between traces is larger due to the early arrival of the traces at the shortest offsets. In contrast to the results in Figure 7.13, the results in Figure 7.14 at long offsets are biased by the effect of the source at very short offsets. For example, for a 250m long source which is the same length as that used in the MTEM measurements at Saint Illiers la Ville, the result of resistivity analysis based on traces from 200-600m is a resistivity value that is 20% less than the actual value.

In applying resistivity determination to real data it is therefore important to be aware of the effect of the source geometry on the values obtained. Because the effect of the source is independent of the resistivity of the ground, it should be possible to correct for this effect. This would then allow short offset data to be interpreted with confidence.
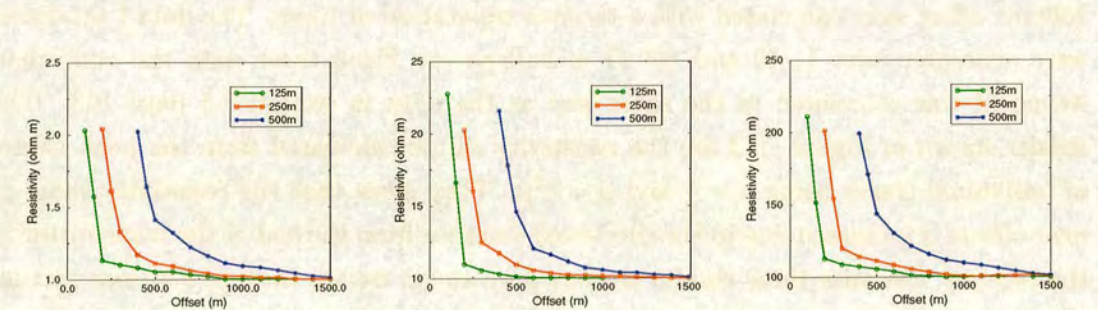

Figure 7.13: The effect of source geometry on resistivity determination calculated using data at single points. Left: Over a 1 Ωm halfspace. Middle: Over a 10 Ωm halfspace. Right: Over a 100 Ωm halfspace.
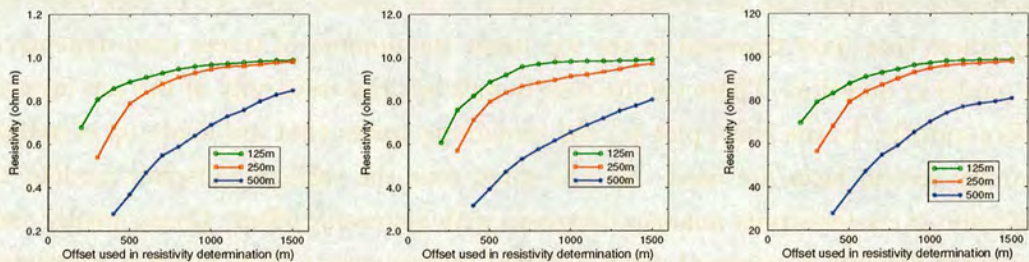
Figure 7.14: The effect of source geometry on resistivity determination calculated using data from a range of offsets. Left: Over a 1 Ωm halfspace Middle: Over a 10 Ωm halfspace. Right: Over a 100 Ωm halfspace.

Resistivity determination in the presence of 2 layers

Having established that the method works for determining the resistivity over a half space over 2.5 orders of magnitude for a point dipole source and obtained a measure of the effect of source geometry, the next test is to extend the model to 2 layers. I created a total of 5 models each consisting of two layers. These are summarised in table 7.1. In the first three models the depth to the second layer is varied, with the resistivity values of the layers kept constant. In the fourth model the resistivity of the top layer is increased to see the effect of changing resistivity. For each of these models the bottom layer is more resistive than the top layer; in model 5 the bottom layer is more conductive than the top layer.

Model	Layer 1 resistivity	Layer 1 thickness	Layer 2 resistivity
1	10 Ωm	250m	200 Ωm
2	10 Ωm	500m	200 Ωm
3	10 Ωm	1000m	200 Ωm
4	50 Ωm	500m	200 Ωm
5	200 Ωm	500m	10 Ωm

Table 7.1: Resistivities and thicknesses used in generating 2 layer models.

The results of DPM and resistivity analysis for these models are presented in Figures 7.15-7.24. For each model a plot is shown of the result in the $R(x, v)$ and the $U(x, q)$ domain with the theoretical moveout curve for the top layer overlain in blue and that of the bottom layer in red. A series of four semblance type plots is also shown for each model. The first one (a) in each case is the result of resistivity analysis using all 36 traces. In each case it is difficult to make a meaningful interpretation of the resistivity structure as the moveout difference between the two arrivals is not large enough to

169

separate the peaks from different arrivals, with the result being that the peak value is somewhere between the two resistivity values. The second plot (b) in each case uses only traces that have travelled in the top layer; the number of traces used depends on the model in question. These results clearly pick out the resistivity of the top layer for all five models. In the third plot (c) the remaining traces that are made up of arrivals from the second layer are used. As was noted over the various halfspace models, the resolution of the resistivity analysis decreases with increasing offset. Consequently these results are difficult to interpret using standard scaling since a large range of resistivities give a large amplitude. The fourth plot (d) shows the same data as (c) but zoomed in, and the scaling has been changed to enable the maximum amplitude to stand out more. Now a single 'bullseye' with the correct resistivity at the centre can be picked out. The correct resistivity is obtained, the width of the peak gives an indication of uncertainty involved in determining the resistivity.

The result of model 5, where a resistor overlies a conductor, surprisingly gives the best result. Two distinct arrivals can be seen that are separated in time in Figure 7.23. This result is more akin to seismic reflection as the arrival from the second layer never becomes the first arrival.

Figure 7.15: The result of DPM by deconvolution in log-time to recover a delta function for model 1. Theoretical moveout curves for the top and bottom layers are overlain in blue and red respectively. Top: $R(x, v)$. Bottom: $U(x, q)$.

Figure 7.16: The result of DPM by deconvolution in log-time to recover a delta function for model 2. Theoretical moveout curves for the top and bottom layers are overlain in blue and red respectively. Top: $R(x, v)$. Bottom: $U(x, q)$.

172
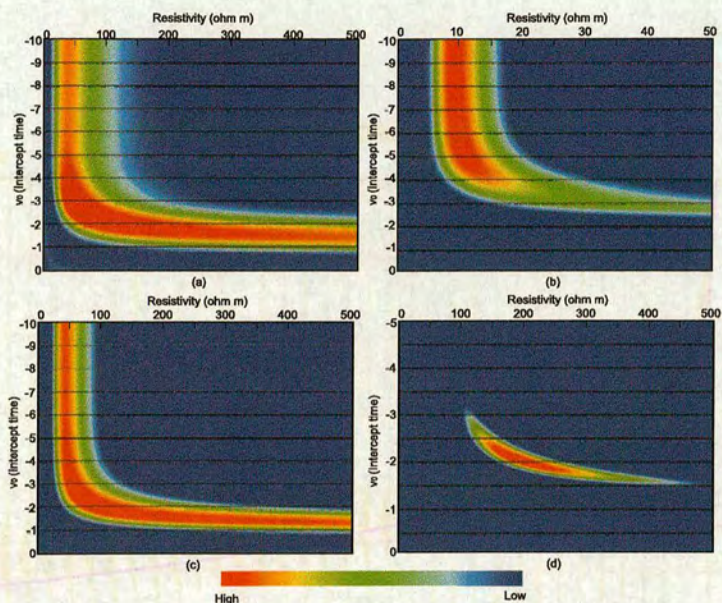
Figure 7.17: Resistivity analysis for model 1. (a) Result using all 36 traces. (b) Result using the first 4 traces. (c) Result using traces 6-36. (d) Same as (c) but zoomed in with different scaling to highlight the maxima.
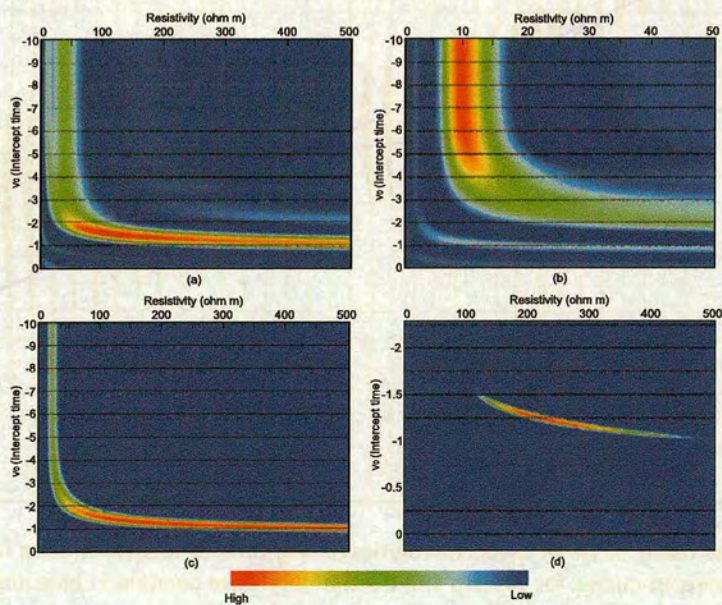
Figure 7.18: Resistivity analysis for model 2. (a) Result using all 36 traces. (b) Result using the first 10 traces. (c) Result using traces 15-36. (d) Same as (c) but zoomed in with different scaling to highlight the maxima.

173
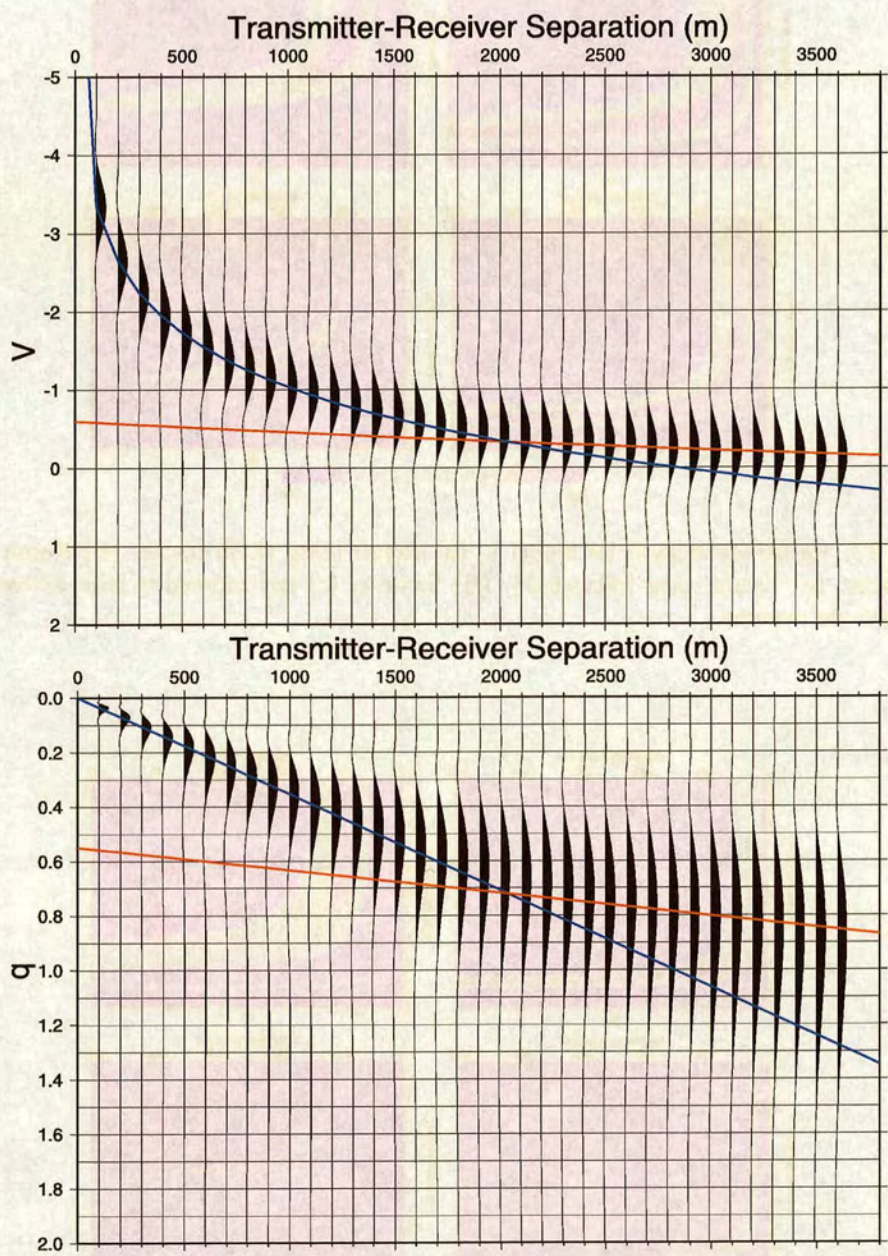
Figure 7.19: The result of DPM by deconvolution in log-time to recover a delta function for model 3. Theoretical moveout curves for the top and bottom layers are overlain in blue and red respectively. Top: $\boldsymbol{R}(x, v)$. Bottom: $\boldsymbol{U}(x, q)$.
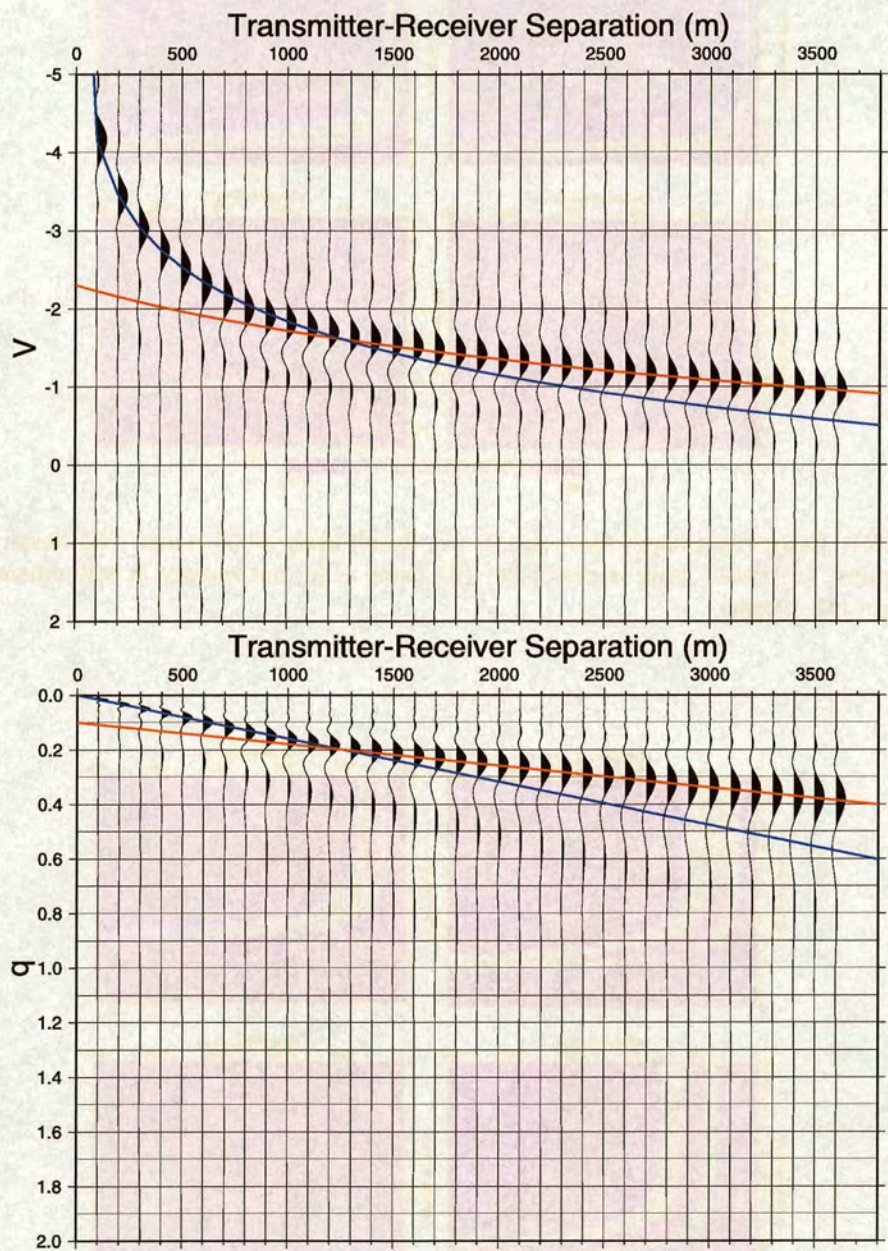
Figure 7.20: The result of DPM by deconvolution in log-time to recover a delta function for model 4. Theoretical moveout curves for the top and bottom layers are overlain in blue and red respectively. Top: $R(x, v)$. Bottom: $U(x, q)$.

175
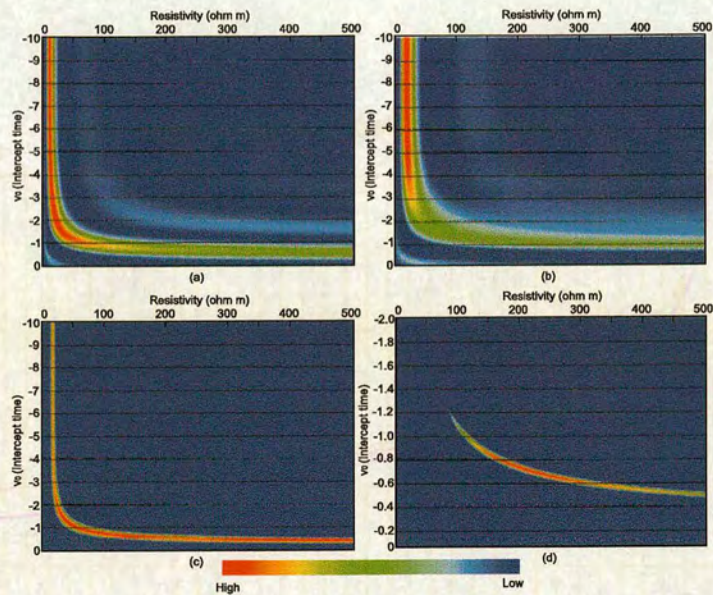
Figure 7.21: Resistivity analysis for model 3. (a) Result using all 36 traces. (b) Result using the first 20 traces. (c) Result using traces 21-36. (d) Same as (c) but zoomed in with different scaling to highlight the maxima.
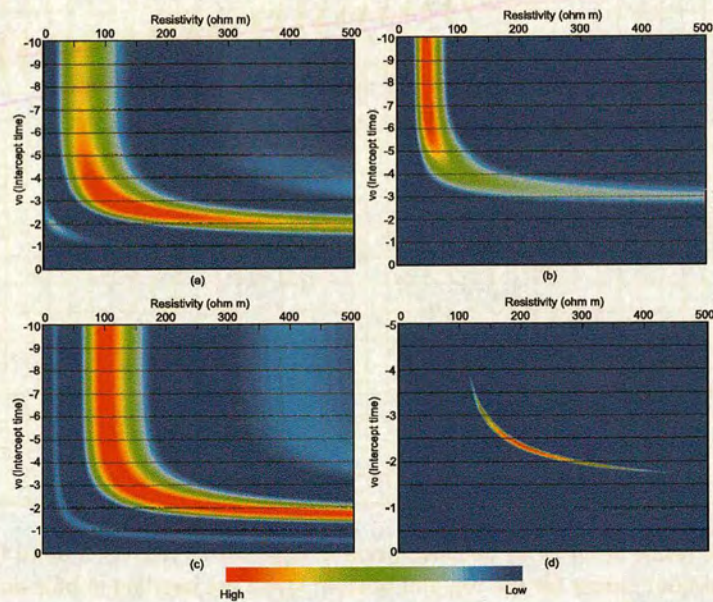
Figure 7.22: Resistivity analysis for model 4. (a) Result using all 36 traces. (b) Result using the first 12 traces. (c) Result using traces 13-36. (d) Same as (c) but zoomed in with different scaling to highlight the maxima.
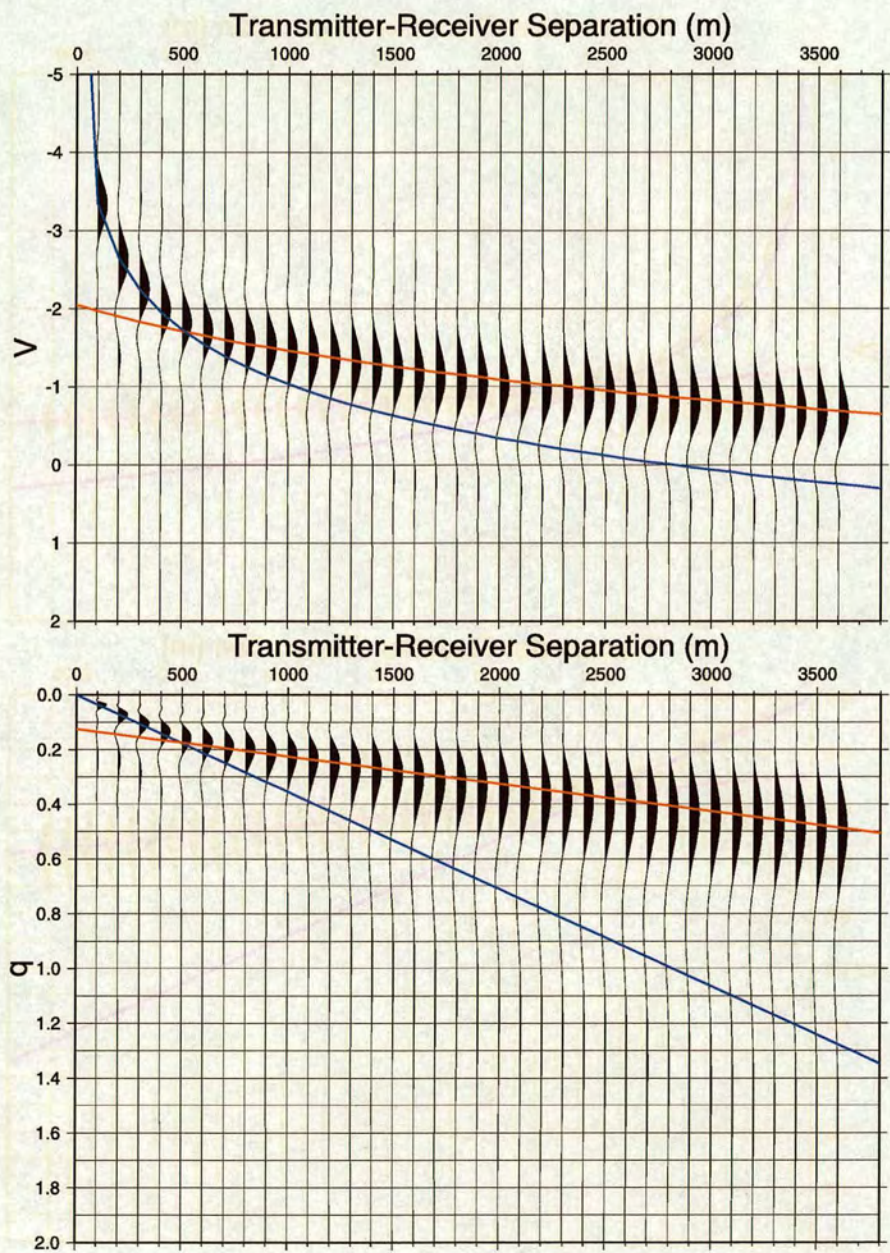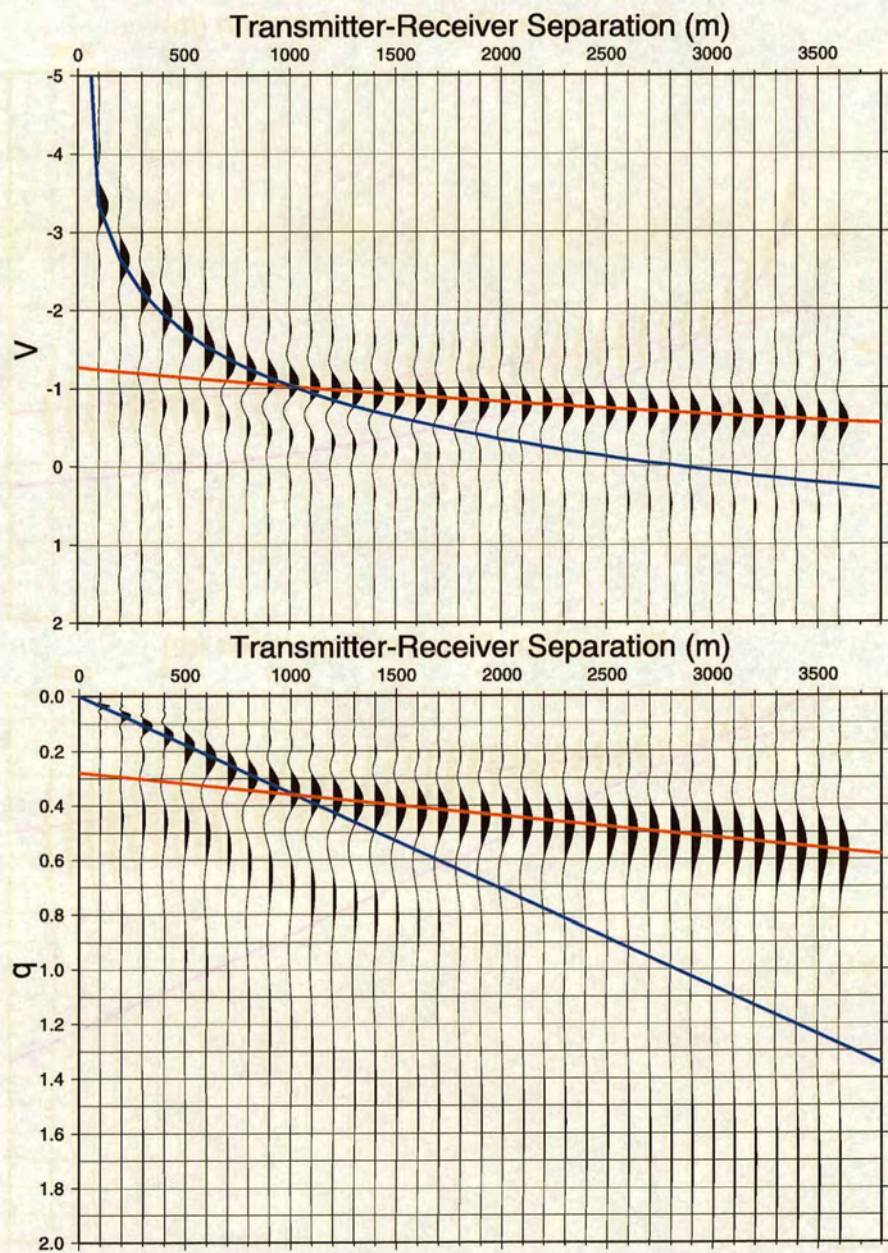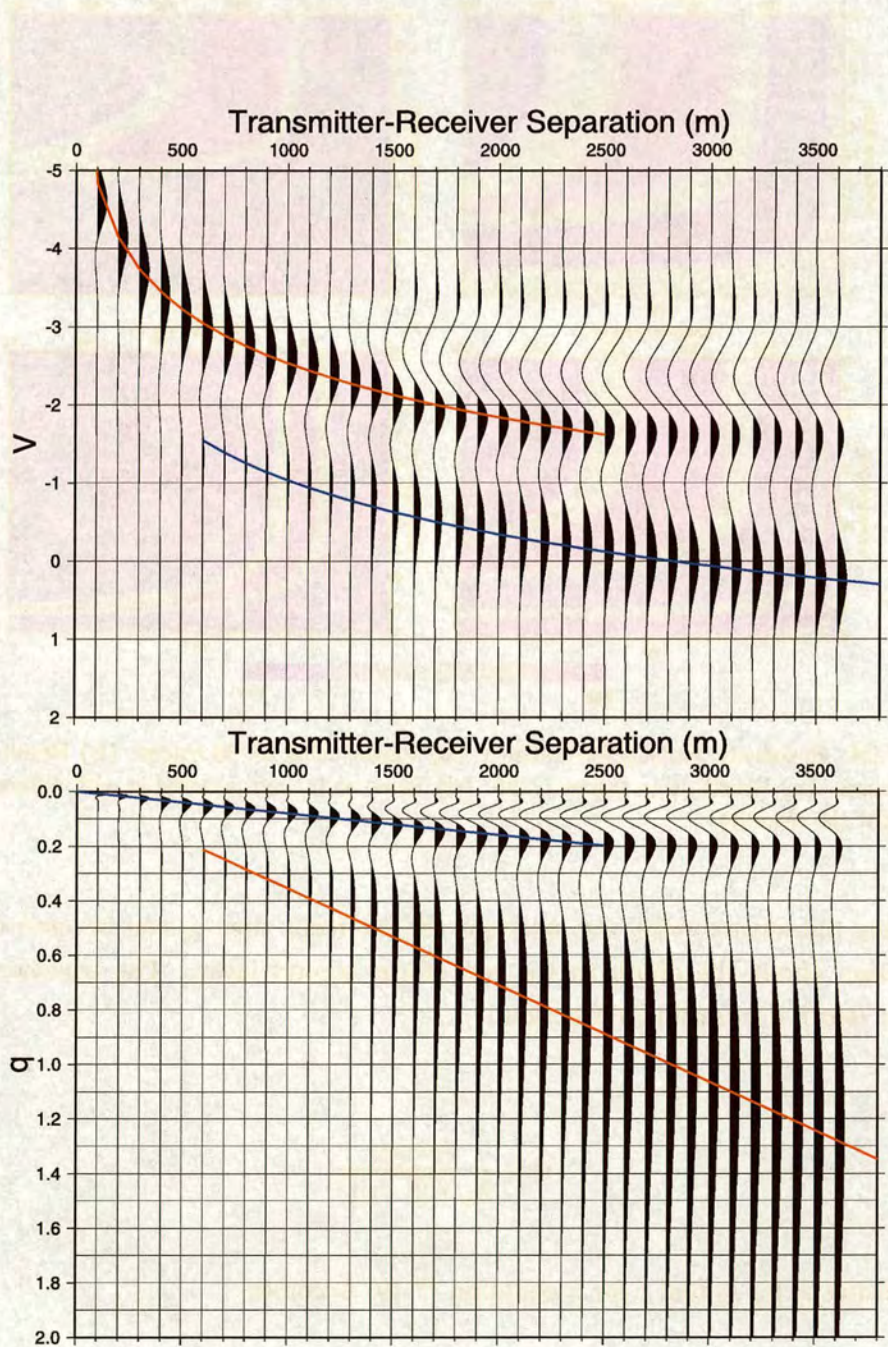
Figure 7.23: The result of DPM by deconvolution in log-time to recover a delta function for model 5. Theoretical moveout curves for the top and bottom layers are overlain in blue and red respectively. Top: $\boldsymbol{R}(x,v)$. Bottom: $\boldsymbol{U}(x,q)$.
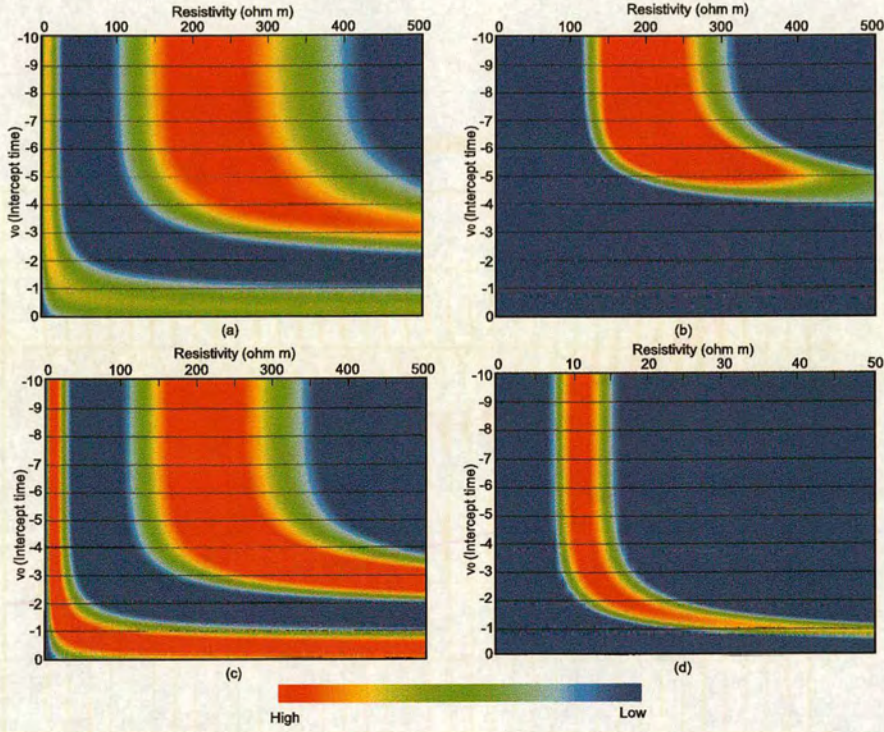
Figure 7.24: Resistivity analysis for model 5. (a) Result using all 36 traces. (b) Result using the first 10 traces. (c) Result using traces 11-36. (d) Same as (c) but zoomed in with different scaling to highlight the maxima.

Extending the seismic refraction analogy, the intercept time q_0 can be used to obtain information about the depth to the top of the second layer. The equation for the refractor depth d in seismic refraction is,

$$d = \frac{t_0 v_1 v_2}{2\sqrt{(v_2^2 - v_1^2)}}.$$ (7.19)

Substituting q_0 for t_0 and c for v equation (7.19) becomes,

$$d = \frac{q_0 c_1 c_2}{2\sqrt{(c_2^2 - c_1^2)}},$$ (7.20)

the crossover distance at which the arrival from the second layer becomes the first arrival is given by,

178

$$x_{cross} = 2d\sqrt{\left(\frac{c_2 + c_1}{c_2 - c_1}\right)}. \qquad (7.21)$$

The results of applying these equations to the results obtained for models 1-5 are given in table 7.2. The values denoted by (M) are the input model values and those denoted (R) are the values recovered from the model data. For the crossover distance the (F) label denotes the value obtained by substituting the recovered values into equation 7.21, the (M) label denotes the value obtained by substituting the model values into equation 7.21 and the (D) label denotes the value obtained from the data itself. For calculation of the depth d (R1) denotes the depth calculated using the recovered values for c_1, c_2 and q_0 in equation 7.20, (R2) denotes the value obtained when substituting the recovered values for c_1 and q_0 into equation 7.23.

It can immediately be seen from these results that despite obtaining the correct resistivity values for the 2 layers in each of the 5 models, the application of equation 7.20, which is taken directly from seismic refraction, does not give the correct value for the depth to the top of the second layer; for each model the depth obtained is approximately 75% of the true value. For model 5, where a resistor overlies a conductor, the refraction analogy does not apply at all. The results for the crossover distance are also not in agreement when the input model values (M) are compared with the results recovered from the model data (D) and those obtained by substituting the numerically recovered values $c1$, $c2$ and d into equation 7.21(F). However, the values for (D) and (F) in quite good agreement.

An alternative approach to obtaining the depth to the top of the second layer is to use the equation for field penetration depth,

$$d = \sqrt{\frac{2t\rho}{\mu}}. \qquad (7.22)$$

This equation is derived up to a multiplicative constant from the scaling properties of Maxwell's equations (Nekut & Spies, 1989). The depth d is the depth for a given time t and resistivity ρ to which a uniform constant EM field has diffused. The q domain intercept time gives the minimum time taken for an EM wave to travel down to the top of the second layer and back again. Converting this intercept time into a real time t using the fact that $t = \frac{q^2}{4}$, this time and the resistivity value recovered for the top

179

Parameter	Model 1	Model 2	Model 3	Model 4	Model 5
c_1	2802(R)	2827(R)	2795(R)	6168(R)	12673(R)
	2821(M)	2821(M)	2821(M)	6308(M)	12616(M)
c_2	12599(R)	12537(R)	11987(R)	12603(R)	2951(R)
	12616(M)	12616(M)	12616(M)	12616(M)	2821(M)
ρ_1	9.87(R)	10.04(R)	9.82(R)	47.8(R)	201.8(R)
	10.0(M)	10.0(M)	10.0(M)	50.0(M)	200.0(M)
ρ_2	199.5(R)	197.5(R)	180.6(R)	199.6(R)	10.94(R)
	200.0(M)	200.0(M)	200.0(M)	200.0(M)	10.0(M)
q_0	0.129	0.271	0.549	0.1098	na
d	185(R1)	393(R1)	789(R1)	389(R1)	na
	255(R2)	539(R2)	1085(R2)	489(R2)	na
	250(M)	500(M)	1000(M)	500(M)	500(M)
x_{cross}	464(F)	1062(F)	2001(F)	1329(F)	na
	628(M)	1255(M)	2511(M)	1732(M)	na
	500(D)	1100(D)	2000(D)	1100(D)	na

Table 7.2: Results for 2 layer models.

layer when substituted into equation 7.22 gives a value for the thickness of this layer. For model 1 a depth of 255m is obtained compared with the true value of 250m, model 2 the value obtained is 539m compared with a true value of 500m, for model 3 1085m is recovered compared to the true value of 1000m and for model 4 a depth of 489m is obtained compared with a true value of 500m. These results are remarkably close to the correct values and provide an easy way of determining the thickness of the top layer. The results appear to be more accurate for smaller resistivity contrasts and shallower depths. Equation 7.22 can be re-written in terms if c_1 and q_o as,

$$d = \sqrt{\frac{c_1^2 q_0^2}{2}}. \tag{7.23}$$

The reason why equation 7.20 gives incorrect results when the data are in an equivalent wavefield that obeys the wave equation is unknown and an area for possible future study.

Resistivity determination in the presence of 3 layers

The previous section illustrated that the correct resistivity could be determined in the presence of two layers for a variety of models. To study the effectiveness of resistivity determination in the presence of three layers I produced synthetic data for three models with three layers. In each case the resistivities of each layer were kept constant as well as the depth to the top of the second layer. The only parameter that was varied was the thickness of the middle layer. The three models are summarised in table 7.3.

Model	Layer 1 resistivity	Layer 1 thickness	Layer 2 resistivity	Layer 2 thickness	Layer 3 resistivity
6	10 Ωm	500m	200 Ωm	25m	10 Ωm
7	10 Ωm	500m	200 Ωm	100m	10 Ωm
8	10 Ωm	500m	200 Ωm	500m	10 Ωm

Table 7.3: Resistivities and thicknesses used in generating 3 layer models.

The results for model 6 which represents a thin resistive hydrocarbon layer are shown in Figure 7.25. It can clearly be seen that there are three distinct arrivals present. The moveout of these arrivals has been highlighted with blue, red and yellow curves for the first, second and third arrivals respectively. The blue curve is the theoretical moveout curve for the top layer while the red and yellow curves are calculated from the maxima of each trace. It can be seen from the bottom plot in this figure that the slope of the blue and the yellow curves are parallel, indicating the same resistivity of 10 Ωm which is the resistivity of both the top and bottom layer. However, the resistivity obtained from the slope of the second arrival of 27 Ωm does not agree well with the actual value of 200 Ωm. The results of resistivity analysis for the data in Figure 7.25 are shown in Figure 7.26. Resistivity values for the first, second and third layers of 9.91, 27 and 11.7 Ωm were obtained, and substituting $q_0 = 0.130$, $c_1 = 2821$ and $c_2 = 4635$ into equation 7.20 gives a depth of $d = 231m$ which does not agree well with the real value of 500m, while substituting values for c_1 and q_0 into equation 7.23 gives a depth of 259m which is also in poor agreement.

Results for model 7 are shown in Figure 7.27. For this model only two distinct arrivals can be seen, with the moveout curve of the first and second arrivals overlain in blue and red respectively. The results of resistivity analysis for the data in Figure 7.27 are shown in Figure 7.28. Resistivity values for the first and second layers of 10.06 and 93.5 Ωm were obtained, and substituting $q_0 = 0.223$, $c_1 = 2829$ and $c_2 = 8624$ into equation 7.20 gives a depth of $d = 333m$, which does not agree well with the real value of 500m but is closer than the value obtained from model 6; substituting these values into equation 7.23 gives a depth of 446m which is also closer to the correct value. Also,

181

the resistivity value of the second layer, although still wrong, is closer to the correct value than that obtained in model 6.

Results for model 8 are shown in Figure 7.29. For this model, as with model 7, two distinct arrivals can be seen, with the moveout curve of the first and second arrivals overlain in blue and red respectively. The results of resistivity analysis for the data in Figure 7.29 are shown in Figure 7.30. Resistivity values for the first and second layers of 9.97 and 198 Ωm were obtained, and substituting $q_0 = 0.2718$, $c_1 = 2817$ and $c_2 = 12553$ into equation 7.20 gives a depth of $d = 393m$ which is closer than the value obtained from model 6 or 7; the result obtained from equation 7.23 is now 539m. Also, the resistivity value of the second layer is now correct. These results for resistivity and depth are almost identical to those obtained for model 2 which consists of a 500m thick top layer of resistivity 10 Ωm underlain by a 200 Ωm halfspace. Figure 7.31 shows the moveout of the first arrival for model 6,7,8 and 2. From this it can be seen how similar the results of models 2 and 8 are. The thickness of the middle layer clearly has an effect on the results obtained. As the thickness of the middle layer is increased, the resistivity value obtained for that layer increases up to a certain thickness at which the correct value is obtained. In this case a thickness of 500m is thick enough to obtain the correct result but a thickness of 100m is not. This result shows where the seismic refraction analogy begins to break down. In seismic refraction the seismic ray only 'sees' the top of the layer and the velocity value obtained is independent of the thickness of the layer. The results obtained in this section suggest that, even though the EM data has been transformed to an equivalent wavefield, it does not obey such simple laws of propagation. The EM signal appears to travel not only in the top of the layer but also in a region beneath the top of the layer. As a result, when the layer is thin it will be influenced by the layer below it, which causes the resistivity value obtained to be affected. This result seriously complicates any attempt to make a meaningful interpretation from data collected over a multilayered earth. The inherent problem of equivalence discussed in Chapter 2 is present even in the equivalent wavefield. The fact that the seismic refraction analogy breaks down is perhaps not surprising given the complexity of EM wave propagation and it may also explain why values obtained for the depth using the seismic refraction formula do not give the right answer. The seismic refraction analogy was based on results presented by Wilson (1997). However, he only considered a three layer case in which the middle layer was 700m thick at a depth of 700m and did not investigate any thin layer models.

Parameter	Model 6	Model 7	Model 8
c_1	2808(R)	2829(R)	2817(R)
	2821(M)	2821(M)	2821(M)
c_2	4635(R)	8624(R)	12553(R)
	12616(M)	12616(M)	12616(M)
c_3	3051(R)	-(R)	-(R)
	2821(M)	2821(M)	2821(M)
ρ_1	9.91(R)	10.06(R)	9.97(R)
	10.0(M)	10.0(M)	10.0(M)
ρ_2	27(R)	93.5(R)	198(R)
	200(M)	200(M)	200(M)
ρ_3	11.7(R)	-(R)	-(R)
	10.0(M)	10(M)	10.0(M)
q_0	0.13(R)	0.223(R)	0.2718(R)
d	231(R1)	333(R1)	393(R1)
	259(R2)	446(R2)	539(R2)
	500(M)	500(M)	500(M)
x_{cross}	932(F)	936(F)	988(F)
	1000(D)	1000(D)	1000(D)
	1255(M)	1255(M)	1255(M)

Table 7.4: Results for 3 layer models.
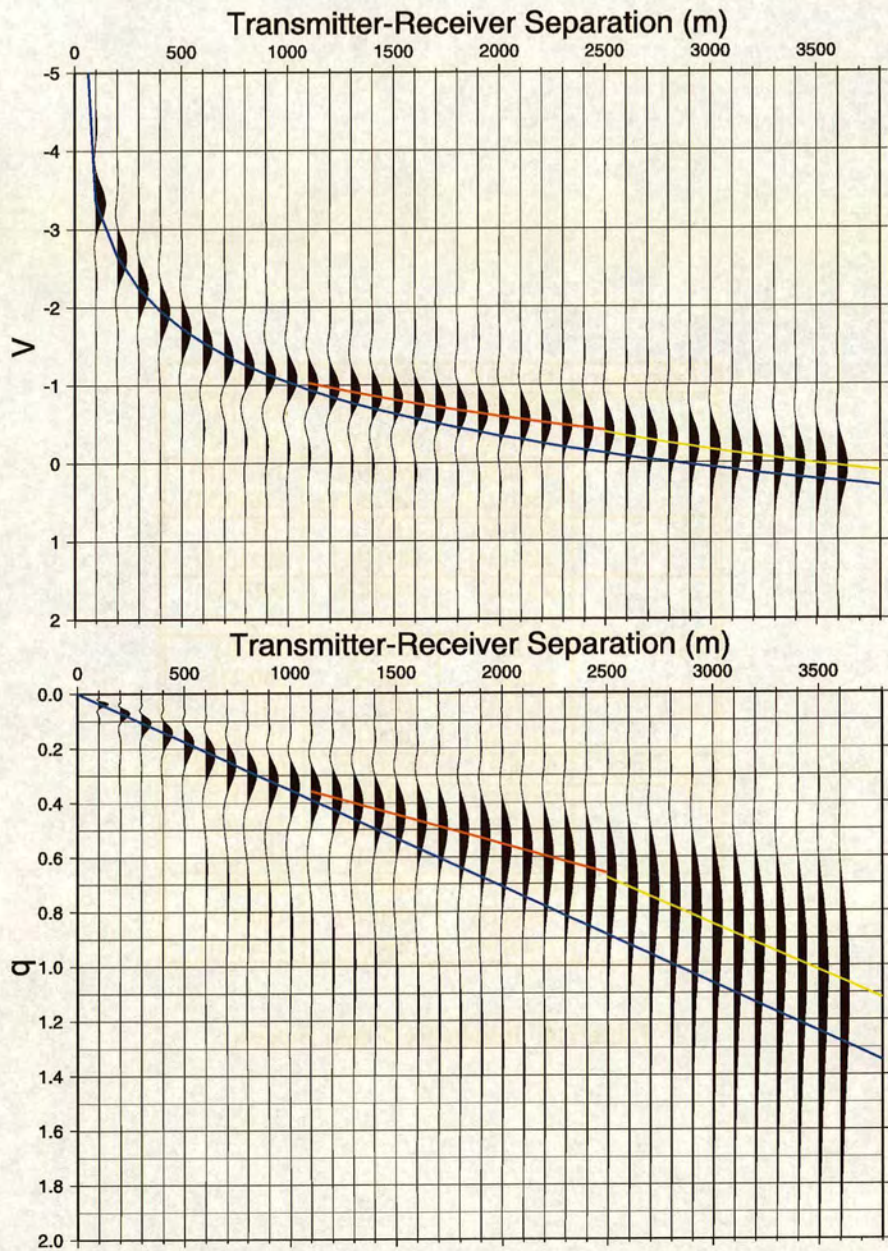
Figure 7.25: The result of DPM by deconvolution in log-time to recover a delta function for model 6. Theoretical moveout curve for the top layer is overlain in blue. Moveout curves for the second and third arrivals are overlain in red and yellow respectively. Top: $R(x, v)$. Bottom: $U(x, q)$.
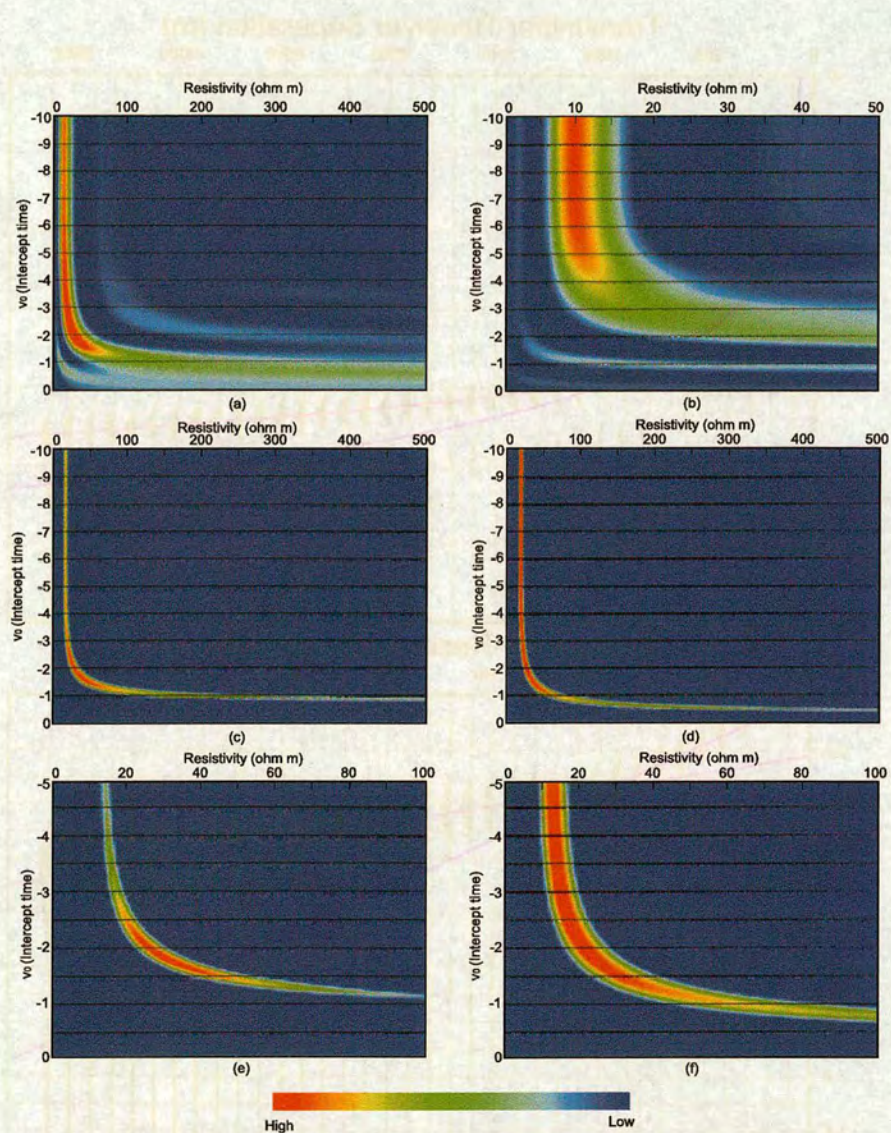
Figure 7.26: Resistivity analysis for model 6. (a) Result using all 36 traces. (b) Result using the first 10 traces. (c) Result using traces 11-24. (d) Result using traces 25-36. (e) Same as (c) but zoomed in with different scaling to highlight the maxima. (f) Same as (d) but zoomed in with different scaling to highlight the maxima.
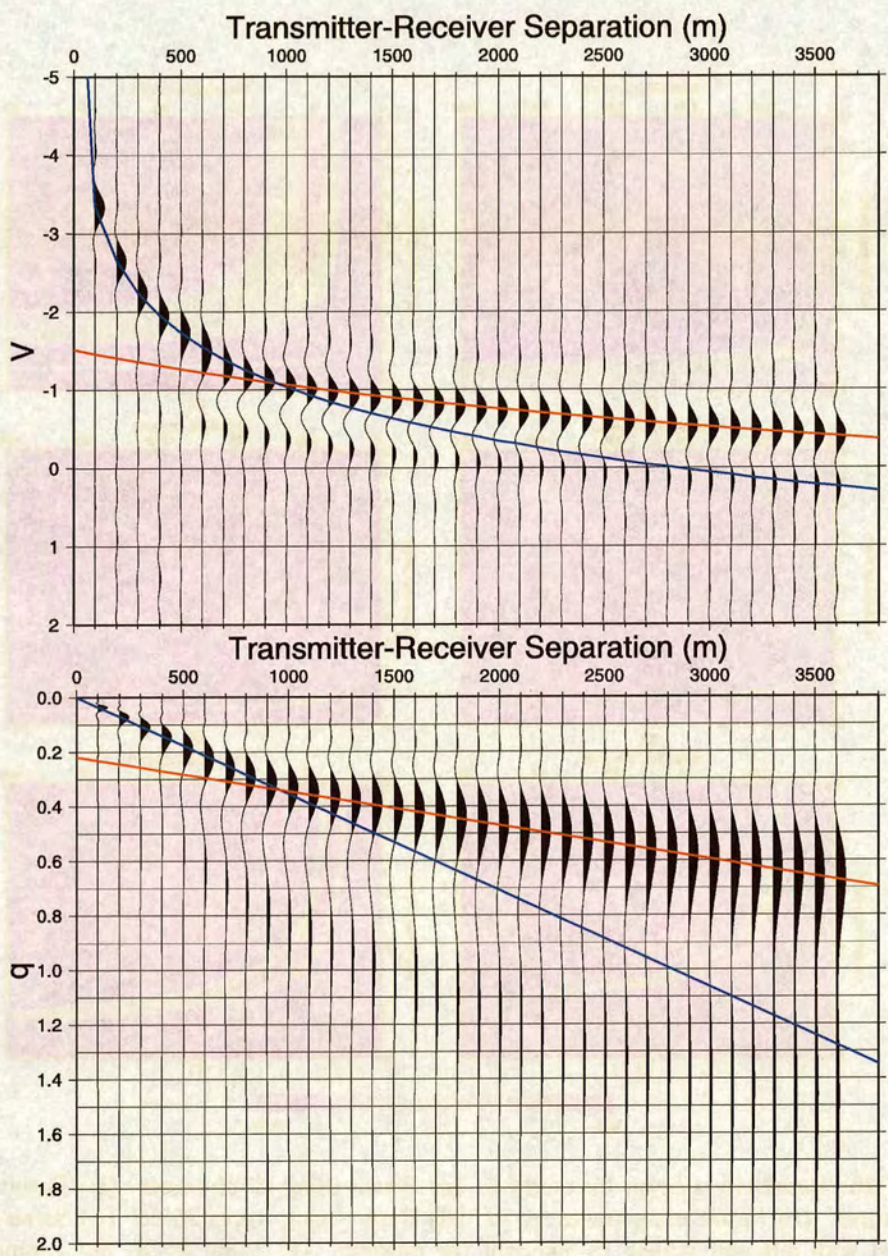
Figure 7.27: The result of DPM by deconvolution in log-time to recover a delta function for model 7. Theoretical moveout curve for the top layer is overlain in blue. Moveout curve of the second arrival is overlain in red. Top: $R(x,v)$. Bottom: $U(x,q)$.

186
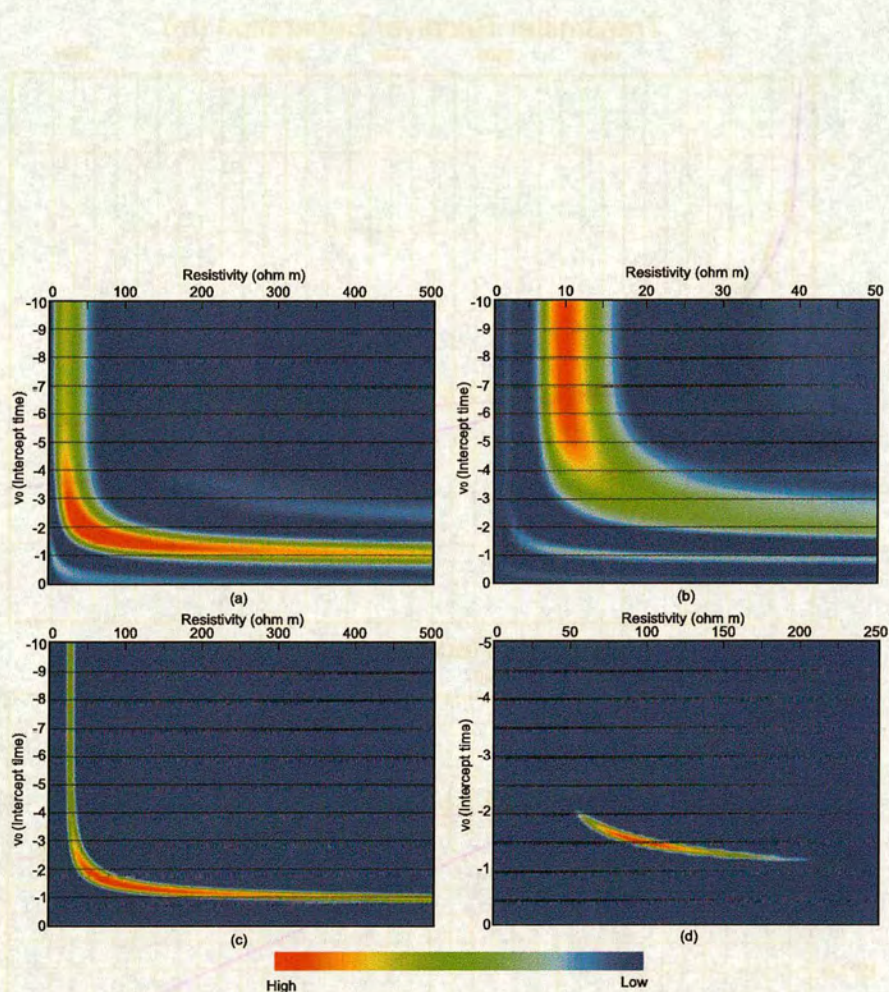
Figure 7.28: Resistivity analysis for model 7. **(a)** Result using all 36 traces. **(b)** Result using the first 9 traces. **(c)** Result using traces 12-36. **(d)** Same as (c) but zoomed in with different scaling to highlight the maxima.
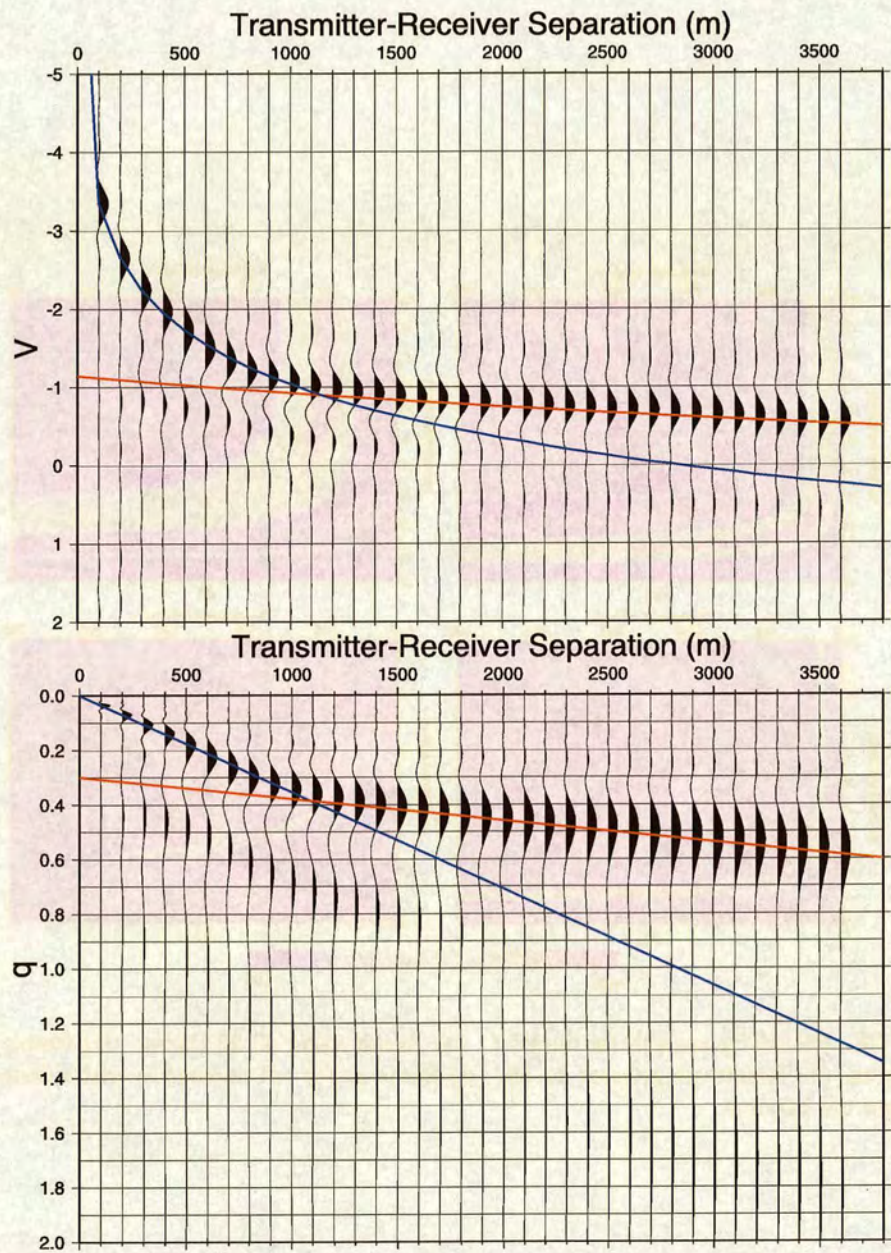
Figure 7.29: The result of DPM by deconvolution in log-time to recover a delta function for model 8. Theoretical moveout curves for the first and second layers are overlain in blue and red respectively. Top: $\boldsymbol{R}(x,v)$. Bottom: $\boldsymbol{U}(x,q)$.

188
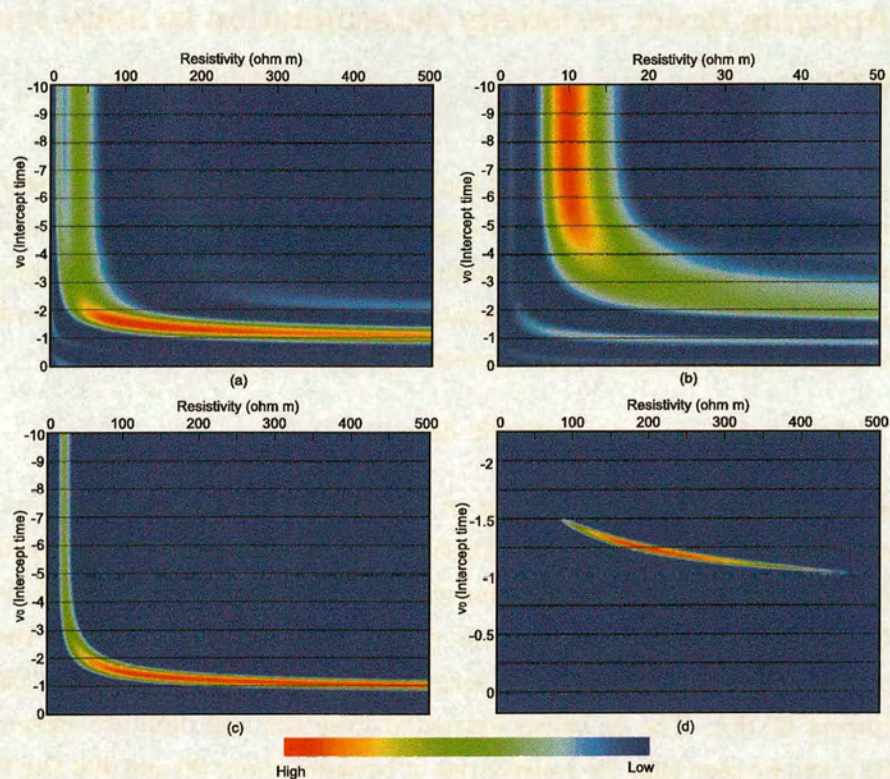
Figure 7.30: Resistivity analysis for model 8. (a) Result using all 36 traces. (b) Result using the first 10 traces. (c) Result using traces 13-36. (d) Same as (c) but zoomed in with different scaling to highlight the maxima.
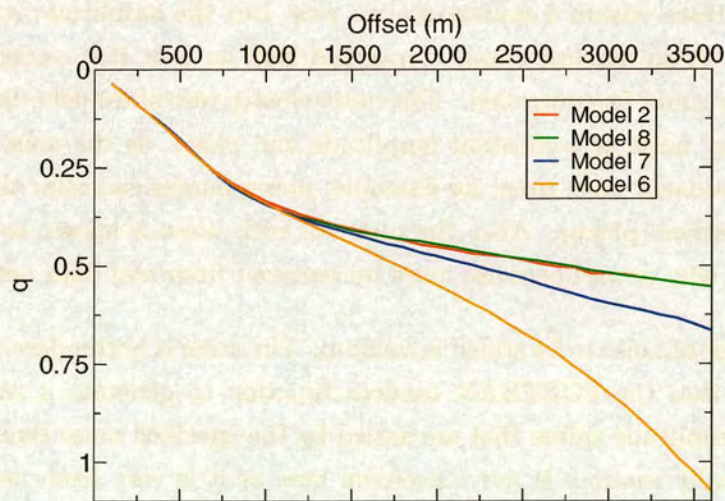
Figure 7.31: The moveout curves of the first arrival for the three layer models 6,7,8 and the two layer model 2.

189

7.6 Applying direct resistivity determination to noisy synthetic data

Having demonstrated the technique of extracting resistivities on noise-free synthetic data, the next step is to simulate real data by adding realistic amounts of both periodic and random noise to synthetic data. This will then allow the optimal survey requirements such as fold of coverage, spatial density and recording time to be determined if the technique is to be used successfully on real data.

Adding realistic noise levels to synthetic data

There are various types of noise present in EM data which were discussed in detail in Chapter 4. Before adding noise to synthetic data it is important to ensure the signal levels of the synthetic data as a function of offset are similar to those seen in the real data. Figure 7.32 shows the value of the dc voltage as a function of offset for resistivities of 1, 10, 100 and 500 Ωm for a source length of 250m, receiver length of 125m and a source current of 16A. The dc values extracted from the real data are shown in pink. From this it can be seen that for resistivities of between about 20 and 400 Ωm the signal strength is in fairly good agreement with the values taken from the Saint Illiers la Ville data. Four types of noise were added to the data from model 2 with 1000 transients created for each of the 36 offsets within a gather. First mono frequency spikes were added at 50, 150, 250, 350 and 450 Hz to recreate the effect of electrical pickup. In order to make the noise more realistic, the amplitude and phase of this noise was randomised between each trace within a source-receiver pair, but the amplitude was only allowed to vary by a certain amount about a specified level so that the average amplitude of each frequency could be controlled. This more closely resembles field data than adding mono frequency noise of a constant amplitude and phase, as the noise present in the field is not stationary with time; for example, power surges can alter the amplitude of noise from electrical pickup. Also, the phase of such noise is known to be unstable in time, which is why powerline noise must be removed from real data before stack.

The second type of noise to be added is random. The noise is better described as pseudorandom as it uses the FORTRAN random function to generate a series of random polarity and amplitude spikes that are scaled by the specified noise level. Adding noise that is not totally random is not a problem here as it is very likely that the random noise present in the real data is not totally random in the mathematical sense either.

A third type of noise to be added is a band-limited noise burst. This is seen in much of the real data and is characterised by high amplitudes in the amplitude spectrum up
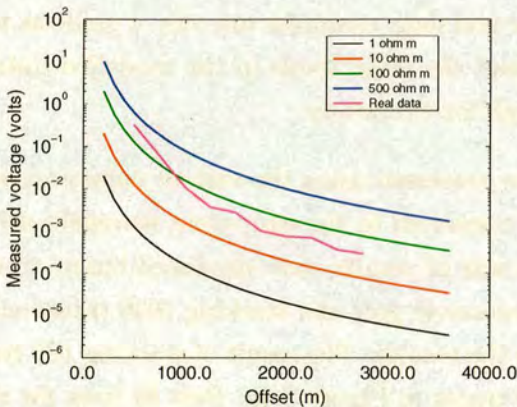
Figure 7.32: The dc voltage as a function of offset for various halfspace models using a 250m long 16A source, with values from the real data overlain for comparison.

to approximately 150Hz, followed by a sharp fall off. An example of such a noise burst can be seen in the amplitude spectrum of the data at 1750m in Figure 7.33a.

The final type of noise to be added is a spike. Spikes occur frequently in real data and are usually tackled by selective stacking, as discussed in Chapter 4. These noise events consist of a single large amplitude data point and can be of either polarity. Their amplitude is random but always much larger than that of the background. Such spikes do not normally appear on every trace, so they are added randomly to about 1 trace in 5 although some traces may have more than one spike.

The amplitudes for the noise were the same for all offsets so that the relative effect of the noise increased with offset as the signal amplitude decreased. The values chosen were calculated by examining the amplitude spectrum of real data over a range of offsets and selecting the value that gave the best match over a wide range of frequencies. In reality, of course, the noise level at larger offsets will be larger than at short offsets even after the reduction in signal amplitude has been taken into account, since there will be extra sources of noise between the source and receiver that do not affect data at shorter offsets. However, this is not considered here. Figure 7.33 shows the result of attempting to synthesize the real data. Figure 7.33(a) shows real transients and their amplitude spectra from 500 to 2000m, while Figure 7.33(b) shows synthetic data and the corresponding amplitude spectra with noise added to try and replicate the data shown in Figure 7.33(a). The similarity between the real and modelled data appears very good up to about 1250m, with the real data being slightly noisier beyond this, as might be expected, given the additional noise sources the real data is exposed to

191

between the source and receiver, which the synthetic data does not take into account. The synthetic data also has no geological noise in it which is certainly present in the real data. However, the real data examples are only a guide as to the noise levels to be expected in real data and the noise levels in the modelled data in Figure 7.33(b) are certainly realistic enough for this study.

The synthetic data were processed using the various noise removal techniques discussed in Chapter 4 and then converted to the equivalent wavefield using the same procedure as in section 7.5. Two sets of results were produced based on stacking 100 transients within the same source-receiver pair and stacking 1000 transients to see what effect the fold of coverage had on the results. The result of stacking 100 traces is shown in Figure 7.34 and stacking 1000 traces in Figure 7.35. Best fit lines for the moveout of the first and second layer are overlain in blue and red respectively. It can be seen that the results of stacking 1000 transients give a better result than stacking just 100 transients, as would be expected. The improvement is more noticeable for transients at offsets greater than 1500m in the $U(x, q)$ domain. The results of resistivity analysis for these two models are shown in Figure 7.36. The advantage of stacking 1000 transients can be seen when comparing plot (d) for each case where the peak for the second arrival stands out much more after stacking 1000 transients. The results obtained from these models are summarised in table 7.5, where the letters next to each result have the same meaning as in table 7.2. It can be seen from these results that the value obtained for the resistivity when stacking only 100 transients is overestimated for the top layer and underestimated for the bottom layer with values of 17.3 and 165 Ωm being obtained compared with the true values of 10 and 200 Ωm. When stacking 1000 transients the values obtained are again slightly out but are now much closer to the true values, with values of 13.4 and 184 Ωm now being obtained. The results obtained for the depth are disappointing; when stacking 100 transients the value obtained using equation 7.20 is 611m and using equation 7.23 gives 818m, while stacking 1000 transients gives a depth of 509m and 693m. This error is mainly due to the fact that the resistivity values are not accurate enough, but also because the intercept time q_0 is greater than that obtained for the same model without noise; as a result the value obtained for the depth is overestimated compared with the noise-free result. By chance the value for the depth when stacking 1000 traces and using equation 7.20 is almost exactly right. However, this is more by luck than design, as the resistivity values used to obtain this value are not correct.

Parameter	Model2 +noise 100 traces	Model 2 +noise 1000 traces
c_1	3706(R) 2821(M)	3266(R) 2821(M)
c_2	11469(R) 12616(M)	12112(R) 12616(M)
ρ_1	17.3(R) 10.0(M)	13.4(R) 10.0(M)
ρ_2	165(R) 200(M)	184(R) 200(M)
q_0	0.312	0.300
d	611(R1) 818(R2) 500(M)	509(R1) 693(R2) 500(M)
x_{cross}	1709(F) 1255(M) 1200(D)	1342(F) 1255(M) 1100(D)

Table 7.5: Results for model 2 with noise added.

193
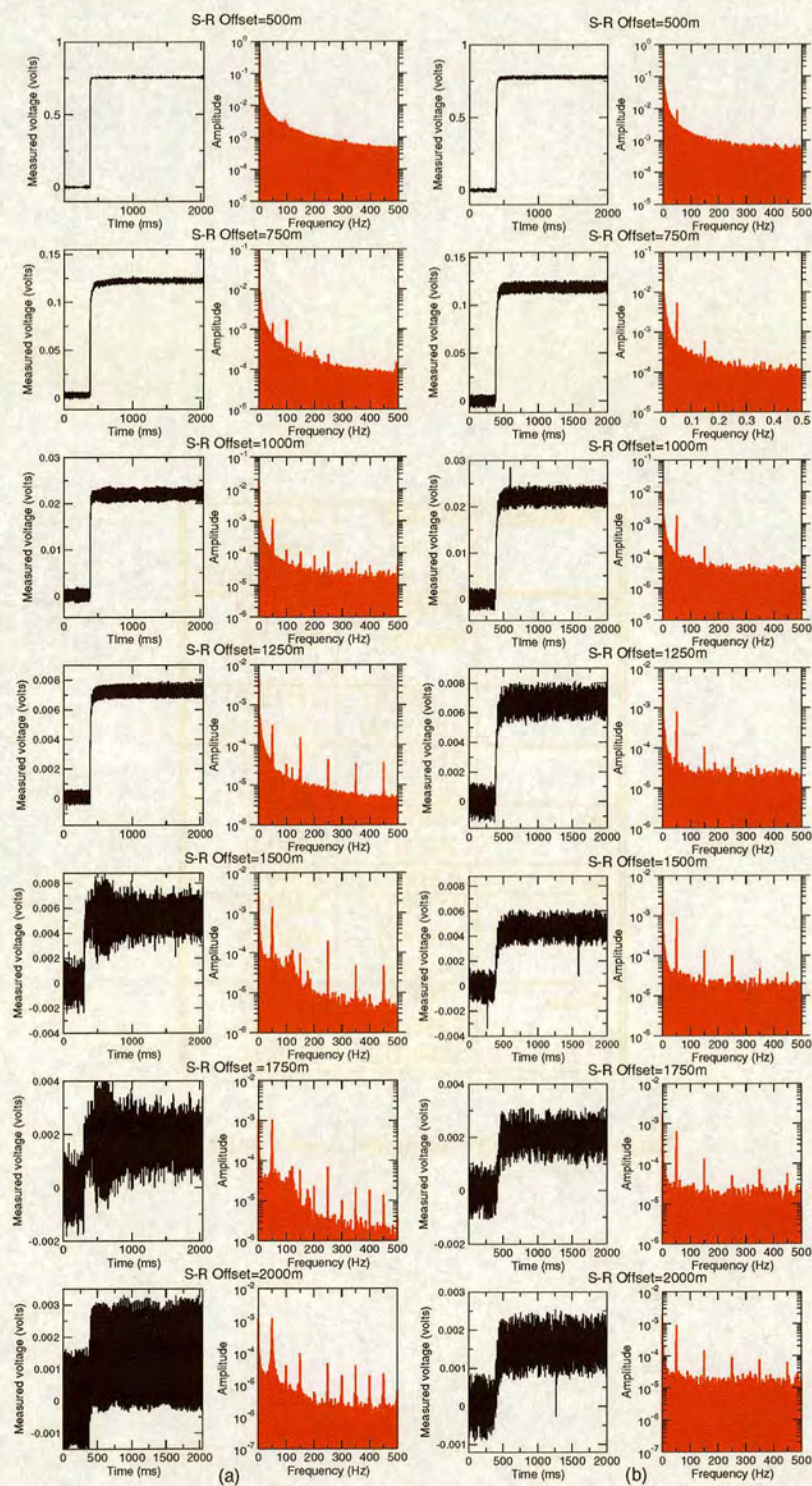
Figure 7.33: (a) Representative field data and amplitude spectra for offsets ranging from 500 to 2000m. (b) Synthetic data and amplitude spectra with noise added to try and replicate the real data shown in (a).

194
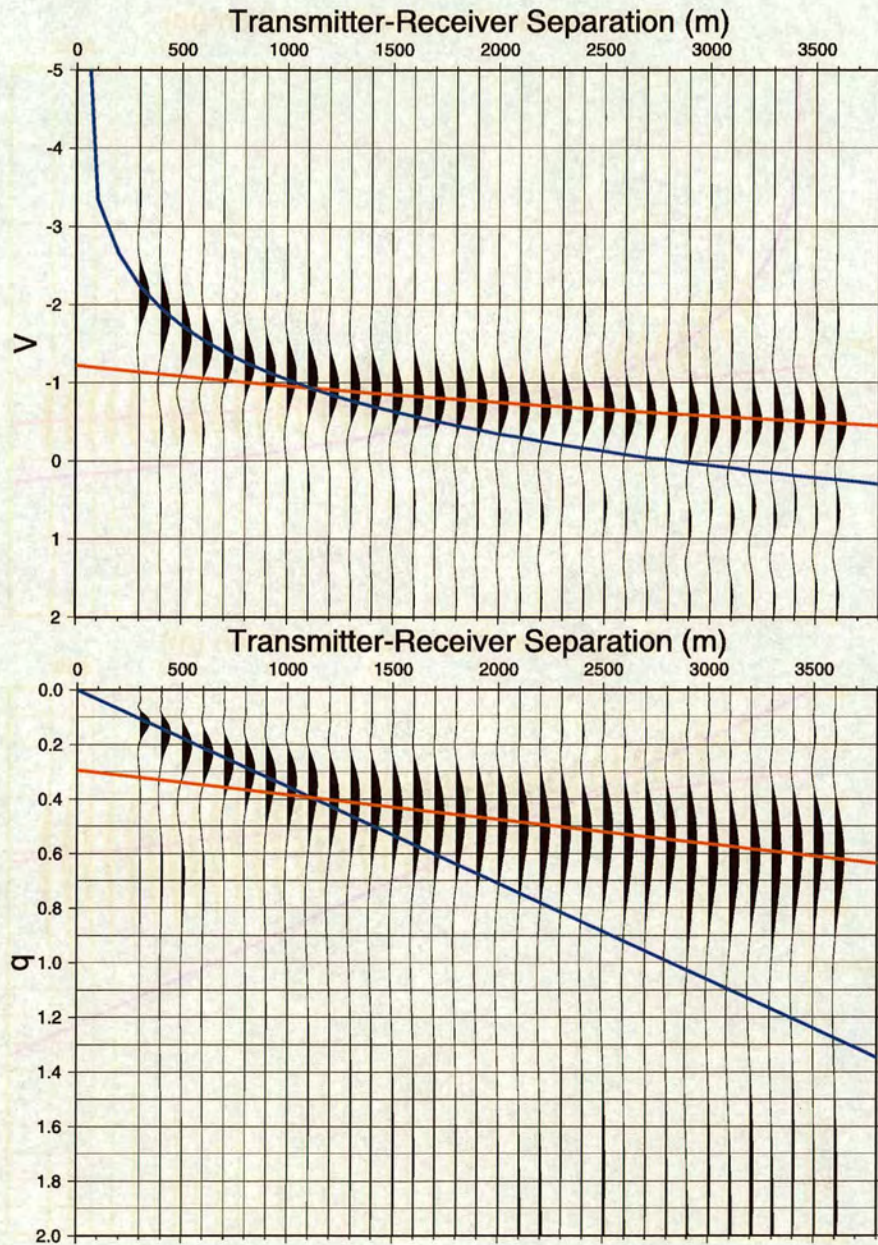
Figure 7.34: The result of DPM by deconvolution in log-time to recover a delta function for model 2 with added noise after stacking 100 traces. Best fit moveout curves for the top and bottom layers are overlain in blue and red respectively. Top: $R(x, v)$. Bottom: $U(x, q)$.

195
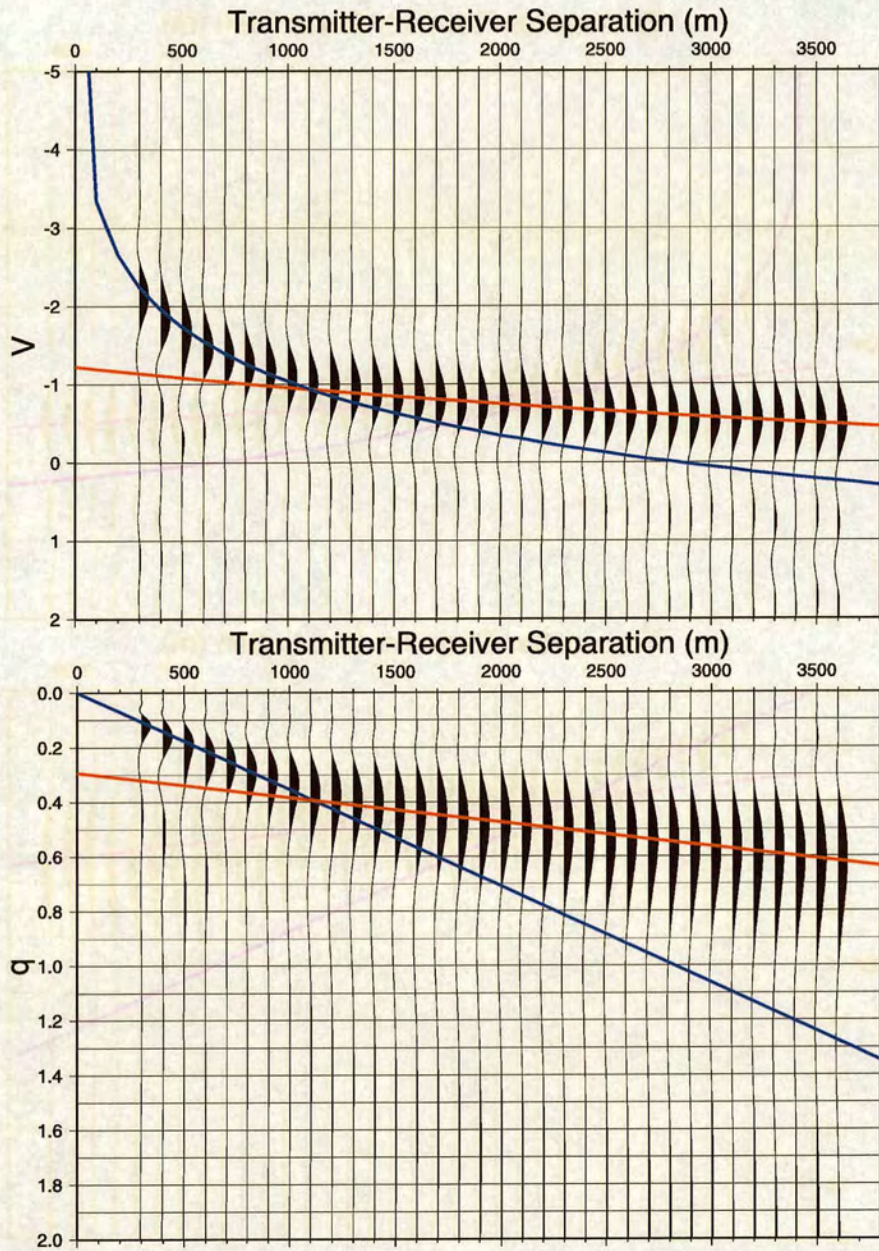
Figure 7.35: The result of DPM by deconvolution in log-time to recover a delta function for model 2 with added noise after stacking 1000 traces. Best fit moveout curves for the top and bottom layers are overlain in blue and red respectively. Top: $R(x, v)$. Bottom: $U(x, q)$.
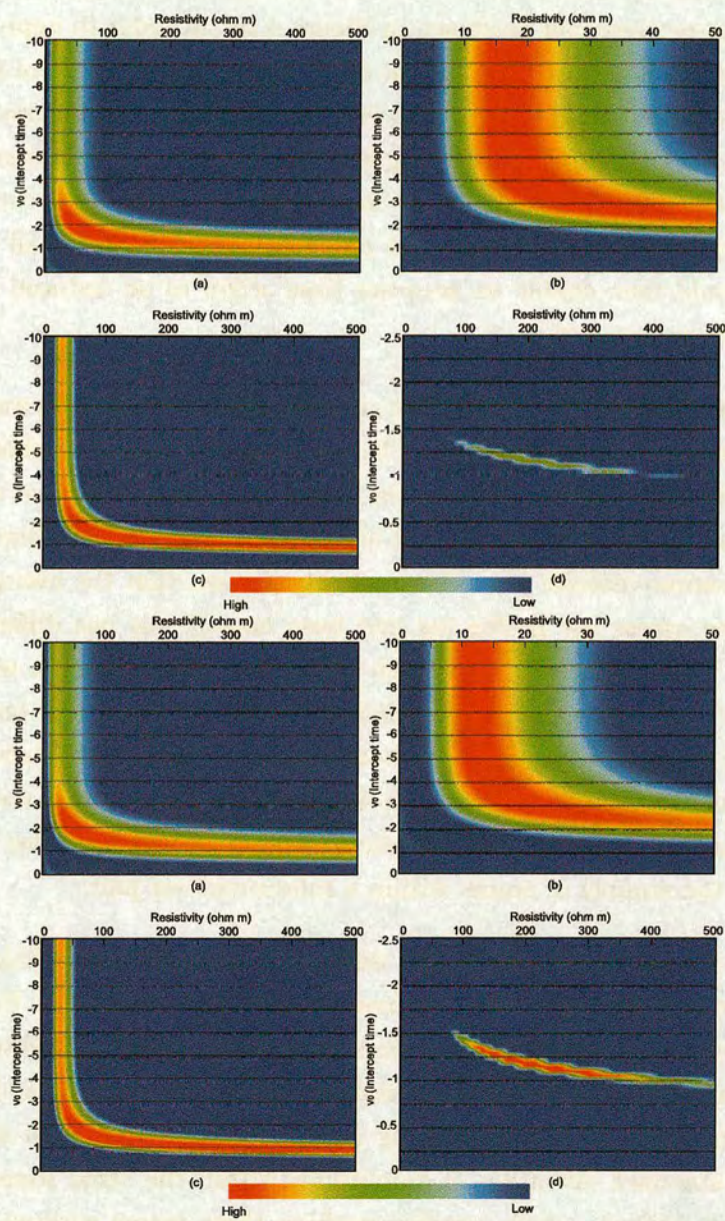
Figure 7.36: Resistivity analysis for model 2 with added noise and stacking 100 traces. (a) Result using all 36 traces. (b) Result using the first 8 traces. (c) Result using traces 13-36. (d) Same as (c) but zoomed in with different scaling to highlight the maxima. Top: The result of stacking 100 traces. Bottom: The result of stacking 1000 traces.

7.7 Applying direct resistivity determination to real data

The data collected at Saint Illiers la Ville has timing errors of typically $\pm$ 2ms within the same source-receiver pair as shown in Figure 4.14. In order to apply the technique of direct resistivity determination to real data, the precise location of the time origin must be known since the first step is to take the logarithm of the time axis. Timing errors prevent the time origin from being known. However, if the statistical properties of the timing error are the same for all source-receiver pairs, then the average of all the time origins within a source-receiver pair will be the same for all source-receiver pairs. This would then enable an accurate time origin to be deduced when applying the technique to a shot gather.

In order to test this idea, the 1996 1000m common offset section data was analysed and the results are shown in Figure 7.37. The top plot in Figure 7.37 shows the number of traces within each source-receiver pair, which is a useful reference when analysing the results that follow. The second plot shows the average and median of the arrival time for each source-receiver pair. It can clearly be seen that the average arrival time is not the same across the profile (as had been hoped) but has differences of up to 8ms present. These differences are much larger than those present within the same source-receiver pair and make it impossible to define $t = 0$ and still have any hope of extracting any meaningful results. The bottom plot in Figure 7.37 shows the standard deviation σ_{sd} of the timing error for each source-receiver pair across the profile. It can clearly be seen that there is little variation in σ_{sd} across the profiles with it mainly dependent on the number of traces within a source-receiver pair.

The variation in the amplitude of the differentiated transients within and between source-receiver pairs for the 1000m common-offset section is shown in Figure 7.38. The top plot shows the average and median amplitudes of the differentiated traces across the profile: the amplitude between source-receiver pairs is quite variable due to different source currents being used and differing ground conditions at each source location. However, the standard deviation of amplitudes within the same source-receiver pair is only about 3 percent, which justifies stacking these traces without normalisation. Because there is a large variability in amplitude for different source positions, the traces must be normalised post-stack to allow comparison.

The error in timing between source-receiver pairs is clearly too great to allow the time origin to be determined accurately enough to extract resistivities. But, the real data can still be used to study how stable the result of applying DPM is. The function $\mathbf{R}(x, v)$ and the equivalent wavefield $\mathbf{U}(x, q)$ of the 1996 1000m common offset section

are shown in Figure 7.39 top and bottom respectively. The data are for an offset of only 1000m and so are not as noisy as data at larger offsets; nevertheless the application of DPM enabled a stable result to be obtained. These results can be compared with the plot of the same data before applying DPM which is shown in Figure 6.12. The results shown in Figure 7.39 do not tell us about resistivity values but do provide another way of displaying the data and show the early times in more detail. They also indicate that DPM applied to real EM data gives a stable result.
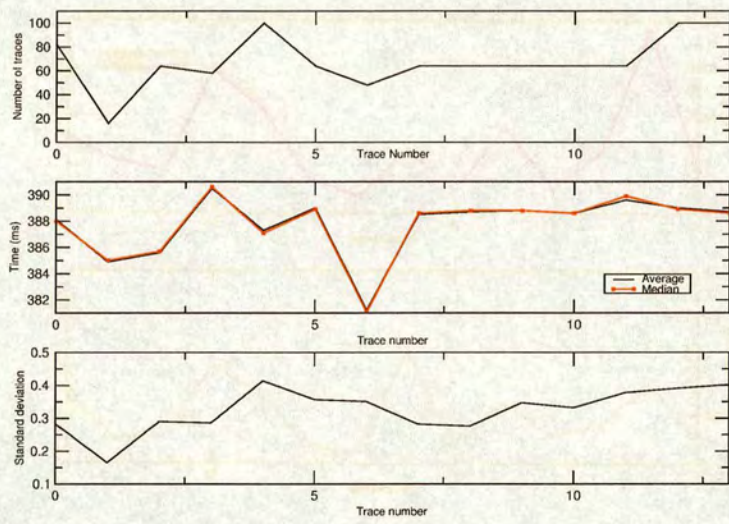
Figure 7.37: Statistical properties of the timing error. Top: The number of traces within each source-receiver pair for the 1000m common-offset section. Middle: The mean and median of the time origin for the same data. Bottom: The standard deviation of the timing error within each source-receiver pair.
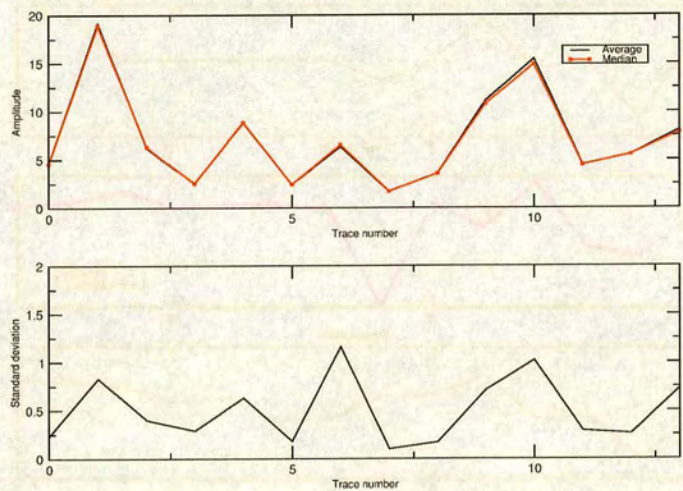
Figure 7.38: Amplitude variation between traces. Top: The average and median of the amplitude of differentiated transients within the same source-receiver pair for the 1000m common-offset section. Bottom: The standard deviation of the amplitude data in the above plot.
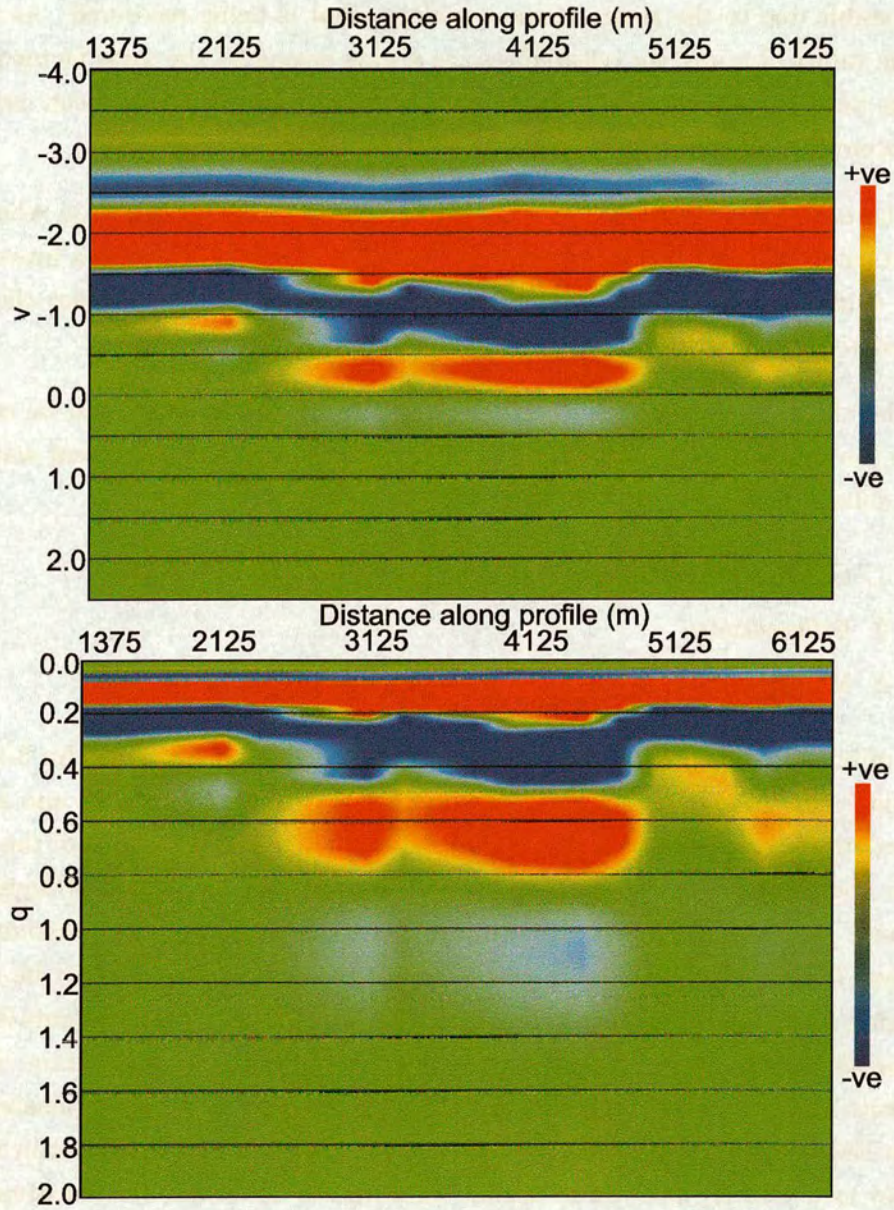
Figure 7.39: Common offset section for 1000m of the 1996 data. Top: The function $R(x, v)$. Bottom: The equivalent wavefield function $U(x, q)$.

7.8 Summary

- Recovery of the equivalent wavefield for the electric field response to an electric current dipole source in order to determine resistivity values correctly is not possible due to the shape of the waveform that is being recovered. As a result, the values obtained for resistivities are always wrong by the same factor provided the data are noise-free and the same amount of white noise has been used in the deconvolution step.

- The numerical transformation of a diffusive response to a function whose theoretical equivalent wavefield is a delta function at $q = \frac{x}{c}$ results in a function that is symmetric being recovered from the deconvolution, this enables the correct resistivity values to be recovered in the presence of two layers.

- The electric field response to an electric current dipole source can be converted to the function $\boldsymbol{G}(x,v)$ for the function whose theoretical equivalent wavefield is a delta function at $q = \frac{x}{c}$ as follows:

  1. Convert to log-time $v = \frac{1}{2}ln(4t)$
  2. Differentiate
  3. Multiply be $\sqrt{\pi}exp(v)$

- Applying this technique, the correct resistivity values are obtained for 3 halfspace and 5 two layer models including a conductor overlying a resistor and a resistor underlying a conductor. Resistivities are extracted from the slope of the maxima on the moveout curve, in the $\boldsymbol{U}(x,q)$ domain: the slope is a straight line of slope $\frac{1}{c_n}$ where n denotes the nth layer. This is related to the resistivity of the layer by $\rho = c^2\mu$. The depth to the top of the second layer cannot be obtained using formulae from seismic refraction despite the fact that the data has been transformed to the equivalent wavefield which obeys the wave equation. Accurate depth values can be obtained using the equation for the depth of penetration for an EM field, equation 7.23. A resistivity analysis can be carried out in the same way as a velocity analysis in seismic reflection to determine the resistivity values directly from the data. To identify the correct resistivity value in the presence of more than 1 layer the analysis must be carried out on only a few adjacent traces at a time as the differential moveout between individual arrivals is too small to separate individual arrivals sufficiently.

- In the presence of three layers the resistivity obtained for the middle layer depends on the thickness of the layer. The thinner the layer the lower the resistivity that is

obtained; beyond a thickness of approximately 500m the resistivity value obtained is the correct value. In the presence of a thin layer the depth value obtained to the top of the layer is underestimated.

- The addition of noise has an effect on the resistivity value obtained. The resistivity of the top layer tends to be over estimated and that of a deeper layer underestimated with the depth to the top of the second layer overestimated. Stacking more traces produces a result that is closer to the correct one.

- In order to apply the technique to real data it is crucial that the time origin of the data be known precisely. Because the logarithm of the data is taken, errors in this value will have a large effect on any resistivity values obtained.

- The resistivity of the top layer will be affected by the source geometry for traces recorded less than about 5 source lengths from the source. The effect is independent of the resistivity of the layer and it should be possible to correct for this.

Chapter 8

Conclusions

The determination of the presence of hydrocarbons in a reservoir is crucial in hydrocarbon exploration. The change in resistivity that takes place when hydrocarbons replace water in a rock is the greatest of any physical quantity. Electromagnetic methods are sensitive to changes in resistivity, making them suitable for determining whether a reservoir contains high resistivity hydrocarbons or low resistivity brine. The transient electromagnetic method offers the best resolution of any EM method. Multichannel transient electromagnetic systems with a field layout similar to seismic profiling enable a huge amount of data to be collected with very dense spatial coverage and a depth of exploration suitable for hydrocarbon exploration. The modelling and inversion of such large amounts of data is computationally prohibitive and fails to exploit the information present in the data. A new acquisition processing and interpretation methodology is therefore needed in order to exploit MTEM data fully.

The approach taken in this thesis is similar to the analysis of seismic data in that the data are processed rather than modelled. The processing of the data can be split into two parts. The first part, known as pre-processing, seeks to recover the impulse response of the earth by, first, removing periodic and random noise from the data, and second, by removing the effect of the system response by measuring it every time the source is fired and then performing deconvolution. The removal of random noise pre-stack using a frequency domain dip filter greatly improves the signal-to-noise ratio of noisy data whilst preserving the signal. The use of selective stacking procedures in reducing random noise can produce artefacts in the result and introduces high frequency noise when large amounts of data are stacked. Visually inspecting and completely removing noisy traces prevents any bias or high frequency noise appearing and produces a result that in almost all cases is as good, if not better, than selective stacking. Deconvolution

of the system response in order to recover the impulse response of the earth should be done by measuring the system response every time the source is fired. Only then can the system response recorded on the data be removed properly.

The second part of the processing, known as diffusive to propagative mapping (DPM), transforms the impulse response of the earth to a non-diffusive domain by performing deconvolution in log-time. In this domain the moveout of the peak arrival on traces in a common shot gather enables the resistivity of 2-layer subsurface models to be determined by applying a 'resistivity analysis' in a manner similar to a velocity analysis in seismic data processing. Applying DPM processing to synthetic 3-layer models the result is found to depend on the thickness of the layer. For a resistor, the thinner the layer the lower the resistivity that is obtained; beyond a certain thickness the correct value for the resistivity is obtained. This suggests that the propagation is not analogous to seismic refraction in that the so-called 'refracted' wave does not 'see' just the top of the layer as in seismic refraction. Instead the 'EM wave' travels in a region below the top of the layer, making its arrival time dependent on the thickness of the layer and the resistivity of the underlying layer. An alternative approach is therefore necessary in order to extract resistivity values from EM data without inversion, this is an area for further work.

In formulating these two processing schemes, analysis of the two MTEM datasets from Saint Illiers la Ville revealed that they were far from ideal. Many areas for improvement in terms of the data acquisition have been identified. First, the system response was found to vary in a non-linear manner with current, resulting in unphysical results when using the wrong system response in deconvolution. Ideally, the system response should be measured for each source current and each source position that is occupied, and also for every shot fired. Only then can the correct system response be deconvolved from the data. Second, once the data have been differentiated, the earth impulse response for these data is only about 20ms long. Recording for two seconds produced a record length that was too long by a factor of about 100, in future a record length of 100ms would be long enough for most targets. Recording at a sampling interval of 1ms is too coarse, a much higher sampling rate of,say 0.05ms, should be used. Together these changes would greatly improve resolution and reduce considerably the time needed to acquire the data, allowing orders of magnitude more traces to be collected, enabling both the resolution and signal-to-noise ratio to be greatly increased. Errors in the timing for traces within the same source-receiver pair of $\pm$ 2ms were found after differentiating the data. These errors are in addition to timing errors present between traces in different source-receiver pairs, and traces for the same source-receiver pair for different years that were already known about. Failure to correct for these timing errors results in the stacked response

being smeared over several ms masking the actual response. These timing errors would have been detected if the system response was measured, we can therefore think of them as part of the system response. Another consequence of the various timing errors was that the time $t = 0$ was not known and so DPM processing could not be applied to the data. Any future system should have all timing and synchronisation controlled by GPS clocks to prevent such errors.

The processing scheme applied to the Saint Illiers la Ville data was a pragmatic version of the ideal pre-processing scheme and sought to recover an approximate earth impulse response. Whilst not ideal, it was necessary in order to overcome the limitations of the data.

1-D modelling indicates that, of the six different field components that were measured, the in-line E_{xx} component of the electric field is most sensitive to a thin buried resistor and is also the largest signal. The cross-line E_{yy} component is the second most sensitive, but its response is smaller and in the opposite sense to E_{xx}. In-line and cross-line measurements of the time rate of change of the vertical component of the magnetic field are insensitive to a thin buried resistor. For the electric field components E_{xy} and E_{yx}, where the source and receiver are perpendicular at an azimuthal angle of 0 or 90 degrees, the 1-D response is zero. At other azimuthal angles there is a response which is maximum at an angle of 35.3 degrees. The E_{xy} and E_{yx} responses are identical in a 1-D earth, any difference between the two is an indication of 2 or 3-D structure.

Analysis of common-offset sections of the derivative of the approximate impulse response of the earth for the E_{xx} data reveal the presence of the reservoir. The reservoir response is clearly seen on data an offset of 750-1500m and at a time of about 4ms. The lateral extent of the response is in good agreement with that of the reservoir determined by monitor wells at the site. Simple 1-D modelling indicates that the effect of the reservoir is not detectable at short offset of about 600m or less, and at larger offsets the response is seen at a time of about 3-15ms. In addition, the shape of the response seen in the E_{xx} data can be reproduced by modelling if the shape of the source function is chosen to be a ramp, as it probably is in reality, rather than a perfect step, and the full rise of the transient is captured by sampling the field before the time break. The modelling results show that the response of the reservoir increases for larger resistivities (more gas). This agrees with what is seen in the approximate earth responses for the same source-receiver pair from the two surveys. Subtraction of the 1996 common-offset impulse response section from the corresponding 1994 section showed a positive anomaly at the southern edge of the reservoir, indicating there was more gas present in 1994. This is confirmed by the data from the monitor wells.

These results illustrate, using data far from ideal, that it is possible to detect hydro-carbons and their movement using surface-based MTEM. A new system based on these conclusions and recommendations could clearly make orders of magnitude increases in efficiency whilst acquiring data of higher resolution and much higher fold. Such data could then be processed using the processing methodology described in the thesis.

Bibliography

Alsdorf, D. (1997). Noise reduction in seismic data using fourier correlation coefficient filtering. *Geophysics*, **62**, 1617–1627.

Alumbaugh, D.L. & Morrison, H.F. (1995a). Monitoring subsurface changes over time with cross-well electromagnetic tomography. *Geophysical Prospecting*, **43**, 873–902.

Alumbaugh, D.L. & Morrison, H.F. (1995b). Theoretical and practical considerations for crosswell electromagnetic tomography assuming a cylindrical geometry. *Geophysics*, **60**, 846–870.

Archie, G. (1942). The electrical resistivity log as an aid in determining some reservoir characteristics. *Trans. AIME*, **146**, 54–62.

Árnason, K. (1995). A consistent discretization of the electromagnetic field in conducting media and application to the TEM problem. In *International Symposium on 3-D Electromagnetics Schlumberger Doll Research, Ridgefield Conneticut, USA*, 167–179, Expanded Abstracts.

Azad, J. (1973). Direct oil prospecting with electrical transient reflections. *J. Canadian Society of Exploration Geophysicists*, **9**, 1–11.

Best, M. & Spies, B. (1990). Recent developments in analysis and presentation of large data sets in mineral exploration. *The Leading Edge*, **09**, 37–43.

Blau, L.W. (1936). Black magic in geophysical prospecting. *Geophysics*, **01**, 1–8.

Bourgeois, B., Suignard, K. & Perrusson, G. (2000). Electric and magnetic dipoles for geometric interpretation of three-component electromagnetic data in geophysics. *Inverse Problems*, **16**, 1225–1261.

Bragg, L. & Dettman, J. (1969). Related problems in partial differential equations. *Bull. Amer. Math. Soc*, **74**, 375–378.

Buselli, G. (1982). The effect of near-surface superparamagnetic material on electromagnetic measurements. *Geophysics*, **47**, 1315–1324.

Cagniard, L. (1953). Basic theory of the magneto-telluric method of geophysical prospecting. *Geophysics*, **18**, 605–635.

Cairns, G., Evans, R. & Edwards, R. (1996). A time domain electromagnetic survey of the TAG hydrothermal mound. *Geophysical Research Letters*, **23**, 3455–3458.

Canales, L.L. (1984). Random noise reduction. *54th Ann. Internat. Mtg., Soc. of Expl. Geophys., Expanded Abstracts*, 3455–3458.

Carlson, S. & Pearlman, G. (1993). *Paired dimmers for controlling harmonic currents*. United States Patent 5,506,480.

Chave, A. & Cox, C. (1982). Controlled electromagnetic sources for measuring electrical conductivity beneath the oceans, 1., Forward problem and model study. *Journal of Geophysical Research*, **87**, 5327–5338.

Chave, A., Constable, S. & Edwards, R. (1991). Electrical exploration methods for the seafloor. In M.N. Nabighian, ed., *Electromagnetic Methods in Applied Geophysics, Volume 2, Application*, 931–966, Soc. Expl. Geophys.

Cheesman, S.J., Edwards, R.N. & Chave, A.D. (1987). On the theory of sea-floor conductivity mapping using transient electromagnetic systems. *Geophysics*, **52**, 204–217.

Cheesman, S.J., Edwards, R.N. & Law, L.K. (1990). A test of a short-base-line sea-floor transient electromagnetic system. *Geophysical Journal International*, **103**, 431–437.

Christopherson, K. (2002). EM in the 21st century - Looking for oil, gas and water. In *16th IAGA EM induction workshop - EM applications in industry*.

Coggon, J.H. & Morrison, H.F. (1970). Electromagnetic investigation of the sea-floor. *Geophysics*, **35**, 476–489.

Constable, S. & Cox, S. (1996). Marine controlled-source electromagnetic sounding 2- The pegasus experiment. *Journal of Geophysical Research*, **101**, 5519–5530.

Constable, S.C., Hoversten, G.M. & Morrison, H.F. (1998a). Marine magnetotellurics for petroleum exploration, part II: Numerical analysis of subsalt resolution. *Geophysics*, **63**, 826–840.

Constable, S.C., Orange, A.S., Hoversten, G.M. & Morrison, H.F. (1998b). Marine magnetotellurics for petroleum exploration part I: A sea-floor equipment system. *Geophysics*, **63**, 816–825.

Das, K., Becker, A. & Lee, K. (2002). Experimental validation of the wavefield transform of electromagnetic fields. *Geophysical Prospecting*, **50**, 441–451.

de Hoop, A. (1996). Transient electromagnetic vs. seismic prospecting - a correspondence principle. *Geophysical Prospecting*, **44**, 987–995.

Duncan, P.M., Hwang, A., Edwards, R.N., Bailey, R.C. & Garland, G.D. (1980). The development and applications of a wide-band electromagnetic sounding system using a pseudonoise source. *Geophysics*, **45**, 1276–1296.

Duren, R. & Warren, R. (1995). *Detection and mapping of hydrocarbon reservoirs with radar waves*. United States Patent 5,400,030.

Eadie, T. (1981). Detection of hydrocarbon accumulations by surface electrical methods: a feasibility study. *Research in Applied Geophysics*, **15**.

Eaton, P.A. & Hohmann, G.W. (1987). An evaluation of electromagnetic methods in the presence of geologic noise. *Geophysics*, **52**, 1106–1126.

Eaton, P.A. & Hohmann, G.W. (1989). A rapid inversion technique for transient electromagnetic soundings. *Physics of the Earth and Planetary Interiors*, **53**, 384–404.

Edwards, R.N. (1997). On the resource evaluation of marine gas hydrate deposits using sea-floor transient electric dipole-dipole methods. *Geophysics*, **62**, 63–74.

Edwards, R.N. & Chave, A.D. (1986). A transient electric dipole-dipole method for mapping the conductivity of the sea-floor. *Geophysics*, **51**, 984–987.

Edwards, R.N., Cheesman, S.J. & Chave, A.D. (1986). Sea floor conductivity mapping using transient EM systems. *56th Ann. Internat. Mtg., Soc. of Expl. Geophys., Expanded Abstracts*, Session:EM3.2.

Eidesmo, T., Ellingsrud, S., MacGregor, L., Constable, S., Sinha, M., Johansen, F., Kong, F. & Westerdahl, H. (2002). Sea Bed Logging (SBL), a new method for remote and direct identification of hydrocarbon filled layers in deepwater areas. *First Break*, **20**, 144–152.

Ellingsrud, S., Eidesmo, T., Johansen, S., Sinha, M., MacGregor, L. & Constable, S. (2002). Remote sensing of hydrocarbon layers by Sea Bed Logging (SBL): Results from a cruise offshore Angola. *The Leading Edge*, **21**, 972–982.

Erdélyi, A. (1954). *Tables of Integral Transforms*. McGraw-Hill.

Everett, M. (1990). *Mid-ocean ridge electromagnetics*. Ph.D. thesis, University of Toronto.

Evjen, H.M. (1948). Theory and practice of low-frequency electromagnetic exploration. *Geophysics*, **13**, 584–594.

Filatov, V.V. (1984). Construction of focusing transformations of transient electromagnetic fields. *Geol. i Geofiz. (Soviet Geology and Geophysics)*, **25**, 89–95.

Fitterman, D.V., Mazzella, A.T. & Anderson, W.L. (1989). What pipes can do to your transient EM interpretation. *59th Ann. Internat. Mtg., Soc. of Expl. Geophys., Expanded Abstracts*, 219.

Flis, M.F., Newman, G.A. & Hohmann, G.W. (1989). Induced-polarization effects in time-domain electromagnetic measurements. *Geophysics*, **54**, 514–523.

Garg, N.R. & Keller, G.V. (1986). Spatial and temporal analysis of electromagnetic survey data. *Geophysics*, **51**, 85–89.

Gershenson, M. (1993). Simple interpretation of time-domain electromagnetic sounding using similarities between wave and diffusion propagation. *63rd Ann. Internat. Mtg., Soc. of Expl. Geophys., Expanded Abstracts*, 1342–1345.

Gershenson, M. (1997). Simple interpretation of time-domain electromagnetic sounding using similarities between wave and diffusion propagation. *Geophysics*, **62**, 763–774.

Goldman, M., Tabarovsky, L. & Rabinovich, M. (1994). On the influence of 3-D structures in the interpretation of transient electromagnetic sounding data. *Geophysics*, **59**, 889–901.

Gulunay, N. (1986). F-X decon and complex wiener prediction filter. *56th Ann. Internat. Mtg., Soc. of Expl. Geophys., Expanded Abstracts*, Session:POS2.10.

Gunderson, B.M., Newman, G.A. & Hohmann, G.W. (1986). Three-dimensional transient electromagnetic responses for a grounded source. *Geophysics*, **51**, 2117–2130.

Guptasarma, D. (1984). Positivity of the coincident loop transient electromagnetic response (short note). *Geophysics*, **49**, 194.

Haldorsen, J.B.U. & Farmer, P.A. (1989). Suppression of high-energy noise using an alternative stacking procedure. *Geophysics*, **54**, 181–190.

Hatton, L., Worthington, W.M. & Makin, J. (1986). *Seismic Data Processing, theory and practice*. Blackwell Scientific Publications.

Helwig, S.L., Hanstein, T. & Hordt, A. (1995). Cluster analysis and digital filtering of TEM data. *57th Ann. Mtg., Eur. Assn. of Expl. Geophys., Expanded Abstracts*, Session:D050.

Hobbs, B.A. (1992). Terminology and symbols for use in studies of electromagnetic induction in the earth. *Surveys in Geophysics*, **13**, 489–515.

Hobbs, B.A. (2003). Personal communication.

Hoekstra, P., Blohm, M. & Blohm, R. (1991). Utility and limitations of 1-D inversions of time domain EM data over strong 2-D structures. *61st Ann. Internat. Mtg., Soc. of Expl. Geophys., Expanded Abstracts*, 410–412.

Hohmann, G. (1988). Numerical modelling for electromagnetic methods of geophysics. In M.N. Nabighian, ed., *Electromagnetic Methods in Applied Geophysics, Volume I, Theory*, 314–363, Soc. Expl. Geophys.

Hohmann, G.W. & Newman, G.A. (1990). Transient electromagnetic responses of surficial, polarizable patches (short note). *Geophysics*, **55**, 1098–1100.

Hördt, A. & Müller, M. (2000). Understanding LOTEM data from mountainous terrain. *Geophysics*, **65**, 1113–1123.

Hördt, A., Druskin, V.L., Knizhnerman, L. & Strack, K.M. (1992). Interpretation of 3-D effects in long-offset transient electromagnetic (LOTEM) soundings in the Munsterland area, Germany. *Geophysics*, **57**, 1127–1137.

Hördt, A., Vozoff, K. & Neubauer, F.M. (1995). Multichannel transient electromagnetics for underground gas storage monitoring. *57th Ann. Mtg., Eur. Assn. of Expl. Geophys., Expanded Abstracts*, Session:D051.

Hördt, A., Andrieux, P., Neubauer, F., Rüter, H. & Vozoff, K. (2000). A first attempt at monitoring underground gas storage by means of time-lapse multichannel transient electromagnetics. *Geophysical Prospecting*, **48**, 489–509.

Hoversten, G., Newman, G., Morrison, H.F., Gasperikova, E. & Watts, A.B. (2001). Reservoir characterization using crosswell electromagnetic inversion: A feasibility study for the Snorre field, north sea. *Geophysics*, **66**, 1177–1189.

Hughes, L., Zonge, K. & Carlson, N. (1985). The application of electrical techniques in mapping hydrocarbon-related alteration. In M. Davidson, ed., *Unconventional methods in exploration for petroleum and natural gas , Symposium IV*, Southern Methodist University Press, Dallas.

Johnston, R. (2000). *Deterministic free surface multiple removal of marine seismic data*. Ph.D. thesis, University of Edinburgh.

Jones, A.G. (1988). Static shift of magnetotelluric data and its removal in a sedimentary basin environment. *Geophysics*, **53**, 967–978.

Kaufman, A. (1989). A paradox in geoelectromagnetism, and its resolution, demonstrating the equivalence of frequency and transient domain methods. *Geoexploration*, **25**, 287–317.

Kaufman, A. & Keller, G. (1983). *Frequency and transient soundings*. Elsevier.

Keller, G. (1971). Electrical characteristics of the earth's crust. In J. Wait, ed., *Electromagnetic probing in Geophysics*, 13–79, Golem Press.

Keller, G.V. (1984a). The role of source orientation in time-domain electromagnetic sounding. *54th Ann. Internat. Mtg., Soc. of Expl. Geophys., Expanded Abstracts*, Session:EM2.5.

Keller, G.V., Pritchard, J.I., Jacobson, J.J. & Harthill, N. (1984). Megasource time-domain electromagnetic sounding methods. *Geophysics*, **49**, 993–1009.

Keller, G.V., Jordan, J.M. & Tasci, M.T. (1996a). Case histories using time domain electromagnetics in oil and gas exploration: From inversion to imaging. *66th Ann. Internat. Mtg., Soc. of Expl. Geophys., Expanded Abstracts*, 222–225.

Keller, G.V., Tasci, M.T. & Jordan, J.M. (1996b). Electromagnetic imaging for indirect detection of hydrocarbons: A discovery. *66th Ann. Internat. Mtg., Soc. of Expl. Geophys., Expanded Abstracts*, 226–229.

Kirichek, M., Korkh, Z., Ratner, E. & Khar'lovskaya, V. (1974). *Geoelectric model of oil and gas deposits*, 63–70. VNII Geofizika, Nedra, Moscow (in Russian).

Kunetz, G. (1972). Processing and interpretation of magnetotelluric soundings. *Geophysics*, **37**, 1005–1021.

Kuo, J. & Cho, D. (1980). Transient time-domain electromagnetics. *Geophysics*, **45**, 271–291.

Lavrent'ev, M.M., Romanov, V.G. & Shishatskii, S.P. (1980). Ill-posed problems of mathematical physics and analysis. *Nauka*.

Lee, K.H. (1988). A new approach to interpreting electromagnetic sounding data. Tech. rep., Ernest Orlando Lawrence Berkeley National Laboratory. Annual report 1988, 24-27. LBL-26362.

Lee, K.H. & Xie, G.Q. (1993). A new approach to imaging with low-frequency electromagnetic fields. *Geophysics*, **58**, 780–796.

Lee, K.H., Liu, G. & Morrison, H.F. (1989). A new approach to modeling the electromagnetic response of conductive media. *Geophysics*, **54**, 1180–1192.

Lee, S., McMechan, G.A. & Aiken, C.L.V. (1987). Phase-field imaging - The electromagnetic equivalent of seismic migration. *Geophysics*, **52**, 678–693.

Lee, T. (1984). The effect of a superparamagnetic layer on the transient electromagnetic response of a ground. *Geophysical Prospecting*, **32**, 480–496.

Levy, S., Oldenburg, D. & Wang, J. (1988). Subsurface imaging using magnetotelluric data. *Geophysics*, **53**, 104–117.

MacGregor, L. (1997). *Electromagnetic investigation of the Reykjanes ridge near 58 degrees north*. Ph.D. thesis, Cambridge University.

Macnae, J. & Lamontagne, Y. (1987). Imaging quasi-layered conductive structures by simple processing of transient electromagnetic data. *Geophysics*, **52**, 545–554.

Macnae, J.C., Lamontagne, Y. & West, G.F. (1984). Noise processing techniques for time-domain electromagnetic systems. *Geophysics*, **49**, 934–948.

Mallick, K. & Verma, R.K. (1979). Time-domain electromagnetic sounding - Computation of multilayer response and the problem of equivalence in interpretation. *Geophysical Prospecting*, **27**, 137–155.

Malvern, L. (1969). *Introduction to the mechanics of a continuous medium*. Prentice Hall.

Martner, S.T. & Sparks, N.R. (1959). The electroseismic effect. *Geophysics*, **24**, 297–308.

Maxwell, J. (1892). *A treatise on electricity and magnetism*. Clarendon Press.

McCracken, K.G., Oristaglio, M.L. & Hohmann, G.W. (1986). A comparison of electromagnetic exploration systems. *Geophysics*, **51**, 810–818.

Mehanee, S. & Zhdanov, M. (2003). 3-D finite-difference electromagnetic modelling based on the balance method and quasi-analytical boundary conditions. *Submitted to Journal of Computational Physics*.

Mogilatov, V. & Balashov, B. (1996). A new method of geoelectrical prospecting by vertical electric current soundings. *Journal of Applied Geophysics*, **36**, 31–41.

Moran, J. & Gianzero, S. (1979). Effects of formation anisotropy on resistivity logging measurements. *Geophysics*, **44**, 1266–1286.

Morrison, H., Shoham, Y., Hoversten, G., & Torres-Verdin, C. (1996). Electromagnetic mapping of the electrical conductivity beneath the Columbia basalts. *Geophysical Prospecting*, **44**, 963–986.

Morrison, H.F., Phillips, R.J. & O'Brien, D.P. (1969). Quantitative interpretation of transient electromagnetic fields over a layered halfspace. *Geophysical Prospecting*, **17**, 82–101.

Nabighian, M.N. (1979). Quasi-static transient response of a conducting half-space - An approximate representation. *Geophysics*, **44**, 1700–1705.

Nabighian, M.N. & Macnae, J. (1991). TEM systems. In M.N. Nabighian, ed., *Electromagnetic Methods in Applied Geophysics, Volume 2, Application*, 479–483, Soc. of Expl. Geophys.

Naess, O.E. & Burland, L. (1985). Stacking methods other than simple summation. In A.A. Fitch, ed., *Developments in Geophysical Exploration Methods 6*, 189–223, Elsevier, London.

Nekut, A.G. (1987). Direct inversion of time-domain electromagnetic data (short note). *Geophysics*, **52**, 1431–1435.

Nekut, A.G. (1994). Electromagnetic ray-trace tomography. *Geophysics*, **59**, 371–377.

Nekut, A.G. (1995). Crosswell electromagnetic tomography in steel-cased wells. *Geophysics*, **60**, 912–920.

Nekut, A.G. & Eaton, P.A. (1990). Effects of pipelines on EM soundings. *60th Ann. Internat. Mtg., Soc. of Expl. Geophys., Expanded Abstracts*, 491–494.

Nekut, A.G. & Spies, B. (1989). Petroleum exploration using controlled-source electromagnetic methods. *Proc. IEEE*, **77**, 338–362.

Newman, G. & Alumbaugh, D. (1996). 3-D electromagnetic modeling and inversion on massively parallel computers. In M. Oristaglio & B. Spies, eds., *Three-Dimensional Electromagnetics*, 229–321, Soc. Expl. Geophys.

Newman, G.A. (1989). Deep transient electromagnetic soundings with a grounded source over near-surface conductors. *GJI*, **98**, 587–601.

Newman, G.A., Hohmann, G.W. & Anderson, W.L. (1986). Transient electromagnetic response of a three-dimensional body in a layered earth. *Geophysics*, **51**, 1608–1627.

Newman, G.A., Anderson, W.L. & Hohmann, G.W. (1987). Interpretation of transient electromagnetic soundings over three-dimensional structures for the central-loop configuration. *Geophysical J. R. Astr. Soc.*, **89**, 889.

Oehler, D. & Sternberg, B. (1984). Seepage-induced anomalies, 'false' anomalies and implications for electrical prospecting. *Bull. Am. Assn. Petr. Geol.*, **68**, 1121–1145.

Oliver, D. (1994). Application of a wave transform to pressure transient testing in porous media. *Transport in Porous Media*, **16**, 209–236.

Oristaglio, M.L. & Hohmann, G.W. (1984). Diffusion of electromagnetic fields into a two-dimensional earth - A finite-difference approach. *Geophysics*, **49**, 870–894.

Orsinger, A. & van Nostrand, R. (1954). A field evaluation of the electromagnetic reflection method. *Geophysics*, **19**, 478–489.

Palacky, G. (1988). Resistivity characteristics of geologic targets. In M.N. Nabighian, ed., *Electromagnetic Methods in Applied Geophysics, Volume 1, Theory*, 53–129, Soc. Expl. Geophys.

Passalacqua, H. (1983). Electromagnetic fields due to a thin resistive layer. *Geophysical Prospecting*, **31**, 945–976.

Polzer, B., MacNae, J., Miura, Y. & Takasugi, S. (1990). Stripping cultural conductor responses from EM data. *60th Ann. Internat. Mtg., Soc. of Expl. Geophys., Expanded Abstracts*, 487–490.

Pratt, R. (1953). New oil finding method tested. *World Oil*, **November**, 98–105.

Pridmore, D.F., Hohmann, G.W., Ward, S.H. & Sill, W.R. (1981). An investigation of finite-element modeling for electrical and electromagnetic data in three-dimensions. *Geophysics*, **46**, 1009–1024.

Qian, W. (1994). On small-scale near-surface distortion in controlled-source tensor electromagnetics. *Geophysical Prospecting*, **42**, 501–520.

Qian, W. & Boerner, D.E. (1995). Electromagnetic modelling of buried line conductors using an integral equation. *GJI*, **121**, 203–214.

Qian, W. & Pedersen, L. (1991). Industrial interference magnetotellurics: An example from the Tangshan area, China. *Geophysics*, **56**, 265–273.

Qian, W. & Qian, . (1985). Automatic powerline interference canceller for geophysical instruments. *Australian Soc. Explor. Geophys. Bull.*, **16**, 266–268.

Raiche, A. (1983). Comparison of apparent resistivity functions for transient electromagnetic methods. *Geophysics*, **48**, 787–789.

Raiche, A., Sugeng, F. & Xiong, Z. (2000). Are 3-D electromagnetic modeling and inversion useful. *70th Ann. Internat. Mtg., Soc. of Expl. Geophys., Expanded Abstracts*, 296–299.

Rauzi, S.L. (2003). Want to drill an oil well? *Arizona Geology*, **33**, 1–6.

Rice, R., Allen, S., Gant Jr, O., Hodgson, R., Larson, R., Lindsey, J., Patch, J., LaFehr, T., Pickett, G., Schneider, W., White, J. & Roberts, J. (1981). Developments in exploration geophysics, 1975-1980. *Geophysics*, **46**, 1088–1099.

San Filipo, W.A., Eaton, P.A. & Hohmann, G.W. (1985). The effect of a conductive halfspace on the transient electromagnetic response of a three-dimensional body. *Geophysics*, **50**, 1144–1162.

Schenkel, C.J. & Morrison, H.F. (1994). Electrical resistivity measurement through metal casing. *Geophysics*, **59**, 1072–1082.

Schlumberger, C., Schlumberger, M. & Leonardon, E. (1934). A method of determining bottom hole data by electrical measurements. *Trans. AIME*, **110**, 237–272.

Sheng, Y. (1986). A single apparent resistivity expression for long-offset transient electromagnetics. *Geophysics*, **51**, 1291–1297.

Sheriff, R.E. (1984). *Encyclopedic Dictionary of Exploration Geophysics*. Soc. Expl. Geophys.

Sheriff, R.E. & Geldart, L.P. (1995). *Exploration Seismology, second edition*. Cambridge University Press.

Sinha, M., Patel, P., Unsworth, M., Owen, T. & MacCormack, M. (1990). An active source electromagnetic sounding system for marine use. *Marine Geophysical Research*, **12**, 59–68.

Slob, E., Habashy, T.M. & Torres-Verdin, C. (1995). A new stable numerical procedure for computing the Q-transform of TEM data. *57th Ann. Mtg., Eur. Assn. of Expl. Geophys., Expanded Abstracts*, Session:D053.

Smith, R.S. & West, G. (1989). Field examles of negative coincident-loop transient electromagnetic responses modelled with polarizable half-planes. *Geophysics*, **54**, 1491–1498.

Smith, R.S., Edwards, R.N. & Buselli, G. (1994). Automatic technique for presentation of coincident-loop, impulse-response, transient, electromagnetic data. *Geophysics*, **59**, 1542–1550.

Spies, B. & Frischknecht, F. (1991). Electromagnetic sounding. In M.N. Nabighian, ed., *Electromagnetic Methods in Applied Geophysics, Volume 2, Application*, 285–425, Soc. of Expl. Geophys.

Spies, B.R. (1980). A field occurrence of sign reversals with the transient electromagnetic method. *Geophys. Prosp.*, **28**, 620–632.

Spies, B.R. (1983). Recent developments in the use of surface electrical methods for oil and gas exploration in the Soviet Union. *Geophysics*, **48**, 1102–1112.

Spies, B.R. (1988a). Local noise prediction filtering for central induction transient electromagnetic sounding. *Geophysics*, **53**, 1068–1079.

Spies, B.R. (1988b). *Method and apparatus for cancelling powerline noise in geophysical electromagnetic exploration*. United States Patent Number 4,996,484.

Spies, B.R. (1989). Depth of investigation in electromagnetic sounding methods. *Geophysics*, **54**, 872–888.

Spies, B.R. & Eggers, D.E. (1986). The use and misuse of apparent resistivity in electromagnetic methods. *Geophysics*, **51**, 1462–1471.

Spies, B.R. & Greaves, R.J. (1991). Numerical modeling of surface-to-borehole electromagnetic surveys for monitoring thermal enhanced oil-recovery. *Geoexploration*, **28**, 293–311.

Stephan, A. (1989). *Interpretation von transient elektromagnetischen Messungen (LOTEM) im Bereich der Halterner Sande und Entwicklung der lokalen Rauschkompensation*. Master's thesis, University of Cologne.

Stephan, A. & Strack, K.M. (1991). A simple approach to improve the S/N ratio for TEM data using multiple receivers. *Geophysics*, **56**, 863–869.

Sternberg, B.K., Washburne, J.C. & Pellerin, L. (1988). Correction for the static shift in magnetotellurics using transient electromagnetic soundings. *Geophysics*, **53**, 1459–1468.

Stoyer, C. (1998). Vertical resolution and equivalence in EM soundings. In *SAGEEP Workshop Course Notes*.

Stoyer, C.H. & Damron, L. (1986). Integrated geophysical study in the Eastern basin and range Milford Valley, UT. Tech. rep., Integrated Geosciences Inc., (Unpublished technical report).

Strack, K. & Vozoff, K. (1996). Integrating long-offset transient electromagnetics (LOTEM) with seismics in an exploration environment. *Geophysical Prospecting*, **44**, 997–1017.

Strack, K., Hanstein, T., & Eilenz, H. (1989a). LOTEM data processing for areas with high cultural noise levels. *Physics of the Earth and Planetary Interiors*, **53**, 261–269.

Strack, K.M. (1992). *Exploration with Deep Transient Electromagnetics*. Elsevier.

Strack, K.M., Hanstein, T., Brocq, K.L., Moss, D.C., Vozoff, K. & Wolfgram, P.A. (1989b). Case histories of LOTEM surveys in hydrocarbon prospective areas. *First Break*, **7**, 467–477.

Strack, K.M., Hordt, A., Wolfgram, P. & Vozoff, K. (1991). Integrated electromagnetic and seismic methods for petroleum exploration. *Exploration Geophysics*, **22**, 375–378.

Stratton, J.A. (1941). *Electromagnetic theory*. McGraw-Hill Book Co.

Sumner, J.S. (1985). *Principles of Induced Polarization for Geophysical Exploration*. Elsevier.

Szarka, L. (1988). Geophysical aspects of man-made electromagnetic noise in the earth. *Surveys in Geophysics*, **9**, 287–318.

Tabarovsky, L., Goldman, M., Rabinovich, M. & Strack, K.M. (1996). 2.5-D modelling in electromagnetic methods of geophysics. *Journal of Applied Geophysics*, **35**, 261–284.

Tasci, M. & Jordan, J. (1996). *Electromagnetic imaging device and method for delineating anomalous resistivity patterns associated with oil and gas traps.* United States Patent 5,563,513.

Tasci, M.T. & Jordan, J.M. (2003). Case histories using the time domain electromagnetic sounding method in oil and gas exploration. *Submitted to Geophysics.*

Tournerie, B. & Gibert, D. (1995). Inversion of the COPROD2 magnetotelluric data using a diffusive-to-propagative mapping (DPM). *Geophysical Research Letters*, **22**, 2187–2190.

Tseng, H.W., A., B., Wilt, M. & Deszcz-Pan, M. (1998). A borehole-to-surface electromagnetic survey. *Geophysics*, **63**, 1565–1572.

Udias, A. (1999). *Principles of seismology.* Cambridge University Press.

Unsworth, M.J., Travis, B.J. & Chave, A.D. (1993). Electromagnetic induction by a finite electric dipole source over a 2-D earth. *Geophysics*, **58**, 198–214.

Vanyan, L. (1967). *Fundamentals of EM sounding.* Consultants Bureau.

Verma, R.K. & Mallick, K. (1979). Detectability of intermediate conductive and resistive layers by time-domain electromagnetic sounding. *Geophysics*, **44**, 1862–1878.

Vozoff, K. & Jupp, D. (1975). Joint inversion of geophysical data. *Geophys. J. R. Astr. Soc.*, **42**, 977–991.

Walker, P. & West, G. (1992). Parametric estimators for current excitation on a thin plate. *Geophysics*, **57**, 766–773.

Wang, T. & Hohmann, G.W. (1993). A finite-difference time-domain solution for three-dimensional electromagnetic modeling. *Geophysics*, **58**, 797–809.

Ward, S. (1983). Controlled source electrical methods for deep exploration. *Geophysical Surveys*, **6**, 137–152.

Ward, S.H. & Hohmann, G.W. (1988). Electromagnetic theory for geophysical applications. In M.N. Nabighian, ed., *Electromagnetic Methods in Applied Geophysics, Volume 2, Application*, 131–311, Soc. Expl. Geophys.

Watt, T. & Bednar, J.B. (1983). Role of the alpha-trimmed mean in combining and analyzing seismic common depth-point gathers. *53rd Ann. Internat. Mtg., Soc. of Expl. Geophys., Expanded Abstracts*, Session:S3.5.

Weidelt, P. (1972). The inverse problem of geomagnetic induction. *Zeit. fur Geophysik*, **38**, 257–289.

Weidelt, P. (1982). Response characteristics of coincident loop transient electromagnetic systems. *Geophysics*, **47**, 1325–1330.

Weir, G. (1980). Transient electromagnetic fields about an infinitesimally long grounded horizontal electric dipole on the surface of a uniform halfspace. *Geophys. J. Roy. Astr. Soc.*, **61**, 41–56.

West, G.F., Macnae, J.C. & Lamontagne, Y. (1984). A time-domain EM system measuring the step response of the ground. *Geophysics*, **49**, 1010–1026.

Wilson, A. (1997). *The Equivelant Wavefield Concept in Multichannel Transient Electromagnetic Surveying*. Ph.D. thesis, University of Edinburgh.

Wilson, A., Ziolkowski, A. & Hobbs, B. (1998). Interpreting the equivalent wavefield of a mtem survey over a layered earth. *60th Ann. Mtg.Eur. Assn. Geosci. Eng., Expanded Abstracts*, Session:P111.

Wilt, M. & Alumbaugh, D. (1998). Electromagnetic methods for development and production: State of the art. *The Leading Edge*, **17**, 487–490.

Wilt, M. & Becker, A. (1986). Effects of vertical contacts on time-domain electromagnetic sounding. *56th Ann. Internat. Mtg., Soc. of Expl. Geophys., Expanded Abstracts*, 177–180.

Withers, R., Eggers, D., Fox, T. & Crebs, T. (1994). Case study of integrated hydrocarbon exploration through basalt. *Geophysics*, **59**, 1666–1679.

Wright, D., Ziolkowski, A. & Hobbs, B. (2002). Hydrocarbon detection and monitoring with a multicomponent transient electromagnetic (MTEM) survey. *The Leading Edge*, **21**, 852–864.

Wu, X. & Habashy, T.M. (1994). Influence of steel casings on electromagnetic signals. *Geophysics*, **59**, 378–390.

Yost, W.J. (1952). The interpretation of electromagnetic reflection data in geophysical exploration - Part I: General theory. *Geophysics*, **17**, 89–106.

Yost, W.J., Caldwell, R.L., Beard, C.I., McClure, C.D. & Skomal, E.N. (1952). The interpretation of electromagnetic reflection data in geophysical exploration - Part II: Metallic model experiments. *Geophysics*, **17**, 806–826.

Young, P. & Cox, C. (1981). Electromagnetic active source sounding near the east pacific rise. *Geophysical Research Letters*, **08**, 1043–1046.

Yungul, S. (1996). *Electrical methods in geophysical exploration of deep sedimentary basins*. Chapman and Hall.

Zhdanov, M. & Frenkel, M. (1983). The solution of the inverse problems on the basis of the analytical continuation of the transient electromagnetic field in reverse time. *Journal of Geomag. Geoelectr.*, **35**, 747–765.

Zhdanov, M. & Keller, G. (1994). *The geoelectrical methods in geophysical exploration*. Elsevier.

Zhdanov, M., Traynin, P. & Booker, J. (1996). Underground imaging by frequency-domain electromagnetic migration. *Geophysics*, **61**, 666–682.

Zhdanov, M., Varenstov, I., Weaver, J., Golubev, N. & Krylov, V. (1997). Methods for modelling electromagnetic fields. Results from COMMEMI-the international project on the comparison of modelling methods for electromagnetic induction. *Journal of Applied Geophysics*, **37**, 133–271.

Ziolkowski, A. & Hobbs, B. (1998). CMP method applied to multichannel transient electromagnetic data. *60th Ann. Mtg. Eur. Assn. Geosci. Eng., Expanded Abstracts*, Session:10–05.

Ziolkowski, A.M., Hobbs, B.A., Rüter, H., Hördt, A., Neubauer, F. & Andrieux, P. (1998a). *Delineation and Monitoring of Oil Reservoirs using Seismic and Electromagnetic Methods*. Final Technical Report.

Appendix A

Elastic wave propagation in the earth

Seismic waves are known to obey the wave equation and can be thought of as parcels of elastic strain energy that propagate outwards from a seismic source such as an explosion or an airgun. Except in the immediate vicinity of the source, the strains associated with the passage of a seismic pulse are minute and can be assumed to be elastic. A perfectly elastic body is one which recovers completely after being deformed; to a good approximation, rocks in the earth can be considered to be perfectly elastic in response to small deformation. This section derives the vector wave equation starting from the basic principles of stress and strain.

Stress, strain and displacement

Stress is defined as the force per unit area. A force applied perpendicular to an area is a normal stress while one applied tangentially is known as a shearing stress. Stress is defined mathematically by the stress tensor τ_{ij} [1] where the subscripts denote the x, y and z axes. So for example, τ_{xy} denotes a stress parallel to the y axis acting on a surface perpendicular to the x axis. For $i = j$ the stress is normal while for $i \neq j$ the stress is tangential. The stress tensor may therefore be written as the sum of two parts, dilatational and deviatoric, representing changes of volume and shape, respectively (Johnston, 2000):

---

[1] In seismology the symbols σ, ρ and μ are used to represent stress, density and a Lamé parameter respectively. However, these are the same as the symbols for conductivity, charge density and magnetic permeability in EM. Therefore, τ, ϱ and μ are used here to describe stress, density and a Lamé parameter in order to avoid confusion.

$$\tau_{ij} = -p\delta_{ij} + \tau'_{ij}, \tag{A.1}$$

where $-p\delta_{ij}$ is the volumetric part, δ_{ij} is the Kronecker delta (which equals 1 when $i = j$, and 0 otherwise) and the deviatoric part is represented by

$$\tau'_{ij} = \tau_{ij}(1 - \delta_{ij}). \tag{A.2}$$

The volume changes are caused by the mean inward directed force acting on the particles, and therefore related to the pressure by

$$p = -\frac{1}{3}\tau_{kk} \tag{A.3}$$

where the repeated subscript implies a summation ($\tau_{kk} = \tau_{xx} + \tau_{yy} + \tau_{zz}$). In an ideal fluid, which cannot support changes in shape, or shear, only the dilatational stresses are present. The effect of equal stresses acting on opposite sides of an element of volume is shown in Figure A.1a.

Whenever an elastic body is subjected to stresses, changes in shape and dimension occur, known as strains. Consider a point P within a body displaced to a position P' as a result of an applied stress. If all the other points within the body are displaced by the same amount then the effect of the stress is merely to displace the body as a whole without changing its size or shape. However, if different parts of a body undergo different displacements there is a change in size and shape, and strains exist. The displacement of particles is denoted by $\mathbf{u} = (u_x, u_y, u_z)$. Strain is described mathematically by the strain tensor ε_{ij} and can be normal $i = j$ or shearing $i \neq j$ in nature, in the same way as described for stress. The strains and associated displacements for a 2-D area are shown in Figure A.1b. The strain tensor can be written as

$$\varepsilon_{ij} = \frac{1}{2}\left(\frac{\partial u_i}{\partial x_j} + \frac{\partial u_j}{\partial x_i}\right) = \frac{1}{2}(u_{i,j} + u_{j,i}) \tag{A.4}$$

224

where the comma is used to represent partial derivatives with respect to the corresponding spatial coordinate. It accounts for the deformation associated with a displacement, like the stress tensor, it is a symmetric second order tensor.

In addition to these strains, the body is subjected to simple rotation about the three axes given by the rotation tensor (e.g.Udias (1999))

$$\omega_{ij} = \frac{1}{2}(u_{i,j} - u_{j,i}). \tag{A.5}$$

The rotation tensor is related to the curl of the displascements as follows,

$$\boldsymbol{\omega} = \boldsymbol{\nabla} \times \boldsymbol{u}. \tag{A.6}$$

The rotation tensor ω is antisymmetric. Using the tensors $\boldsymbol{\varepsilon}$ and $\boldsymbol{\omega}$ the partial derivatives of the displacements are given by

$$u_{i,j} = \varepsilon_{ij} + \omega_{ij}. \tag{A.7}$$

The partial derivatives of **u** are therefore totally defined by the two tensors ε_{ij} and ω_{ij}. This means that the variations of displacements from one point to another in a deformable medium include both strains and rotations.

Changes in dimension given by the normal strains result in volume changes when a body is stressed. Change in volume per unit volume is called dilatation and represented by Δ. For a cube of side length dx, dy, dz when unstrained, in the strained state the medium has sides of length $dx(1 + \varepsilon_{xx})$, $dy(1 + \varepsilon_{yy})$ and $dz(1 + \varepsilon_{zz})$ respectively, this is illustrated in Figure A.1c. So the change in volume per unit volume is,

$$\Delta = \varepsilon_{xx} + \varepsilon_{yy} + \varepsilon_{zz} = u_{1,1} + u_{2,2} + u_{3,3} = \nabla \cdot \boldsymbol{u}. \tag{A.8}$$

A disturbance that results in a volume change is the result of P-wave motion while one

225

that results in pure rotation is the result of S-wave motion. Both of which satisfy the wave equation as will be shown.
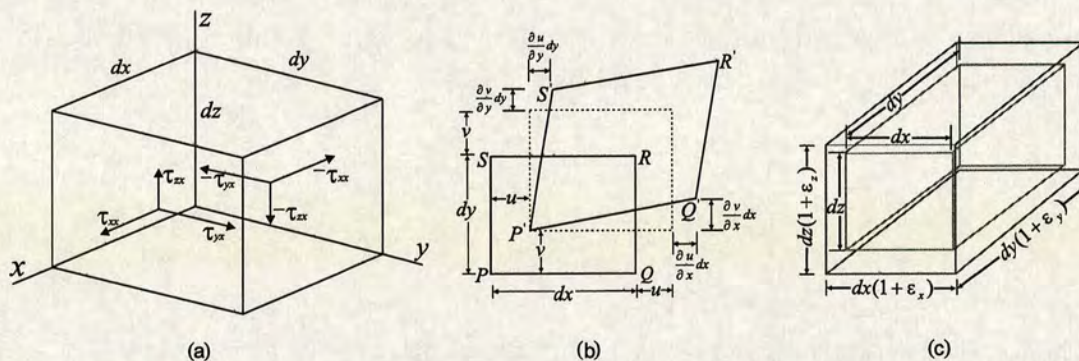

Figure A.1: The concepts of stress, strain and dilatation. (a) Equal stresses acting on opposite sides of a volume. (b) The strains and deformations associated with an unbalanced stress. (c) Volume change within a volume due to an applied stress giving rise to Δ.

Elasticity coefficients and Hooke's law

The mechanical behaviour of a continuous material is defined by the relation between stress and strain. For a linear elastic body, this relation is given by Hooke's law, which states that the strain is proportional to the stress. The tensor form of this law can be written as

$$\tau_{ij} = C_{ijkl}\varepsilon_{kl} \tag{A.9}$$

with indices summed according to the Einstein summation convention. This equation states the linear relation between the stress and strain tensors and is the foundation of the theory of linear elasticity. The fourth order tensor C_{ijkl} is the tensor of the elasticity coefficients or moduli (also known as the stiffness tensor or Hooke's tensor) and has 81 components. Owing to the symmetry of τ_{ij} and ε_{ij} the number of coefficients can be reduced to 21 (Malvern, 1969).

The simplest case for the elastic coefficients corresponds to an isotropic medium, that is, a medium with the same properties in all directions. For such a medium the tensor C_{ijkl} is characterised by two independent coefficients only, the Lamé paramters λ and μ:

$$C_{ijkl} = \lambda \delta_{ij} \delta kl + \mu(\delta_{ik}\delta_{jl} + \delta_{il}\delta_{jk}). \tag{A.10}$$

Substituting (A.10) into (A.9) the relation between stress and strain is found to be

$$\tau_{ij} = \lambda \delta_{ij}\varepsilon_{kk} + 2\mu\varepsilon_{ij} \tag{A.11}$$

where ε_{kk} is the cubic dilatation. Substituting (A.4) into (A.11) yields the relationship between stress and displacement:

$$\tau_{ij} = \lambda \delta_{ij}u_{k,k} + \mu(u_{i,j} + u_{j,i}). \tag{A.12}$$

The equation of motion

The linearised equation of motion (Newton's second law) of an elastic solid can be written as

$$\frac{\partial \tau_{ij}}{\partial x_j} + F_i = \varrho \frac{\partial^2 u_i}{\partial t^2}, \tag{A.13}$$

where ϱ is the density of the solid and F is the body force density (Udias, 1999). Equation (A.13) can be written in terms of the strain for an elastic medium by substitution of (A.9) into it:

$$\frac{\partial}{\partial x_j}(C_{ijkl}\varepsilon_{kl}) + F_i = \varrho \frac{\partial^2 u_i}{\partial t^2}. \tag{A.14}$$

For an isotropic material, using equation (A.12) and substituting into (A.13), we obtain

227

$$[\lambda\delta_{ij}u_{k,k} + \mu(u_{i,j} + u_{j,i})]_{,j} + F_i = \varrho\ddot{u}_i \qquad (A.15)$$

where the double overdot $\ddot{}$ denotes the second partial derivative with respect to time. For a homogeneous material, that is, for λ and μ constant, we can write the equation of motion in index notation as

$$(\lambda + \mu)u_{k,ki} + \mu u_{i,jj} + F_i = \varrho\ddot{u}_i, \qquad (A.16)$$

and vector notation as

$$\boxed{(\lambda + \mu)\nabla(\nabla \cdot \boldsymbol{u}) + \mu\nabla^2\boldsymbol{u} + \boldsymbol{F} = \varrho\ddot{\boldsymbol{u}}.} \qquad (A.17)$$

The wave equation

The equation of motion (A.17) can also be expressed in terms of the cubic dilatation Δ and the rotation vector $\boldsymbol{\omega}$, whose relations to displacements are given in (A.8) and (A.6), respectively. Using the vector identity

$$\nabla \times (\nabla \times \boldsymbol{A}) =$$
$$\nabla(\nabla \cdot \boldsymbol{A}) - \nabla^2\boldsymbol{A} \qquad (A.18)$$

snd substituting for the Laplacian of $\boldsymbol{u}$ in (A.16) yields,

$$(\lambda + \mu)u_{k,ki} - \mu\varepsilon_{ijk}\varepsilon_{kln}u_{n,lj} + F_i = \varrho\ddot{\boldsymbol{u}}. \qquad (A.19)$$

Replacing Δ and $\boldsymbol{\omega}$ according to (A.8) and (A.6) and dividing by ϱ yields

228

$$\alpha^2 \Delta_{,i} - \beta^2 \varepsilon_{ijk} \omega_{k,j} + \frac{F_i}{\varrho} = \ddot{u}_i \tag{A.20}$$

and in vector notation,

$$\alpha^2 \boldsymbol{\nabla} \Delta - \beta^2 \boldsymbol{\nabla} \times \boldsymbol{\omega} + \frac{\boldsymbol{F}}{\varrho} = \ddot{\boldsymbol{u}}. \tag{A.21}$$

In equations (A.20) and (A.21) the parameters α and β have been introduced, their values in terms of the elastic coefficients are

$$\alpha^2 = \frac{\lambda + 2\mu}{\varrho}, \quad \beta^2 = \frac{\varrho}{\mu}.$$

The parameter α and is related to changes in Δ and, in consequence, to changes in volume, and β is related to $\boldsymbol{\omega}$, that is, to changes in form without changes in volume. In the earth α and β are better known as the P-wave and S-wave velocities respectively.

The displacements $\boldsymbol{u}(\boldsymbol{x}, t)$ in an elastic medium form a vector field. We can, therefore, apply Helmholtz's theorem that allows their representation in terms of two potential functions, a scalar potential φ and a vector potential $\boldsymbol{\psi}$:

$$\boldsymbol{u} = \nabla \varphi + \boldsymbol{\nabla} \times \boldsymbol{\psi} \tag{A.22}$$

The vector potential $\boldsymbol{\psi}$ must satisfy the condition that its divergence is zero ($\boldsymbol{\nabla} \cdot \boldsymbol{\psi} = 0$). Using equations (A.8) and (A.6) it is easy to deduce the relations of the two potentials to the cubic dilatation Δ and the rotation $\boldsymbol{\omega}$:

$$\Delta = \nabla^2 \varphi \tag{A.23}$$

$$\boldsymbol{\omega} = -\nabla^2 \boldsymbol{\psi} \tag{A.24}$$

229

These relations indicate that φ is related to changes in volume and $\boldsymbol{\psi}$ to changes in form. The body forces $\boldsymbol{F}$ can also be represented in a similar form by two potential functions, a scalar potential Φ and a vector potential of divergence zero $\boldsymbol{\Psi}$:

$$\boldsymbol{F} = \nabla\Phi + \boldsymbol{\nabla} \times \boldsymbol{\Psi} \qquad (A.25)$$

Equation (A.21) may now be written in terms of potentials using equations (A.23-A.25) and can be separated into a scalar equation and a vector equation:

$$\nabla^2\varphi - \frac{1}{\alpha^2}\frac{\partial^2\varphi}{\partial t^2} = -\frac{\Phi}{\alpha^2\varrho} \qquad (A.26)$$

$$\nabla^2\boldsymbol{\psi} - \frac{1}{\beta^2}\frac{\partial^2\boldsymbol{\psi}}{\partial t^2} = -\frac{\boldsymbol{\Psi}}{\beta^2\varrho} \qquad (A.27)$$

More generally, the wave equation including a source term $\boldsymbol{S}(\boldsymbol{x}, t)$ may be written as,

$$\boxed{\nabla^2\boldsymbol{U}(\boldsymbol{x}, t) - \frac{1}{c^2}\frac{\partial^2\boldsymbol{U}(\boldsymbol{x}, t)}{\partial t^2} = \boldsymbol{S}(\boldsymbol{x}, t)} \qquad (A.28)$$

where $\boldsymbol{U}(\boldsymbol{x}, t)$ is a wavefield and c is the wave speed.

Appendix B

Testing 1-D Modelling Codes

Various 1-D modelling codes were used throughout the course of this thesis. The three codes used are MODALL (Strack, 1992), TEMD written and by Knúter Árnason of the Icelandic energy authority and marine modelling code written by Nigel Edwards of the University of Toronto and described in (Edwards, 1997). I am grateful to all three authors for making their software freely available.

Both TEMD and MODALL can calculate the components E_{xx}, E_{yy}, E_{xy}, E_{yx} and $\frac{dH_z}{dz}$ in response to a grounded electric dipole source. The program by Edwards calculates only E_{xx}. Although the Edwards program is designed for marine modelling it can be used to model the land case by setting the water depth equal to 0.001m as will be shown. All three pieces of software calculate the response in the frequency domain and then transform back to the time domain to recover the transient response.

In addition to the three modelling codes mentioned already the in-line electric field response to a grounded electric dipole over a halfspace can be calculated from the analytic solution (Weir, 1980):

$$\boldsymbol{E}_{xx}(r, t > 0) = \frac{\mathcal{D}}{2\pi\sigma r^3}(erf(\frac{r}{c2\sqrt{t}}) - \frac{2}{\sqrt{\pi}}\frac{r}{c2\sqrt{t}}\exp(-\frac{r^2}{c^2 4t})). \qquad (B.1)$$

The analytic solution provides a definitive way of checking that the modelling codes are correct for the simple case of a uniform halfspace.

The electric field: E_{xx}

Figure B.1 shows the E_{xx} response over a 10 Ωm halfspace at an offset of 1000m for the analytic solution and all three 1-D modelling codes.
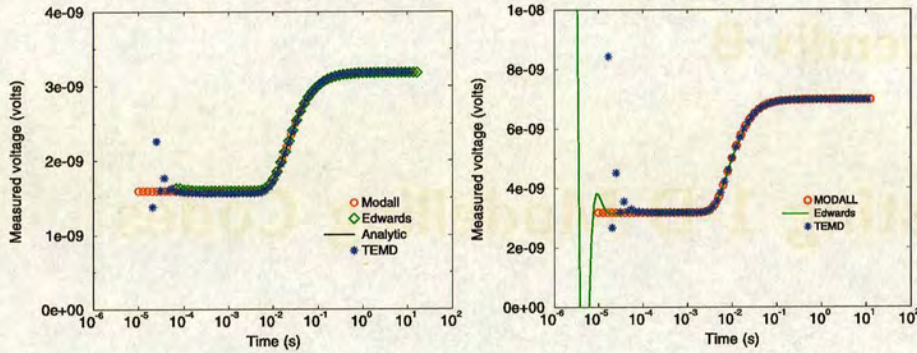

Figure B.1: The E_{xx} transient response for the analytic solution and three 1-D modelling codes. Left: Over a 10 Ωm halfspace at an offset of 1000m. Right: Over a 400 Ωm 25m thick resistor buried at a depth of 500m in a 20 Ωm halfspace at an offset of 1000m.

It can be seen from Figure B.1 that for times greater than about 0.1ms all three modelling codes are in agreement with the analytic solution. For times shorter than 0.1ms the TEMD and Edwards code become unstable while the MODALL code is stable up to 0.01ms which is the minimum time that the program can calculate.

The electric field: E_{yy}

The E_{yy} transient response at an offset of 1000m for a halfspace and a buried resistor are shown in Figure B.2 for the TEMD and MODALL modelling codes. The results for the two codes in both models are in agreement up to 0.01ms. At times shorter than this the TEMD code is unstable while the MODALL code cannot calculate time values shorter than this.

The electric field: E_{xy} and E_{yx}

Figure B.3 shows the E_{xy} and E_{yx} transient response for the TEMD and MODALL modelling codes over a halfspace and a resistor buried in a halfspace. In both cases the response is zero for both modelling codes. This result is in agreement with that obtained by Eadie (1981) who observeed that the E_{xy} and E_{yx} responses are zero over a uniform halfspace and any 1-D model when the azimuthal angle between the source and receiver is 0 or 90 degrees.
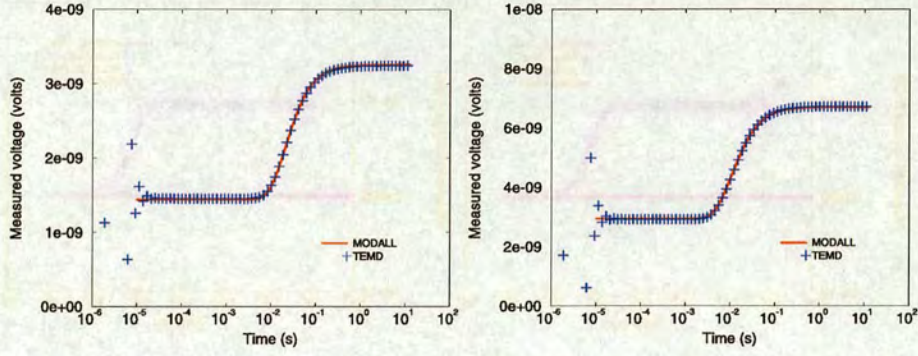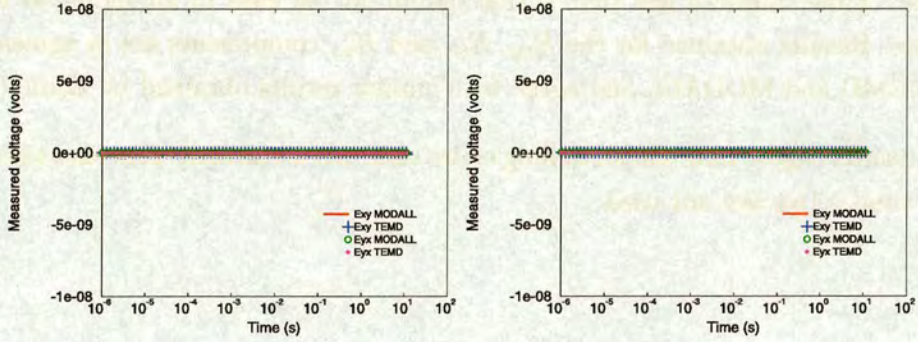
Figure B.2: The E_{yy} transient response for the TEMD and MODALL 1-D modelling codes. Left: Over a 10 Ωm halfspace at an offset of 1000m. Right: Over a 400 Ωm 25m thick resistor buried at a depth of 500m in a 20 Ωm halfspace at an offset of 1000m.

Figure B.3: The E_{xy} and E_{yx} transient response for the TEMD and MODALL 1-D modelling codes. Left: Over a 10 Ωm halfspace at an offset of 1000m. Right: Over a 400 Ωm 25m thick resistor buried at a depth of 500m in a 20 Ωm halfspace at an offset of 1000m.

The magnetic field: H_{xz} and H_{yz}

Figure B.4 shows the H_{xz} and H_{yz} transient response for the TEMD and MODALL modelling codes over a halfspace and a resistor buried in a halfspace. Over the halfspace the response is zero for the H_{xz} component for both modelling codes, again this is in agreement with similar results obtained by Eadie (1981). The response of the H_{yz} component is the same for both modelling codes for times greater than 0.1ms which is similar to the results for the other components.

Conclusions

For the E_{xx} component the three modelling codes MODALL, TEMD and Edwards are in agreement with each other in the presence of a halfspace and a buried resistor for times later than 0.1ms. They are also in greement with the analytic solution for a
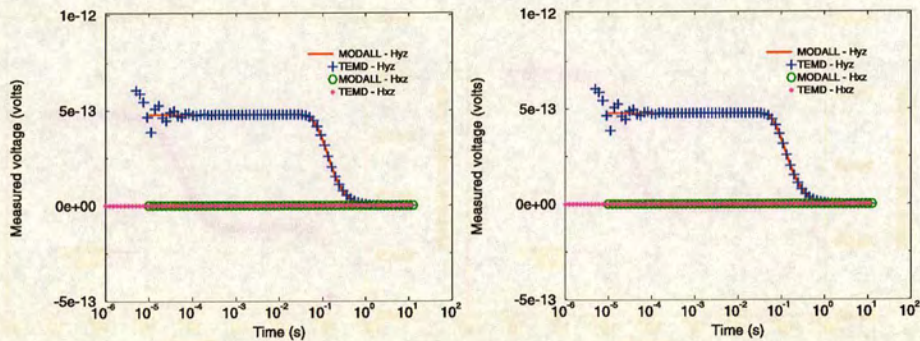
233

Figure B.4: The H_{xz} and H_{yz} transient response for the TEMD and MODALL 1-D modelling codes. Left: Over a 1 Ωm halfspace at an offset of 1000m. Right: Over a 200 Ωm 25m thick resistor buried at a depth of 500m in a 1 Ωm halfspace at an offset of 1000m.

halfsace. Time values of less than 0.1ms should not be used in modelling as they are unstable. Results obtained for the E_{xy}, E_{yx} and H_{xz} components are in agreement for both TEMD and MODALL and agree with similar results obtained by Eadie (1981).

These results sugest that the modelling codes used work correctly provided time values of less than 0.1ms are not used.

Appendix C

Leading Edge Paper

Hydrocarbon detection and monitoring with a
multicomponent transient electromagnetic
survey

David Wright, Anton Ziolkowski and Bruce Hobbs, The
University of Edinburgh, U.K.

235

THE METER READER

Hydrocarbon detection and monitoring with a multicomponent transient electromagnetic (MTEM) survey

DAVID WRIGHT, ANTON ZIOLKOWSKI, and BRUCE HOBBS, The University of Edinburgh, U.K.

We present results from a transient electromagnetic experiment to detect hydrocarbons and to monitor their movement within a reservoir. The method is illustrated with data obtained from multichannel transient electromagnetic (MTEM) surveys.

In the petroleum industry, seismic reflection is used extensively to determine subsurface structure, and to locate potential reservoirs, but it is usually unable to determine the nature of the fluid content in the rocks. Because we wish to avoid drilling dry holes, it is obviously very important to know before drilling whether a reservoir contains hydrocarbons or not.

EM methods have the potential to reduce the risk of drilling dry holes because they can discriminate between water-saturated reservoirs (low resistivity) and hydrocarbon-saturated reservoirs (high resistivity). Until now, however, decades of research and development have failed to enable this potential to yield results of much value to the petroleum industry.

The bulk resistivity of a rock depends on its porosity, pore fluid resistivity, and saturation. Consequently, resistivity well logs are used routinely to calculate the porosity and saturation of reservoir rocks. When the pore fluid within a rock changes from water to hydrocarbons, most physical properties of the rock change. Electrical resistivity is most affected. Replacement of brine by oil in a reservoir can cause a change in electrical resistivity of reservoir rock of as much as four orders of magnitude; on the other hand, it has very little effect on acoustic impedance (Figure 1).

Figure 2, an example of a typically strong resistivity contrast, shows part of a resistivity log from a well in the underground gas storage reservoir used in our experiment. Gas is present at a depth of 490 m and resistivity increases from approximately 20 Ohm-m in the rocks above the reservoir to approximately 400 Ohm-m in the gas-saturated reservoir.

The main reason that surface EM methods have rarely been used by the petroleum industry is because resolution of conventional EM data has been very low compared with seismic resolution. EM propagation in rocks obeys the diffusion equation, and EM "pulses" disperse with both time and distance. Seismic wave propagation obeys the wave equation and seismic "pulses" travel great distances with relatively little loss of resolution. However, new multichannel recording systems have greatly increased the dynamic range of EM data, and MTEM provides EM data of higher resolution and spatial coverage.

Our data were obtained in an experiment that formed part of THERMIE project OG/0305/92/NL-UK, which ran from 1992 to 1998. The project was 40% funded by the European Commission and was also supported by Elf Enterprise Caledonia. The project was led by the University of Edinburgh and partnered by Compagnie Générale de Géophysique (CGG), Deutsche Montan Technologie (DMT), and the University of Cologne.

The experiment was performed in cooperation with Gaz de France. Two MTEM surveys were carried out in 1994 and
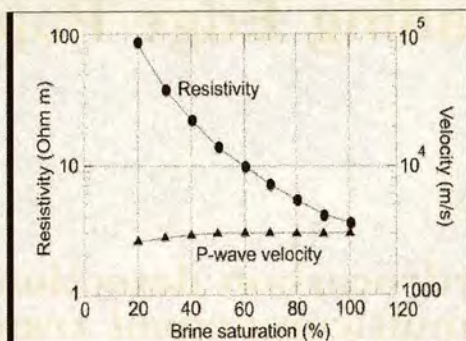

Figure 1. The effect of changing brine saturation on resistivity and P-wave velocity (redrawn from Wilt and Alumbaugh, 1998).

1996 at an underground gas storage reservoir at St. Illiers la Ville, France. The reservoir is a 30% porosity sandstone anticline about 25 m thick at a depth of about 500 m. In summer, gas is pumped in, the gas pressure rises, and the gas-water contact falls; in winter, gas is extracted, the gas pressure decreases, and the gas-water contact rises. The position of the contact is known from constant monitoring at more than 40 wells. The surveys had two objectives: first, to attempt to detect the reservoir directly from the data and, second, to detect the movement of the gas-water contact between the two survey times. A recent breakthrough in the understanding of the system has allowed both objectives to be achieved.

The basic idea of the transient electromagnetic method involves injecting a current into the ground in one place and measuring the response of the earth (the gradient of the electric potential, or the rate of change of magnetic field) at another place. The flow of current in the earth is determined by the resistivity of the rocks. The objective of the measurements is to determine these resistivities. In our experiment we injected a step in current (Figure 3). Figure 4 shows a typical response, the gradient of the electrical potential (including noise).

Information about the earth's resistivity is contained in the rise from zero to the dc level. The dc level itself corresponds to conventional dc resistivity surveying. The transient electromagnetic method in principle allows a huge range of frequencies in the EM spectrum to be used and can
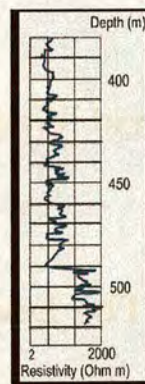

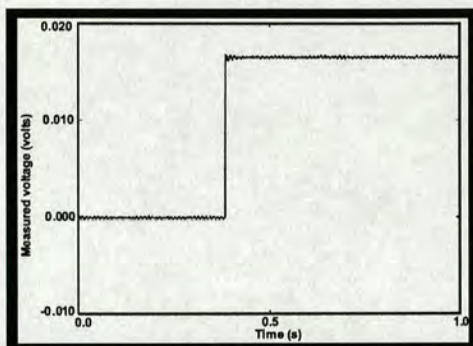Figure 2. Part of a resistivity log from St. Illiers la Ville.

236

Figure 3. Electric potential difference between two electrodes a few cm apart and a few cm from the 250 m current dipole source. This potential difference is proportional to the injected current at the source. The electrodes are so close to the source that the transient effect of the earth is negligible.
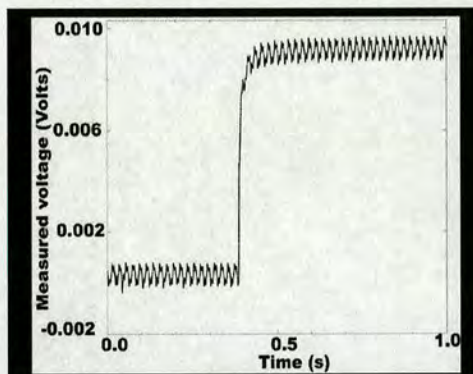

Figure 4. Typical in-line gradient of the electric potential response to a step in current at the source.

thereby give much more information about subsurface resistivity than dc resistivity or shallow single-frequency EM survey equipment. We should mention that the well-established magnetotelluric method is passive, using natural broadband EM signals that are generally in a lower frequency range than that of the active controlled-source transient EM method. Magnetotellurics therefore yields information about deep targets with low resolution.

Data acquisition. The location of our experiment was 30 km west of Paris. The reservoir contains the maximum amount of gas in October, when the gas-water contact is at its lowest level, and the least amount in April, when the gas-water contact is highest. As resistive gas is replaced by more conductive salt water, the resistivity of several million cubic meters of reservoir rock changes.

The first survey took place in October 1994 when the reservoir was full. The second survey was to be carried out in April 1996 but, due to operational difficulties at the site, did not begin until August 1996. Modeling by Hördt et al. (2000) indicated the change in the EM response between maximum and minimum gas would be about 5% and would be accompanied by a lateral movement of the gas-water con-
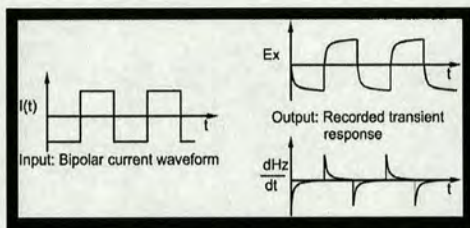
Figure 5. Diagram of source current waveform and resulting transient responses.

tact of about 100 m. As a result of the delay, the estimated decrease in the gas volume between the two surveys was only 1.8% (because of the increase in gas content between April and August). This caused an estimated change in the electromagnetic response of 0.5% and a lateral movement of the gas-water contact of just 8 m (Ziolkowski et al., 1998). Even with a data repeatability of 1%, the actual differences in the reservoir are below the limit of what was originally estimated to be possible to resolve. Detection of the reservoir itself was not originally regarded as very likely, because the metal pipes were expected to induce large EM fields that would be difficult to distinguish from the effects of the reservoir.

However, from our new analysis of the data, we now recognize that the effect of the pipes was negligible and the change in gas content between the two surveys is detectable.

The MTEM method evolved from the long-offset transient electromagnetic (LOTEM) method (Strack et al., 1989) and offers an increased dynamic range which allows data to be collected at much nearer offsets than was previously possible. MTEM also yields unprecedented (for EM) data volumes and spatial coverage. The system used for the data acquisition was TEAMEX, developed by DMT based on its SEAMEX system for seismic acquisition. Field work was similar to seismic reflection profiling—"firing" a controlled current source at one location and measuring EM responses at 16 receiver stations.

The source was a Zonge transmitter that produced a bipolar current waveform switching between plus and minus 30 amperes (Figure 5). Current was injected into the ground via two vertical metal pipes 250 m apart and connected to the transmitter by a wire. Each source position "fired" into 16 receiver boxes with two channels per box. The source was fired 50-100 times for both in-line and cross-line orientations at each location. The electric field parallel to the transmitter was recorded at every receiver station and the electric field perpendicular to the transmitter and the time derivative of the vertical magnetic field were recorded at every second station (Figure 6). For each "shot," a record was made of 2048 samples at 1-ms sampling interval at each channel, with, typically, 384 pretrigger samples. The first second of a raw E_{xx} transient is shown in Figure 4. The recorded transients are in six forms—the E_{xx}, E_{yy}, E_{xy}, and E_{yx} components of the electric field and

$$\frac{\partial H_{xz}}{\partial t} \text{ and } \frac{\partial H_{yz}}{\partial t},$$

the vertical rate of change of the magnetic field for the two source orientations. The first subscript refers to the source orientation and the second to the receiver. The system response for each component and three different currents was also measured in the field in 1996 at two source locations.

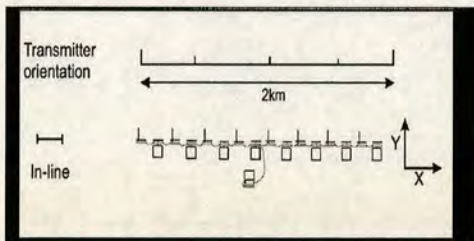Figure 7 shows the field layout of the MTEM line in rela-

237

Figure 6. Field layout showing transmitter and receiver orientation. The receiver line has 16 boxes, each with two channels. For the in-line source configuration every box recorded the in-line E_{xx} potential difference over a distance of 125 m. The odd-numbered boxes also recorded the cross-line E_{xy} potential difference over 125 m. The even-numbered boxes also recorded the rate of change of the vertical component of the magnetic field, measured with 50 m square loops with many turns. The 32 recorded transient responses from the 16 boxes were downloaded onto the hard drive of a computer before the source current was reversed.

Figure 7. Location of MTEM profile relative to reservoir and monitoring wells.

tion to the subsurface anticline and monitoring wells. Figure 8 shows the layout of the survey in relation to the edge of the gas bubble; receiver positions are red. For E_{xx} data a total of 29 source locations were occupied along a profile length of 7 km. Source interval was 250 m and receiver separation was 125 m.

Processing. We outline three approaches to processing transient electromagnetic data: first, the conventional approach based on forward modeling; second, what we believe to be the ideal approach, which uses measurements we did not make; and third, a pragmatic approach which we are not advocating but which allowed us to make an interpretable section across the underground gas storage reservoir with the acquired data.

Conventional approach. Interpretation of EM data has traditionally relied on fitting synthetic responses of simple models to the observations. Models are parameterized in terms of a limited number of resistivities and positional information, and either forward modeling or inversion is carried out in 1-3 dimensions. The conventional approach is described by Keller et al. (1996). Model acceptability is usually measured in a minimum least-squares sense, testing model responses against derived quantities such as apparent resistivity. A variety of subsurface images may be constructed but most ultimately rely on forward calculations based on models with few parameters compared with the amount of raw data acquired.

Ideal approach. The recorded signal is the convolution of the system response with the earth response and added noise:

$$a_k(\mathbf{x}_s, \mathbf{x}_r, t) = s_k(\mathbf{x}_s, \mathbf{x}_r, t) * g(\mathbf{x}_s, \mathbf{x}_r, t) + n_k(\mathbf{x}_r, t), \quad (1)$$

where $a_k(\mathbf{x}_s, \mathbf{x}_r, t)$ is the kth measured signal at source position $\mathbf{x}_s$ receiver position $\mathbf{x}_r$ and time t, $s_k(\mathbf{x}_s, \mathbf{x}_r, t)$ is the system response, $g(\mathbf{x}_s, \mathbf{x}_r, t)$ is the impulse response of the earth and $n_k(\mathbf{x}_r, t)$ is added noise. The asterisk * denotes convolution. We need to deconvolve $s_k(\mathbf{x}_s, \mathbf{x}_r, t)$ from $a_k(\mathbf{x}_s, \mathbf{x}_r, t)$ to recover $g(\mathbf{x}_s, \mathbf{x}_r, t)$. Once the impulse response of the earth has been found, a variety of techniques can recover the resistivities.

In order to deconvolve the system response from the recorded data, it must first be measured. For a number of reasons, however, the system response was not measured and a more pragmatic approach was applied. Before out-
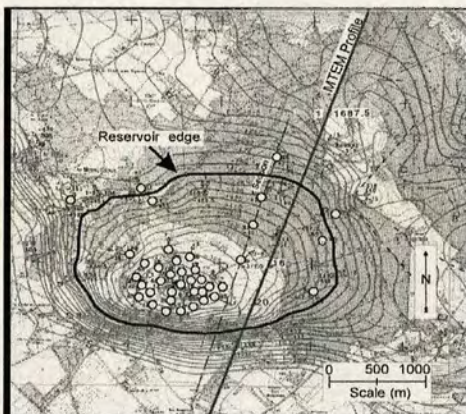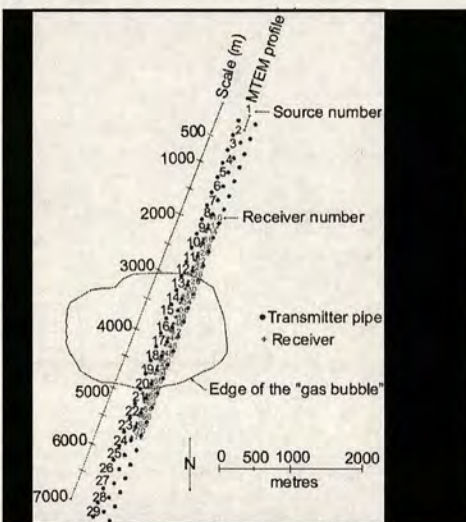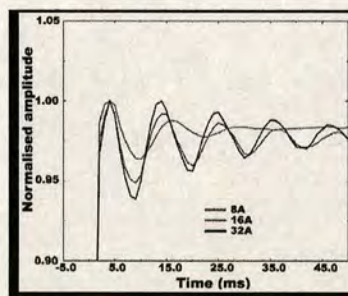

Figure 8. Layout of the entire survey, showing source and receiver locations in relation to the edge of the gas bubble.

Figure 9. Normalized system responses for 8, 16, and 32A source currents, showing nonlinearity of the response with current.
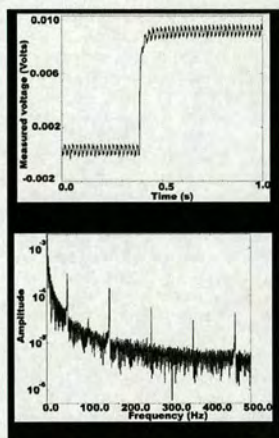
238

Figure 10. *Frequency spectrum of a single electric field transient. Upper diagram shows a time-domain transient response and lower diagram its amplitude spectrum.*
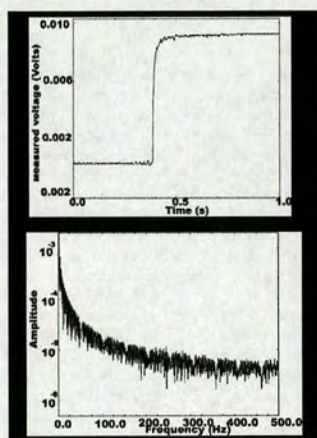

Figure 11. *The result of notch filtering. Upper diagram is transient of Figure 10 after notch filtering and lower diagram its amplitude spectrum after notch filtering.*
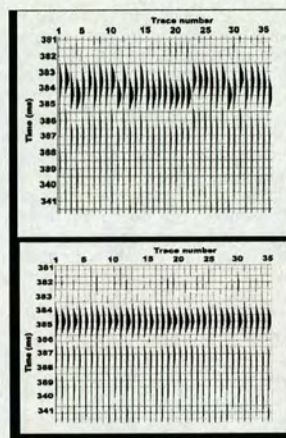

Figure 12. *Traces in the same source-receiver pair. Upper figure is before timing correction and lower figure after timing correction.*
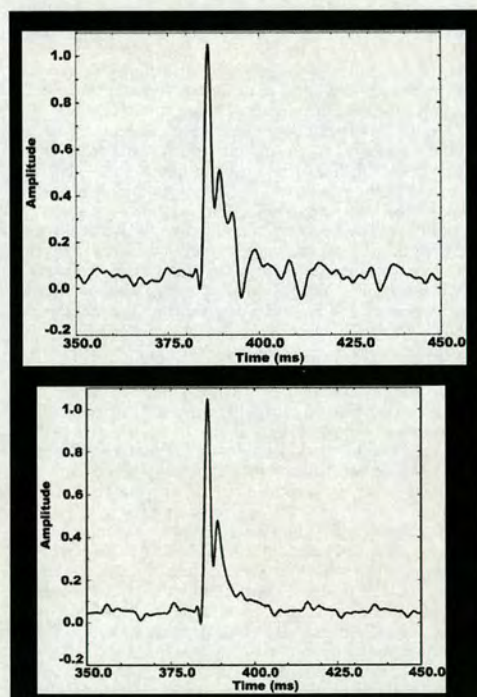

Figure 13. *Result of differentiation and stacking. Upper figure shows a single approximate earth impulse response and lower figure shows the result of stacking all approximate impulse responses within the same source-receiver pair. The periodic behavior of the noise is the result of notch filtering.*
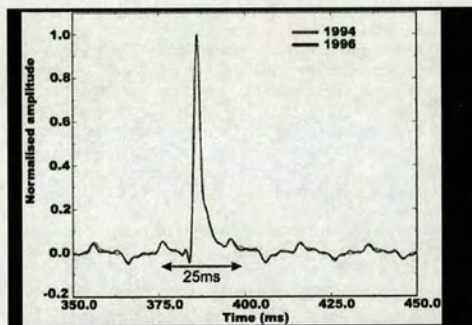

Figure 14. *Stacked approximate earth impulse responses for 1994 and 1996 from the same source-receiver pair, 1000-m offset; both source and receiver were north of the reservoir.*
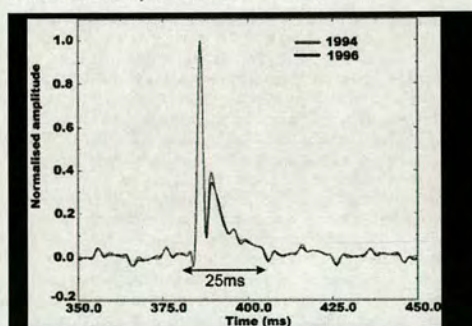

Figure 15. *Stacked approximate earth impulse responses for 1994 and 1996 from the same source-receiver pair, 1000-m offset; both source and receiver were over the reservoir. Notice that the second peak is slightly smaller in 1996 than in 1994 because there was less gas in 1996.*

239

lining our pragmatic approach, we briefly remark on the measurement of the system response, as this is the key to an ideal approach to the problem.

Measurement of the system response. The system response is the source time function convolved with the receiver recording system response. It is measured by placing receiver electrodes close to the source so that the effect of the earth is removed from the recorded signal. Measurements of the system response in May 1993 in Specking, Germany, had indicated that it was a perfect step function and did not need to be measured during the survey. It was not measured until after the second survey and then only for three different source currents at two different source locations. Figure 3 shows one measurement. Analysis of these system response measurements revealed two problems.

First, it was discovered that the system response was not a perfect step function. In fact, there was a ripple that varied nonlinearly with current (Figure 9). This meant that it was not possible to create a system response curve for known source currents using simple interpolation.

Second, system response data were aliased, which meant that the true impulse response function of the earth could not be recovered. The TEAMEX recording system had a low-pass filter that was sufficiently steep to prevent aliasing of the measured transient responses, such as in Figure 4, but it was insufficient to prevent aliasing of the system response measurement. Thus, even if the system response measurements had been made with TEAMEX, they would have been useless for deconvolution.

Pragmatic approach. Note from Figure 9 that the deviation from a perfect step function is a ripple of the order of a few percent. If we ignore this ripple, we may approximate the measured response $a_k(x_s, x_r, t)$ as the convolution of the impulse response of the earth with a step function, or Heaviside function:

$$a_k(x_s, x_r, t) = H(x_s, x_r, t) * g(x_s, x_r, t) + n_k(x_r, t). \quad (2)$$

It is now convenient to differentiate this expression. The differentiation of a convolution is the derivative of one term convolved with the remaining part. Because the derivative of a Heaviside function is a delta-function, and the convolution of a delta-function with any function is the function itself, we have

$$a'_k(x_s, x_r, t) = g(x_s, x_r, t) + n'_k(x_r, t), \quad (3)$$

where $a'_k(x_s, x_r, t)$ is the time derivative of the measured transient response and $n'_k(x_r, t)$ is the derivative of the noise—and is still noise. Thus, for these data, differentiation of the measured responses is an approximation to the impulse response of the earth $g(x_s, x_r, t)$ plus noise. The signal-to-noise ratio can be increased by stacking.

A problem that affects much EM data is electrical pickup from sources of mains electricity in and around the survey area. This appears at the mains frequency of 50 Hz and its odd harmonics, e.g., 150, 250, 350 Hz, etc. The first step of the processing flow was to notch filter the data at these frequencies. Figure 10 shows a typical transient response and its amplitude spectrum. Figure 11 shows the result of notch filtering on this transient. Note that the filters have not produced large holes in the frequency spectrum of Figure 11.

The next step was to differentiate the data; this removed the DC on the signal and reduced the response to about 20 ms in length. This means that after differentiation, of the 2048 samples recorded for each transient, only about 20 (approximately 1% of the data) contain any useful information.

Clearly, in any future survey, data should be recorded at a much finer sampling interval, for example 0.05 ms, and for a much shorter time. This would significantly improve resolution and reduce the time required to collect the data by about two orders of magnitude.

After we began to differentiate the data, we discovered a very important error in the timing. It had been known that there were timing errors of the order of a few milliseconds between traces in different source-receiver pairs and between the two surveys. However, it was assumed that the timing of the current switch for a given suite of traces for the same source in the same location was always the same. After differentiating all traces in the same source-receiver pair, we found that this was not the case (Figure 12, top) and that a timing correction was necessary to ensure a reasonable response after stack. Figure 12, bottom, shows the result of the timing correction.

Following the timing correction, traces within the same source-receiver pair were visually checked and any noisy traces killed. The remaining traces were then stacked to produce the stacked approximate earth impulse response for the source-receiver pair. Figure 13, which compares the result of stacking approximately 30 traces with a single trace, shows the clear increase in signal-to-noise ratio due to stacking.

Results. The result obtained after our pragmatic processing is a stacked approximate earth impulse for every E_{xx} source-receiver pair. The processed data cover areas north, south, and directly over the reservoir. Figure 14 shows a stacked approximate impulse response for the same source-receiver pair for the 1994 and 1996 data north of the reservoir. Figure 15 shows the result from directly over the reservoir.

Figure 15 shows a very distinct second peak associated with the reservoir that is not on Figure 14, recorded north of the reservoir. The arrival time of this event is also consistent with the results of 1D modeling which suggest the effect of the reservoir should begin to be present at around 3 ms. It is also interesting to note how repeatable the data are between the two surveys. In fact, it is almost impossible to separate the two responses in Figure 14, recorded north of the reservoir. This repeatability is much better than we had expected and is very encouraging. The greater the repeatability of the data in places where no changes in rock resistivities are taking place, the more likelihood there is of detecting changes where they are taking place, for instance in the reservoir. The two signals in Figure 15, recorded over the reservoir, differ significantly only in the height of the second peak, representing a change in the resistivity of the reservoir. The method clearly has potential for measuring the movement of fluids in the reservoir. (The periodic pattern on both the 1994 and 1996 data is an artifact of the notch filtering.)

After processing, data were sorted into common-offset gathers to allow sections of the subsurface to be produced. For display purposes the approximate impulse responses, which must be positive, were differentiated to make them oscillate about zero. Sections of a 1000-m common-offset gather for the differentiated 1994 data are shown in Figure 16 and for the differentiated 1996 data in Figure 17. Results for the two surveys are remarkably similar. What is particularly interesting is that the lateral extent of the green event at about 4 ms corresponds almost exactly to the known horizontal limit of the reservoir gas bubble. The only other possible explanation for such an arrival is the effect of pipes in the area. We believe the effect of the pipes is negligible for two reasons to do with the geometry.
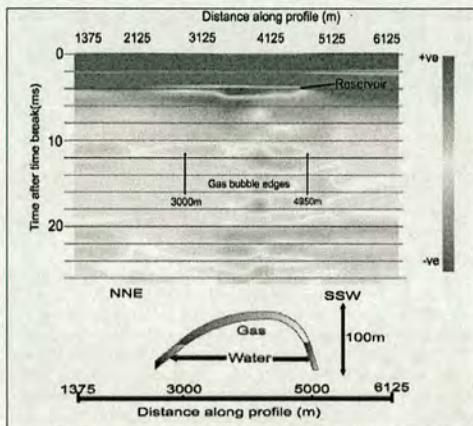
Figure 16. A 1000-m common-offset section of the derivative of the approximate earth impulse response for the 1994 data.
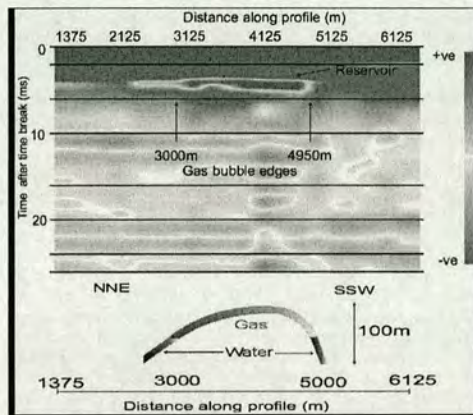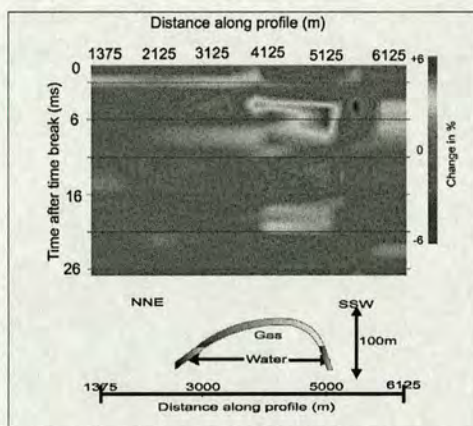

Figure 18. A 1000-m common-offset section of 1996 approximate impulse responses subtracted from 1994 approximate impulse responses.

First, it can be seen from Figure 7 that most pipes (wells) in the reservoir are very close together and to the west of the MTEM profile. Such a distribution of pipes could not produce the very abrupt change in signature at the gas bubble edges. If the pipes had any effect, it would be more concentrated in the south of the profile and its effect would fall off gradually with distance from the pipes. This is not what is seen, which suggests strongly that what we observe is the effect of the gas in the reservoir below. Second, processed data from shorter offsets (500 m, 625 m) do not show the second peak over the reservoir. This agrees with modeling results, which indicate that the reservoir is not detectable at such short offsets. If the effect seen over the reservoir was in fact due to near surface conductors, the short-offset data would be similarly affected. These two lines of reasoning suggest that what we are seeing is the effect of the reservoir.

These results thus show direct hydrocarbon detection using MTEM data.

Figure 17. A 1000-m common-offset section of the derivative of the approximate earth impulse response for the 1996 data.

The final step was to difference the sections in Figures 16 and 17 to see if any changes could be detected. The differencing (Figure 18) shows a distinct positive anomaly across the area where the response from the reservoir was seen in Figures 16 and 17. The positive nature of the anomaly is consistent with more gas and greater pressure existing in the reservoir in 1994 than in 1996. An anomaly is seen only where we expect to see it; there are no significant anomalies visible outside the region of the reservoir. This also indicates that the distinct second peak in Figure 15 is due directly to the presence of hydrocarbons in the reservoir.

Figures 16-18 show that the movement of hydrocarbons in a reservoir can be monitored with MTEM.

Conclusions and recommendations. We have demonstrated that MTEM can be used both for direct hydrocarbon detection and for monitoring fluid movement in a reservoir. The data used were far from ideal and any future survey should incorporate several changes during acquisition to improve data quality and quantity. First, the system response should be measured for each source current and each source position that is occupied, and also for every shot fired. Only when this is done can the correct system response be deconvolved from the recorded data. Second, the earth impulse response in this survey is only about 20 ms long. Any new data should be sampled at a much higher sampling rate, say 0.05 ms, and for a much shorter time, say 100 ms. This would greatly improve resolution and reduce considerably the time needed to acquire the data. Orders of magnitude increases in efficiency are clearly possible. The University of Edinburgh has applied for a patent that incorporates these new ideas.

The potential applications for this method are considerable. The U.S. Department of Energy states that there are 410 underground gas storage reservoirs in the United States. These reservoirs are mostly quite shallow and one would therefore expect the resolution of the MTEM method to be good. A major application would be in areas where potential hydrocarbon-bearing structures have been found using seismic methods and the drilling risk needs to be reduced. In these areas MTEM can discriminate between water and hydrocarbons. MTEM could find by-passed hydrocarbons in existing fields and monitor carbon dioxide sequestration. The method can readily be adapted for use offshore, for example in the North Sea and the Gulf of Mexico. With a

241

magnetic dipole source instead of the electric dipole source used in this experiment, it would be possible to search for conductors and could then be used to search for water.

Suggested reading. "Sea Bed Logging (SBL), a new method for remote and direct identification of hydrocarbon-filled layers in deepwater areas" by Eidismo et al. (*First Break*, 2002). "A first attempt at monitoring underground gas storage by means of time-lapse multichannel transient electromagnetics" by Hördt et al. (*Geophysical Prospecting*, 2000). "Electromagnetic imaging for indirect detection of hydrocarbons: a discovery" by Keller et al. (SEG *Expanded Abstracts*, 1996). "Interpretation of 3D effects in long offset transient electromagnetic (LOTEM) soundings in the Münsterland area, Germany" by Hordt et al. (GEOPHYSICS, 2000). *Exploration with Deep Transient Electromagnetics* by Strack (Elsevier, 1992). "Case histories of LOTEM surveys in hydrocarbon propective areas" by Strack et al. (*First Break*, 1989). "Integrating long-offset transient electromagnetics (LOTEM) with seismics in an exploration environment" by Strack and Vozoff (*Geophysical Prospecting*, 1996). "Electromagnetic imaging in exploration for stratigraphic traps: Anatomy of a discovery" by Tasci et al. (*TLE*, 1997). "A borehole to surface electromagnetic survey" by Tseng et al. (GEOPHYSICS, 1998). "Time-lapse EM" by Wilson et al. (International Symposium on Three-Dimensional Electromagnetics, Schlumberger-Doll Research, Ridgefield, Connecticut, U.S., 1995). "Electromagnetic methods for development and production: State of the art" by Wilt and Alumbaugh (*TLE*, 1998). "Crosshole electromagnetic tomography: A new technology for oil field characterization" by Wilt et al. (*TLE*, 1995). "Time-lapse multichannel transient electromagnetic experiment over an underground gas storage reservoir in France" by Ziolkowski et al. (Proceedings of the 5th E.C. Hydrocarbons Symposium, Edinburgh, 1995). Delineation and Monitoring of Oil Reservoirs using Seismic and Electromagnetic Methods by Ziolkowski et al. (Final technical report of EC THERMIE project OG/0305/92/NL-UK, 1998). TₗE

242

2

Neubauer, F.M., Raschke, E., and Speth, P., (Hrsg.), Mitteilungen aus dem Institut für Geophysik und Meteorologie der Universität zu Köln 42.

[7]   Cheesman, S.J., Edwards, R.N., and Law, L.K., 1990, A test of a short-base-line sea-floor transient electromagnetic system: Geophysical Journal International, 103, 2, 431-437.

[8]   Cairns,G.W., Evans,R.L. & Edwards,R.N., 1996. A time domain electromagnetic survey of the TAG hydrothermal mound, Geophys.Res.Lett.,23,3455-3458.

[9]   Cheesman, S. J., Edwards, R. N., and Chave, A. D., 1987, On the theory of sea-floor conductivity mapping using transient electromagnetic systems: Geophysics, 52, 204-217.

[10]   Yu, L., Evans, R.L., and Edwards, R.N., 1997, Transient electromagnetic responses in seafloor with triaxial anisotropy: Geophysical Journal International, 129, 300-306.

[11]   Eidesmo, T., Ellingsrud, S., MacGregor, L.M., and Constable, S., Sinha, M.C., Johansen, S., Kong, F.N., and Westerdahl, H., 2002, Sea Bed Logging (SBL), a new method for remote and direct identification of hydrocarbon filled layers in deepwater areas: First Break, 20, 144-152.

[12]   MacGregor, L.M., Constable, S., and Sinha, M.C., 1998, The RAMESSES experiment-III. Controlled-source electromagnetic sounding of the Reykjanes Ridge at 57 45N: Geophysical Journal International, 135, 773-789.

[13]   MacGregor, L.M., Sinha, M.C., and Constable, S., 2001, Electrical resistivity structure of the Valu Fa Ridge, Lau basin, from marine controlled source electromagnetic sounding Geophys. J. Int., 146, 217-236.

[14]   Ziolkowski, A., Hobbs, B.A., Andrieux, P., Rüter, H., Neubauer, F., and Hördt, A., 1998. Delineation and monitoring of reservoirs using seismic and electromagnetic methods: Project Number OG/0305/92/NL-UK, Final Technical Report to European Commission, May 1998.

[15]   Wright, D.A., Ziolkowski, A., and Hobbs, B.A., 2001, Hydrocarbon detection with a multi-channel transient electromagnetic survey: Expanded Abstracts 71st SEG Meeting, 9-14 September, San Antonio, p 1435-1438.

Conventionally time domain electromagnetic investigations use a transmitter and a receiver, or a transmitter and a number of receivers. The transmitter may be a grounded dipole (electric source) or a wire loop or multi-loop (magnetic source) and the receiver or receivers may be grounded dipoles (electric receivers - recording potential differences or electric fields) or wire loops or multi-loops or magnetometers (magnetic receivers - recording magnetic fields and/or time derivatives of magnetic fields). The transmitted signal is usually formed by a step change in current in either an electric source or in a magnetic source.

Known prior developments include (1) a methodology frequently termed TDEM and often taken to imply a magnetic source and a magnetic receiver, (2) the Long Offset Time-Domain

3

Electromagnetic   Method   (LOTEM) developed for land surveys, (3) time domain electromagnetics in the marine environment (University of Toronto/Scripps Institution of Oceanography), (4) Sea Bed Logging (SBL) using single frequency electromagnetic measurements in the marine environment (Scripps Institution/ Southampton Oceanography Centre/ Electromagnetic Geophysical Services Ltd.), and (5) our own previous work on multi-channel transient electromagnetic (MTEM) measurements made in collaboration with the University of Cologne, Deutsch Montan Technologie, and Compagnie Générale de Géophysique. These known developments are discussed more fully below.

(1)   The TDEM method is exemplified by commercial equipment such as PROTEM from Geonics Ltd., SMARTem from ElectroMagnetic Imaging Technology Pty Ltd (EMIT), UTEM from the University of Toronto and PATEM, a pulled-array from the University of Aarhus. These systems use magnetic sources and magnetic receivers in central loop, coincident loop, offset loop, or borehole configurations and as a consequence delineate conductive rather than resistive targets. They measure voltage induced in the receiver coil at a number of times (referred to as gates) after the transmitter current has been switched off [1]. A decay curve is then formed which is modelled either directly or through the use of various apparent resistivity measures such as early time and late time apparent resistivity [2], or imaged using a rapid inversion scheme [3]. The modelling approach uses a small number of parameters and makes assumptions about the turn-off characteristics of the source, for example that it is a perfect step function or a perfect ramp. TDEM methods all fail to recognise the importance of measuring the system response and instead put much effort into generating a transient signal with as small a turn-off time or ramp turn-off time as possible. The systems and associated software do not determine the earth's response function as defined in the present invention.

(2)   The LOTEM method (whose principal researchers are Vozoff, Strack and Hördt), and a similar system developed at the Colorado School of Mines, uses a large dimension electric source, typically 1-2 km long with electric and magnetic receivers placed several kilometres from the source. It is designed for land surveys. Decay curves measured by the receivers may be converted to various apparent resistivity curves. The decay or resistivity curves are modelled using a small number of parameters taken to represent sub-surface conditions beneath the receivers only. The collation of transformed curves from adjacent receivers forms an image representation.

The method includes consideration of a measurement of the system response. It is recommended ([4], p154) that this be performed either in the laboratory, or in the field at the beginning of the survey. LOTEM defines the system response as the response due to a delta-function input, which, it is admitted ([4], p49), cannot be achieved in practice. Instead, a square wave is input and the resulting output differentiated. In reality it is not possible to input an exact square wave either. Usually only one system response is obtained, determined as the average of a statistical representative number of transmitted pulses ([4], p68). An assumption is made that switching characteristics do not vary under load ([4], p155).

Most interpretation methods in the literature are based on a knowledge of the step response. This is impossible to obtain without a deconvolution of the measured data which is stated to be inherently unstable [5]. LOTEM recommends that either

4

apparent resistivity curves are obtained after time-domain deconvolution using an iterative scheme [6] or that synthetic data from modelling is convolved with the system response before comparison with the measured data.   A rule of thumb is that this should be done when the length of the system response is more than one third of the length of the transient ([4], p52).

The LOTEM method fails to recognise the importance of measuring the system response for each source transient in the field, and fails to recognise that the decay curves are a function of all the intervening material between the source and corresponding receiver where the induced currents flow.

(3)   The University of Toronto sea-floor EM mapping systems (principal researchers: Edwards, Yu, Cox, Chave and Cheesman), consist of a number of configurations including a stationary electric receiver on the sea floor and a towed electric transmitter, and a magnetic source and several collinear magnetic receivers forming an array which is towed along the sea-floor.   In early experiments, the system response was measured in free space and was convolved with the theoretical impulse response of a simple model of the sea-water and underlying earth in order to model the measured data [7].   In later experiments, for the case of an electric source, the measured current input to the transmitter is convolved with the impulse response of the receiver, again measured in free space, and then with the impulse response of a model to give a synthetic signal for comparison to that measured [8]. No receivers are placed near the transmitter to determine the system response under load.

The group have developed an extensive library of analytic solutions and recursive numerical schemes for the response of simple geological models to a step change source. The models invariably have a small number of parameters and interpretations of measured decay curves are based on this modelling approach [9], [10].

Their technique fails to recognise the importance of measuring the system response for each source transient and using this to deconvolve the measured transients to obtain the estimated earth impulse response functions.

(4)   Sea Bed Logging (SBL) is a realisation of the CSEM (controlled source electromagnetic) method and has been developed by Electromagnetic Geoservices Ltd (EMGS), a subsidiary of Statoil, in conjunction with the University of Cambridge, University of Southampton, and Scripps Institution of Oceanography [11].   It comprises a number of autonomous two-component electric receivers in static positions on the sea floor and an electric source towed approximately 50m above the sea floor.   The receivers remain in their positions on the sea floor recording continuously until instructed to pop up for recovery at the sea surface at the end of the survey. The source (DASI - deep-towed active source instrument) is a 100m long horizontal electric dipole [12]. Electrodes spaced along the source dipole are used to monitor the transmitted fields. These enable the receiver data to be normalised by the source dipole moment for comparison with modelling results [13]. Unlike the above transient systems, in the SBL technique the source transmits at only one frequency which the operators optimise to the target under investigation [11]. The method relies on the towed movable source creating data for several source-receiver separations and

249

5

these data are interpreted by modelling . The method does not involve a transient source and takes no account of the system response.

(5) The University of Edinburgh, the University of Cologne, Deutsch Montan Technologie, and Compagnie Générale de Géophysique collaborated within the European Commission THERMIE Project OG/0305/92/NL-UK (which ran from 1992 to 1998) to obtain multi-channel transient electromagnetic (MTEM) data in 1994 and 1996 over a gas storage reservoir at St. Illiers la Ville in France. The experiment is described in detail in the Final Technical Report to the European Commission, entitled "Delineation and Monitoring of Oil Reservoirs using Seismic and Electromagnetic Methods" [14]. The project had two objectives: first, to develop a method to detect hydrocarbons directly; and second, to monitor the movement of hydrocarbons in a known reservoir. Neither of these objectives was achieved.

Ziolkowski et al. [14] and even Wright et al. [15] failed to recognise the importance of measuring the system response for each source transient.

Disclosure of the Invention

The present invention seeks to provide a routine procedure for acquiring and processing electromagnetic data to enable the mapping of subsurface resistivity contrasts.

According to the present invention there is provided a method of mapping subsurface resistivity contrasts comprising making multichannel transient electromagnetic (MTEM) measurements using at least one source, receiving means for measuring system response and at least one receiver for measuring the resultant earth response, processing all signals from the or each source-receiver pair to recover the corresponding electromagnetic impulse response of the earth, and displaying such impulse responses, or any transformation of such impulse responses, to create a subsurface representation of resistivity contrasts. The locations of the resistivity contrasts can be determined from the source-receiver configuration, and electromagnetic propagation both above and below the receivers.

The method enables the detection and location of subsurface resistivity contrasts. For example, the method enables discrimination between water (brine or fresh water) which is conductive and hydrocarbons (gas or oil) which are resistive. The method also enables the movement of such fluids to be monitored. The method may also be used to find underground aquifers.

Brief Description of Drawings

Embodiments of the invention will now be described, by way of example only, with particular reference to the accompanying drawings, in which:

Figure 1 is a typical layout showing locations of an electromagnetic source and electromagnetic receivers for performing a method according to the invention of mapping resistivity contrasts;

6

Figures 2a-c are schematic diagrams showing a source current waveform and resulting transient responses;

Figure 3 is a schematic cross-section of the earth beneath St Illiers la Ville, France, and illustrating gas trapped above water in a porous sandstone anticline;

Figure 4 is a schematic plan of a typical arrangement of sources and receivers of a multichannel transient electromagnetic measurement system over a subsurface volume of gas used for performing a method according to the present invention;

Figure 5 shows the electric potential difference between two electrodes a few cm apart and a few cm from a 250 m long current dipole source;

Figure 6 shows normalised system responses for 8 A, 16 A and 32 A source currents showing the non-linearity of the system response with current;

Figure 7 is a typical in-line gradient of the electric potential response to a step in current at the source;

Figure 8 shows a single approximate earth impulse response for a source-receiver separation of 1 km;

Figure 9 shows a 1 km common-offset section of the derivative of the approximate earth response for data relating to measurements at the site shown in Figure 3 taken in 1994;

Figure 10 shows a 1 km common-offset section of the derivative of the approximate earth response for data relating to measurements at the site shown in Figure 3 taken in 1996; and

Figure 11 shows a common-offset section of the 1996 earth impulse responses subtracted from the 1994 earth impulse responses, with 1 km offset.

Modes for Carrying Out the Invention

Multichannel Transient ElectroMagnetic (MTEM) data can be acquired in a number of different ways. By way of example only, there is described below elements of the data acquisition system, as used in the THERMIE project OG/0305/92/NL-UK, and as described in [14] above. Figure 1 shows a typical configuration of a source and a line of receivers. The source is a current in a wire grounded at each end; in this case the two ends are 250 m apart. The receivers are represented as boxes in Figure 1, each with two channels, and are spread out over a line 2 km long, which, in this case, is in line with the source. The receivers measure two kinds of electromagnetic response: potential differences, and the rate of change of the magnetic field. Potential differences are measured between two grounded electrodes, typically 125 m apart, while the rate of change of the magnetic field is measured with loops of wire, typically 50 m by 50 m square loops with many turns. Figure 1 shows thirty-two receivers: sixteen in-line potential difference receivers, eight cross-line potential difference receivers, and eight loops measuring the rate of change of the magnetic field. The loops

7

alternate down the line with the cross-line receivers. (This configuration was the result of constraints imposed by the limited number of two-channel recording boxes and the distance over which signals could be transmitted from these units to the data storage disk on the computer.) The source can be positioned outside or within the receiver spread and, in practice, the source or the receiver spread, or both, can be moved, depending on the application. The recorded transient responses from the receivers are suitably downloaded to the hard disk, or other storage medium, of a computer.

Choosing x as the in-line coordinate, y as the cross-line coordinate, and z as the vertical coordinate a notation for the measurements is developed. A receiver position can be denoted $\mathbf{x}_r = (x_r, y_r, z_r)$, and a source position can be denoted $\mathbf{x}_s = (x_s, y_s, z_s)$.

Figure 2 shows schematically the relationship between the current input (shown here as an instantaneous change in polarity) and the expected response. E_x is the potential difference in the in-line or x-direction, and $\dfrac{\partial H_z}{\partial t}$ is the rate of change of the vertical component of the magnetic field, measured with a horizontal loop. From Figure 2 it can be seen that these responses vary with time after the current polarity is reversed at the source. In practice each of these quantities varies with the source position and the receiver position.

The key to the solution of the problem is the recovery of the impulse response of the earth. The configuration consists of an electromagnetic source, for instance a current dipole or a magnetic dipole at a location $\mathbf{x}_s$, and a receiver, for instance two potential electrodes or a magnetic loop at a location $\mathbf{x}_r$. The measurement of the response can be described as

$$a_k(\mathbf{x}_s, \mathbf{x}_r, t) = s_k(\mathbf{x}_s, \mathbf{x}_r, t) * g(\mathbf{x}_s, \mathbf{x}_r, t) + n_k(\mathbf{x}_r, t) \tag{1}$$

and it may be repeated many times. In this equation the asterisk * denotes convolution, and the subscript k indicates that this is the kth measurement in a suite of measurements for a given source-receiver pair; $s_k(\mathbf{x}_s, \mathbf{x}_r, t)$ is known as the system response and may in principle be different for each measurement; $g(\mathbf{x}_s, \mathbf{x}_r, t)$ is the impulse response of the earth and is fixed for any source-receiver pair, and $n_k(\mathbf{x}_r, t)$ is uncorrelated electromagnetic noise at the receiver and varies from measurement to measurement. This equation must be solved for the impulse response of the earth $g(\mathbf{x}_s, \mathbf{x}_r, t)$. To do this, the system response $s_k(\mathbf{x}_s, \mathbf{x}_r, t)$ must be known.

In the acquisition and processing of the data to recover the impulse response of the earth, there are three critical steps which are formulated here for the first time. These are:
1. measurement of the system response for each source-receiver pair and in principle for each transient;
2. deconvolution of the measured signal for the measured system response to recover an estimated impulse response of the earth for each source-receiver pair and in principle for each transient; and
3. stacking of these estimated impulse responses to improve the signal-to-noise ratio and obtain an improved estimate of the earth impulse response for each source-receiver pair.

These steps are now described.

8

1. Measurement of the System Response

The system response $s_k(\mathbf{x}_s, \mathbf{x}_r, t)$ should be determined by measurement in the field. This depends on the source position $\mathbf{x}_s$ and the position $\mathbf{x}_r$ of the receiver and may also depend on the number k of the transient in the sequence, particularly if there are synchronisation problems. There are several ways in which the system response can be measured. In the case of the current dipole source shown in Figure 1, the measurement of the system response for the electric field could be made with two electrodes placed very close (of the order of a few cm) to the source, with the known distance between them very small (of the order of a few cm), to avoid generating voltages that are too large. For the magnetic field system response, a small horizontal loop could be placed close (of the order of a few cm) to the source. Another possibility is to measure the input current directly. The recording system used to measure the system response should, preferably, have the same characteristics as the system used to record the measurement $a_k(\mathbf{x}_s, \mathbf{x}_r, t)$ described by equation (1) and, if the recording is digital, it should be unaliased. If the recording systems are not identical, the transfer function between the two must be known, so that differences can be eliminated. This is seen as follows.

The recording instrument used to measure the system response at the source has an impulse response $r(\mathbf{x}_s, t)$, which must be known, while the recording instrument used to make the measurement $a_k(\mathbf{x}_s, \mathbf{x}_r, t)$ at the receiver has a response $r(\mathbf{x}_r, t)$, which must also be known. Then the response $r(\mathbf{x}_r, t)$ can be related to the response $r(\mathbf{x}_s, t)$ by the equation,

$$r(\mathbf{x}_r, t) = r(\mathbf{x}_s, t) * f(\mathbf{x}_s, \mathbf{x}_r, t), \tag{2}$$

in which the asterisk * represents convolution, and $f(\mathbf{x}_s, \mathbf{x}_r, t)$ is the Fourier transform of the transfer function relating the two responses. If the time function of the input signal at the source is $h_k(\mathbf{x}_s, t)$, then the system response required to solve equation (1) is

$$s_k(\mathbf{x}_s, \mathbf{x}_r, t) = h_k(\mathbf{x}_s, t) * r(\mathbf{x}_r, t). \tag{3}$$

The system response measured with the receiving means and recording system at the source will be
$$s_k(\mathbf{x}_s, \mathbf{x}_s, t) = h_k(\mathbf{x}_s, t) * r(\mathbf{x}_s, t). \tag{4}$$

The system response required to solve equation (1) is obtained from equations (2), (3) and (4) as

$$s_k(\mathbf{x}_s, \mathbf{x}_r, t) = s_k(\mathbf{x}_s, \mathbf{x}_s, t) * f(\mathbf{x}_s, \mathbf{x}_r, t). \tag{5}$$

2. Deconvolution

The earth impulse response $g(\mathbf{x}_s, \mathbf{x}_r, t)$ can be estimated, with noise, from equation (1) by deconvolution, given the known impulse response $s_k(\mathbf{x}_s, \mathbf{x}_r, t)$. That is, an estimate

9

$\hat{g}_k(\mathbf{x}_s, \mathbf{x}_r, t)$ of the earth impulse response is obtained by deconvolution of equation (1). For example, $\hat{g}_k(\mathbf{x}_s, \mathbf{x}_r, t)$ may be obtained as the least-squares Wiener filter that, when convolved with the known function $s_k(\mathbf{x}_s, \mathbf{x}_r, t)$, gives the known function $a_k(\mathbf{x}_s, \mathbf{x}_r, t)$. Any uncertainties in the time origin of the response are resolved automatically by this deconvolution step, provided the system response $s_k(\mathbf{x}_s, \mathbf{x}_r, t)$ and the measurement $a_k(\mathbf{x}_s, \mathbf{x}_r, t)$ are properly synchronised. Synchronisation is important because the time parameter t has the same origin in all the four functions ($a_k(\mathbf{x}_s, \mathbf{x}_r, t)$, $s_k(\mathbf{x}_s, \mathbf{x}_r, t)$, $g(\mathbf{x}_s, \mathbf{x}_r, t)$, and $n_k(\mathbf{x}_r, t)$) of equation (1).

3. Stacking

To improve the signal-to-noise ratio, using a suite of measurements in which k varies from 1 to n, say, a better estimate of $g(\mathbf{x}_s, \mathbf{x}_r, t)$ may be made by stacking. That is, the improved estimate is

$$\overline{g}(\mathbf{x}_s, \mathbf{x}_r, t) = \frac{1}{n} \sum_{k=1}^{n} \hat{g}_k(\mathbf{x}_s, \mathbf{x}_r, t). \tag{6}$$

Subsequent processing of the estimated impulse responses $\overline{g}(\mathbf{x}_s, \mathbf{x}_r, t)$ and display of the results for different source-receiver pairs can use many of the methods commonly used for seismic exploration data.

If the system response $s_k(\mathbf{x}_s, \mathbf{x}_r, t)$ is identical for all n measurements made for the given source-receiver pair, the stacking can be done first and the deconvolution afterwards.

The impulse response of the earth $g(\mathbf{x}_s, \mathbf{x}_r, t)$ is typically only a few milliseconds, or tens of milliseconds, in duration. Therefore, in principle, thousands of repeat measurements of the response may be made in a few minutes.

The invention is illustrated in the following non-limitative example.

Within the European Commission THERMIE Project OG/0305/92/NL-UK [14], MTEM data sets were obtained in 1994 and 1996 over a gas storage reservoir at St. Illiers la Ville in France. Figure 3 shows a schematic section through the underground gas storage reservoir and shows the reservoir and monitoring wells. Figure 4 shows a plan of the MTEM profile in relation to the edge of the underground "gas bubble". The equipment that was used to record the responses $a_k(\mathbf{x}_s, \mathbf{x}_r, t)$ consisted of sixteen two-channel TEAMEX boxes manufactured by Deutsch Montan Technologie. At the time the data were acquired it was not recognised that it was necessary to record the system response for each source-receiver pair. In fact, with this equipment, it would have been impossible to measure the system response properly, because the low-pass filters were insufficient to prevent aliasing of the data at the 1 ms sample interval used in recording.

10

The source input to the ground was essentially a change in polarity of a current of approximately 30 amperes, produced by a generator and Zonge transmitter in a wire 250 m long, grounded at each end. In fact, the source time function was not a perfect step, and there were small oscillations that could be seen on the few aliased measurements of the system response that were made in 1996. One of these can be seen in Figure 5. It was noticed that the system oscillations varied with the current level, which varied with the source position. Figure 6 shows a magnification of the measured system response for three different current levels, normalised to the maximum value. It can be seen that the oscillations differ with current level. In other words, with hindsight, we see that the system response was, in principle, different for every source-receiver pair, and ought to have been measured. In fact, we could not have made this measurement with the available equipment.

A typical measurement $a_k(\mathbf{x}_s,\mathbf{x}_r,t)$ is shown in Figure 7.

The deconvolution step 2 is impossible to apply to these data because the system response for each source-receiver pair was not measured (step 1). To create an *approximate* estimate of the impulse response function we argue that the response $a_k(\mathbf{x}_s,\mathbf{x}_r,t)$ is *approximately* the response to a step:

$$a_k(\mathbf{x}_s,\mathbf{x}_r,t) \approx H(t) * g(\mathbf{x}_s,\mathbf{x}_r,t),\qquad(7)$$

in which $H(t)$ is the Heaviside, or step function. This approximation ignores the oscillations observed in the system responses shown in Figure 6. Differentiating both sides of equation (7) yields

$$\frac{\partial a_k(\mathbf{x}_s,\mathbf{x}_r,t)}{\partial t} \approx \frac{\partial H(t)}{\partial t} * g(\mathbf{x}_s,\mathbf{x}_r,t)$$

$$\approx \delta(t) * g(\mathbf{x}_s,\mathbf{x}_r,t)$$

$$\approx g(\mathbf{x}_s,\mathbf{x}_r,t).\qquad(8)$$

That is, the derivative of the measured response is approximately equal to the impulse response of the earth. These estimated impulse responses had synchronisation errors of the order of ± 3 ms. These errors were a fault of the data acquisition system, but would have been eliminated if we had been able to measure the system response, as noted above. In fact, the timing errors can be estimated because the estimated impulse response has a very sharp peak at the beginning, which should arrive at the same time for all responses for the same source-receiver pair. Figure 8 shows an estimate of the earth impulse response $\bar{g}(\mathbf{x}_s,\mathbf{x}_r,t)$, after stacking the time-corrected earth impulse responses for one source-receiver pair.

Figure 9 shows a common-offset section of the time derivative of estimated earth impulse responses for the 1994 data, in which the source-receiver distance is fixed, the horizontal scale is the position of the mid-point between source and receiver, and the vertical scale is time. The effect of the increased resistivity over the gas-filled reservoir can clearly be seen. Figure 10 shows the corresponding section for the 1996 data. Again, the effect of the resistive gas-filled reservoir can clearly be seen. There was a slight movement of the gas-water content between October 1994, when the reservoir was full, and August 1996, when it

255

11

was less full. Subtracting the 1996 earth impulse responses from the 1994 earth impulse responses yields the difference in response, and shows how the rock resistivity is changed by the change in fluid content. Figure 11 shows a common-offset section of these differences, and clearly shows that there was more gas in the steeply-dipping southern part of the reservoir in 1994.

With this approximate analysis we have shown that it is possible (1) to detect and locate the presence of hydrocarbons with the MTEM method, and (2) to monitor the movement of the fluids in the reservoir. Given all the approximations that were made to obtain this result, it is clear that much better results would be obtained using the method of data acquisition and processing of the present invention.

The data should preferably be digitally recorded and processed in a computer either in real time or subsequently to create a subsurface representation of resistivity contrasts.

The MTEM measurements are made on or near the earth's surface which includes the sea floor. In the case of measurements at or near the sea floor, measurements may be made in the sea close to the actual seabed in view of the conductive nature of the seawater.

It will be appreciated from the above description that a key to the invention is the measurement and deconvolution of the system response $s_k(\mathbf{x}_s, \mathbf{x}_r, t)$, including source-receiver synchronisation, for every measured transient response $a_k(\mathbf{x}_s, \mathbf{x}_r, t)$, as defined in equation (1). This includes any approximation to this, such as is described above with reference to previously obtained data, in which there was an approximation of the deconvolution by differentiation of $a_k(\mathbf{x}_s, \mathbf{x}_r, t)$, the synchronisation errors found being subsequently corrected.

The invention also relates to apparatus for mapping subsurface resistivity contrasts and to a system for mapping subsurface resistivity contrasts.

Industrial Applicability

The invention finds application in locating and identifying underground deposits of fluids, such as hydrocarbons and water.

256

12

CLAIMS

1.   A method of mapping subsurface resistivity contrasts comprising making multichannel transient electromagnetic (MTEM) measurements using at least one source, receiving means for measuring system response and at least one receiver for measuring the resultant earth response, processing all signals from the or each source-receiver pair to recover the corresponding electromagnetic impulse response of the earth, and displaying such impulse responses, or any transformation of such impulse responses, to create a subsurface representation of resistivity contrasts.

2.   A method according to claim 1, wherein the impulse response of the earth is obtained from the equation

$$a_k(\mathbf{x}_s,\mathbf{x}_r,t) = s_k(\mathbf{x}_s,\mathbf{x}_r,t) * g(\mathbf{x}_s,\mathbf{x}_r,t) + n_k(\mathbf{x}_r,t)$$

where k indicates the kth measurement in a suite of measurements for a given source-receiver pair, $a_k(\mathbf{x}_s,\mathbf{x}_r,t)$ is the measured transient response for a given source-receiver pair of said MTEM measurements, * denotes convolution, $s_k(\mathbf{x}_s,\mathbf{x}_r,t)$ is the system response, $g(\mathbf{x}_s,\mathbf{x}_r,t)$ is the impulse response of the earth for a given source-receiver pair, and $n_k(\mathbf{x}_r,t)$ is uncorrelated electromagnetic noise at the receiver.

3.   A method according to claim 2, wherein said source comprises a current dipole and said receiving means measures the system response for the electric field and comprises two closely spaced apart, for example of the order of centimetres, electrodes positioned close to, for example of the order of centimetres from, the source.

4.   A method according to claim 2, wherein said source comprises a current dipole and said receiving means measures the system response for the magnetic field and comprises a horizontal loop positioned close to, for example of the order of a few centimetres from, the source.

5.   A method according to claim 2, wherein said source comprises at least one current loop and said receiving means comprises measuring means, for example a current meter, for measuring the current in the at least one current loop.

6.   A method according to any one of claims 2 to 4, wherein the recording system used to measure the system response has the same characteristics as the system used to record the measurement $a_k(\mathbf{x}_s,\mathbf{x}_r,t)$.

7.   A method according to any one of claims 2 to 5, wherein the recording system used to measure the system response has different characteristics from the recording system used to record the measurement $a_k(\mathbf{x}_s,\mathbf{x}_r,t)$ and wherein these differences are eliminated using the transfer function between the two recording systems.

13

8.   A method according to any one of claims 2 to 7, wherein an estimate of the earth impulse response with noise is obtained by deconvolution of the said equation.

9.   A method according to claim 8, wherein said estimate of the earth impulse response is improved by stacking the estimated impulse responses.

10.   A method according to any one of claims 2 to 9, wherein the measured system response and corresponding measured transient are synchronised.

11.   A method according to any one of claims 2 to 9, wherein any different time origin between the measured system response and corresponding measured transient is measured and compensated for.

12.   A method according to any one of the preceding claims, wherein the MTEM measurements are made on the earth's surface.

13.   A method according to any one of claims 1 to 11, wherein the MTEM measurements are made at or near a sea floor of the earth's surface.

14.   Apparatus for mapping subsurface resistivity contrasts comprising means for making multichannel transient electromagnetic (MTEM) measurements comprising at least one source, receiving means for measuring system response and at least one receiver for measuring the resultant earth response, processing means for processing all signals from the or each source-receiver pair to recover the corresponding electromagnetic impulse response of the earth, and display means for displaying such impulse responses, or any transformation of such impulse responses, to create a subsurface representation of resistivity contrasts.
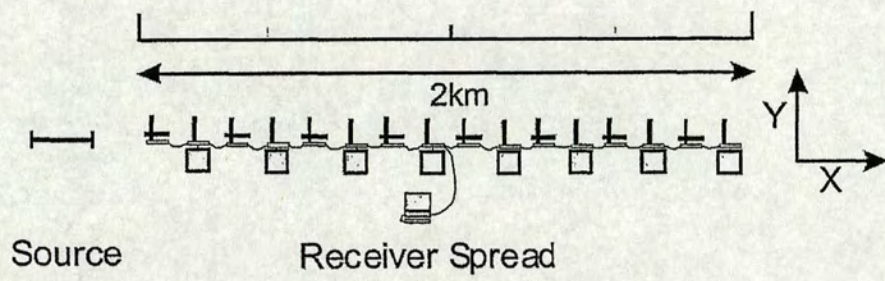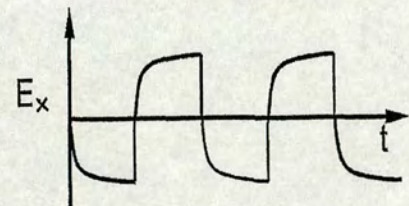
1/10

FIG. 1

2km

Y

X

Source   Receiver Spread

FIG. 2b

E_x

t

FIG. 2a

$I(t)$

t

Input: Bipolar current waveform
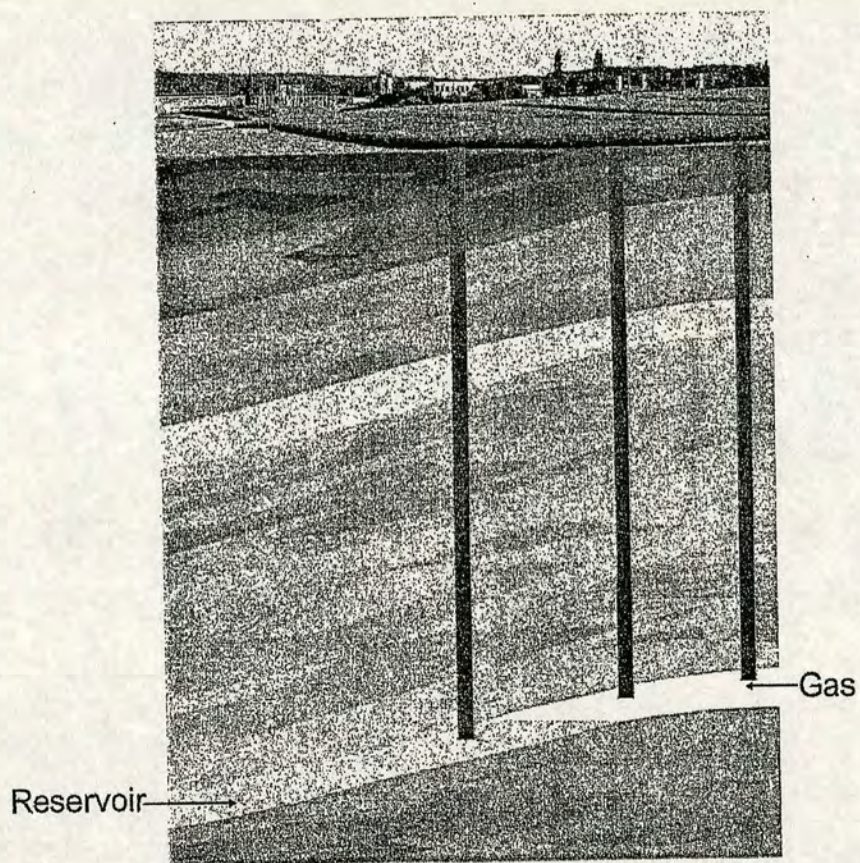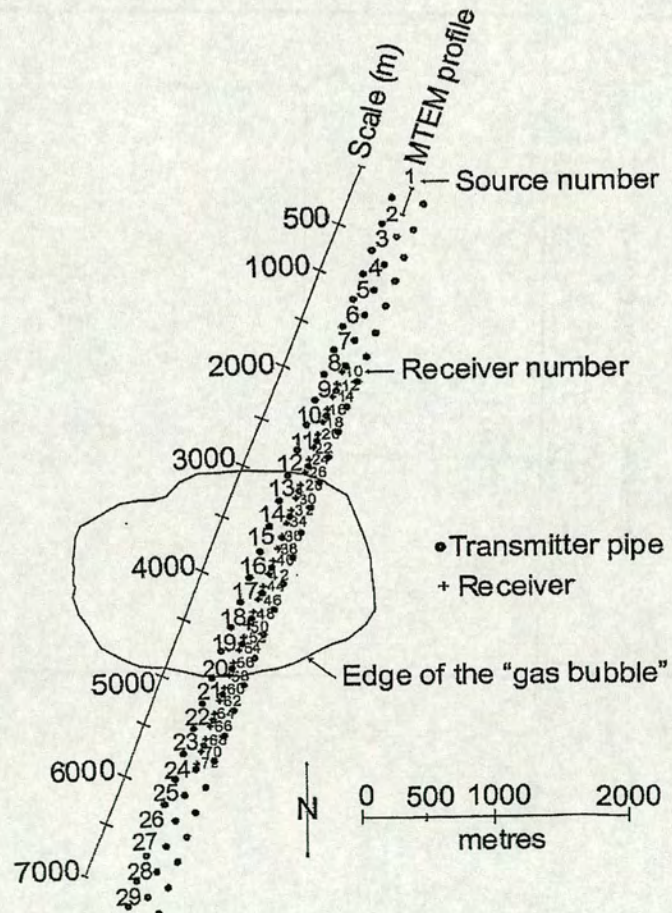
Output: Recorded transient response

$\dfrac{dH_z}{dt}$

t

FIG. 2c

2/10

FIG. 3

260

FIG. 4

4/10

FIG. 5

FIG. 6

6/10

FIG. 7

FIG. 8

8/10

FIG. 9

266
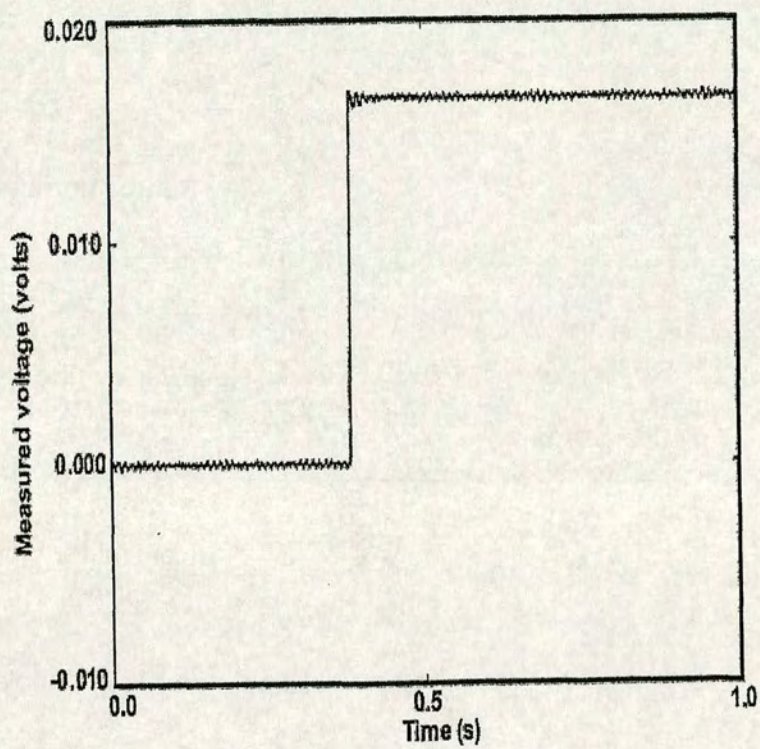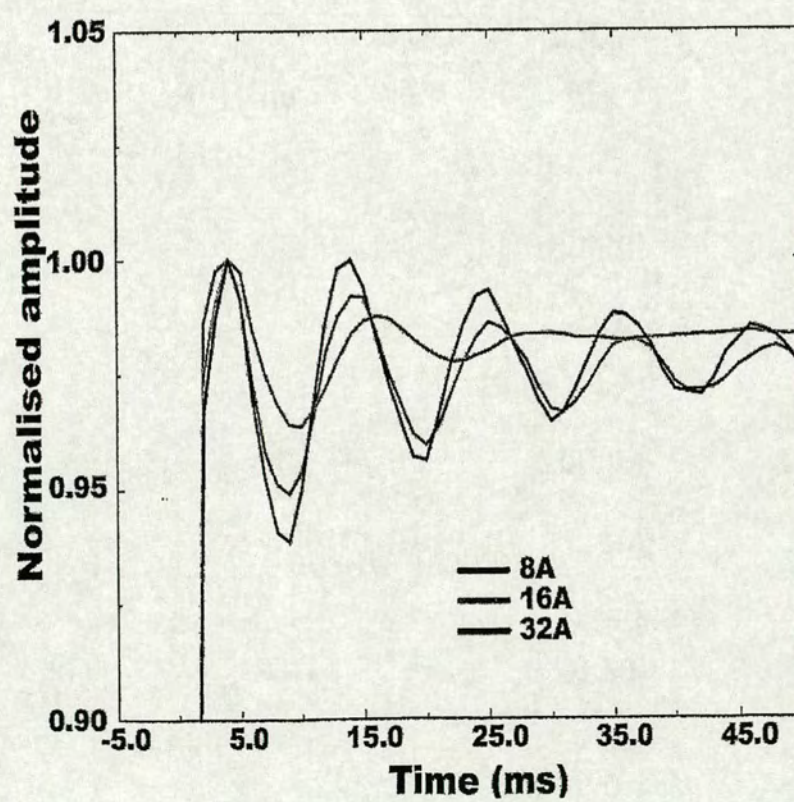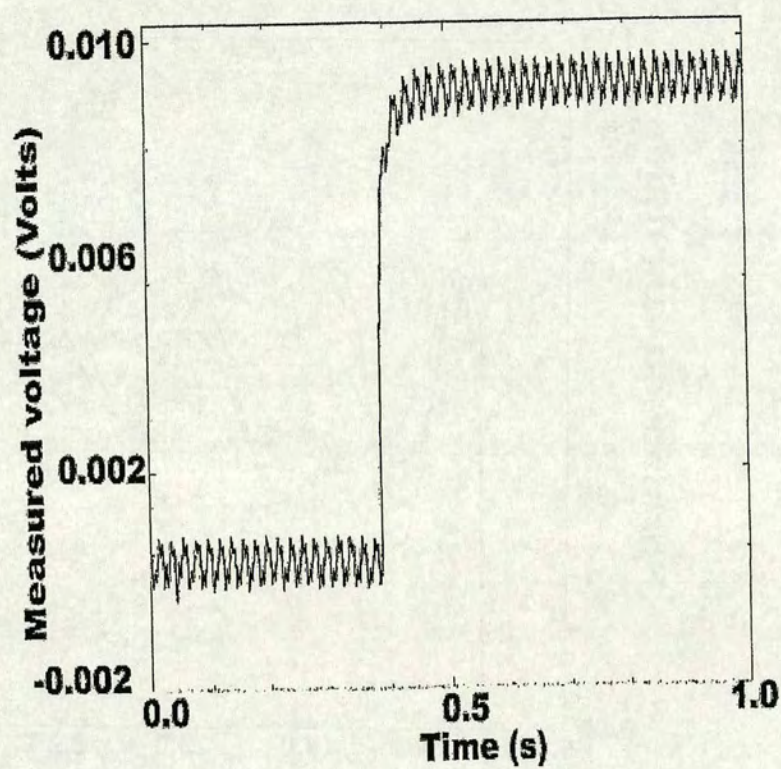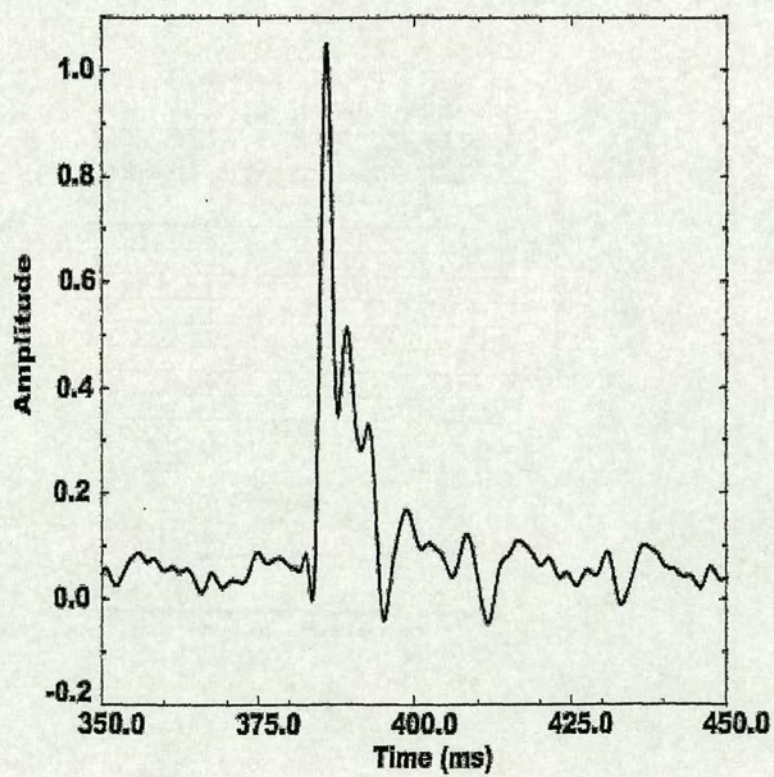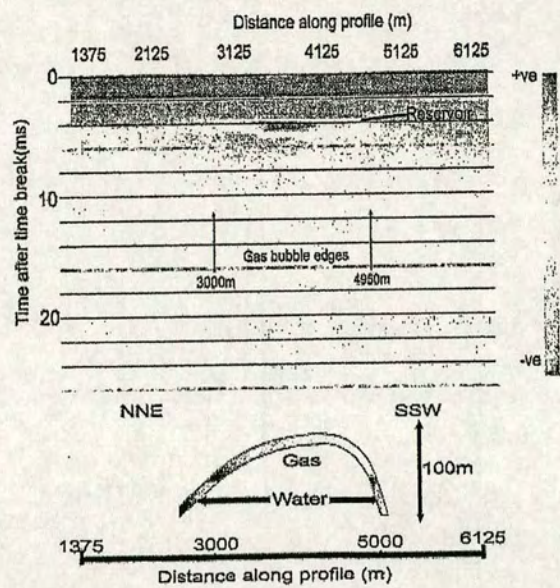
FIG. 10
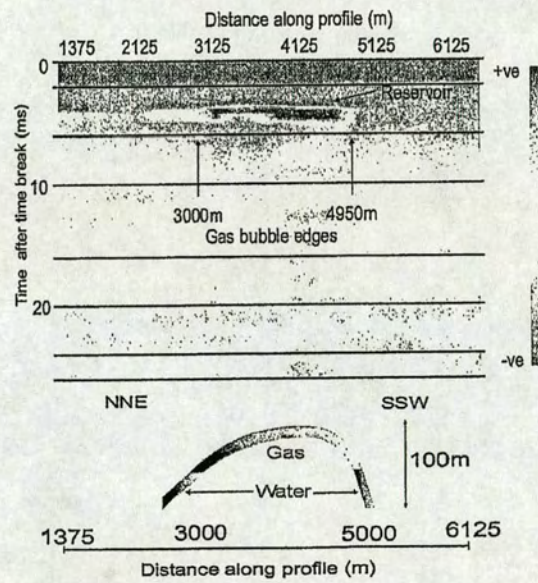
10/10

FIG. 11
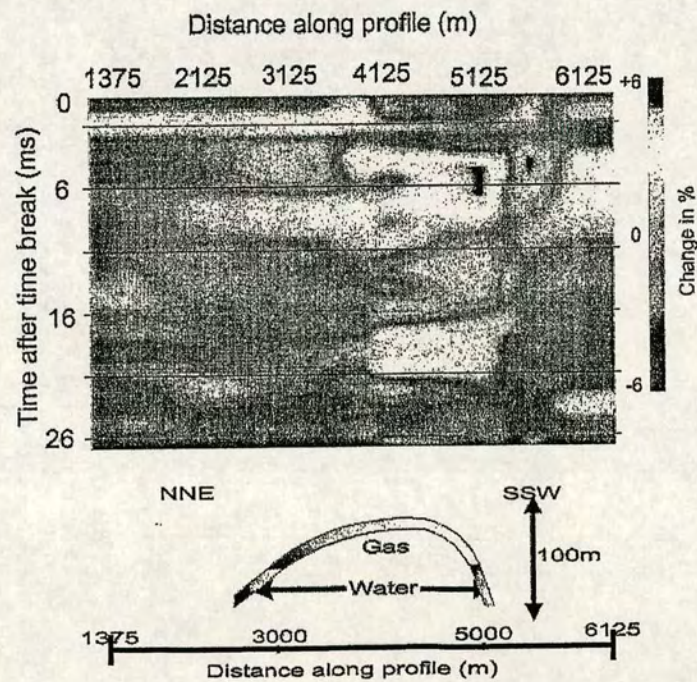
INTERNATIONAL SEARCH REPORT

A. CLASSIFICATION OF SUBJECT MATTER
IPC 7   G01V3/02

According to International Patent Classification (IPC) or to both national classification and IPC

B. FIELDS SEARCHED

Minimum documentation searched (classification system followed by classification symbols)

IPC 7   G01V

Documentation searched other than minimum documentation to the extent that such documents are included in the fields searched

Electronic data base consulted during the international search (name of data base and, where practical, search terms used)

EPO-Internal, INSPEC

C. DOCUMENTS CONSIDERED TO BE RELEVANT

Category°	Citation of document, with indication, where appropriate, of the relevant passages	Relevant to claim No.
X	US 4 417 210 A (ROCROI JEAN-PIERRE ET AL) 22 November 1983 (1983-11-22) column 7, line 58 –column 8, line 64 column 11, line 51 –column 12, line 52	1,9,12, 14
A		2-4,7,8

A	US 5 467 018 A (RUTER HORST ET AL) 14 November 1995 (1995-11-14) column 2, line 60 –column 3, line 42	1,3-6, 10-12,14

	-/--	

[X] Further documents are listed in the continuation of box C.　　[X] Patent family members are listed in annex.

° Special categories of cited documents :

"A" document defining the general state of the art which is not considered to be of particular relevance

"E" earlier document but published on or after the international filing date

"L" document which may throw doubts on priority claim(s) or which is cited to establish the publication date of another citation or other special reason (as specified)

"O" document referring to an oral disclosure, use, exhibition or other means

"P" document published prior to the international filing date but later than the priority date claimed

"T" later document published after the international filing date or priority date and not in conflict with the application but cited to understand the principle or theory underlying the invention

"X" document of particular relevance; the claimed invention cannot be considered novel or cannot be considered to involve an inventive step when the document is taken alone

"Y" document of particular relevance; the claimed invention cannot be considered to involve an inventive step when the document is combined with one or more other such documents, such combination being obvious to a person skilled in the art.

"&" document member of the same patent family

Date of the actual completion of the international search	Date of mailing of the international search report
9 January 2003	20/01/2003

Name and mailing address of the ISA	Authorized officer
European Patent Office, P.B. 5818 Patentlaan 2 NL – 2280 HV Rijswijk Tel. (+31–70) 340–2040, Tx. 31 651 epo nl, Fax: (+31–70) 340–3016	Swartjes, H

Form PCT/ISA/210 (second sheet) (July 1992)

INTERNATIONAL SEARCH REPORT		Int ional Application No
		PCT/GB 02/04121

C.(Continuation) DOCUMENTS CONSIDERED TO BE RELEVANT

Category*	Citation of document, with indication,where appropriate, of the relevant passages	Relevant to claim No.
A	GROENENBOOM J ET AL: "Receiver array ground penetrating radar imaging" IGARSS 2000. IEEE 2000 INTERNATIONAL GEOSCIENCE AND REMOTE SENSING SYMPOSIUM. TAKING THE PULSE OF THE PLANET: THE ROLE OF REMOTE SENSING IN MANAGING THE ENVIRONMENT. PROCEEDINGS (CAT. NO.00CH37120), IGARSS 2000. IEEE 2000 INTERNATIONAL GEOSCIENCE AND, 2000, pages 2368-2370 vol.5, XP010503997 2000, Piscataway, NJ, USA, IEEE, USA ISBN: 0-7803-6359-0 page 2369, left-hand column, line 1-13	1,2
A	US 5 796 253 A (BOSNAR MIRO ET AL) 18 August 1998 (1998-08-18)	

Form PCT/ISA/210 (continuation of second sheet) (July 1992)

page 2 of 2

270

Int   tional Application No
PCT/GB 02/04121

Patent document cited in search report		Publication date	Patent family member(s)		Publication date
US 4417210	A	22-11-1983	FR	2461271 A1	30-01-1981
			FR	2475745 A2	14-08-1981
			AT	4751 T	15-10-1983
			CA	1190599 A1	16-07-1985
			CA	1196689 A2	12-11-1985
			DE	3064918 D1	27-10-1983
			EP	0024961 A1	11-03-1981
			OA	6575 A	31-07-1981
			US	4535293 A	13-08-1985
US 5467018	A	14-11-1995	AU	654945 B2	01-12-1994
			AU	7454091 A	21-10-1991
			CA	2078766 A1	22-09-1991
			WO	9114954 A1	03-10-1991
			JP	5505672 T	19-08-1993
US 5796253	A	18-08-1998	CA	2206173 A1	29-11-1997

271